Additive Manufacturing (3D Print) of Air-coupled Diaphragm Ultrasonic Transducers

Botong Zhu

Department of Electronic and Electrical Engineering

University of Strathclyde

A thesis submitted for the degree of

Doctor of Philosophy

August 2019

Copyright

Signed:

Date:

Acknowledgements

I would first like to thank my primary supervisor Prof James Windmill for all of his support, advice and encourage throughout my PhD. I would also like to express my thanks to Prof Anthony Mulholland for his great pipe organ inspiration and guidance.

I would also like to thank all colleagues in CUE, especially, Dr Benjamin Tiller for his kindly help in 3D printing and Dr Yansheng Zhang for many inspirations about MEMS microphone.

Thanks to all of my friends in Glasgow, particular all members in my band (The Bedtime) - drum Kanghang He, keyboard Chunpeng Li, bass Deyang Guo, rhythm guitar Zhe Wang and saxophone Bolin Song. I am glad to meet you all in this rock city. I will always miss every rehearsal and gig with you.

Lastly but by no means least, thanks to my father Qingcheng Zhu and mother Huaizhen Ma. I can’t be able to finish my PhD without your supports!

Abstract

Air-coupled ultrasound is a non-contact technology that has become increasingly common in Non Destructive Evaluation (NDE) and material evaluation. Normally, the bandwidth of a conventional transducer can be enhanced, but with a cost to its sensitivity. However, low sensitivity is very disadvantageous in air-coupled devices. This thesis proposes a methodology for improving the bandwidth of an air-coupled micro-machined ultrasonic transducer (MUT) without sensitivity loss by connecting a number of resonating pipes of various length to a cavity in the backplate. This design is inspired by the pipe organ musical instrument, where the resonant frequency (pitch) of each pipe is mainly determined by its length. The −6 dB bandwidth of the “pipe organ” inspired air-coupled transducer is 55.7% and 58.5% in transmitting and receiving modes, respectively, which is ∼5 times wider than a custom-built standard device. After validating the concept via a series of single element low-frequency prototypes, two improved designs: the multiple element and the high-frequency single element pipe organ transducers were simulated in order to tailor the pipe organ design to NDE applications.

Although the simulated and experimental performance of the pipe organ inspired transducers are proved to be significantly better than the conventional designs, conventional micro-machined technologies are not able to satisfy their required 3D manufacturing resolution. In recent years, there has been increasing interest in using additive manufacturing (3D printing) technology to fabricate sensors and actuators due to rapid prototyping, low-cost manufacturing processes, customized features and the ability

to create complex 3D geometries at micrometre scale. This work combines the ultrasonic diaphragm transducer design with a novel stereolithographic additive manufacturing technique. This includes developing a multi-material fabrication process using a commercial digital light processing printer and optimizing the formula of custom-built functional (conductive and piezoelectric) materials. A set of capacitive acoustic and ultrasonic transducers was fabricated using the additive manufacturing technology. The additive manufactured capacitive transducers have a receiving sensitivity of up to $0.4\ \mathrm{mV/Pa}$ at their resonant frequency.

Contents

List of Figures

List of Tables

Abbreviations

3D	Three Dimension
AFM	Atomic Force Microscopy
AM	Additive Manufacturing
$BaTiO_3$	Barium Titanate
CAD	Computer-aided design
CMUTs	Capacitive Micromachined Ultrasonic Transducers
CNTs	Carbon Nanotubes
CUE	Centre of Ultrasonic Engineering
DED	Directed Energy Deposition
DLP	Digital Light Processing
EPR	Ethylene Propylene Rubber
FDM	Fused Deposition Modelling
FE	Finite Element
FEA	Finite Element Analysis
FFT	Fast Fourier Transform
Irgacure 819 or I 819	(2, 4, 6-trimethylbenzoyl) Phenylphosphane Oxide
LDV	Laser Doppler Vibrometer
LOM	Laminated Object Manufacturing
MEMS	Microelectronic and Microelectromechanical Systems
MUT	Micromachined Ultrasonic Transducer

MWCNTs	Multiple wall carbon nanotubes
NDT(NDE)	Non-destructive Testing (Evaluation)
PBF	Powder Bed Fusion
$PbTiO_3$	Lead Titanate
PDMS	Polydimethylsiloxane
PEGDA	Poly(ethylene glycol) Diacrylate
PMMA	Poly(methyl methacrylate)
PMN-PT	Lead Magnesium Niobate – Lead Titanate Piezocrystal Material
PMUTs	Piezoelectric Micromachined Ultrasonic Transducers
PVDF	Polyvinylidene Fluorid
PZT	Lead Zirconate Titanate
RVR	receiving voltage response
S1	SUDAN 1
SL	Sheet lamination
SLA	Stereolithography
SNR	Signal to Noise Ratio
SWCNTs	Single wall carbon nanotubes
TMSPM	Copolymer of 3-(trimethoxysilyl) propyl methacrylate
TPP	Two-photon Polymerization
TVR	transmitting voltage response
UAM	Ultrasonic Additive Manufacturing
UV	Ultraviolet

Symbols

$F(F_{RMS})$	(Effect) Force	N
$V(V_{RMS})$	(Effect) Voltage	V
$w(w_{max})$	(Maximum) Displacement	m
α	Absorbance	μm^{-1}
Z	Acoustic Impedance	$MRayl$
AP	Acoustic Pressure	Pa
AG	Amplifier Gain	-
Q	Charge	C
K_n	Constant for Resonance Calculation	-
ρ	Density	kg/m^3
d	Diameter	m
Ep	Electric Potential	MV/m
D_E	Flexural Rigidity	$Pa.m^3$ or $N.m^2$
f	Frequency	Hz
L	Length	m
S_{CS}	Cross-sectional Area	m^2
I	Light Intensity	W/cm^{-2}
d_{xy}	Piezoelectric Coefficient	pC/N or pm/V
μ	Poisson ratio	-

r	Radial Position	m
R	Radium	m
S	Receiving Sensitivity	mV/Pa
t	Time	s
$D(z,t)$	Total Dose of Light	J/cm^{-2}
v	Velocity	m/s
λ	Wavelength	m
wt. %	Weigh Fraction	%
E	Young's modulus	GPa
H_{tf}	Transfer Function of the Amplitude Correction Algorithm	
$G_{SA}(f)$	Record Sensitivity Amplitude	
$G_{RA}(f)$	Amplitude of the Reference Sound Level	

Chapter 1

Introduction

1.1. Project Background and Motivation

1.1.1. Challenges in Air-coupled Technology

Ultrasound has a wide range of applications such as non-destructive testing (NDE), medical imaging and underwater sonar. Conventional liquid coupled ultrasonic transducers require a coupling fluid between the transducer and the testing object to transfer energy more efficiently. Wheel transducer with a solid coupling medium, e.g. rubbers, to couple the ultrasonic waves is becoming popular in recent years. Air-coupled ultrasound is a non-contact technology that has become increasingly common in NDE, as some materials such as wood, foam and missile propellants cannot be contaminated by the coupling gels. In addition, the air-coupled technique can be used to conduct a rapid scan of large area structures or some complex geometries with curving surfaces that the conventional probe finds difficult to contact. More recently, the use of air-coupled technology has been broadened to automatic NDE which integrates the air-coupled transducers with robot arms [1] or drones [2] in order to further enhance efficiency.

However, the primary limitation of the air-coupled technology is the energy losses due to the high attenuation when ultrasound is transmitting in the air and the acoustic impedance mismatch between the air and sample boundary. Usually, more than 99% of the energy

will be lost when the ultrasonic wave is transmitted across the boundary which results in a low signal to noise ratio during air-coupled inspection. There are several standard techniques available to overcome the problem include using high power transmitters to compensate for the reflection loss, combining this with a low-noise preamplifier to increase the receiving sensitivity, utilizing impedance matching layers to match the impedance mismatch between the transducer and the air and using coded ultrasound to boost the transmitting signal strength.

Even though the sensitivity problem can be improved by the solutions mentioned above, the bandwidth of the air-coupled transducer still needs to be improved. A broad bandwidth transducer can achieve better resolution because the pulse width in the time domain is shorter when the bandwidth of the transducer is wider, while the common broadband methods cannot be used in the air-coupled transducer designs. For example, piezoelectric composite transducers have wide bandwidths by optimizing their electrical and mechanical properties [3], [4]. However, the composite transducer has much better performance in water compared to air because the acoustic impedance of the composite piezoelectric material is closer to that of water. Another solution to this is to add matching layers or damping materials to broaden the frequency response around resonances [4]. However, the sensitivity of the air-coupled device should not be allowed to be further reduced. The micromachined ultrasonic transducer (MUT) is a relatively new concept in the field of ultrasonic transducer technology that has been proved to have the potential for air-coupled NDE. The MUT has a thin flexible membrane to transmit and receive ultrasound which is easier to couple with the air, with a more closely matched acoustic

impedance. This thesis is focused on proposing, designing and fabricating several advanced MUTs to solve the limitations in air-coupled ultrasound technology.

1.1.2. Additive Manufacturing (AM) of Air-Coupled Ultrasonic Transducers

Piezoelectricity is described as the electric charge accumulating in certain classes of crystalline materials in response to the external mechanical stress. Conversely, when an electric field is applied, the crystalline structure will change its shape. Piezoelectric ceramic materials have been fabricated into different shapes like a rod, plate, and thin film in order to tailor the materials to numerous applications, e.g. strain gauges, actuators, microphones and ultrasonic transducers. The shape of the piezoelectric material can directly determine the transducer types and applications. For example, conventional manufacturing of a piezoelectric composite transducer is achieved by the dice and fill technique which uses a dicing machine to cutting small channels on a bulk ceramic, this then fills the channels with a passive polymer. In addition, the MUT is frequently fabricated by a sacrificial layer release process. Initially, a sacrificial layer is coated on the substrate. After finishing the fabrication and patterning the flexible membrane layer, the sacrificial layer is disolved through a small opening hole to form the air cavity below the membrane. With the development of finite element analysis (FEA) technology, some complex geometry ultrasonic transducers have been proposed to enhance the performance e.g. nature inspired piezoelectric transducers with wider bandwidth and higher sensitivity [3], musical instrument inspired transducer proposed by the author that can achieve

broader bandwidth without sensitivity loss [5]. However, they are difficult to be manufactured by conventional manufacturing processes.

In recent years, there has been increasing interest in using AM technology (also known as 3D printing) in the fabrication of sensors owing to the possibility to create complex 3D geometries at micrometre-scale using flexible polymers. After integrating multiple nano-fillers with the passive base polymer, the AM nano-composite can exhibit different properties like conductivity [6] or piezoelectricity [7]–[9] which allow the transduction of mechanical energy into electrical form. Many reports of actuators [10], [11] and sensors [8], [12]–[15] were fabricated by using AM printer using functional resins. However, state-of-the-art AM air-coupled transducers (acoustic sensors) show limitations in miniaturization, repeatability (fabrication issue) and sensitivity.

1.2. Aim and Objective

The aim of this thesis is to explore new methods to improve the performance of current air-coupled transducer design, in terms of bandwidth and sensitivity, using pipe organ inspired structures. The improved air-coupled transducers are then fabricated using a novel additive manufacturing technique due to their complex 3D structures. Finally, the performance of the AM transducers is characterized by experiment. The following tasks are addressed in order to achieve the above three objectives.

- Understanding the principle of ultrasound, ultrasonic transducers, modelling and additive manufacturing technologies.

- Seeking nature inspiration as a mechanism for improving the ultrasonic transducers, in particular aiming to achieve improvements in sensitivity and bandwidth.
- Simulating novel and conventional transducer designs for comparison by using a commercial FE software COMSOL MULTIPHYSICS. The steps above are iterative until promising results that prove better performance are found.
- Exploring novel additive manufacturing technology to fabricate ultrasonic transducers with complex 3D structures, which includes developing high-resolution and functional materials and the multi-material 3D printing technology.
- Experimentally characterizing the performance of the novel transducers and then comparing against conventional products.

1.3. Contribution to Knowledge

The contribution of this PhD thesis includes proposing the "pipe organ" inspired ultrasonic diaphragm transducer design and implementing the novel stereolithography additive manufacturing technique in diaphragm transducer fabrication.

The pipe organ inspired ultrasonic diaphragm transducer can provide a significantly improved bandwidth without sensitivity loss in both transmitting and receiving. The list below describes the main contribution in the pipe organ transducer section.

- Present a methodology for improving the bandwidth of air-coupled PMUTs without sensitivity loss by connecting a number of resonating pipes of various

length to a cavity. A prototype piezoelectric diaphragm ultrasonic transducer is presented to prove the theory.

- The behaviour of the pipe organ transducers was investigated by an FE Comsol model and math equations. The pipes length and positions were optimized by using the same FE model.
- The main part of this novel device was fabricated by additive manufacturing (3D printing) and consists of a PVDF thin film over a stereolithography designed backplate.
- The -6dB bandwidth of the "pipe organ" air-coupled transducer is 55.7% and 58.5% in transmitting and receiving modes, respectively, which is ~5 times wider than a custom-built standard device. The central frequencies of the vertical and orientated pipes transducers prototypes are 27 kHz and ~50 kHz respectively.
- Proposed two advanced approach, which are firstly a multiple element pipe organ with ~50 kHz frequency range, and secondly a single element pipe organ PMUT with ~500 kHz, in order to tailor the original pipe organ design to NDE applications and then use the commercial Finite Element (FE) software COMSOL MULTIPHYSICS to optimize the designs. Limited by the manufacturing resolution available during this work, both designs cannot be prototyped immediately.

The author implements the high-resolution stereolithography additive manufacturing technology in the ultrasonic diaphragm transducer manufacturing. The detail contributions are listed below.

- The AM capacitive transducer encompasses the development of a capacitive diaphragm transducer, including its fabrication process using a commercial digital light processing printer and output signal characterization with a custom-made amplification circuit.
- A set of capacitive diaphragm transducers was fabricated and tested using different diaphragm diameters from 1.8-2.2 mm, for comparison, with a central operating frequency between $19 - 54$ kHz, respectively.
- This capacitive diaphragm transducer design has a receiving sensitivity of up to $0.4\ \mathrm{mV/Pa}$ at its resonant frequency, and a comparison with a commercial reference microphone is provided.
- The formula of the AM piezoelectric material was optimized for diaphragm transducer applications. The piezoelectric property of the AM nanocomposite material was found to be $\sim 5\ \mathrm{pm/V}$ which is much lower than that of the conventional piezoelectric materials.

1.4. Publications

All publications have been attached in appendix 1.

Peer-reviewed Journals

- B. Zhu, B. Tiller, A. J. Walker, A. J. Mulholland, J. F. C. Windmill, ""Pipe Organ" Inspired Air-Coupled Ultrasonic Transducers With Broader Bandwidth" IEEE Trans. Ultrason. Ferroelectr. Freq. Control, 65 (10), pp. 1873-1881, 2018.

- B. Zhu, J. Guerreiro, Y. Zhang, B. Tiller, J. F.C. Windmill, "Additive Manufacturing (AM) Capacitive Acoustic Transducer Using a Commercial Direct Light Processing (DLP) Printer" IEEE Sens J, Accepted at 10/2019
- B. Tiller, A. Reid, B. Zhu et al., "Piezoelectric microphone via a digital light processing 3D printing process" Material & Design, 165, pp. 1-27, 2019.

Conferences Publications

- B. Zhu, B. Tiller, A. J. Walker, A. J. Mulholland, J. F. C. Windmill, ""Pipe Organ" Air-Coupled Broad Bandwidth Transducer," IEEE International Ultrasonics Symposium (IUS), pp. 1–4, 2017.

1.5. Thesis Structure

The thesis is comprised of a further 6 chapters:

Chapter 2 has a literature review of micromachined ultrasonic transducers (MUTs) and additive manufacturing technologies. In particular, the MUTs design criteria, state of the art broad bandwidth transducers, the principle of the stereolithography AM printer and stereolithography nanocomposite resins were introduced in detail.

Chapter 3 proposed a novel transducer design, which is called "pipe organ" inspired transducer, to improve the bandwidth of air-coupled diaphragm transducer. Firstly, the pipe organ inspired backplate design was simulated and studied by using an FEA COMSOL model. And then introduced the manufacturing technique for the stereolithography pipe organ inspired backplate, an improved resin formula, and the rest

of the fabrication steps of prototypes using the stereolithography backplate and commercial polyvinylidene fluoride (PVDF) thin film. Finally, the performance of this air-coupled transducer was fully characterized and compared with a custom-built conventional diaphragm transducer.

Chapter 4 proposed the multiple element pipe organ inspired transducer design to further enhance the overall sensitivity and bandwidth and the miniaturized single element pipe organ transducer design to increase the central frequency to NDE applications (500 kHz). Both designs were validated by using an FEA software and the simulated results were promising.

Chapter 5 introduced a novel methodology that encompassed the development of a capacitive acoustic transducer, including its fabrication process using a commercial digital processing printer and output signal characterization with a custom-made amplification circuit. A set of capacitive acoustic transducers was fabricated and then tested against the commercial capacitive transducer.

Chapter 6 evaluated the piezoelectric coefficient of the nanocomposite thin films in order to optimize their formulation for SLA AM application. Previous studies reported that adding MWCNT to the polymer matrix could significantly enhance the d_{33} of the two-phase (piezo-powder/polymer) nanocomposite. However, this reported promising result could not be repeated in this work.

Chapter 7 included a number of conclusions based on the results from Chapter 3, 4, 5 and 6. It also makes several suggestions for the short and long term future works respectively.

Chapter 2

Review of the Ultrasonic Transducers and Additive Manufacturing Technologies

2.1. Review of Micromachined Ultrasonic Transducers (MUTs)

2.1.1. Introduction

Ultrasonic transducers have many applications where the most well known two are non-destructive evaluation (NDE) and medical imaging. With the development of micromachined technology, some researchers [16]–[20] started to micro-machine small transducer elements which are easier to integrate with electronic components. The micromachined ultrasonic transducers (MUTs) have a thin flexible film to transmit and receive ultrasound. The MUTs' family includes capacitive micromachined ultrasonic transducers (CMUTs) as shown in Figure 2.1 (a) and piezoelectric micromachined ultrasonic transducers (PMUTs) as shown in Figure 2.1 (b).

The CMUT is a miniaturised capacitor which consists of a one-side-metalised dielectric thin film, rigid and conductive backplate and an air gap between the film and the backplate as shown in Figure 2.1 (a). Initially, a DC voltage is applied between the conductive film and the backplate, generating an electrostatic force to attract the thin film toward the

backplate and bias the capacitive transducer. When an AC voltage is applied across the bias electrodes, the vibrating membrane will compress the air and generate ultrasound waves. In contrast, when the receiving ultrasonic wave is applied to the membrane, the transducer will output an AC signal as the capacitance of the transducer changes.

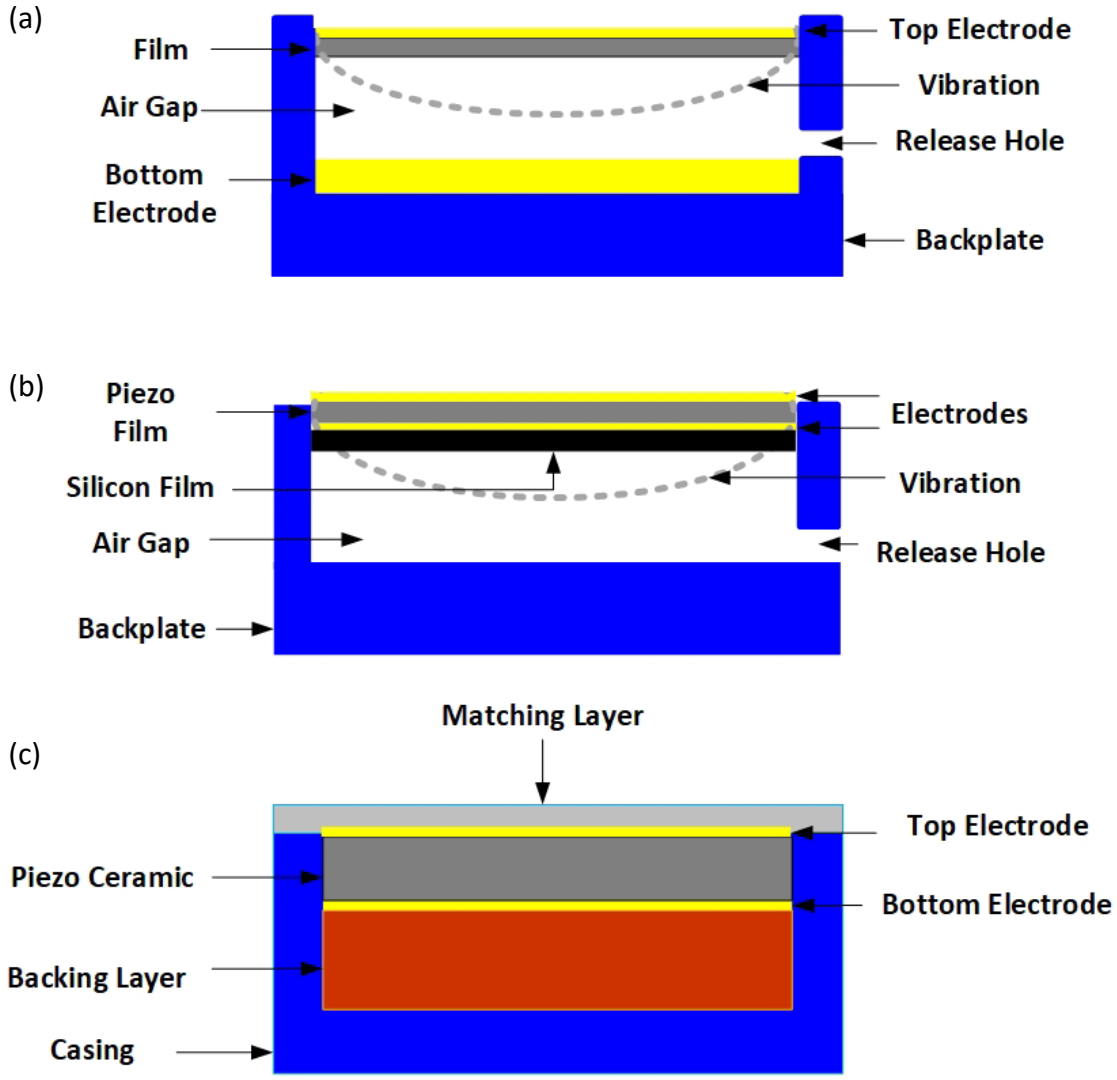

Figure 2.1. Schematic of (a) CMUT (b) d_{31} mode PMUT (c) d_{33} mode Bulk Ceramic transducer

Similar to the CMUT, the PMUT utilises a piezoelectric layer on the top of a silicon membrane and operates in a flexural mode as shown in Figure 2.1 (b). After applying an electrical field to the thin plate, the lateral strain makes the piezoelectric thin film bend. The vibrating membrane compresses the air and produces ultrasound. In contrast, the received ultrasound wave vibrates the film which causes charge migration between the two electrodes on the piezoelectric layer, which then can be detected by a receiving circuit [21]. The deflection of the PMUTs' membrane is caused by lateral strain generated from the piezoelectric effect (d_{31} mode) of its piezoelectric layer [18]. The different vibration mechanism provides PMUTs with a larger transmission sensitivity than CMUTs, and furthermore, no bias voltage is required [18], [22].

Figure 2.1 (c) is a conventional bulk ceramic ultrasonic transducer which is fabricated with a thick block of piezoelectric material such as PZT with top and bottom electrodes. This type of transducer utilises longitudinal vibration mode (also known as d_{33} mode) of the bulk piezoelectric ceramic to transmit or receive ultrasound. Normally, the bulk ceramic transducer is not suitable for non-contact detection in air because of impedance mismatch. The acoustic impedance of the typical piezoelectric material used in bulk ceramic transducer, e.g. PZT-5H is 31-35 $MRayl$, and the air as a coupling media is $0.413\ MRays$ which results in more than 99% energy loss because of the ultrasound reflection. Moreover, the bandwidth of bulk ceramic transducer is also reduced when working in the air [18]. MUTs have better performance in the air than the conventional piezoelectric bulk transducers because the flexible film is easier to couple with the media,

with a more closely matched mechanical impedance. Further, as the film stores much less kinetic energy than the bulk piezoceramic, the MUTs have larger bandwidths when in resonance [4].

2.1.2. Modelling of a MUT Structure

The structure of a typical MUT introduced in the above section can be simplified as a classic mass-spring-damper model as shown in Figure 2.2 (a) and the key parameters of MUT modelling are given in Figure 2.2 (b).

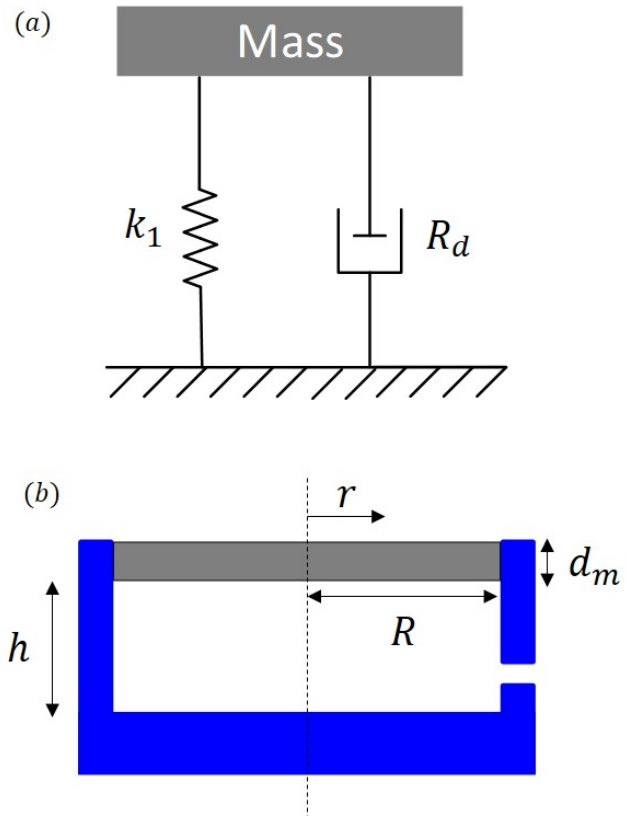

Figure 2.2. (a) Simplified mass-spring-damper model of a typical MUT structure and (b) key parameters in MUT modelling for a cylindrical geometry

The total pressure applied on the circular thin film can be calculated by $P = P_{atm} + P_e$, where the P_{atm} and P_e are the atmospheric and electrostatic pressure, respectively. For a uniform pressure, the deflection of a thin film can be expressed as a function of the radial position r (see equation (2.1)) [23]. R is the radius of the thin plate, P is total pressure and D_E is the flexural rigidity of the circular thin plate.

$$w(r) = \frac{PR^4}{64D_E}\left(1 - \frac{r^2}{R^2}\right)^2 \tag{2.1}$$

The flexural rigidity (D_E) is related to the thickness and material property of the thin film which is given by (2.2), where d_m is the thickness of the thin film, ρ is the density of the thin film, E is Young's modulus and μ is the Poisson ratio.

$$D_E = \frac{Ed_m^3}{12(1-\mu^2)} \tag{2.2}$$

For equation (2.1), the maximum deflection occurs at the centre of the diaphragm ($r = 0$). Then the equation of peak displacement w_{max} is given by (2.3). The averaged displacement (2.4) of the transducer can be derived by integrating (2.1) over the entire flexible area ($A = \pi R^2$).

$$w_{max} = \frac{PR^4}{64D_E} \tag{2.3}$$

$$w_{ave} = \frac{1}{A}\int_0^R 2\pi r\, w(r)dr = \frac{1}{3}w_{max} \tag{2.4}$$

Equation (2.4) can be rewritten as a format of Hooke's law (2.5). Therefore, the equivalent spring constant of the film can be illustrated as in (2.6).

$$w_{ave} = \frac{R^4}{192 D_E} P = \frac{R^2}{192 \pi D_E} F \tag{2.5}$$

$$k_1 = \frac{192 \pi D_E}{R^2} \tag{2.6}$$

The intrinsic stress of the thin plate is the factor that may affect the resonant frequency of the transducer. When the transducer has an edge-clamped film with low intrinsic stress, the fundamental resonant frequency of the thin circular plate (f_{tp}) can be estimated by plate theory (2.7) [18], where K_n is a constant and takes the value 10.22 for a clamped circular thin film in the fundamental resonance mode and ρ is the density of the thin plate.

$$f_{tp} = \frac{K_n}{2\pi R^2} \sqrt{\frac{D_E}{\rho d_m}} \tag{2.7}$$

2.1.3. Higher Resonance of MUTs

Kinsler [24] describes the mode shapes of a clamped circular membrane and names each mode by two integers (m, n) as shown in Figure 2.3, where the integer m is the number of radial nodal lines and the integer n is the number of nodal circles. The node is a point (or a line) on the membrane that does not move while the membrane is vibrating. There is a $180°$ phase difference between two adjacent red regions which are the maximum positive and negative positions. The nodal line separates the adjacent red areas. f_{tp} is the resonant frequency of the $(0,1)$ mode and the resonant frequency of higher modes are all relate to the fundamental modes (as shown in Table 2.1).

Table 2.1. Higher resonant frequencies modes of the clamped circular thin film with low intrinsic stress [24]

Name of modes	Resonant Frequency
(0,1)	f_{tp}
(1,1)	1.59 f_{tp}
(2,1)	2.14 f_{tp}
(0,2)	2.30 f_{tp}
(3,1)	2.65 f_{tp}
(1,2)	2.92 f_{tp}
(4,1)	3.16 f_{tp}
(2,2)	3.50 f_{tp}

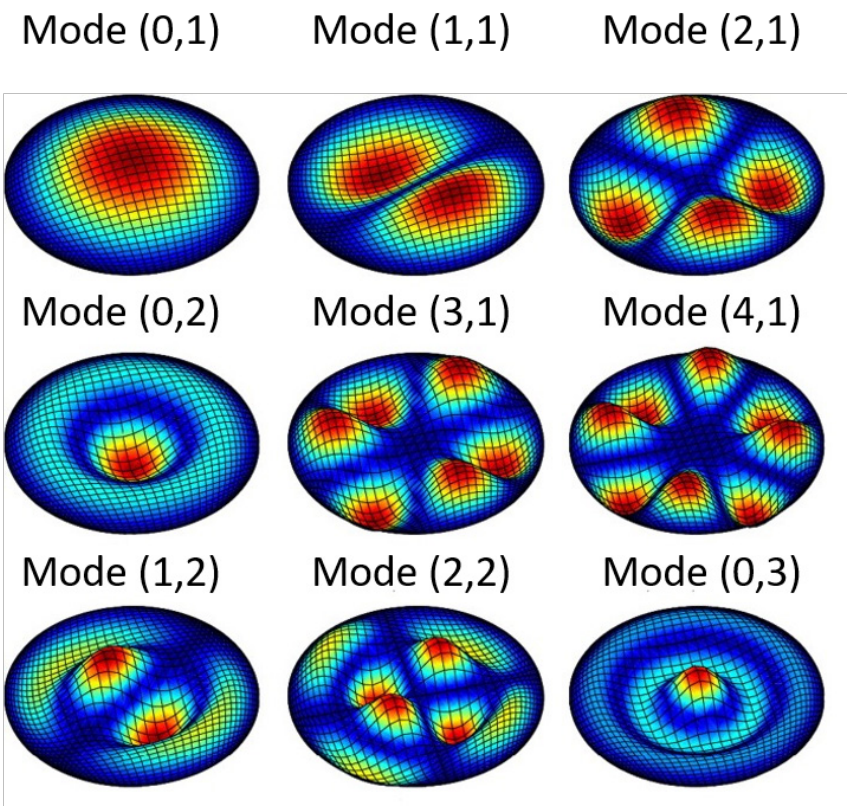

Figure 2.3. Vibrating modes of clamped circular membrane [25]

2.1.4. Laser Doppler Vibrometry (LDV)

The micro-scanning laser Doppler vibrometry (LDV) is a widely used technology to investigate the mechanical response of vibrating surface or body. In this thesis, this equipment was used in studying the mechanical response of the diaphragm transducers in Chapter 3 and 5 and characterize the piezoelectric property of piezoelectric thin film in Chapter 6. The Doppler effect is the fundamental theory of this device which defines that if a wave is reflected by a moving body and then detected by an instrument, the wave will have a frequency shift as shown in equation (2.8), where v is the object's velocity, λ is the wavelength of the laser. For a LDV, the wavelength of the laser wave is known. The velocity of the object can be conversely determined when the Doppler frequency shift f_D is measured and the wavelength is known. This process is done by a laser interferometer which will be introduced below.

$$f_D = \frac{2v}{\lambda} \tag{2.8}$$

The schematic diagram of the component of an LDV is shown in Figure 2.4 [26]. The laser generating by the helium-neon laser head is split into two coherent laser beams, which are named as Reference Beam (RB, blue arrow) and Measure Beam (MB, red arrow) respectively, after passing through the beam splitter BS1. The reflect optics are used to focus the measuring surface via manually adjusting the distance between lens and object.

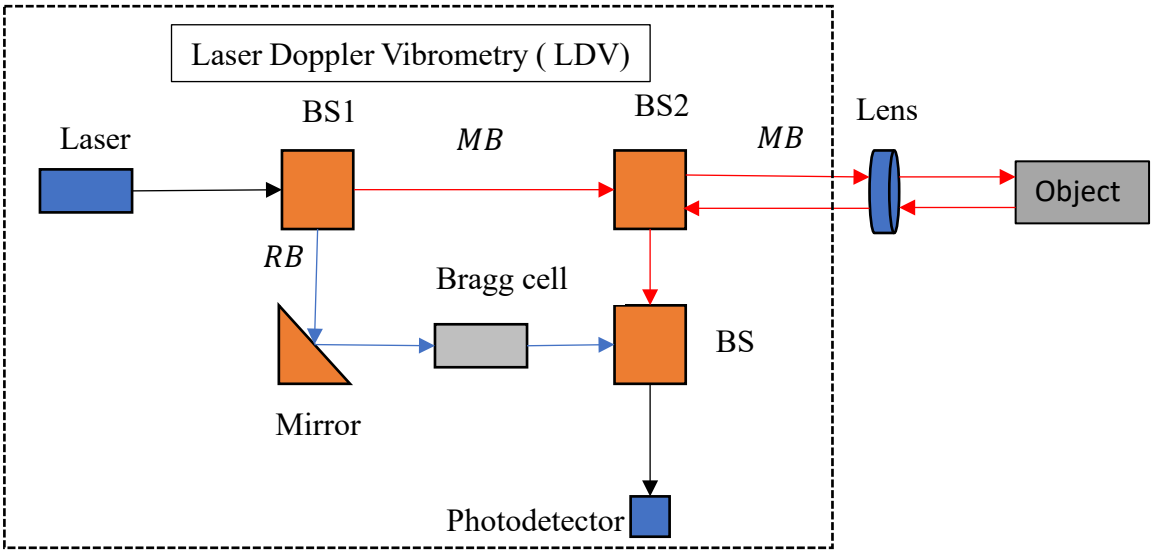

Figure 2.4. Internal component of an LDV. The schematic is modified by [26]

The MB laser is reflected back by the sample, re-entered the LDV, passed through the BS2, overlapped with RB in BS3 and finally detected by the photodetector. The total intensity of both beams can be evaluated by the interferometry equation (2.9), where the I_{RB} and I_{MB} are the light intensity, $L_{MB} - L_{RB}$ is the path length difference between the measurement beam and the reference beam. Assuming the thermal effect is negligible, the L_{RB} remain constant and the L_{MB} varies regarding to the vibration of the object. The photodetector will detect the total light intensity change (dark/light pattern) because of the interferometer. The frequency of light/dark cycle determined by the photodetector is proportional to the velocity of the sample.

$$I_{total} = I_{RB} + I_{MB} + 2\sqrt{I_{RB} I_{MB} * \cos\left[2\pi(L_{MB} - L_{RB})\lambda\right]} \qquad (2.9)$$

In order to determine the moving direction of the object, an acousto-optic modulator called Bragg cell is placed in the reference beam to shift the light frequency by 40 MHz. The

detected modulation frequency becomes lower than 40 MHz when the sample moves toward the interferometer, whilst the frequency is higher than 40 MHz when the sample moves away from the interferometer.

2.1.5. Broad Bandwidth Ultrasonic Transducers

The axial resolution of ultrasound instruments improves by increasing the transducer's frequency, bandwidth and some other factors like focal length, F-ratio, element size and sector scanning modes. This section will explain why the bandwidth of the transducer can affect the imaging resolution and then introduce several state-of-art broad bandwidth ultrasonic transducer designs.

2.1.5.1. Background

The bandwidth of an ultrasonic transducer is usually a nominal distribution in the frequency domain. The majority of the energy emitted from an ultrasonic transducer will stay on its central frequency (fundamental resonant frequency), and the rest of the energy will remain on the surrounding frequencies [27]. The Fast Fourier Transform (FFT) is an algorithm to express any time domain signal in the frequency domain. Some examples of FFT between common time domain and frequency domain signals are given in Figure 2.5 left and right columns respectively. Figure 2.5 (a) is a continuous 2 MHz sine wave with infinitely long cycles in the time domain and its frequency domain signal can be expressed with all of the energy concentrating at 2 MHz with an amplitude the same as the time domain signal. Figure 2.5 (b) is a 2 MHz sine wave with 5 cycles and its frequency domain expression is shorter and broader than Figure 2.5 (a). Figure 2.5 (c) is a 2 MHz Gaussian

sine pulse with 3 cycles, and the frequency response of this wave is even flatter and shorter than Figure 2.5 (b). Figure 2.5 (d) indicates that a pulse has ultra-wide bandwidth and low amplitude in the frequency domain if the time domain signal is very short.

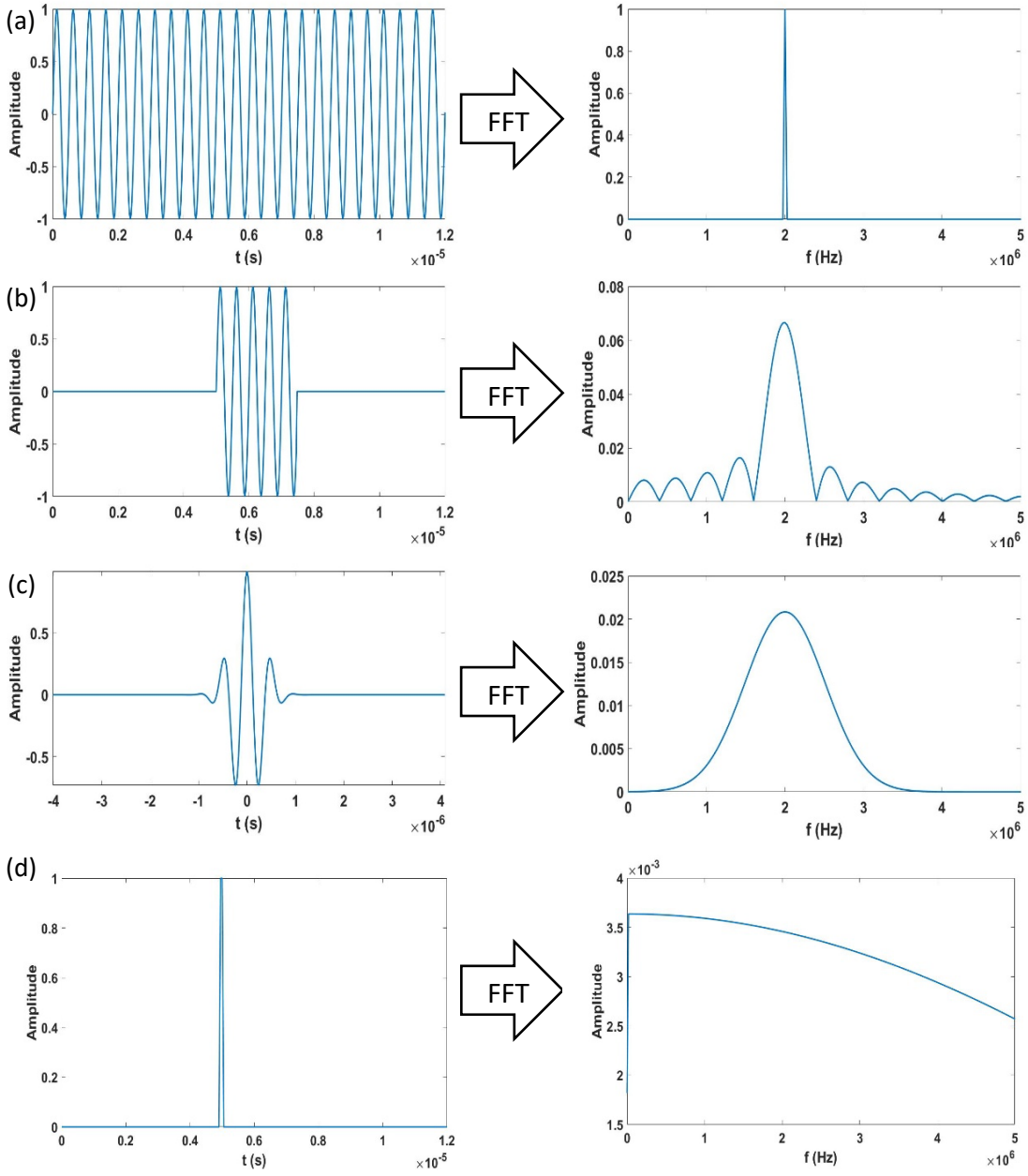

Figure 2.5. Some examples of Fast Fourier Transform. The bandwidth increase and amplitude (energy) decrease as pulse duration decrease.

In conclusion, the bandwidth increase and amplitude (energy) decrease in the frequency domain as the pulse duration decreases in the time domain. With the FFT algorithm, the bandwidth of an ultrasonic transducer can be evaluated by transforming its time domain output signal to the frequency domain as shown in Figure 2.6. The –6 dB bandwidth is usually expressed as the frequency range where the transducer's efficiency is more than half of its maximum, where f_1 and f_2 are the cut-off frequencies and the f_c is the central operating frequency. In addition, the -6 dB bandwidth of a transducer can be also expressed by (2.10).

$$Bandwidth = \frac{f_2 - f_1}{f_c} \tag{2.10}$$

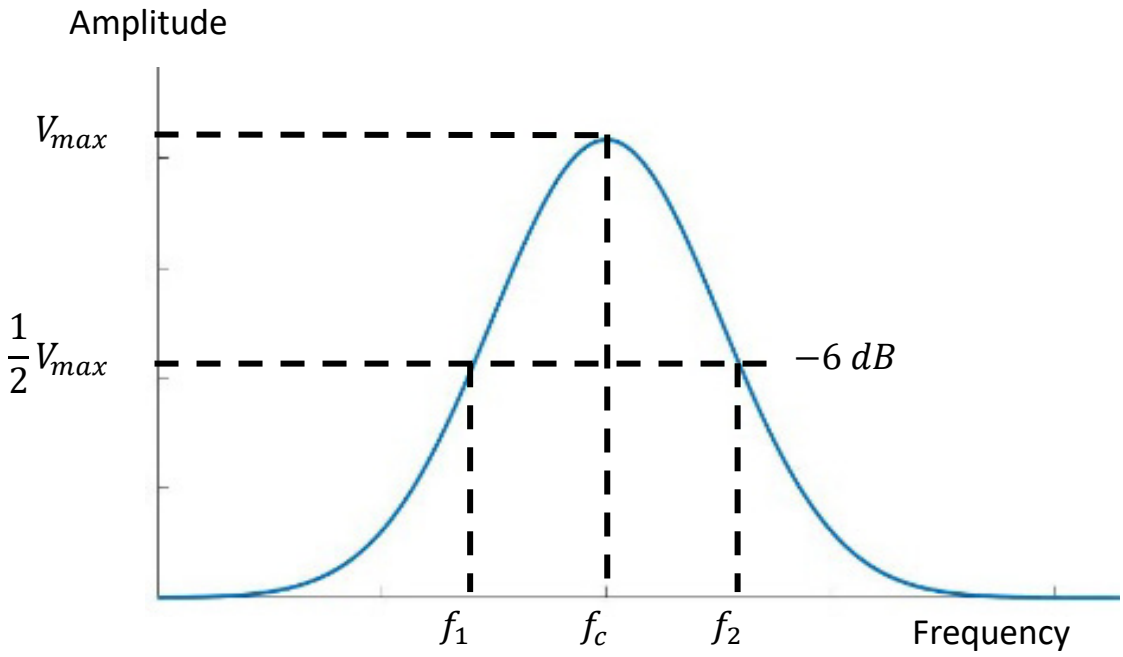

Figure 2.6. The -6 dB bandwidth of a transducer is the range between $f_1$and f_2. Where the f_c is the central frequency that the transducer can generate maximum energy and f_1 and f_2 are the cut-off frequencies at which the transducer can generate half of the maximum energy.

The effect of resolution improvement corresponding to pulse length can be explained from Figure 2.7. The schematic illustrates a reflecting wave from a testing sample with the thickness of d. When the pulse length of the narrow bandwidth signal is longer than $2d$ as shown in Figure 2.7 (a), the thickness of sample d cannot be evaluated from the reflecting signal because the reflecting signals from face A and B are overlapped. In contrast, when the pulse length is much shorter than $2d$ as shown in Figure 2.7 (b), the reflected echoes allow evaluation of the thickness d by calculating the time of flight. In conclusion, a short pulse signal which is usually generated by a broad bandwidth transducer can enhance the resolution due to less overlap. Users can therefore distinguish different reflecting signals easily.

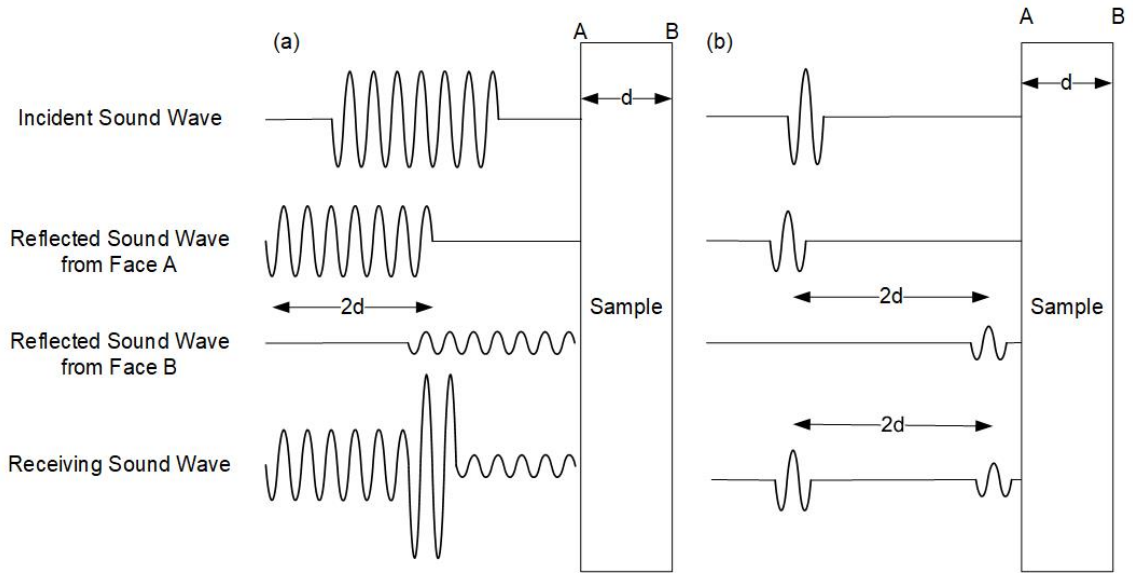

Figure 2.7. Schematic to explain the effect of resolution improvement corresponding to pulse length. (a) Narrow bandwidth (long pulse) and (b) wide bandwidth (short pulse) to measure the thickness of the sample.

2.1.5.2. State of Art Broad Bandwidth Transducers

As the benefits of using wide bandwidth transducers have been introduced above, ultrasonic transducers with a large frequency bandwidth are generally preferred [18], [19]. Bulk ceramic piezoelectric transducers have dominated ultrasound technology for decades, however, they are limited by relatively narrow bandwidth. The concept of the "piezoelectric composite transducer" was established to enhance the bandwidth of the bulk ceramic transducer [28][29]. The ultrasonic composite transducer comprises a piezoelectric phase and a passive phase which can improve the sensitivity and be easier to match with low acoustic impedance media. Figure 2.8 shows a conventional 1-3 piezoelectric composite ultrasonic transducer where the red squares are the active phase (piezoelectric pillars), and the blue part is the passive phase (polymer). There are three standard methods [30] to improving the bandwidth of piezoelectric ceramic transducers. (1) Enhance the properties of the piezoelectric material, e.g. using PMN-PT piezoelectric single crystal material [31] or a circular piezoelectric plate with gradient piezoelectric constant [32]. (2) Adding matching and backing layers to damp the displacement and so result in broader frequency response around the central frequency. Nevertheless, this will decrease the sensitivity of the transducer. (3) Optimise the structure of the pillar [28][29] or replace the pillars with piezoelectric fibres [33], but this requires stricter fabrication constraints.

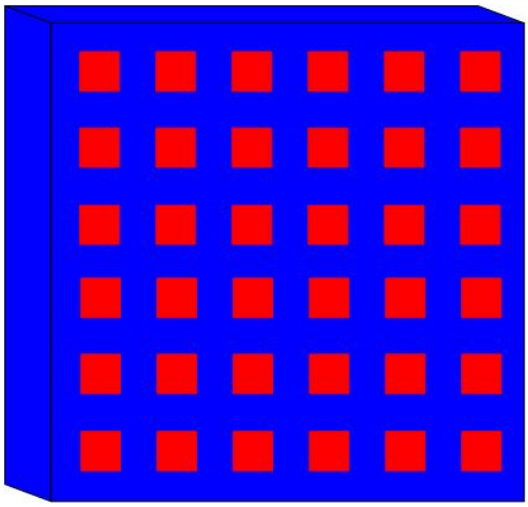

Figure 2.8. Schematic of 1-3 piezoelectric composite transducer where the red parts are the active phase (piezoelectric pillars) and the blue part is the passive phase (polymer).

Whereas the piezoelectric bulk transducers use thickness mode resonances, the micromachined ultrasonic transducers (MUTs) have a thin flexible film to transmit and receive ultrasound. MUTs have better performance in the air because the flexible film is easier to couple with the media, with a more closely matched mechanical impedance. Furthermore, as the film stores much less kinetic energy than a bulk piezoceramic, the MUTs have larger bandwidths when in resonance [4].

CMUTs can achieve a remarkable bandwidth of more than 100%, however, the transmitting power is much weaker than the bulk ceramic transducer when both of the transducers are well coupled by couplants [19]. CMUTs can still provide higher transmitting power in air. Ultrasonic imaging applications, especially for air-coupled technology, require high transmitting pressure to achieve better signal to noise ratio and better penetration. The collapse mode was proposed during the last decade to enhance the transmitting power of CMUT without sacrificing bandwidth [34]. The bias voltage enables

a static deflection of the membrane toward the backplate, and the level of diaphragm deflection (volume of air-gap) changes with a different bias voltage. When CMUTs operate in a collapse mode, the bias voltage should be higher than the collapse voltage and the centre of the membrane is in contact with the bottom electrode at all times. Figure 2.9 shows the conventional and collapse operating mode of CMUTs.

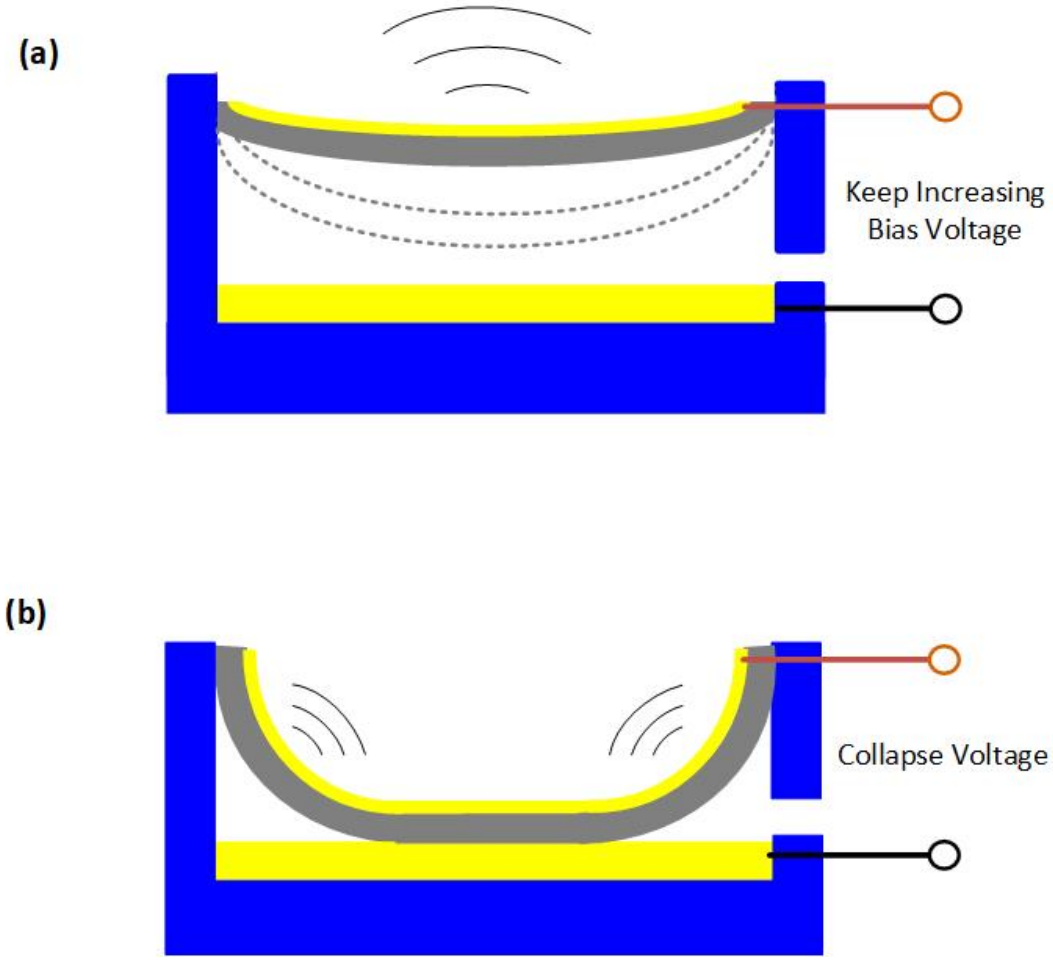

Figure 2.9. (a) Conventional and (b) collapse operating mode of CMUT. The volume of air will change when applying a different bias voltage. The diaphragm will collapse when the bias voltage is higher than the collapse voltage.

In the conventional mode as shown in Figure 2.9 (a), the membrane has a piston-like flexure vibration as the centre of the layer is free to vibrate. In contrast, the centre of the layer is supported by the backplate and only the doughnut-shaped area of the layer can vibrate during the collapse mode. Thus, the collapse mode can be considered as the $(0,2)$ vibrating modes of the circular clamped diaphragm (as shown in Figure 2.3). Therefore, the transducers can work across a higher frequency range when operating in collapse mode.

Compared with the conventional and collapse modes of CMUTs, the PMUT does not require any bias voltage, and no collapse mode exists. Hence, the bandwidth of conventional PMUTs are narrow [18],[22],[16], thus making them unsuitable for wide bandwidth applications [19],[35]. A PMUT's bandwidth can be broadened by applying some modified structures [18],[36].

T. Wang *et al.* [19] reported that rectangular shape PMUTs have a broader bandwidth than circular devices by merging multiple resonant modes when working in high damping media like water. Unlike the vibration modes of the circular membrane given in Figure 2.3, the associated resonant mode shapes of a rectangular membrane (see Figure 2.10 (b) [19]) are different, and its resonant frequencies (see Figure 2.10 (a) [19]) are close to each other. When the PMUT works under water, all of the resonant modes are merged because the water damps the displacement of the thin film. The -6dB bandwidth is measured as 95% with a central frequency of 1.24MHz. However, the square, rectangular and circular membrane is well discussed for MEMS or CMUTs. There is evidence [37] that proves that the square or rectangular membrane has smaller displacement compared with the circular membrane under the same level of sound (ultrasound) pressure. In other words,

the rectangular PMUTs trade off sensitivity to achieve broader bandwidth. Moreover, the rectangular membrane cannot achieve broad bandwidth when operating in air.

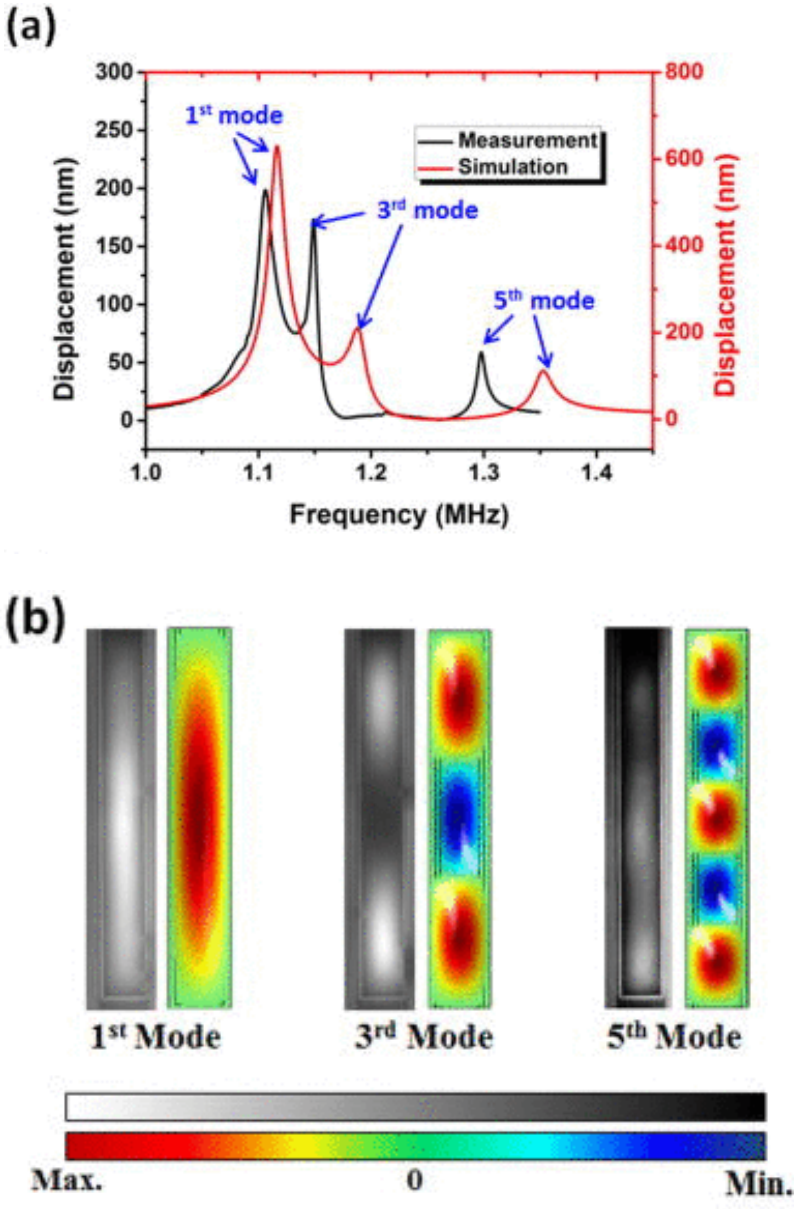

Figure 2.10. (a) Frequency response of the air-coupled rectangular shape PMUT. (b) Experimental and simulated displacement of 1st 3rd and 5th *mode* [19].

Hajati et al. [38] proposed a method to broaden the bandwidth of PMUTs by overlapping and arranging the frequency spectrum of membranes of different size and shape as shown in Figure 2.11 [38]. The measured -3 dB bandwidth can reach 55% when working underwater. However, Wang *e.t. al* [19] suggested that this broad bandwidth is not available in an individual pixel.

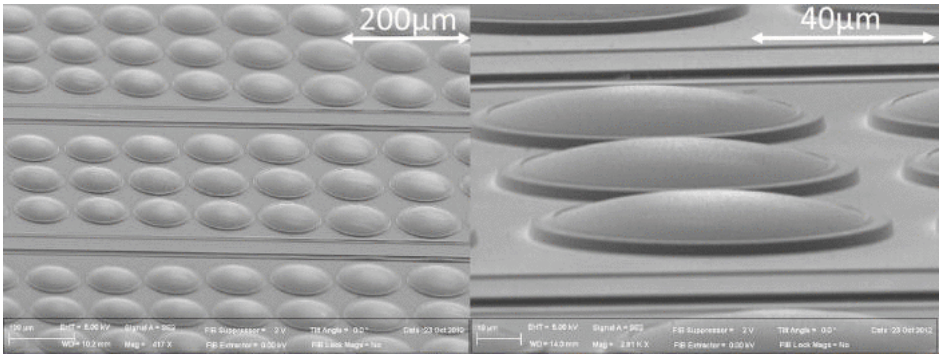

Figure 2.11. SEM and optical images of a 64 channel 5 MHz linear array exploiting five different dome sizes with cavities ranging from 74 to 90 µm diameter [38].

2.2. Review of Additive Manufacturing Technologies

2.2.1. Introduction

Additive manufacturing (AM), which is also known as 3D printing, can create a complex 3D geometry by adding materials layer by layer, whether the material is plastic, metal, or concrete. The manufacturing process starts from using a 3D modelling software, e.g. Computer Aid Design (CAD), to build the 3D model, slicing the 3D model into 2D images. Once the slices are produced, the AM printer reads the data from images and creates successive layers from liquid resin, powder, metal sheet or other materials, adding layer-

upon-layer to fabricate the 3D structure. More recently, AM has been commercialized to fabricate end-use products, e.g. aircraft components, customized hearing aids, jewellery, dental restorations, or even human organs [39]. Although the public likes to use "3D printing" as a synonym to name all of AM processes, there are actually seven categories of AM printer defined by International Organization for Standardization ISO/ASTM52900-15 [40], as described below.

Material Jetting

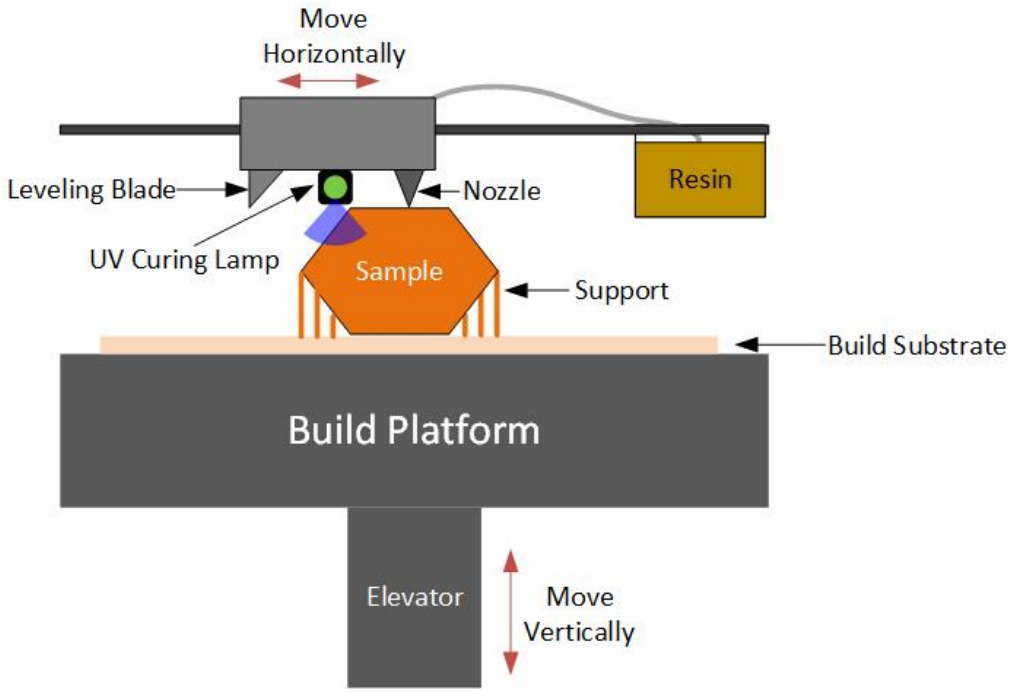

Figure 2.12. Schematic of the material jetting additive manufacturing technology

The working process of the material jetting printer (as shown in Figure 2.12) is similar to a 2D inkjet printer, such that the material is directly jetted on the building stage or the sample surface. When the last layer is solidified by exposing under the ultraviolet (UV) light, the building stage moves down and prints the next layer. The process repeats until

the build is completed. The material is deposited from a nozzle that is perpendicular to the building stage. The complexity of the machines and the methods of controlling the material deposition might be different. Usually, the nozzle can only move in the horizontal plane, and the building stage can move in the vertical plane.

Binder Jetting

Different to the material jetting technique's use of photopolymer as printing materials, the binder jetting process uses a powder form material and a liquid form binder during the additive manufacturing. As shown in Figure 2.13, the roller spreads the powder material over the building platform evenly. The inkjet deposits a layer of the binder with a specific shape on the top of powder layer as an adhesive. Then lowers down the build platform and applies the next layer of powder. Repeating the process until the entire object is completed.

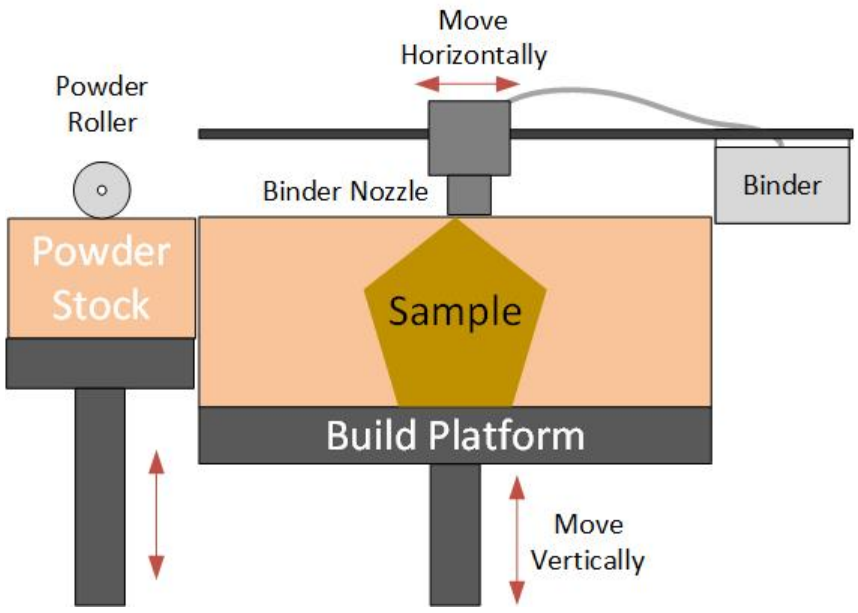

Figure 2.13. Schematic of the binder jetting additive manufacturing technology

Material Extrusion

Material Extrusion, which is usually known as the trademark term fused deposition modelling (FDM), is one of the most common commercialized AM processes. Similar to the material jetting printer, the FDM printer (see Figure 2.14) also includes a nozzle and build platform structure. The printing material, usually a continuous filament or thermoplastic material, is heated up by a coil, fed to the nozzle and then deposited layer by layer.

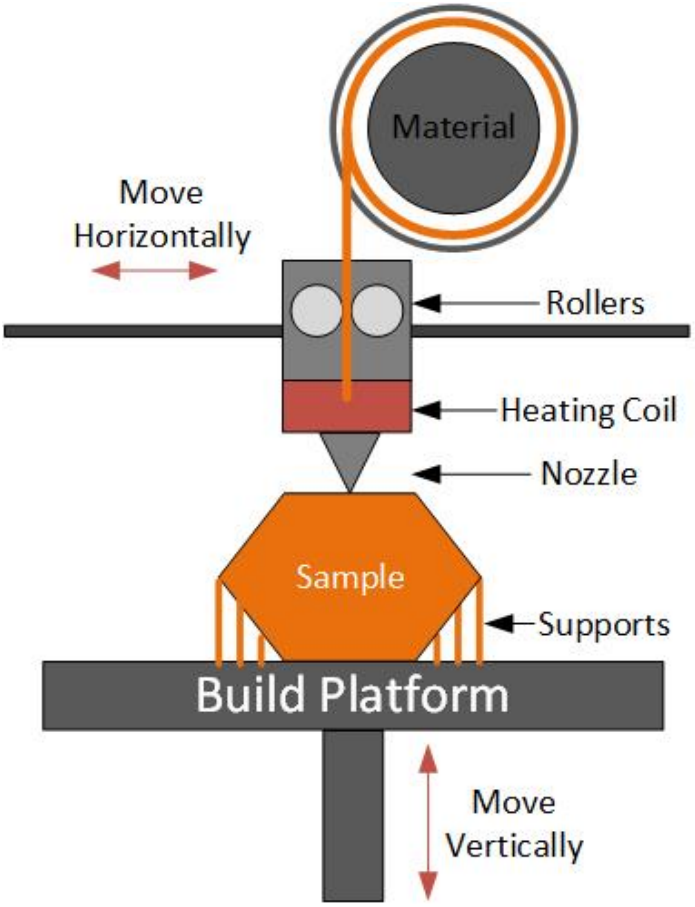

Figure 2.14. Schematic of the material extrusion additive manufacturing technology

Powder Bed Fusion

The Powder Bed Fusion (PBF) (as shown in Figure 2.15) covers several printing technologies which include Direct Metal Laser Sintering, Electron Beam Melting, Selective Laser Melting and Selective Laser Sintering. Once the slicing layers are uploaded to the PBF printer, the build platform is lowered down, and simultaneously, a roller spreads the next layer across the building platform. A laser dot or an electron beam, guided by the digital data of the uploaded slice, melts the metal powder selectively. Then the previous layer cools down and adheres to the preceeding layer. This is repeated until the object is fully printed.

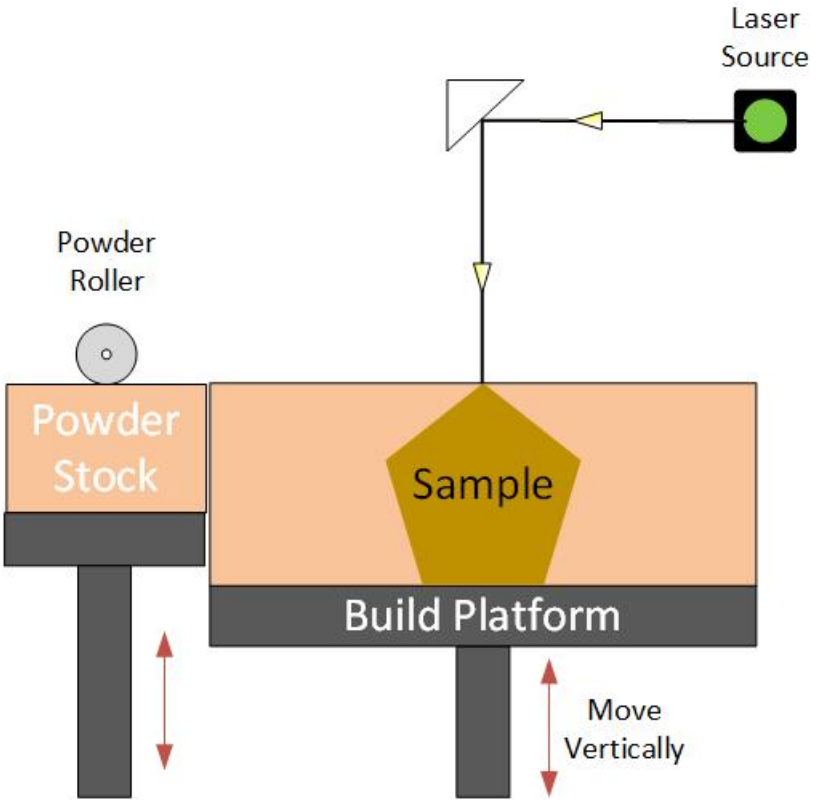

Figure 2.15. Schematic of the powder bed fusion additive manufacturing technology

Sheet Lamination

Sheet lamination (SL) technology can create complex geometries by binding thin layers like aluminium foil or paper. The layered materials are cut into appropriate shape layers by layers or sharp blades. The SL processes usually include ultrasonic additive manufacturing (UAM) and laminated object manufacturing (LOM). For the UAM methods, the metal layers, usually aluminium, copper, stainless steel and titanium, are bound together using ultrasonic welding. In contrast, the LOM process as shown in Figure 2.16 uses paper layers coated with adhesive and glues them together.

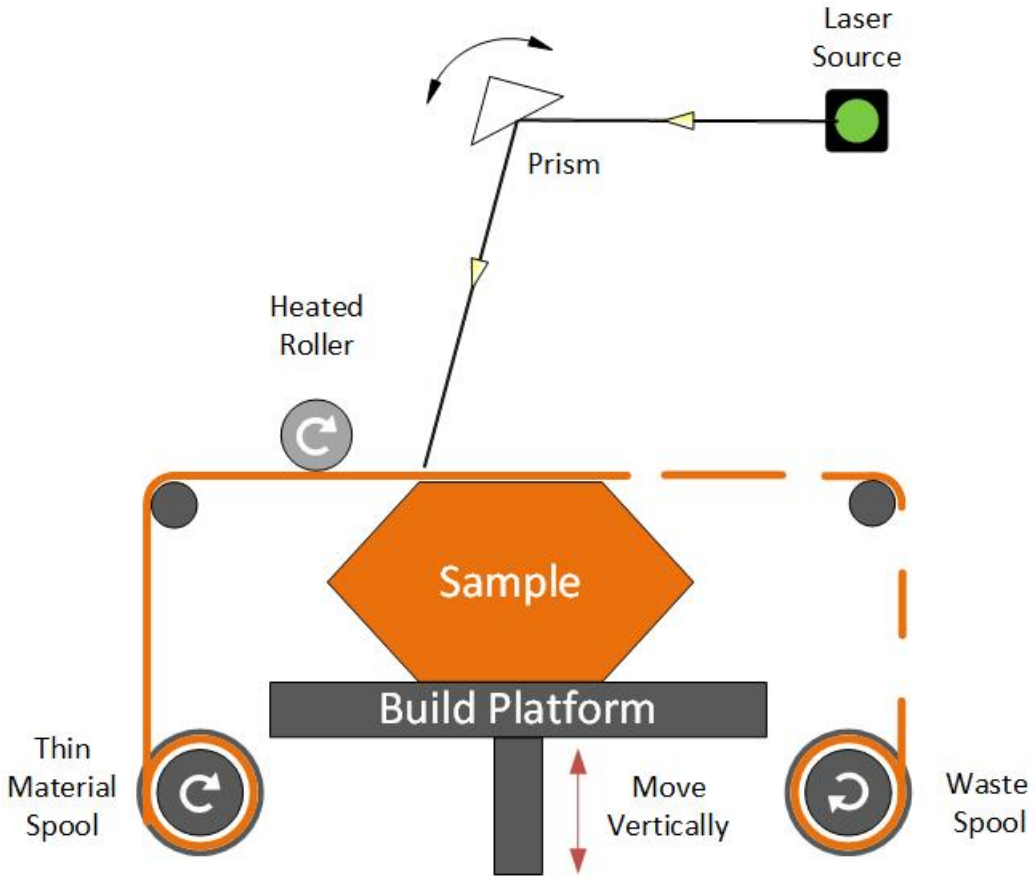

Figure 2.16. Schematic of the sheet lamination additive manufacturing technology

Directed Energy Deposition

Directed Energy Deposition (DED) (See Figure 2.17) is commonly used to create 3D structures by using metals or alloy. Even though it is not popular, this technology can also be applied for creating a 3D model from polymers, glass or ceramic. Comparing with other AM technologies building whole structures, the DED is usually used to repair or add materials in existing components [41]. The DED device typically includes a robot arm which can move along multiple axis and an electron beam or high power laser nozzle to melt the fed wire material and then deposited the melt material onto the structure surface layer upon layer.

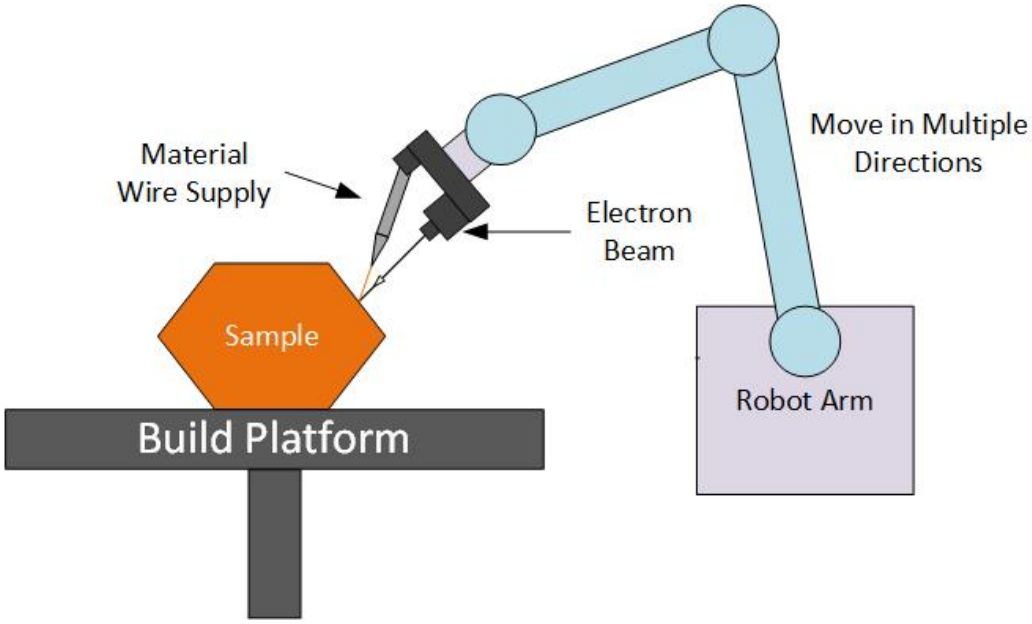

Figure 2.17. Schematic of the direct energy deposition additive manufacturing technology

VAT Photopolymerisation

The VAT Photopolymerisation which is also known as stereolithography will be introduced in more detail in the section below.

2.2.2. Stereolithography (SLA) Printers

The early concept of SLA technology was proposed in 1981 with the invention of the AM equipment and the photo-hardening thermoset polymer. This technology can produce parts layer by layer using polymerization which is a process causing molecule chains to link to each other by exposing the resin under an area of UV light. Three years later in 1984, Charles Hull filled a patent for the stereolithography fabrication system, and let designers create 3D models using digital STL data which is still the most popular 3D printing format today.

By definition, both Laser-based Stereolithography (Laser-based SLA) and Digital Light Processing (DLP) are types of stereolithography. The theory of Laser-based SLA and DLP are very similar, such that they use a liquid photopolymer resin which is able to be cured (polymerized) under a light source. Figure 2.18 shows the printing progress of typical Laser-based SLA and DLP printers. As shown in Figure 2.18 (a), both Laser-based SLA and DLP have building blocks and build trays to hold the photopolymer resin. The bottom side of the build tray is transparent to expose the light source on the building block. Once the 2D printing slices are uploaded to the printer, the building block moves down and submerges into the resin tray. The Laser-based SLA and DLP utilise different ways to create the layers. As shown in Figure 2.18 (b), the DLP exposes the layer images with a projector screen. In contrast, the Laser-based SLA selects the exposing path by using a laser beam as shown in Figure 2.18 (c). The process is repeated until the 3D structure is completed as shown in Figure 2.18 (d). Then the samples are moved up from the build

tray, drained of the extra resin, the support structure removed and finally the printing is finished.

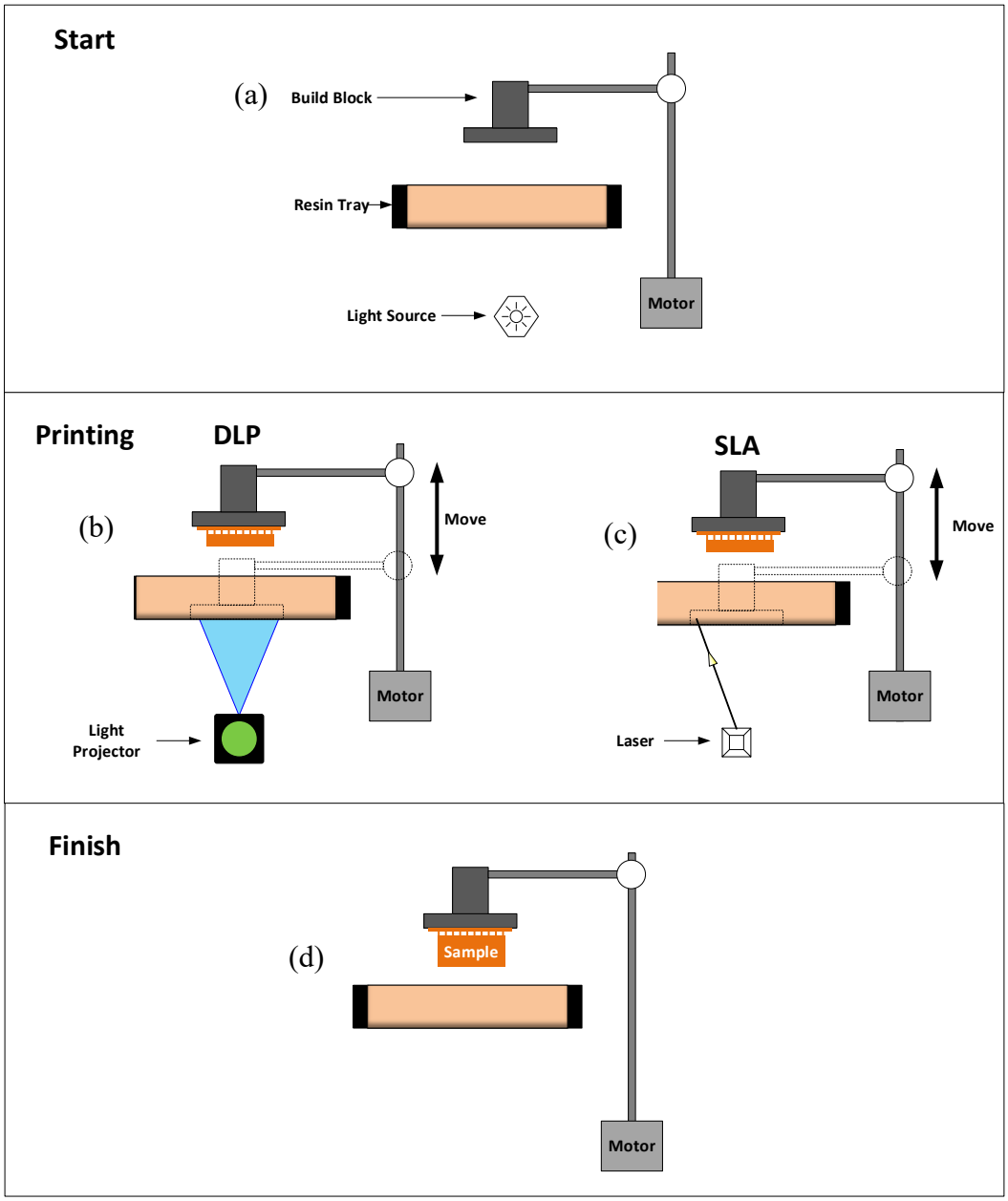

Figure 2.18 Printing progress between Laser-based SLA and DLP. (a) The starting point of the stereolithography printing process, and main components in stereolithography printer. (b) DLP create layers by projecting the pattern of light. (c) SLA create layers by selecting the exposure area or line by laser (d) Finish printing

Figure 2.19 indicates that the Laser-based SLA and DLP draw the layers in completely different ways. Laser-based SLA utilizes two motors in the X-Y axis to aim the laser beam on the printing area and solidify the UV curable resin along the moving path of the laser spot. Similar to painting, the printing area in the individual slice has been divided into different lines and points. In contrast, the DLP has many square pixels to image the printing area and then project it on the building block by flashing a UV light. The thickness of the individual layer can be controlled by the exposure time and the light absorption property of the resin fluid. Thinner building layers result in higher resolution but require a longer time to print.

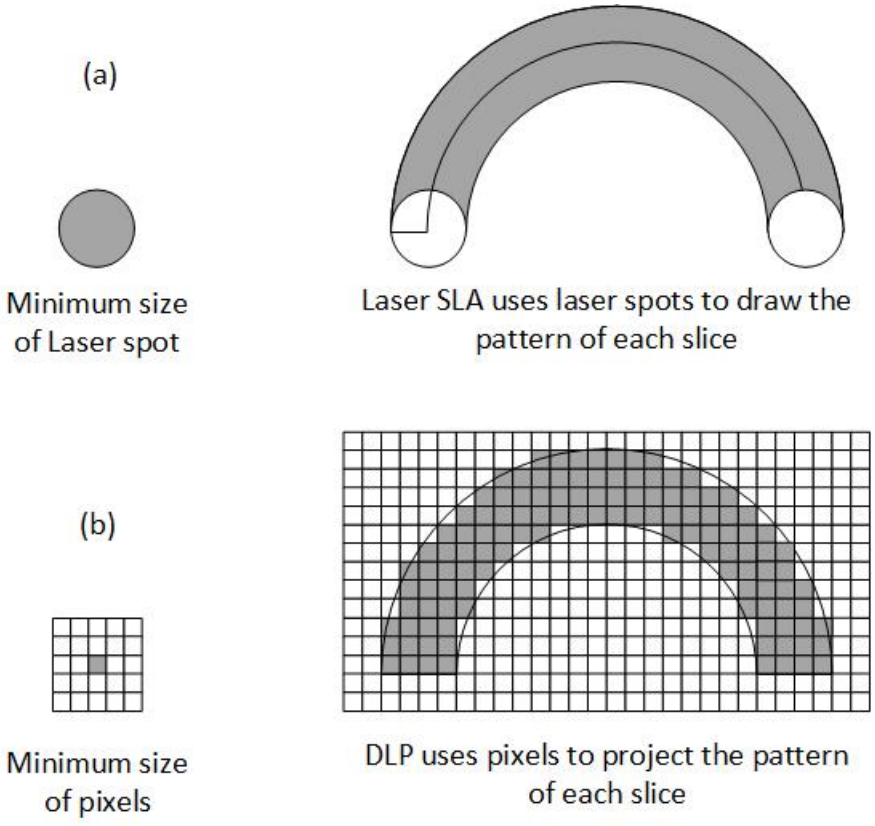

Figure 2.19 Project layers by (a) Laser SLA and (b) DLP

Due to the difference in creating the layers between Laser-based SLA and DLP, they specialize in fabrication with different types of samples. When the sample is large enough to fill up the building platform, the projector in the DLP printer can expose the slice pattern faster than the Laser-based SLA printer. Moreover, the DLP printer can achieve high resolution in a small sample because the projector has a specific number of pixels. When the required printing area is small, all of the pixels will focus on a small area and provide a good resolution. However, the resolution of the DLP printer will be reduced if a larger printing area is required.

2.2.3. Two photon polymerization (2PP)

Two-photon polymerization (2PP) uses femtosecond (Fs) laser pulses to directly write the 3D geometry into a volume of photopolymer resin. Similar to the SLA, TPP also uses the femtosecond laser to trigger a chemical reaction leading to the polymerization of liquid polymer. The comparison of SLA and 2PP process can be explained byFigure 2.20. The SLA can only create 3D geometry layer by layer because its polymerization process takes place near the surface between the photopolymer resin and the build block. This process is also called single-photon polymerization (1PP). However, the 2PP process enables two photons simultaneously focusing on one position. The photoinitiator triggered by both photons and then start the polymerization reaction. Therefore, this allows the light to directly build a desired 3D structure into a volume of photopolymer resin. Due to the threshold behaviour and nonlinear nature of the 2PP process, printing resolution beyond the diffraction limit of the optics can be realized by controlling the laser pulse energy and the number of applied pulses. The 2PP usually can achieve up to 200 nm [42] printing

resolution which is much higher than that of the SLA. However, the printing speed of 2PP is much slower because of its tracing method.

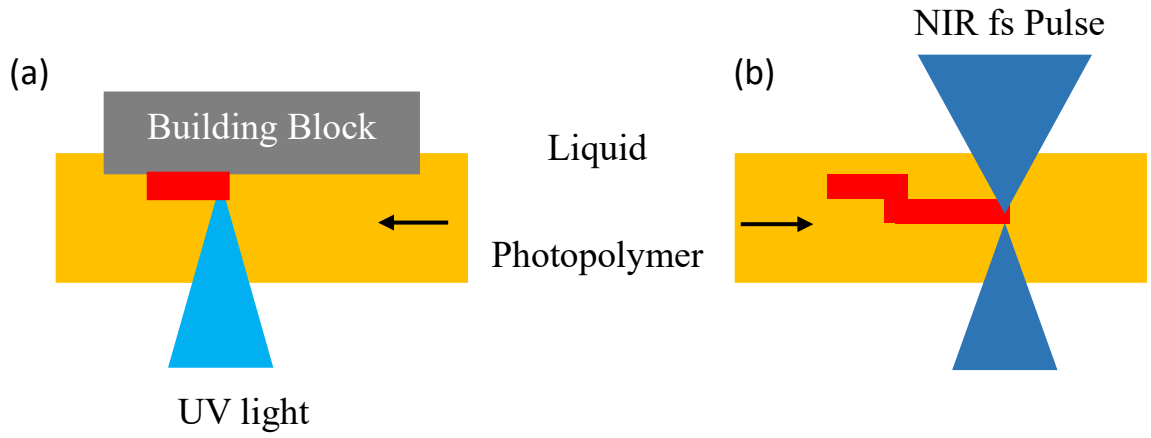

Figure 2.20 (a) Schematic of SLA single-photon polymerization and two-photon polymerization

2.2.4. Photopolymerisation

Stereolithography AM technology makes use of a liquid photopolymer resin that is able to harden under a UV light source. This chemical reaction is called photopolymerisation, and those SLA resins are called photopolymer or light-activated resin. During the polymerization process, small molecules (monomers) are linked into a larger molecule (polymer) which is comprised of many small monomer units [43]. As the distance between polymers decreases, the liquid systems turn into a solid system and the density of the polymer increase. The free radical photopolymerisation is one of the important types that developed for the SLA process by using acrylate chemistry [43]. The free radical mechanism can be explained in Table 2.2 which includes three steps: Initiation, Propagation and Termination, where **PI** represents the photoinitiator, **I** is the radical, and

$\boldsymbol{M}$ is a monomer. The process is initialised by introducing a photoinitiator to the base resin as a catalyst. In the free radical formation step, the photoinitiator absorbs light and generates free radicals to induce the crosslink reactions inside the mixture liquid resin [44]. In the initiation step, the first active monomer is formed after combining with a free radical. And then, the active monomer propagates to grow its polymer chain. The active monomer can easily link more than 1000 units of monomers in the propagation step. The termination reaction usually ends by combination or disproportionation. The combination joins two radical chains together, and the disproportionation occurs when a hydrogen atom transfers from one chain to another chain resulting in two chain-polymers [45]. Radical chains keep growing inside the cured polymer for up to several months which may result in polymer shrinkage and warping [45].

Table 2.2 Table for explaining the free radical photopolymerisation. The table is modified from [43]

$\mathbf{PI} + \mathrm{hv} \rightarrow \mathbf{I}^{\bullet}$	Free radical formation
$\mathbf{I}^{\bullet} + \boldsymbol{M} \rightarrow \boldsymbol{IM}^{\bullet}$	Initiation
$\boldsymbol{IM}^{\bullet} + (\mathbf{M})_{\mathbf{n}} \rightarrow \boldsymbol{I}(\boldsymbol{M})_{\boldsymbol{n}}\boldsymbol{M}^{\bullet}$	Propagation
$\boldsymbol{I}(\boldsymbol{M})_{\boldsymbol{n}}^{\bullet} + {}^{\bullet}(\mathbf{M})_{\mathbf{m}}\mathbf{I} \rightarrow \mathbf{I}(\mathbf{M})_{\mathbf{m+n}}\boldsymbol{I}$	Termination: combination
$\boldsymbol{I}(\boldsymbol{M})_{\boldsymbol{n}}^{\bullet} + {}^{\bullet}(\mathbf{M})_{\mathbf{m}}\mathbf{I} \rightarrow \boldsymbol{I}(\boldsymbol{M})_{\boldsymbol{n}} + \boldsymbol{I}(\boldsymbol{M})_{\boldsymbol{m}}$	Termination: disproportionation

2.2.5. Piezoelectric Materials

Piezoelectric Effect and Crystal Structure

Piezoelectricity is an effect of certain materials (like quartz crystal, ceramic) to generate an electric field in response to applied mechanical stress, that is caused by their microscopic lattice structure. The piezoelectric effect is also a reversible process which generates internal mechanical strain in response to an applied electrical field. Single phase and homogenous piezoelectric ceramics such as Lead Zirconate Titanate (PZT), Lead Titanate ($PbTiO_3$) and Barium Titanate ($Batio_3$) are perovskite materials. The general chemical formulae of perovskite crystal structure can be written as ABO_3 where the A is a larger metal ion, for example, lead (Pb) or Barium (Ba), B is a smaller metal ion, normally titanium (Ti) or zirconium (Zr) and the O is oxygen ions. Figure 2.21 shows the crystal structure of PZT at the temperature above and below the Curie point. When the temperature is above the Curie point, the perovskite crystal is in paraelastic phase which is a simple cubic symmetry without dipole moment (Figure 2.21 (a)). When the temperature is below the Curie point, the perovskite crystal is in ferroelectric phase where the crystal exhibits a tetragonal or rhombohedral symmetry leading to a dipole moment (Figure 2.21 (b)) [46]. The piezoelectric ceramic can be manufactured by mixing the fine piezoelectric powder and metal oxides with a specific formula, steering with an organic binder and form into a desired shape like disk, cube and disk. The elements are kept heating for a period until the particles sinter to obtain a dense crystalline structure. Finally, the elements are cooled down, and electrodes applied on the top and bottom surface.

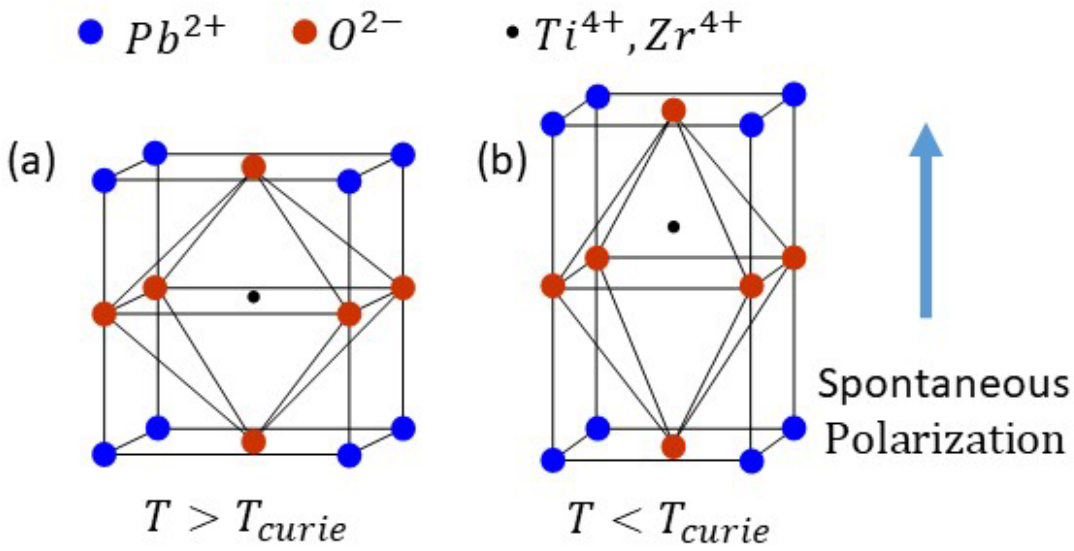

Figure 2.21. Perovskite structure of PZT piezoelectric ceramic (ABO_3) (a) above and (b) below the Curie point

Poling a Homogenous Piezoelectric Material

A homogenous piezoelectric ceramic comprises many small electric dipoles in its macroscopic crystalline structure as shown in Figure 2.22. The dipoles can be represented by blue arrows where the beginning arrow is the positive side, and the tail is the negative side. When external mechanical stress is applied, each dipole rotates from its original orientation toward a new direction in order to minimize the electrical and mechanical energy stored in the dipole. Figure 2.22 (a) indicates that the initial direction of the electric dipoles are found to be randomly oriented before polarization, and the macroscopic net polarization of the dipoles is almost zero. The rotation of the dipoles which is caused by mechanical stress cannot change the macroscopic net polarization of the material. Hence, the material doesn't have a piezoelectric effect. However, if the direction of the dipoles can orient from random to the same direction, the net polarization of the bulk ceramic will

change. The polling progress can align the direction of dipoles and make the bulk ceramic become piezoelectric.

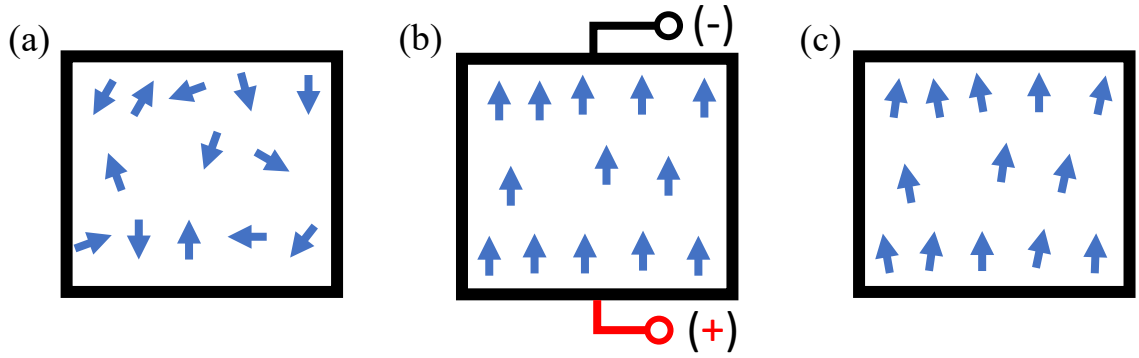

Figure 2.22. (a) Random orientation of electric dipoles before polarization. The dipoles are represented by arrows where begin arrow represents the positive side and the tail represents the negative side. (b)The dipoles are aligned during poling. (c)The dipoles are nearly aligned after polarization.

Figure 2.22 (b) shows that a high external electric field can orient all dipoles in the same direction. After removing the external electric field as shown in Figure 2.22 (c), instead of all dipoles returning back to the random orientation, they roughly stay in the aligned direction. However, the material might be de-poled when placing it under a high external electric field oriented opposite to the polling direction or a temperature higher than the Curie point.

2.2.6. Multiple Phase Piezoelectric Nano-composite

Piezoelectric materials are widely used as sensors, actuators and transducers over many applications. However, the brittle nature of homogenous ceramic piezoelectrics limits their operational strain, life cycle and their ability to be fabricated as a complex structure [47]. Researchers proposed different two-phase piezoelectric nano-composite materials

by embedding piezoelectric nano-particles within a continuous polymer matrix like PZT-EPR [48], PZT-PDMS [49], $BaTiO_3$-PDMS [50] $NaNbO_3$-PDMS [9] and $BaTiO_3$-PEGDA [7]. Comparing with the conventional bulk piezoelectric ceramic, the nano-composite material has better flexibility, ease of processing and lower acoustic impedance. However, the electrical property of nano-composite is much lower due to the dielectric property mismatch between the insulating polymer and the piezoelectric powder [47], [49], [50], which decreases the polarization of the electric dipoles [47]. Researchers also indicated that the piezoelectric property of two-phase nano-composites can be enhanced by adding another phase of material as an energy improver e.g., adding carbon nanotubes (CNTs) [7], [47], [49]–[52] to match the dielectric property between piezoelectric particles and the base polymer or adding TMSPM to link the piezoelectric particle surfaces to the polymer matrix [7], [53].

2.2.7. Polymer/Carbon Nanotubes (CNTs) Composite

Carbon nanotubes (CNTs) have emerged primarily in recent years as one of the most promising nano-fillers. CNTs are long cylinders of covalently bonded carbon atoms only a few nanometers in diameter, but usually tens of microns long [54]. The longest CNT was reported to be $18.5\ cm$ with an aspect ratio of 132,000,000, which is much larger than any other materials in the world [55]. Figure 2.23 [56] shows that the Multi-Walled Carbon Nanotube (MWCNT) is made up of several coaxial graphene cylinder sheets, as opposed to the Single-Walled Carbon Nanotube (SWCNT) which only consist of one sheet of the graphene.

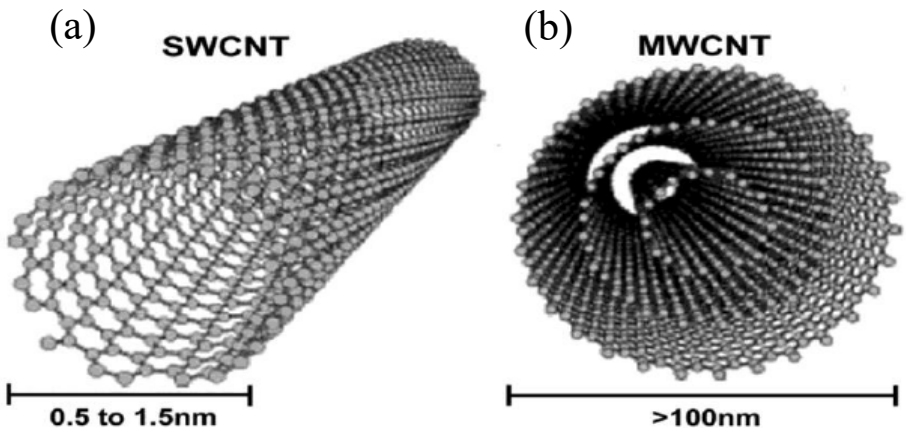

Figure 2.23. (a) Single and (b) Multi-Wall Carbon Nanotube [56]

CNT was first discovered by Morinobu Endo as part of his PhD in 1978 and the first CNT/polymer composite was reported by Ajayan in 1994 [54]. Currently, polymer composite is the biggest application area for CNT which is widely used in transportation, automotive, aerospace, defence, sporting goods, and infrastructure section due to their high durability, high strength and lightweight. CNT/polymers are also used in sensor fabrication [6] because they enhance the conductivity of base materials. However, the conductivity of the composite strongly depends on the homogeneous dispersion of CNT and the types of CNT and polymers [6]. The reported dispersion methods include dry powder mixing, solution blending, melt mixing, in-situ polymerization and surfactant mixing [6]. Researchers indicate that beyond a certain weight fraction, which is called the percolation threshold, of CNTs, there is a sharp rise in the conductivity due to the formation of an electrically conductive pathway inside the CNTs/Polymer composite [57]. Moreover, V. Chaudhary and A. Gupta [57] listed the percolation threshold, dispersion methods and the weight fraction at maximum observed conductivity after reviewing more

than 100 polymers. The maximum conductivity was reported to be 10,000 S/m by mixing PMMA with $10\ wt\%$ $SOCL_2$ treated SWCNTs and the related percolation threshold is 0.17 wt% [58].

2.2.8. AM Acoustic and Ultrasonic Devices

The concept of utilizing AM technology to fabricate electronics was firstly proposed in the early 1990s [59]. During 1994 to 2000, series of AM transistors were reported to be fabricated by different researching groups [60]–[62]. The manufacturing of those simple electronics also demonstrates the applicability of creating sensor and transducers by using AM technology. Recently, there has been increasing interest in using AM technology (also known as 3D printing) in the fabrication of acoustic sensors or ultrasonic transducers owing to the possibility of creating complex 3D geometries at micrometre-scale using highly flexible polymers. After integrating multiple nano-fillers with the passive base polymer, the AM nano-composite can exhibit different properties like conductive [6] or piezoelectric effects [7]–[9] with appropriate benefits to sensor fabrication. Traditional manufacturing methods for acoustic and ultrasonic devices have several drawbacks, such as time-consuming, tedious fabrication steps, lack of manufacturing scalability and relatively high fabrication cost for complex or high-resolution 3D structures [63]. Although introducing AM technologies to the manufacturing of acoustic device can partly overcome those obstacles, like less manufacturing time in 3D complex geometry and lower fabrication cost in customized devices [63], state of the art AM acoustic devices show limitations.

Similar to a conventional acoustic or ultrasonic device, the AM device also needs to follow the fundamental diaphragm-cavity or the bulk ceramic structures as shown in Figure 2.1. Haque et al. [14] reported fabricating capacitive acoustic resonators combining the 3D printing and 2D inkjet printing technology. In that work, the diaphragm part was fabricated by using a 2D inkjet to print the conductive silver layer and then the diaphragm was manually attached on a 3D printed resonating cavity. The capacitive device can provide adequate sensitivity and predictable resonant frequency, however, the manual assembling process limits the resolution and operational frequency in the lower range.

Tiller et al. [15] reported fabricating a piezoelectric microphone using a commercial digital light processing (DLP) 3D printer. This microphone integrates a conductive nanocomposite polymer, a piezoelectric nanocomposite and a base polymer in a single print with the structure similar to PMUT (as shown in Figure 2.1(c)). However, the piezoelectric behaviour (d_{33}) of the AM piezoelectric nanocomposite was measured to be $2 - 3$ pC/N which is far smaller than conventional piezoelectric ceramics and limits the sensitivity of the piezoelectric microphone.

Domingo-Roca et al. [8] proposed a bio-inspired piezoelectric device for acoustic frequency selection and then fabricated it by using the same AM technique as above. The authors concluded that the piezoelectric sensor shows poor sensitivity and further research is required to improve the d_{33} coefficient of the AM piezoelectric nanocomposite material.

In addition, using AM technology to fabricate bulk piezoelectric composite transducers (similar to Figure 2.8) has been reported by different research groups [64]–[67]. The manufacturing process includes preparing the piezoelectric slurry by mixing a

ferroelectric powder e.g. $BaTiO_3$, PZT and PMNT with a passive resin, additive manufacturing the piezoelectric pillars, heating up the piezoelectric part to typically 1000 degree in order to burn out the binder polymer and finally sintering the remaining structure. The sintered $BaTiO_3$ exhibits much higher d_{33} coefficient (up to $160\ pC/N$) than the non-sintered part ($2-3\ pC/N$), however, this will cause ~70% structure shrinkage [68].

2.3. Chapter Summary

In this chapter, background knowledge was introduced in two main sections: ultrasound technologies and additive manufacturing technologies respectively. In more depth, the author reviewed the different types of air-coupled ultrasonic transducers and the motivations for enhancing the bandwidth of air-coupled ultrasonic transducers. In the AM technologies section, the author briefly introduced mainstream commercial AM printers, where the stereolithography type AM printer and stereolithography resins are highlighted.

Chapter 3

"Pipe Organ" Inspired Single Element Ultrasonic Transducer with Broader Bandwidth

All of the results in this chapter has been published in IEEE IUS and TUFFC (see Appendix 1 "Pipe Organ" Inspired Air-Coupled Ultrasonic Transducers With Broader Bandwidth and "Pipe organ" Air coupled Broad Bandwidth Transducer)

3.1. Development of Pipe Organ Inspired Ultrasonic Transducer

The pipe organ backplate proposed in this chapter is a novel design that can improve the bandwidth of air-coupled PMUTs without sensitivity loss or an increase of active area. In this section, the author is going to introduce the development of pipe organ transducer and then clarify the contribution.

The initial idea of fluidically amplified ultrasonic transducer (FLAUT) was studied in 2006 which utilized many liquid-filled pipes with same length to amplify the sensitivity of the electrostatic transducer. In 2017, the pipe organ inspired design and the related mathematical model were proposed to enhance the bandwidth of an electrostatic

transducer. However, none of the existing manufacturing processes can meet the fabricating accuracy required by the pipe organ electrostatic transducer design. At the same year, the author took over the project and used additive manufacturing to fabricate the pipe organ inspired piezoelectric diaphragm transducer with a broader bandwidth.

3.1.1. Fluidically Amplified Ultrasonic Transducer (FLAUT)

An approach of connecting pipes and cavities to the backplate of a capacitive device was proposed by Campbell in 2006 [69]. The concept, Fluidically Amplified Ultrasonic Transducer (FLAUT), aims to amplify the sensitivity in electrostatic devices by employing the resonances of pipe and cavity which are same as the resonance of membrane. Comparing with the typical capacitive sensor with an air-gap and a few releasing holes, the FLAUT air-gap has an individual pipe with a paired cavity as shown in Figure 3.1. The resonant frequency of the cavity-pipe structure can be calculated by using the equation (3.3), that is determined by the pipe length and the sound velocity in the fluid. In the FLAUT theory, the transducer should operate inside liquid media and the membrane that is already excited by the alternated voltage will be amplified by the fluid-filled pipes. Comparing with a standard device without pipes, the FLAUT has a 24dB sensitivity improvement [69]. Because the working principle and the structure of FLAUT is very similar to that of the pipe organ inspired transducer, it can be considered as a predecessor of pipe organ inspired transducer.

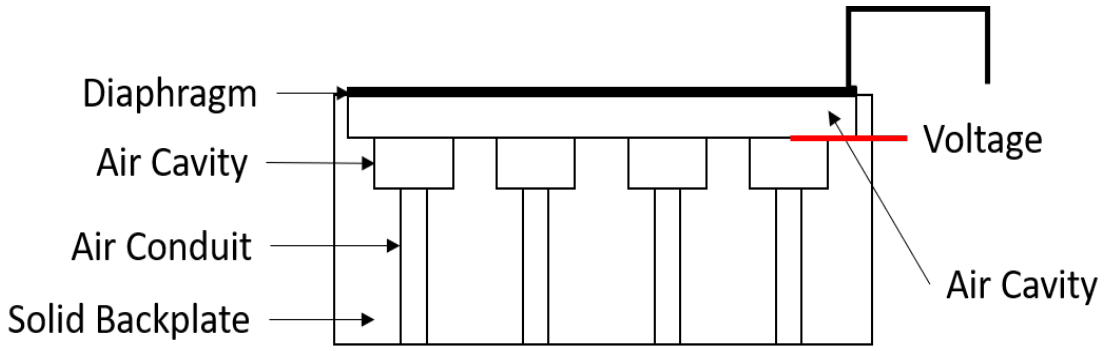

Figure 3.1. Simplified schematic of Fluidically Amplified Ultrasonic Transducer (FLAUT)

3.1.2. Pipe Organ Inspired Electrostatic Ultrasonic Transducer

The initial concept of pipe organ inspired electrostatic ultrasonic transducer was firstly proposed by Walker and Mulholland in 2017 [5]. The design is inspired by the principle of a music instrument. The pipe organ produces sound by driving pressurized air into each individual pipe via the keyboard and pump system. The shape of individual pipes affects the sound produced. However, the resonant frequencies of pipes are mainly determined by the length of the pipes and the velocity of sound. The resonant frequency can be calculated by the theory of pipes which states that the fundamental resonant frequency of an open pipe (both ends open) occurs when the length of pipe is equal to $\lambda/2$. The new pipe organ transducer is based on the conventional electrostatic design but connects many acoustic amplifying pipes with different lengths to the backplate (as in Figure 3.2). The design stage involves optimising each pipe's length - so their resonant frequencies are very close but not equal to the membrane's resonant frequency and in so doing the overall bandwidth is increased. The pipe organ backplate can be thought of as a "musical instrument" which can play different frequencies (pitches) at the same time.

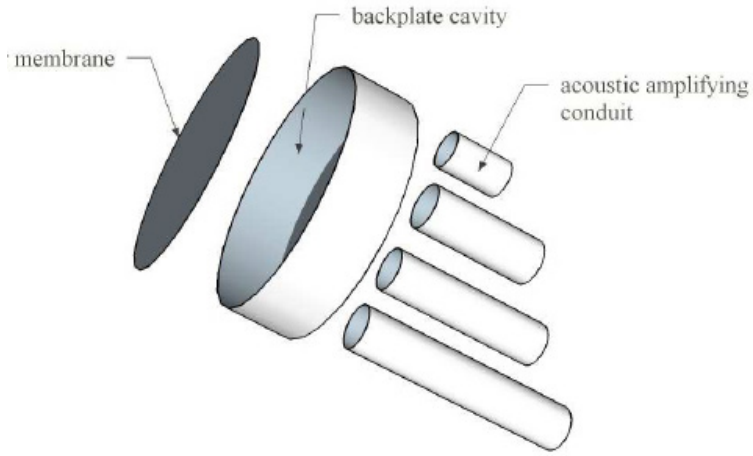

Figure 3.2. Pipe organ inspired electrostatic air-couple ultrasonic transducer [5].

Walker and Mulholland also proposed a 1D transmission line model to simulate the transmission voltage response (TVR) and reception force response (RFR) of both a conventional transducer and the pipe organ electrostatic transducer [5]. The bandwidth and sensitivity of both transducers can then be calculated and compared. Generally speaking, the 1D mathematical model can be divided into 3 parts. First of all, the acoustic impedance of one amplifying pipe is computed. Secondly, a lumped impedance profile of the entire backplate is calculated, which includes many amplifying pipes with different lengths and an air-filled cavity. Finally, the membrane's displacement model is inserted into the backplate's model to compute the bandwidth and sensitivity of the transmitting and receiving modes. This model runs extremely quickly and takes less than 1 second for each design.

In order to set up the simulation, the material and the size of each component on the transducer must be considered. The initial parameters of the backplate design are given in Table 3.1 and Figure 3.3, respectively. Five thousand different designs are simulated and

compared. Each design is given a random number of pipes from 10 to 100. Each pipe has the same radius but the length was randomly chosen from a linear distribution between 0.4 mm and 1.4 mm. The bandwidth of the TVR and RFR are generated and plotted against the number of pipes as shown in Figure 3.4. The 1D mathematical model indicates that the more amplifying pipes present in the device, the larger the bandwidth improvement. And if the pipe number is more than 90, the bandwidth will no longer be significantly improved. Even though the 1D mathematical result suggests around 90 pipes for the backplate, there are manufacturing constraints and so a pipe organ prototypes with 4 or 8 pipes were studied by author [70] from the initial experimental side.

Table 3.1. Initial parameters of pipe organ electrostatic transducer backplate design

Design Parameters	**μm**
Height of cavity (h)	35
Diameter of pipes (d)	52
Radius of cavity/membrane (R)	300

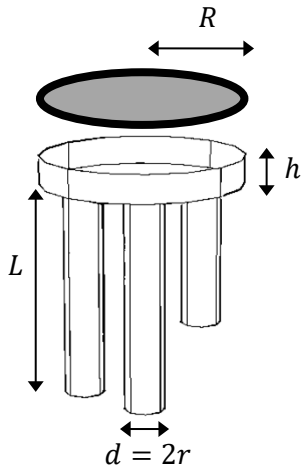

Figure 3.3. Parameters of the pipe organ backplate.

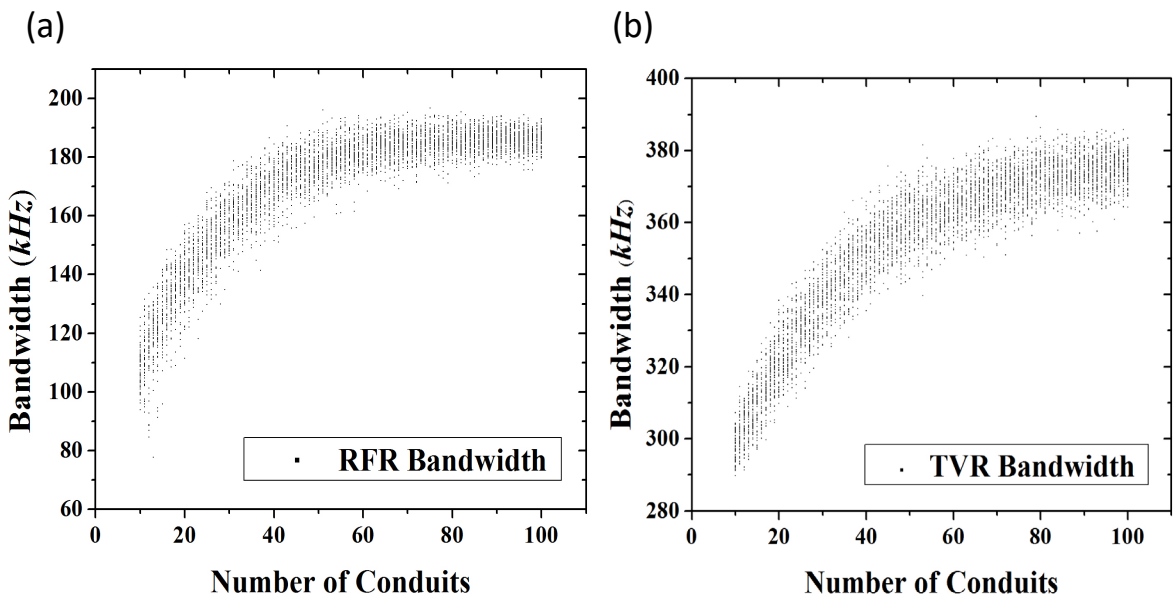

Figure 3.4. The bandwidth of (a) RVR and (b) TVR measured from 5000 sample devices. Plots are generated from the 1D mathematical model

3.1.3. FEA and Experimental study of pipe organ prototypes

The author took over this project from 2017 and finished some initial studies which include creating a FEA model by using a commercial software COMSOL Multiphysics to prove the concept of pipe organ inspired transducer, fabricating the pipe organ inspired prototypes by using a commercial additive manufacturing printer and a commercial passive Kapton thin film and finally characterize the performance by using an LDV.

In the COMSOL model, the transducer is located in the middle of the spherical computational region and surrounded by an air sphere. This model can calculate the resonant frequencies of the circular membrane, pipes and cavity accurately and can simulate the coupling effect between them. After considering the limitations of

manufacturing and optimizing the coupling of pipes and the circular membrane, the practical parameters of the backplate are given in Table 3.2.

Table 3.2. Practical parameters of the backplate design.

Device (mm)	8 pipes	4 pipes	0 pipes
Height of cavity (h)	0.4	0.4	0.4
Diameter of pipes (d)	0.48	0.6	n/a
Radius of cavity/membrane (R)	1.5	1.5	1.5
Length of pipes (L)	5.4 5.4 5.2 5.0 4.8 4.6 4.4 4.4	5.0 4.8 4.8 4.5	n/a

Figure 3.5(a) indicates that the resonance frequency of the membrane is 34 kHz. Figure 3.5 (b) (c) and (d) are the pressures inside the pipes and the cavity. When the frequency of the incident sound is 27 kHz, the shortest pipe starts to resonate (as shown in Figure 3.5 (c)). When the frequency is 36 kHz, the longest pipe reaches its resonance (as shown in Figure 3.5 (b)). When the frequency is 11 kHz, all the pipes are coupled together with the cavity and start to resonate (as shown in Figure 3.5 (d)). The pipe organ backplate has introduced the different pipes' resonances between 27 kHz and 36 kHz in order to improve the bandwidth of the membrane, and a Helmholtz resonance located at 11 kHz that will improve the overall sensitivity. Compared with the 1D mathematical model, the 3D FE model took ~2 hours for each design, but is much more realistic.

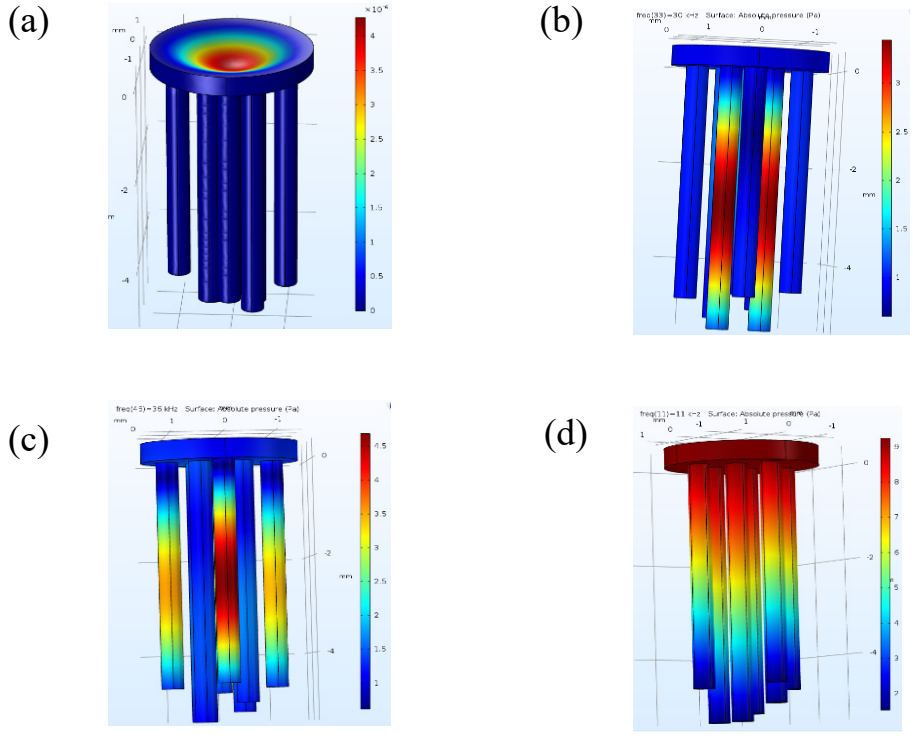

Figure 3.5. (a) The circular membrane resonates at 34kHz. The pressure (resonance) in the pipes and cavity when frequency is (b) 36kHz (the longest pipe's 1st resonance) (c) 27kHz (the shortest pipe's 1st resonance) (d) 11kHz (1st Helmholtz resonance of pipes and cavity)

After building a CAD model, an Asiga Pico Plus 27 3D printer was utilized to fabricate the pipe organ backplate (see Figure 3.6). This is a commercial stereolithography 3D printer with 27 µm resolution in the X-Y plane and 1 μm resolution in Z plane. Instead of using commercial resins directly, the improved resins [71] author used in this project are prepared by mixing Polyethylene (glycol) Diacrylate (PEGDA) along with (2, 4, 6-trimethylbenzoyl) phenylphosphane oxide (Irgacure 819) (1% by weight) and Sudan I (0.1% by weight) vigorously in a spinner. Hua Gong et al [71] proposed that the resins formed by this improved formula will present long-term stability in water and higher printing resolution. The exposure time is set to be 2 seconds with a 10 μm build layer.

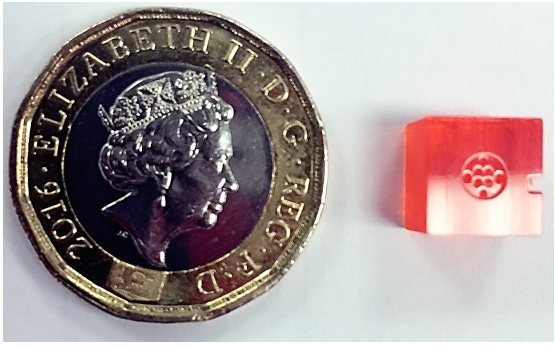

Figure 3.6. 3D printed 8 pipes pipe organ backplate and £1 coin for scale.

Before adding an electrical circuit to the transducer, the average displacement of the membrane was measured using a laser vibrometer to estimate the bandwidth and sensitivity. The performance of the pipe organ design and the conventional cavity-only design were then compared. The membrane was a passive Kapton diaphragm of thickness $d_m = 125$ µm which was attached to the top of the 3D printed backplate with general purpose superglue. The experimental setup is illustrated in Figure 3.7. Initially, wideband periodic chirps covering frequencies from 5 kHz to 50 kHz were generated by a signal generator, and passed through a voltage amplifier, to a broadband ultrasound electrostatic transmitter (Ultra Sound Advice Loudspeaker). The transmitter was enough far away from the sample to ensure that there were no near field effects. A 1/8 inch reference microphone (Brüel and Kjær, Type 4138) was used to measure the reference sound pressure around the sample. An amplitude correction algorithm was utilized to compensate for the transmitter's output variance. This algorithm will be introduced in Chapter 3.5.2. The front face displacement of the sample was obtained by using a Polytec PSV-300 scanning laser vibrometer (LDV) (Polytec, Inc., Waldbronn,Germany) as shown in Figure 3.7.

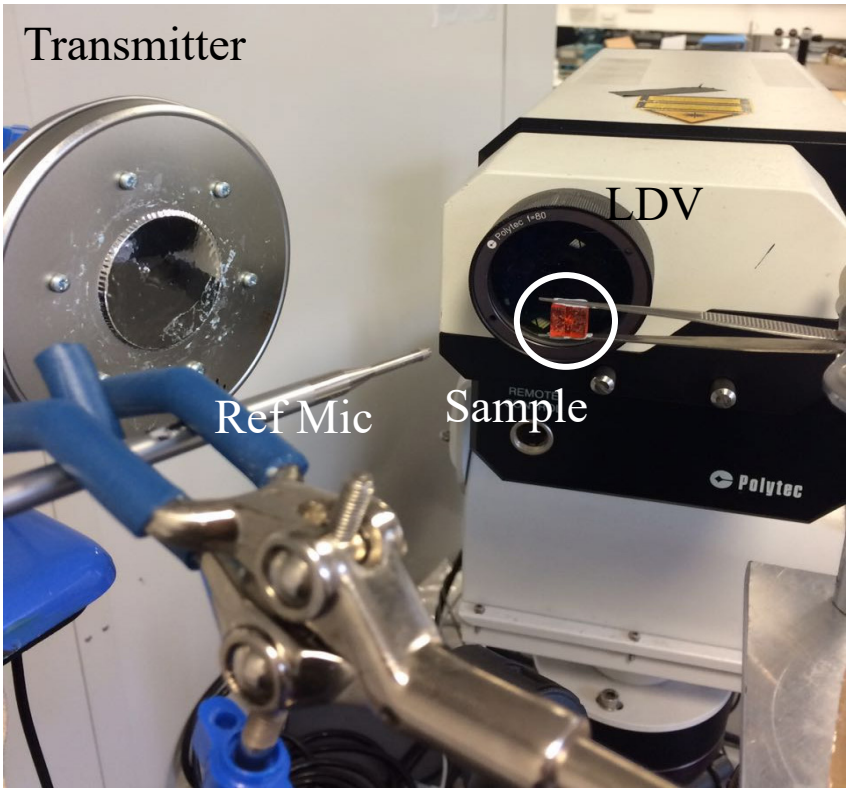

Figure 3.7. Photo of experimental setup

In this section, the frequency response of a device with no pipes (customer built standard device), is compared with a 4 pipes device and an 8 pipes device in terms of bandwidth, central frequency and sensitivity. The design parameters are those given in Table 3.2, and the simulation and experimental results are shown in Figure 3.8 (a) and (b) respectively. The Comsol model does not include any loss factors, and the fluctuations in the simulation result arise from the resonances of different pipes or the cavity. In the simulation result, the Helmholtz resonance is located at 11 kHz and this enhances the overall sensitivity of the transducer. The multiple pipes' resonances vary from 30 kHz to 37 kHz, which are close to the membrane's resonance frequency. Compared with the 4 pipes device, there are more fluctuations in the 8 pipes device at ~31 kHz. So the bandwidth of the 8 pipes

device should be larger than the 4 pipes device. Figure 3.8 (b) is the average displacement of the three devices, a noise floor is defined as 6dB below peak gain of each individual device to calculate the bandwidth of displacement. The central frequency and sensitivity are also evaluated and shown in Table 3.3.

Table 3.3. Bandwidth, central frequency and sensitivity comparison with respect to the displacement of no pipe, 4 pipes and 8 pipes device.

	Bandwidth	**Central Frequency**	**Sensitivity**
No pipe device	3.8%	33.5 kHz	-103dB
4 pipes device	7.2%	34.2 kHz	-97.9dB
8 pipes device	9.6%	36.2 kHz	-102.8dB

The results in Table 3.3 and Figure 3.8 indicate that the respective bandwidths of the pipe organ devices are larger than the device with no pipes. The central frequency shift is due to manufacturing tolerance. When attaching the Kapton membrane with super glue, some of the super glue may enter the cavity which makes the cavity smaller (or larger) than the designed size. However, the frequency shift is less than 8%. There is no sensitivity loss because the pipe organ backplate improves the bandwidth by amplifying the frequencies instead of damping the resonance. Both the device with no pipes and the 8 pipes device have the same gain. The sensitivity of the 4 pipes device is slightly larger than the other two devices because the resonant frequency of the circular membrane overlaps with one of the pipes' resonances. The measured bandwidth and sensitivity of the transducer are regarding to the displacement of a passive polymer membrane. The sensitivity and bandwidth of the electrical output signal will be evaluated in the following sections.

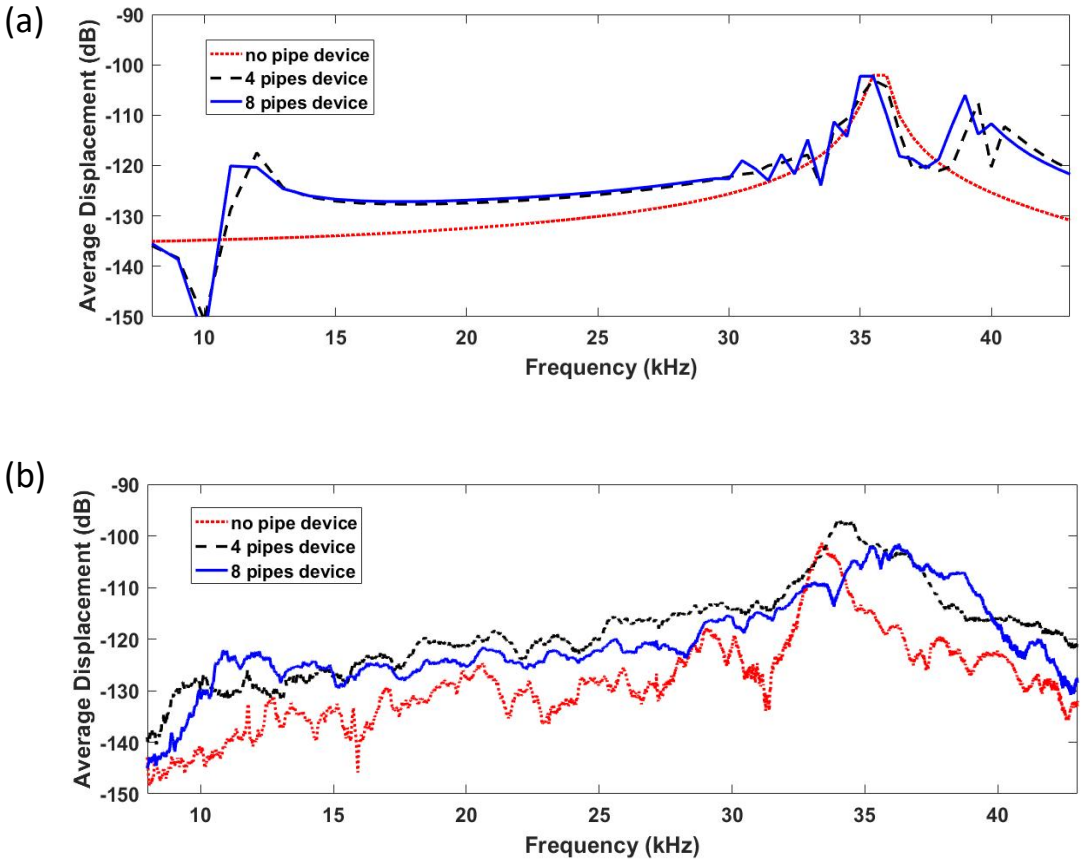

Figure 3.8. Average displacement against frequency in (a) simulation and (b) experiment

3.1.4. Section Conclusion

This section reviews the development of the pipe organ inspired ultrasonic transducer. In 2006, Campbell proposed a FLAUT which utilized fluid-filled pipes and cavity structure to amplify the sensitivity of electrostatic ultrasonic transducers. In 2017, Walker and Mulholland proposed the pipe organ inspired transducer concept which used different length of air-filled pipes to enhance the sensitivity of electrostatic ultrasonic transducers. Their 1D mathematical model indicates that the more amplifying pipes present in the

device, the larger the bandwidth improvement. And if the pipe number is more than 90, the bandwidth will no longer be significantly improved. At the same time, the author took over the project and started to validate the concept in the engineering side. The FEA (Comsol Multiphysics) simulation was used to locate the membrane's and pipes' resonant frequencies more accurately and also simulated the coupling effects between the membrane, pipes and cavity. A pipe organ inspired backplate was built with an improved resin formula and a commercial stereolithography 3D printer and then a passive Kapton thin film was attached on the top of the backplate by using superglue. Moreover, some promising results were found. The -6dB bandwidth of average displacement improvement was found to be up to 9.6% (2.5 times larger than the customer-build conventional device).

The following sections in this chapter will give a detail introduction of the pipe organ inspired ultrasonic transducer with broader bandwidth. The passive Kapton membrane will be replaced by a piezoelectric PVDF thin film to generate electrical signals and receive acoustic signals. Section 3.1 describes the theoretical background of the pipe organ backplate. Section 3.1 uses a commercial FEA (COMSOL) model to simulate the device and detailly explain the resonant frequencies created from the backplate. Section 3.4 introduces the manufacturing technique for the stereolithography pipe organ backplate, an improved resin formula, the printer calibration technique and the rest of the fabrication steps of the prototypes using the stereolithography backplate and commercial

Polyvinylidene Fluoride (PVDF) thin film. Section 3.5, 3.6 and 3.7 shows the experiment set-up, results and discussion. Section 3.8 is the chapter conclusions.

3.2. Theoretical Background of Pipe Organ Transducer

A PMUT utilizes a piezoelectric layer on the top of a silicon membrane and operates in a flexural mode. After applying an electrical field to the thin plate, the lateral strain in its thickness direction makes the structure bend [21]. The vibrating membrane compresses the air and produces ultrasound. In contrast, the received ultrasound wave vibrates the film which causes charge migration between the two electrodes on the piezoelectric layer, which then can be detected by a receiving circuit [21]. The intrinsic stress of the thin plate is the factor that can dominate the resonant frequency of the transducer. When the transducer has an edge-clamped film with low intrinsic stress, the resonant frequency of the thin circular plate (f_{tp}) can be estimated by (3.1) and (3.2) [18], where K_n is a constant that takes the value 10.22 for a clamped circular thin film in the fundamental resonance mode, R is the radius of the thin plate, D_E is the flexural rigidity of the circular thin plate, d_m is the thickness of the menbrane, ρ is the density of the thin plate, E is the Young's modulus and μ is the Poisson ratio. The squeeze film effect occurs when the air gap (depth of cavity) is very narrow [72]. Squeeze film damping becomes more important than the drag force damping of air if the thickness of the gas film is smaller than one-third of the width of the plate [72]. However, this effect can be ignored in the pipe organ design presented here because the air gap is four times higher than the thickness of the thin plate. Moreover, the change of the gap depth introduced by the vibration of the thin plate is

always less than 1% of the depth of the gap and will not affect the transducer's performance.

$$f_{tp} = \frac{K_n}{2\pi R^2}\sqrt{\frac{D_E}{\rho d_m}} \tag{3.1}$$

$$D_E = \frac{E d_m^3}{12(1-\mu^2)} \tag{3.2}$$

A pipe organ produces sound by driving pressurized air into each individual pipe via the keyboard and pump system. The shape of individual pipes affects the sound produced, however, the resonant frequencies of the pipes are mainly determined by the length of the pipes and the velocity of sound [5]. The resonant frequency can be calculated by the theory of pipes which states that the fundamental resonant frequency of an open pipe (both ends open) occurs when the length of pipe is equal to $\lambda/2$, where λ is the wavelength of sound, and the fundamental resonant frequency of a closed pipe (one end is closed and the other end is open) occurs when the length of pipe is equal to $\lambda/4$ [69]. The resonant frequency of open cylindrical pipes is given by equation (3.3), where v is the speed of sound in air, L is the length of pipe, r is the radius of the pipe and n is the number of the resonance mode. The pipes connecting the cavity to the atmosphere enable air to flow in and out which can further reduce the effect of squeeze film damping and squeeze film resistance.

$$f_p = \frac{nv}{2(L+1.6r)} \tag{3.3}$$

A Helmholtz resonator is an air-filled cavity with one open end. When a sound wave gives an initial force to a portion of air (depicted as the grey part in Figure 3.9), the air will vibrate since the air inside the cavity acts as a spring. Therefore, the Helmholtz

resonator can be regarded as a very typical spring-mass system that can support the harmonic motion. In the pipe organ backplate, the pipes and cavity are formed into a Helmholtz resonator [73]. Similar to the organ pipes with different length and resonant frequencies, this resonator also has a resonant frequency (f_h) that can improve the sensitivity in a specific frequency range. The central frequency can be calculated by equation (3.4), where S_{cs} is the total cross-sectional area of the pipe, and V is the volume of the cavity.

Helmholtz resonators are well-documented in many acoustic applications including acoustic energy harvesters [74], [75] and MEMS microphones [76], where they are used to enhance sensitivity when receiving sound. The pipe organ diaphragm ultrasonic transducer proposed in this paper is based on the conventional MUTs design (diaphragm-cavity structure), but connects many acoustic amplifying pipes with different lengths to the backplate (as in as in Figure 3.2) to enhance the bandwidth in both transmitting and receiving modes. The design stage involves optimizing each pipe's length, and the cavity's size, so their resonant frequencies are close but not equal to the thin plate's resonant frequency and in so doing the overall bandwidth is increased. Moreover, the pipe-organ inspired resonator can amplify selected frequencies in receiving and transmitting ultrasound. As shown in Figure 3.10, the metalized PVDF layer is clamped on the top of the backplate as an active part to produce (or receive) ultrasound and the pipe organ

backplate can be thought of as a "musical instrument" which can amplify different selected frequencies (pitches) at the same time.

$$f_h = \frac{v}{2\pi}\sqrt{\frac{S_{cs}}{VL}} \tag{3.4}$$

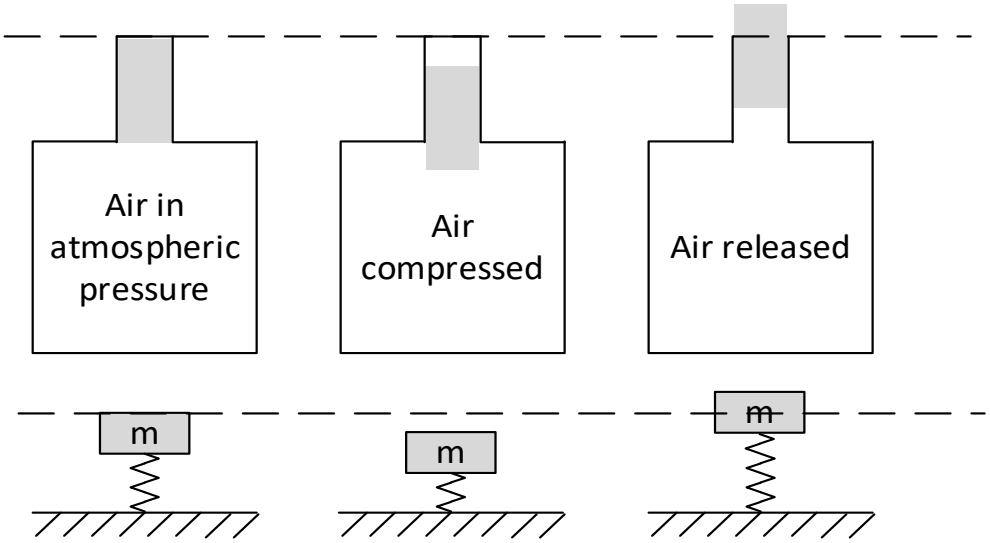

Figure 3.9 Schematic of a Helmholtz resonator

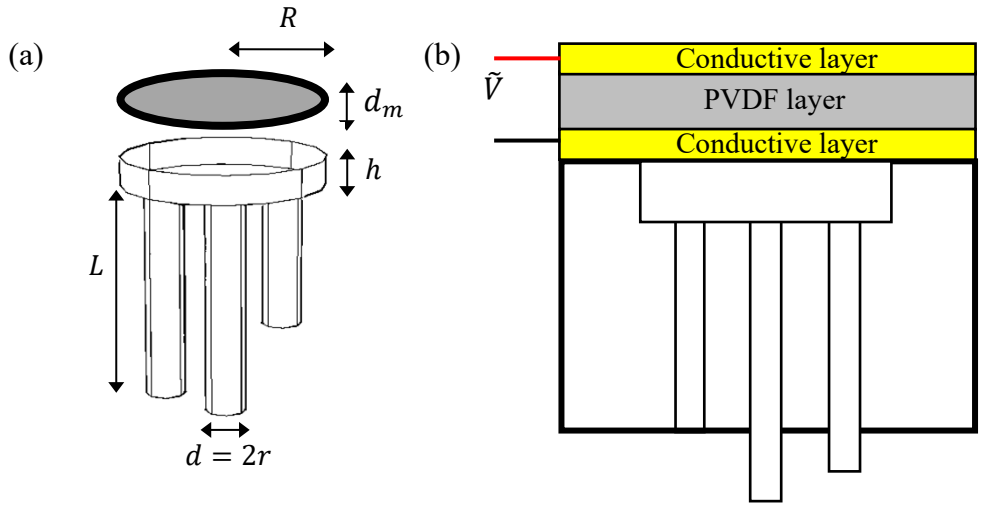

Figure 3.10. (a) Parameters of the pipe organ transducer. (b) Sectional-cut plot of the backplate and the piezoelectric membrane

3.3. Finite Element Modelling

Walker and Mulholland investigated the relationship between the number of pipes and the bandwidth improvement of the pipe organ transducers through 1D mathematical models [5], [77], [78]. They concluded that the bandwidth increased as the number of pipes increased, up to a perceived limit when over 80 pipes were used. In this present work, there were manufacturing constraints, the maximum pipe number is eight in straight pipe design and thirteen in oriented pipe design. It is the reason why the devices with no pipes, 4 pipes (straight pipe design), 8 pipes (straight and oriented pipe designs) and 13 pipes (oriented pipe design) emerging from the back cavity were investigated in this section. The effect of the orientation of pipes on the performance of the transducers was also discussed in this section.

Figure 3.11 (a) is a schematic of the pipe organ transducer which was simulated by using a commercial FE software COMSOL Multiphysics (Comsol AB, Stockholm, Sweden) to optimize the design parameters. This model can calculate the resonant frequencies of the circular thin plate, pipes and cavity more realistic than the 1D mathematical model [78] and also simulate the transducer in transmitting and receiving modes. The simulation model included the Solid Mechanics Domain to simulate the mechanical vibration of both the pipe organ backplate and the PVDF film, the Pressure Acoustic Domain to simulate the absolute pressure and coupling effect between the cavity and pipes, the Electrostatics Domain to simulate the charge migration inside the piezoelectric material, and finally a Multiphysics Model was applied to simulate the coupled boundaries between different physical domains. An air-sphere was defined to enclose the transducer to simulate its

working environment. The boundary layer of the air-sphere was defined as a perfectly matching layer to make sure that sound waves can pass through the boundary without reflection as shown in Figure 3.11 (a) & (b). Viscous damping was added to the air-domains to make the model more realistic. Acoustic wave excitation (electric signals) were introduced to vibrate the thin film to simulate the receiving or transmitting modes of the transducer.

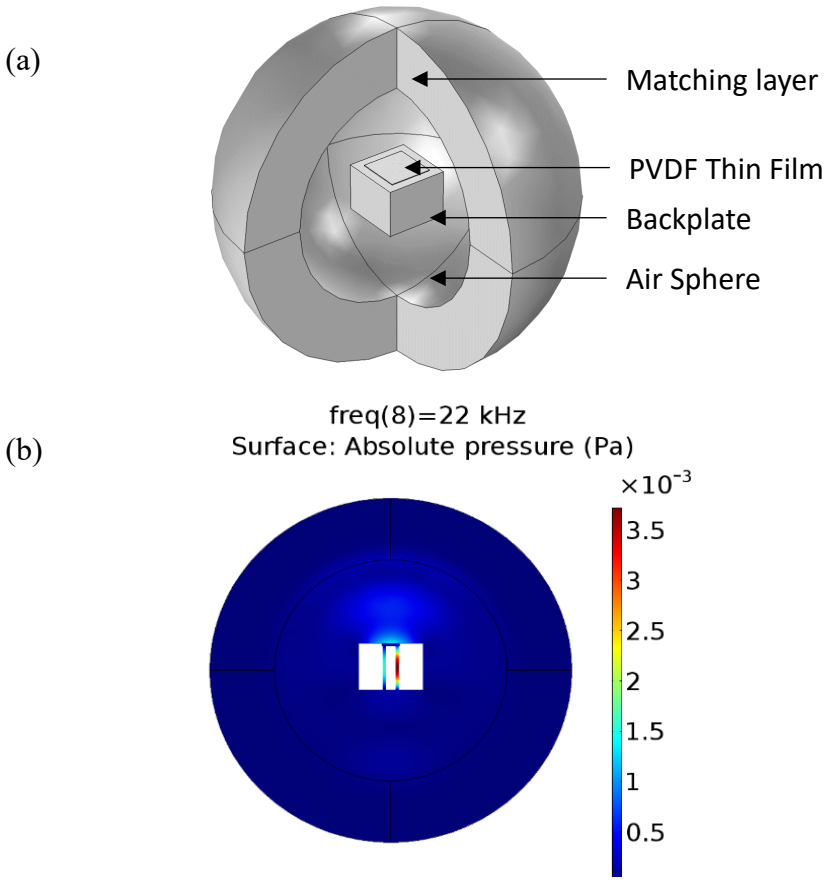

Figure 3.11. (a) Schematic of the COMSOL Model. The pipe organ inspired transducer is surrounded by a air-sphere and a perfect matching layer which can absorb the sound. (b) The x-z cut plane of a pressure plot in the cavity, pipes and the surrounding air sphere. The transducer is transmitting ultrasound and one of the pipe is resonating.

Finally, a Frequency Domain simulation evaluated the system with a 0.5 kHz sampling rate. The simulated frequency range in the section of the resonance investigation (Chapter 3.3.1 and 3.3.2) is from $1 - 70$ kHz because the author is going to investigate all of the resonances arising from the pipe organ inspired backplate. The simulating frequency range in the section of transducer optimizing (Chapter 3.3.3) is from 15-70 kHz because it is the interested frequency range of the pipe organ inspired transducer.

3.3.1. Investigating the Resonance of the Cavity and Pipes

The relationship between the parameters of the pipes and the absolute pressure level inside the cavity of the transducer was investigated with the COMSOL model described above. The absolute pressure level inside the cavity directly correlates with the vibration and the electric potential of the piezoelectric thin plate [75]. There are four designs (as shown in Table 3.4) which have different size or number of pipes for comparison: no pipe device (I), 4 pipes devices with different pipe diameters (II) and (III) and 8 pipes device (IV). The simulated frequency spectrum is given in Figure 3.12 where the area (a) to (e) are the acoustic pressure in different resonance. And the related pressure and displacements plot are given in Figure 3.13 (a) to (e). The dashed boxes in Figure 3.12 from left to right represent: (a) the fundamental mode of the Helmholtz resonator, (b) the fundamental mode of the pipes, (c) the 2^{nd} harmonic mode of the Helmholtz resonator, (d) the fundamental mode of the circular thin plate, (e) the 2^{nd} harmonic mode of pipes, and (f) the 3^{rd} harmonic mode of the Helmholtz resonance respectively. It is easy to find out that the pipe's resonances are superimposed on the frequency response of the Helmholtz resonator. Four conclusions can be obtained from Figure 3.12 and Figure 3.13.

- Figure 3.12 indicates that the designs III and IV have the same frequency response at 7 and 27 kHz (area (a) and (c)) which are the 1st and 2nd Helmholtz resonance respectively. The reason is that their cross-sectional area, the volume of the cavity and the average pipe length are equal (as shown in equation (3.4)). Figure 3.13 (a) shows that the absolute acoustic pressure of the cavity reaches the maximum (turns red) when the pipe-cavity structure is on the 1st Helmholtz resonance. The 2nd Helmholtz resonance is close to the 1st resonance of the pipes, therefore the acoustic pressure plot in Figure 3.13 (c) contains both of the 2nd Helmholtz and pipes resonances.
- Design IV has more frequency spectrum fluctuations in Figure 3.12 (b) & (e) than designs II and III because it has more pipes. Dash boxes (b) and (e) are the 1st and 2nd resonance of pipes. Figure 3.13 (b) and (e) show the absolute acoustic pressure plot of the 1st and 2nd resonance of one pipe, respectively
- All of the pipe organ designs (II, III, IV) have larger gain than the reference no pipe device (I) because the Helmholtz resonance can improve the overall sensitivity.
- The 1st and 2nd resonant frequencies of the circular membrane are in 30 and 60 kHz and the displacement of the membrane are shown in Figure 3.13 (d) and (f).

Table 3.4 Six designs to illustrate the coupling effect between the cavity, the multiple pipes and the circular membrane. Where V is the volume of cavity, h is the depth of cavity, d is the diameter of the pipes, R is the radius of cavity, L is the length of pipes and S is the total opening area of the pipes.

Pipes number	**No (I)**	**4 (II)**	**4 (III)**	**8 (IV)**	**8 (V)**	**13 (VI)**
Orientation pipe	n/a	No	No	No	Yes	Yes
V (mm^3)	6.38	6.38	6.38	6.38	6.38	6.38
$\boldsymbol{h}$ $(\boldsymbol{mm})$	0.97	0.97	0.97	0.97	1.45	1.45
$\boldsymbol{d}$ $(\boldsymbol{mm})$	n/a	0.424	0.6	0.424	0.424	0.424
$\boldsymbol{R}$ $(\boldsymbol{mm})$	1.45	1.45	1.45	1.45	1.45	1.45
$\boldsymbol{L}$ $(\boldsymbol{mm})$	n/a	7.1, 6.8, 6.6, 6.4	7.1, 6.8, 6.6, 6.4	7.1, 7.0, 6.9, 6.8, 6.7, 6.6, 6.5, 6.4	7.1, 7.0, 6.9, 6.8, 6.7, 6.6, 6.5, 6.4	7.4 7.3, 7.2, 7.1, 7.0, 6.9, 6.8, 6.7, 6.6, 6.5, 6.4, 6.3, 6.2
$\mathbf{S_{SC}}$ $(\boldsymbol{mm^2})$	n/a	0.56	1.13	1.13	1.13	1.68

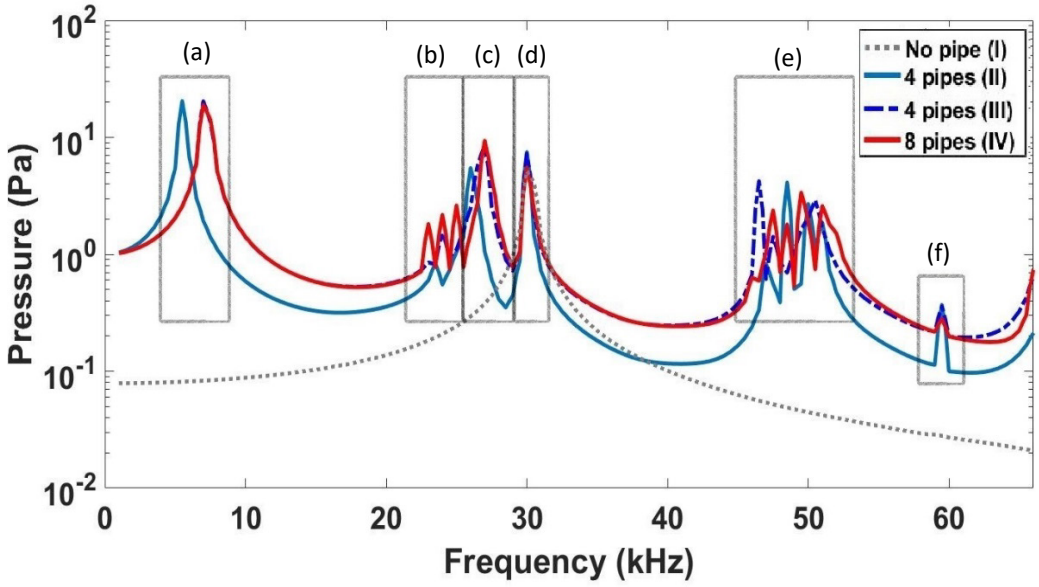

Figure 3.12 Absolute pressure in the cavity against frequency to investigate the number and length of pipes, where (a) the fundamental mode of the Helmholtz resonator, (b) the fundamental mode of the pipes, (c) the 2nd harmonic mode of the Helmholtz resonator, (d) the fundamental mode of the circular thin plate, (e) the 2nd harmonic mode of pipes, and (f) the 3rd harmonic mode of the Helmholtz resonance respectively.

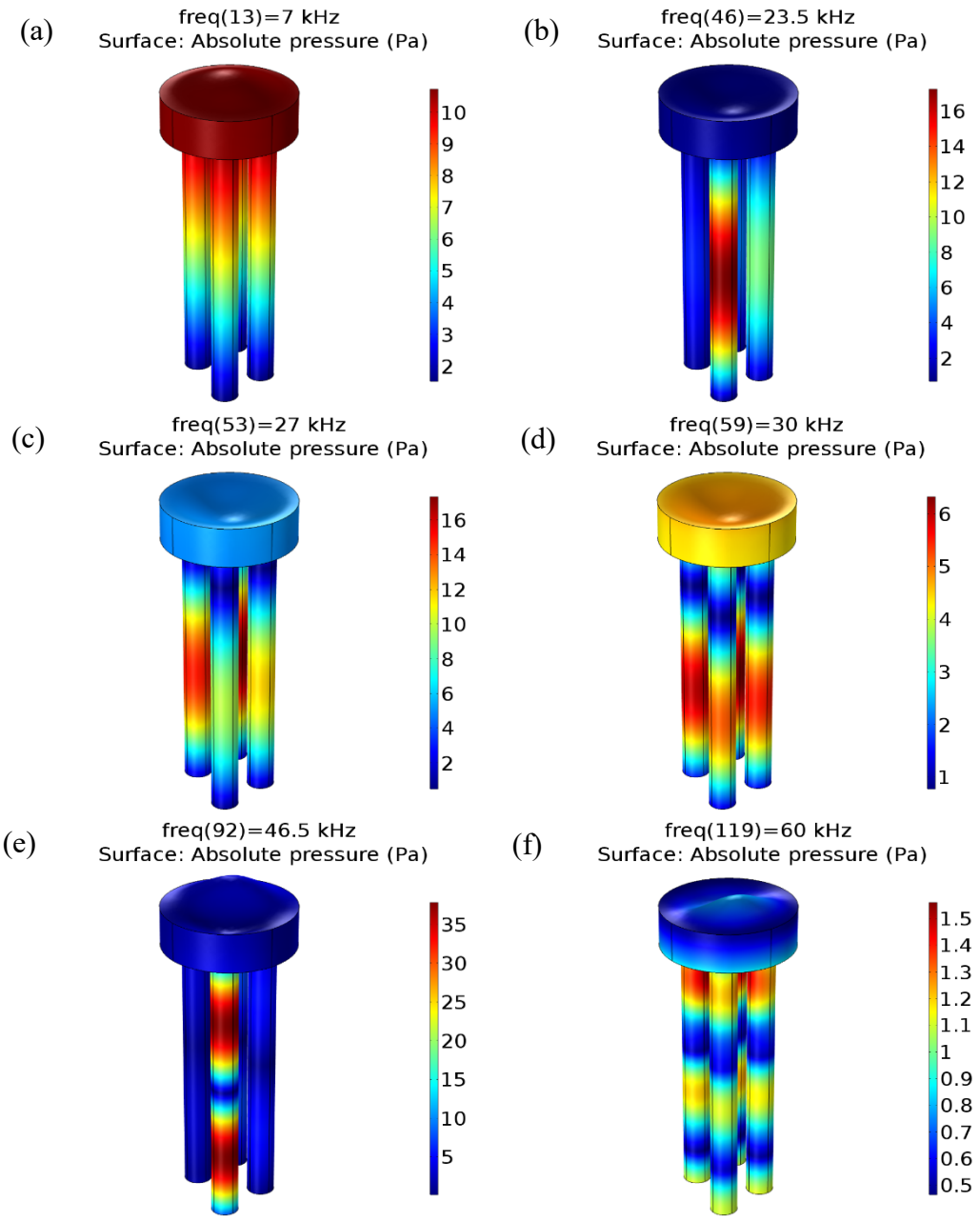

Figure 3.13. The pressure (different resonances) in the pipes and cavity and the vibration of the thin plate when frequency is (a) 7kHz (b) 23.5kHz (c) 27kHz, (d) 30kHz, (e) 46.5kHz, (f) 60kHz for the 4 pipes device (III), with (a)-(f) corresponding to the frequency in Figure 3.12.

3.3.2. Investigating the Orientation of the Pipes

A further improved pipe organ backplate design (hedgehog design) was proposed in order to increase the number of pipes (as in Figure 3.14(b)) with the same fabrication resolution, which was called the "hedgehog" design. The half-sphere cavity gives a larger surface area to accommodate more pipes and also helps the ultrasonic energy focus to the centre of the thin plate. In this section, there are three designs (as shown in Table 3.4) for comparison: 8 pipes without orientation (IV), 8 pipes with orientation (V) and 13 pipes with orientation(VI). Two conclusions can be obtained from Figure 3.15:

- The "hedgehog" 13 pipes device (VI) provides the greatest Helmholtz resonance pressure, which is around 7 kHz, and the "hedgehog" 8 pipes device (V) has larger resonance pressure than the vertical 8 pipes device (IV).
- The 13 pipes "hedgehog" device (VI) gives more frequency spectra fluctuations in the pipes' 2nd harmonics than the other two devices around 50 kHz.

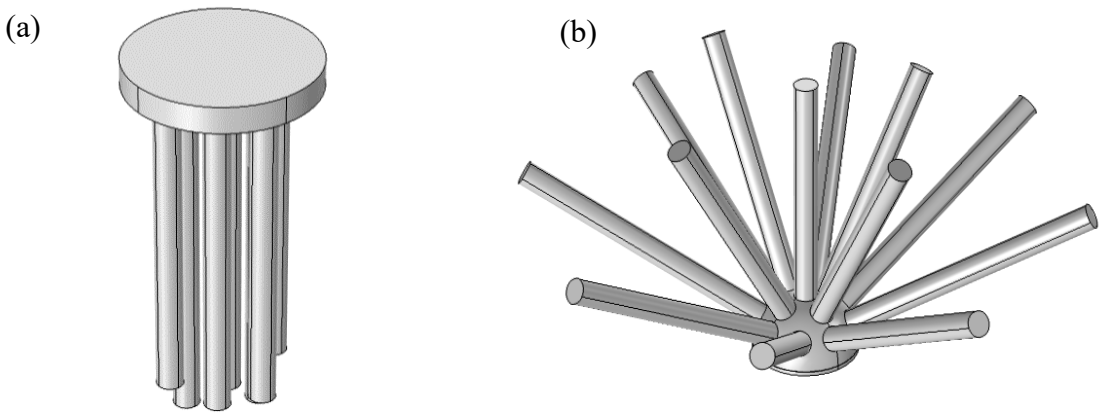

Figure 3.14 Air domain of the pipe organ backplate without (a) and with (b) pipe orientation.

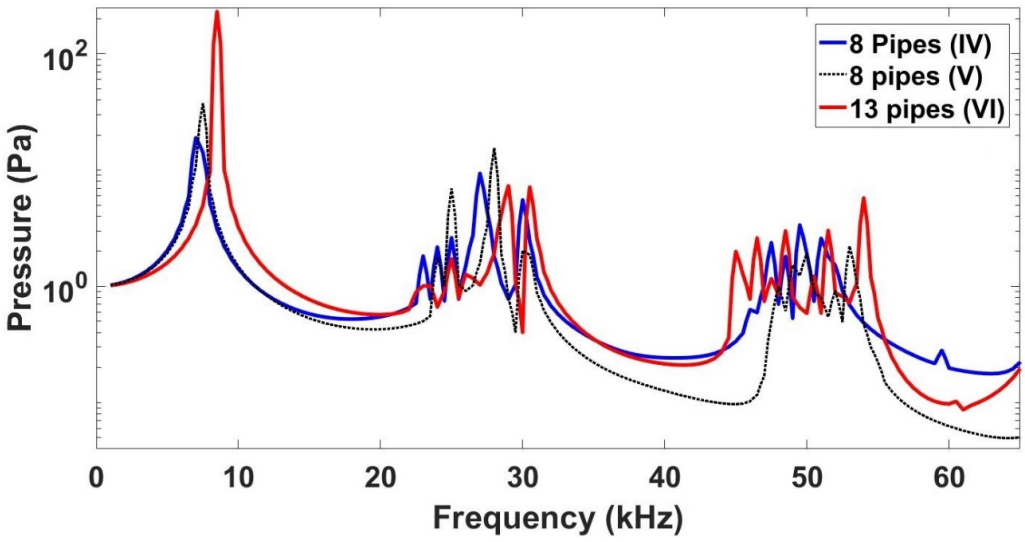

Figure 3.15 Absolute pressure in the cavity against frequency to investigate the orientation of pipes.

3.3.3. Optimized Samples

The parameters given in Table 3.4 were only used to study and quantify the resonant frequencies of the pipe organ backplate. The resonances are far away from each other in order to locate individual ones clearly. In a practical design, the resonances should be much closer to each other in order to provide more stable gain in a specific frequency range. This section provides two optimized pipe organ (vertical and hedgehog pipes) designs to compare against the standard device (as in Table 3.5).

The extra overall size of this pipe organ transducer arises from the length of the pipes. The active areas (piezoelectric thin plate) are the same. The normalized transmitting voltage response (TVR) and receiving voltage response (RVR) are plotted in Figure 3.16. The no pipe device has a very narrow bandwidth at 29 kHz, whereas the pipe organ devices have many small peaks at around 30 kHz and 55 kHz. In other words, the pipe organ

transducers should have larger operating frequency ranges (wider bandwidth), which matches the 1D theoretical conclusions made by Walker and Mulholland [5]. This model only includes the air damping (but not the material damping) which makes the amplitude much larger than the practical situation at the resonant frequency. Manually adding a material damping does improve the simulation result, but it will take away the possibility of easily locating the different resonant frequencies in the design stage. Therefore, the bandwidth of the transducers is not compared in the simulation section of this chapter, but will be in the experimental section.

Table 3.5 Three optimized samples in practical manufacturing

Device	**13 pipes**	**8 pipes**	**No pipe**
Orientation pipe	Yes	No	n/a
Depth of cavity h (mm)	1.45 (half-sphere)	0.4	0.4
Diameter of pipes d (mm)	0.424	0.424	n/a
Radius of thin plate R (mm)	1.45	1.45	1.45
Length of pipes L (mm)	5.1, 5.1, 5.2, 5.3, 5.4, 5.5, 6.2, 5.5, 6.0, 6.6, 6.7, 6.9, 7.0	7.9, 7.9, 7.8, 7.7, 7.6, 7.4, 7.2, 7.2	n/a
Overall Size (mm^2)	126.7	50.2	2.46

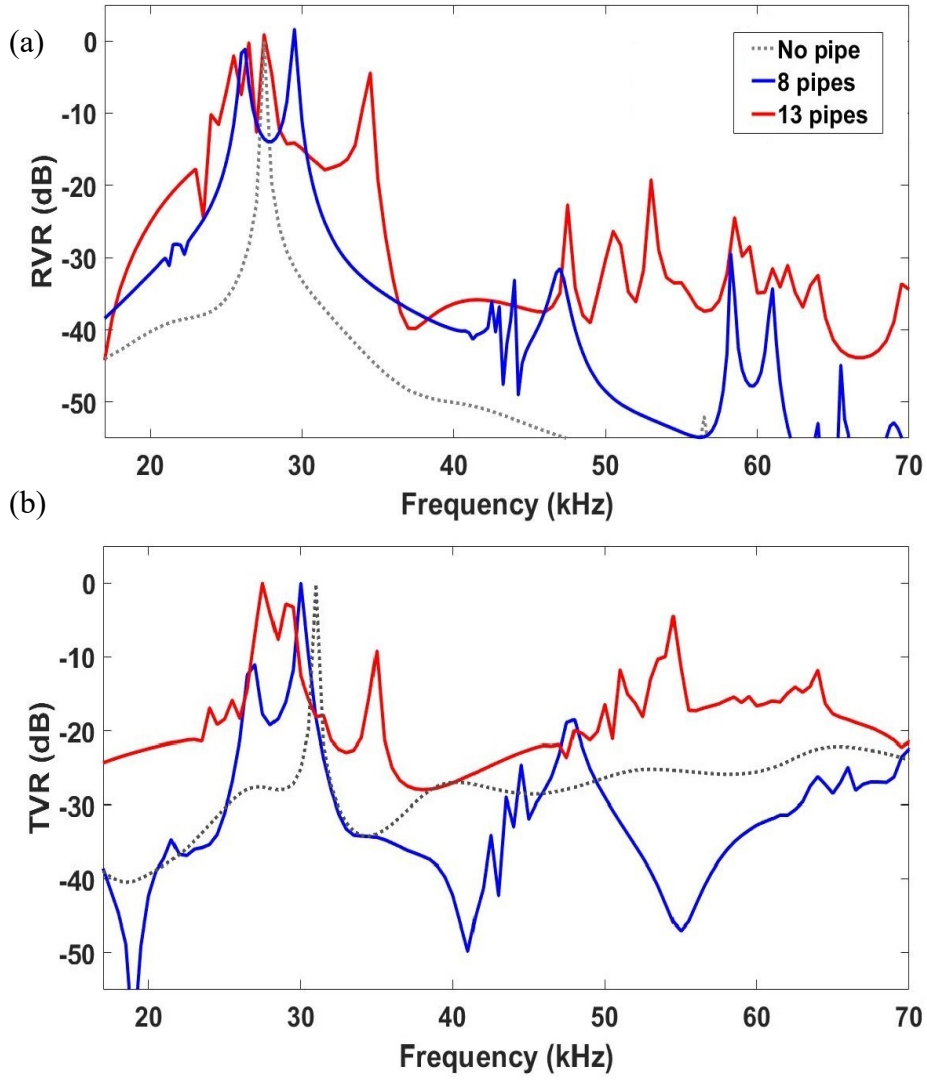

Figure 3.16. Simulated normalized (a) Receiving Voltage Response (RVR) and (b) Transmitting Voltage Response (TVR)

3.4. Fabrication

3.4.1. Stereolithography Backplates

After building a CAD model, an Asiga Pico Plus 27 additive manufacturing machine was utilized to fabricate the pipe organ backplate (see Figure 3.17). This is a commercial

stereolithography 3D printer with 27 μm pixel resolution in the X-Y plane and ~ 1 μm in Z resolution. However, the actual print resolution is worse than this as it also depends on many other factors such as the constituents of the printer resin and the exposure time for each layer, among other things. Instead of using commercial resins directly, the improved resins [79] used in this project are prepared by mixing Polyethylene (glycol) Diacrylate (PEGDA) with molecular weight of 250 along with (2, 4, 6-trimethylbenzoyl) phenylphosphane oxide (Irgacure 819) (1% by weight) and Sudan I (0.2% by weight) vigorously in a spinner. Hua Gong et al. [79] proposed that the resins formed by this improved formula will present long-term stability in water and higher printing resolution. The exposure time is set to be 2s with a 10 μm build layer.

During manufacture, the actual printed size was found to always be smaller than the target size because of polymer shrinkage [45]. So a correction factor was required to compensate for this. First of all, calibration pipes were printed with different lengths and diameters. Secondly, a high-resolution optical microscope system was used to measure the radii. The mean value between five measurements was then calculated. Finally, the correction factor was calculated from Equation (3.5) and the data plotted in Figure 3.18 with an error bar to show that when the diameter is less than 0.5mm, the correction factor dramatically decreases. In other words, a 0.424 mm diameter pipe is the smallest diameter that can be fabricated with this technology. In order to connect more pipes to the cavity, the diameter

$$Correction\ factor = \frac{Actual\ Diameters}{Target\ Diameters} \tag{3.5}$$

of the pipes should be as small as possible. This is the reason why $d = 0.48mm$ is chosen for this work.

Figure 3.17 . £1 coin and stereolithography pipe organ backplates for scale

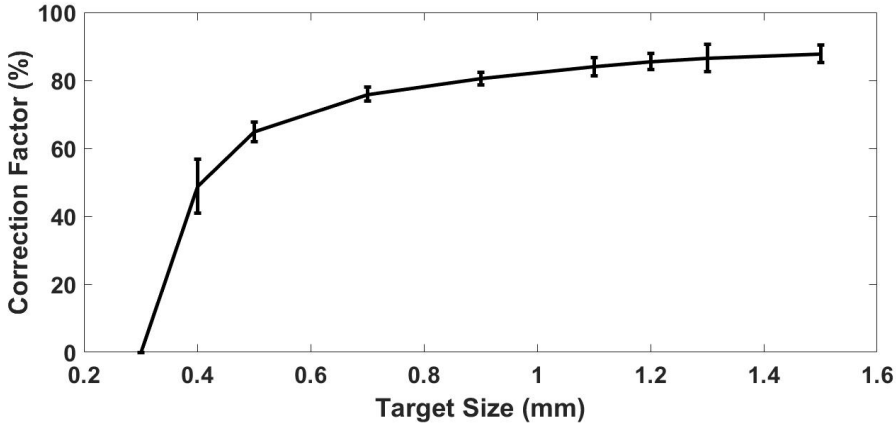

Figure 3.18. Correction factor against target diameter. The error bar was from five measurements.

3.4.2. PVDF Thin Film and Circuit

Figure 3.19 shows a schematic illustrating the further four steps of the fabrication. The manufacture starts with (a) the additive manufactured pipe organ backplate with a gap on the side; (b) two-side-metalized PVDF film (Precision Acoustics Ltd, Dorset, UK) is attached on the top backplate with superglue; (c) the gap is filled with silver paint to connect the bottom surface of PVDF thin film. Finally, (d) a copper wire is connected to the silver gap and another one to the top surface of the film. When attaching the PVDF

film with super glue, some of the super glue may enter the cavity which makes the diameter smaller (or larger) than the designed size, and thus changes the resonance of the thin plate's flexure mode.

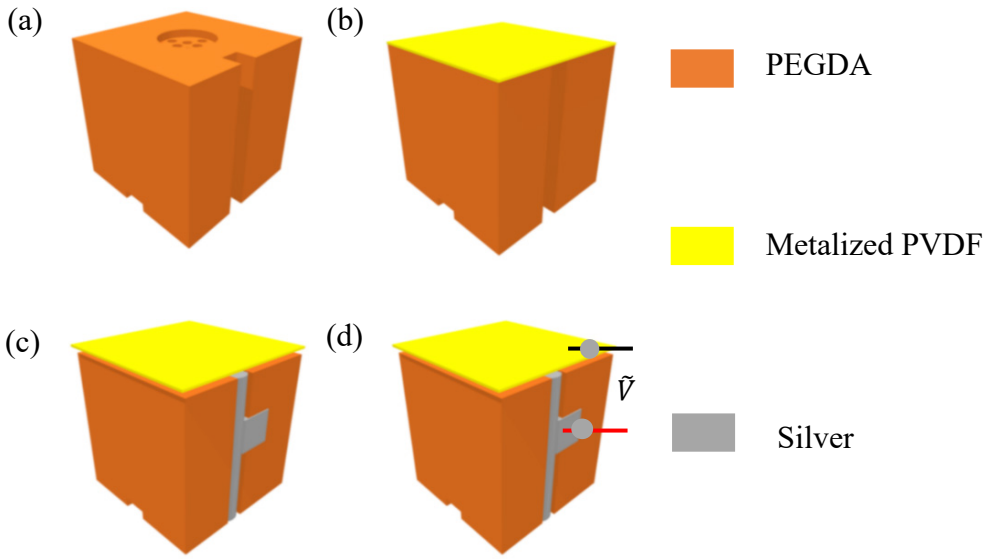

Figure 3.19. Four steps fabricate the pipe organ transducer (a) stereolithography pipe organ backplate. (b) Gluing metalized PVDF thin film. (c)Silver paint the gap (d) Connect copper wire to the electrode.

3.5. Experiment Set-Up

The evaluation of the pipe organ ultrasonic transducer includes measuring the vibration of the active film and the electrical signal in both time and frequency domain.

3.5.1. 3D Laser Doppler Vibrometer (LDV)

Initially, 10 V wideband periodic chirps with equal energy across frequencies from 15 to 70 kHz were generated internally by the arbitrary signal generator (National Instruments PCI-6111; Austin, TX) within the vibrometer workstation to drive the active film into vibration. The signal strength was chosen to be 10 V because it is the maximum output

voltage of the function generator. The periodic chirps used in the LDV experiment is different to the input signal in simulation model. This is because the COMSOL model is a frequency domain simulation. However, the LDV system is well calibrated by Polytec that can compensate the output performance from the input signal. Secondly, the front face average displacement was obtained by a 3D LDV (MSA100-3D, Polytec, Inc., Waldbronn, Germany). Finally, the frequency spectrum and the vibration modes of the resonant frequencies were plotted (see Figure 2.20).

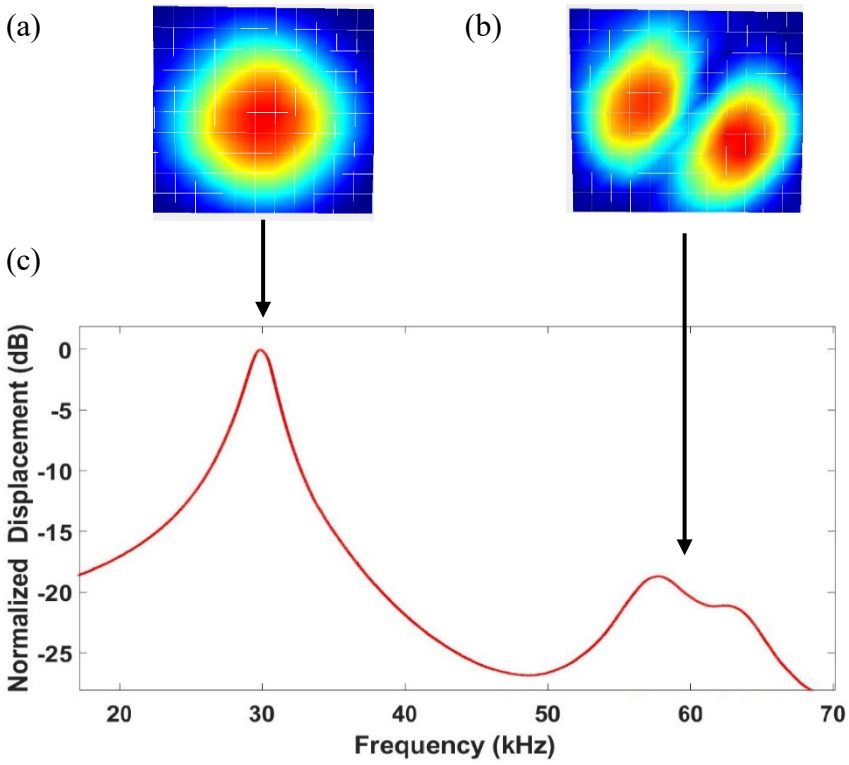

Figure 3.20. (a) Fundamental, (b) 2nd harmonic flexure mode of the circular PVDF film and the colours represent the displacement in the out of plane direction and (c) Average displacement spectrum of the active area measured by 3D LDV. The experimental 1st resonance is 29kHz and 2nd resonance is 58kHz

From this test, the fundamental and 2nd harmonic flexure modes of the circular PVDF film between the three devices (as in Table 3.5) were 29 ± 3 kHz and 58 ± 6 kHz

respectively which are very close to the theoretical prediction (30 and 60 kHz). The manufacturing tolerant explained in chapter 3.4.2 is probably the reason that the simulated resonant frequency can not be perfectly matched to the experimental resonant frequency.

3.5.2. Electrical Signal Measurement

The experimental setup for measuring the receiving and transmitting bandwidth is shown in Figure 3.21 (a) and (b), respectively. In Figure 3.21 (a), the function generator produced a 70 kHz pulse which has equal energy up to ~70 kHz to drive a broadband ultrasonic electrostatic transmitter (Ultra Sound Advice Loudspeaker). This transmitter is chosen because it is an air-couple transmitter with a frequency range from 10kHz to 200kHz which is broader than the interested frequency range of the pipe organ transducer. The sample was far enough away from the transmitter to avoid near field effects. The electrical signal generated from the sample was amplified by a commercial charge amplifier (Brüel and Kjær type 2692) with a custom built bandpass filter (bandwidth 10-100 kHz) system which was manufactured by Dr Yansheng Zhang in CUE and finally acquired on an oscilloscope. A 1/8 inch reference microphone (Brüel and Kjær, Type 4138) was used to measure the reference sound pressure around the sample. The frequency response of this microphone is calibrated to be flat up to 110 kHz. An amplitude correction algorithm was utilized to compensate for the transmitter's output variance. This allows the sensitivity of a sample to be computed as the transfer function of the transverse amplitude gain to the reference sound level, using the below equation .

$$\mathrm{H_{tf}} = \frac{G_{SA}(f)}{G_{RA}(f)} \tag{3.6}$$

Where the H_{tf} is the transfer function of the amplitude correction algorithm, $G_{SA}(f)$ is the record sensitivity amplitude of the sample crossing the frequency spectrum and the $G_{RA}(f)$ is the amplitude of the reference sound level in related frequency.

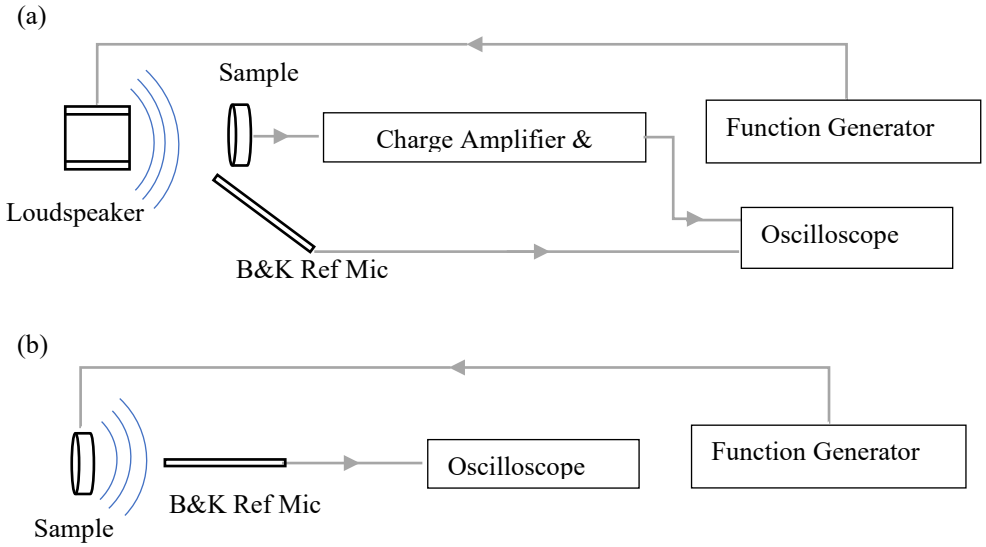

Figure 3.21. Simplified schematic of the experimental (a) setup of the receiving and (b) transmitting modes

In Figure 3.21 (b), the function generator produced a 10V pulse to drive the film into vibration, and the ultrasound field generated by the sample was measured by the reference microphone directly. Since the frequency range of our device is lower than 110 kHz, no amplitude compensation is required.

Figure 3.22 and Figure 3.23 show the electrical signal response in TVR and RVR between the standard no pipe, 8 pipes and "hedgehog" 13 pipes devices. Both TVR and RVR experiments used a pulse signal (instead of a chirp) to drive the transducer because the

pipe organ transducers didn't include a shielding package to cancel the electromagnetic noise and it is easy to separate the acoustic signal from the electromagnetic noise.

3.6. Results

The definition of -6 dB bandwidth has been introduced in Figure 2.6 and equation (2.10) which states that the bandwidth of transducer is the frequency range that the transducer can generate half (-6 dB) of its maximum energy. The signal strength is measured by the maximum peak-peak value of the amplificated transmitting and receiving sensitivity of the transducer. The central frequency is where the transducer has the highest transmitting and receiving sensitivity in the frequency domain. The 20% Peak-Peak Pulse length is the time interval that the amplitude of the signal oscillation reaches 20% of its maximum peak-peak value.

The receiving voltage response (RVR) and transmitting frequency response of the pipe organ inspired transducers and reference transducer were given in

Figure 3.22 and Figure 3.23 and the experimental results are compared in Table *3.6*. The TVR bandwidth of "hedgehog" 13 pipes transducer is 55.7% which is 1.9 times broader than the straight 8 pipes transducer and 4.5 times broader than the custom-built reference transducer. The RVR bandwidth of "hedgehog" 13 pipes transducer is 58.5% which is 2.25 times broader than the straight 8 pipes transducer and 6.0 times broader than the custom-built reference transducer. The signal strength of 13 pipes transducer is 1.89 times higher than 8 pipes transducer but 0.14 times lower than the reference transducer in TVR mode. In contrast, the signal strength of 13 pipes transducer is 3.7 times higher than 8

pipes transducer and 2.5 times higher than the reference transducer in RVR mode. The central frequency of 13 pipes transducer in both TVR and RVR modes is ~1.8 times higher than 8 pipes and reference transducers. Moreover, the pulse length of the 13 pipes transducer in both TVR and RVR is ~1.8 times shorter than the 8 pipes transducer and ~2.2 times shorter than the reference transducer.

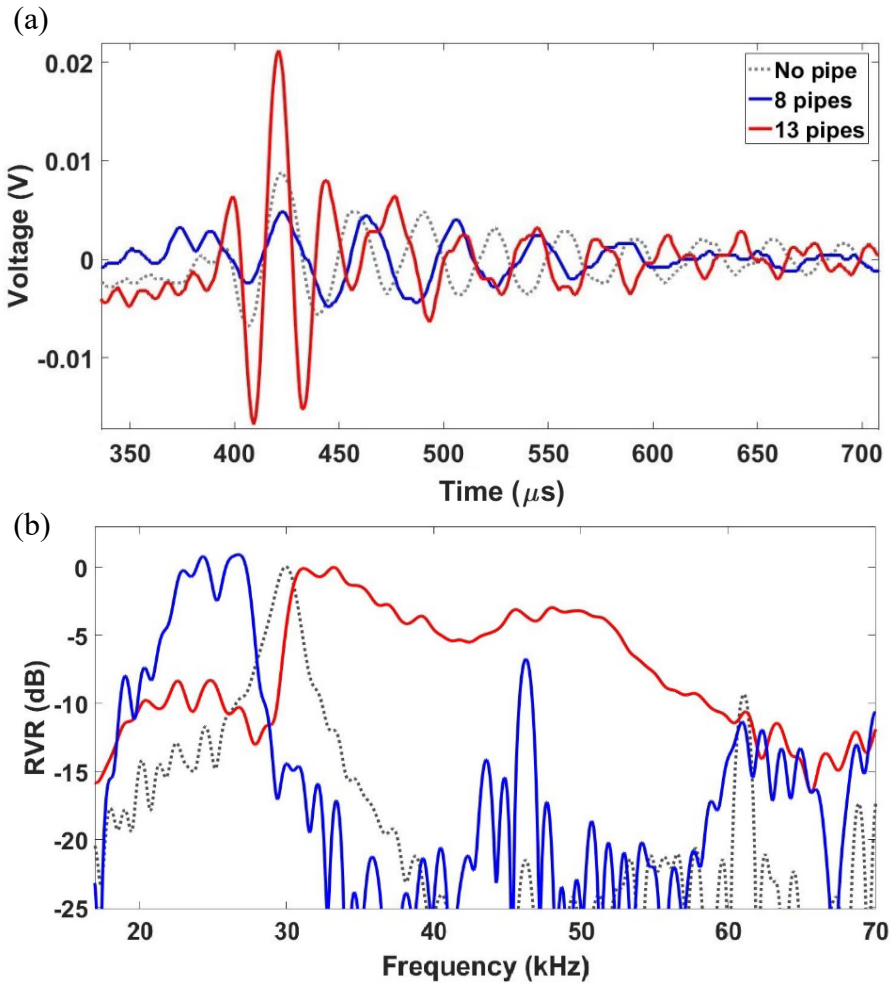

Figure 3.22. Receiving voltage response (RVR) in (a) time domain (b) Frequency domain

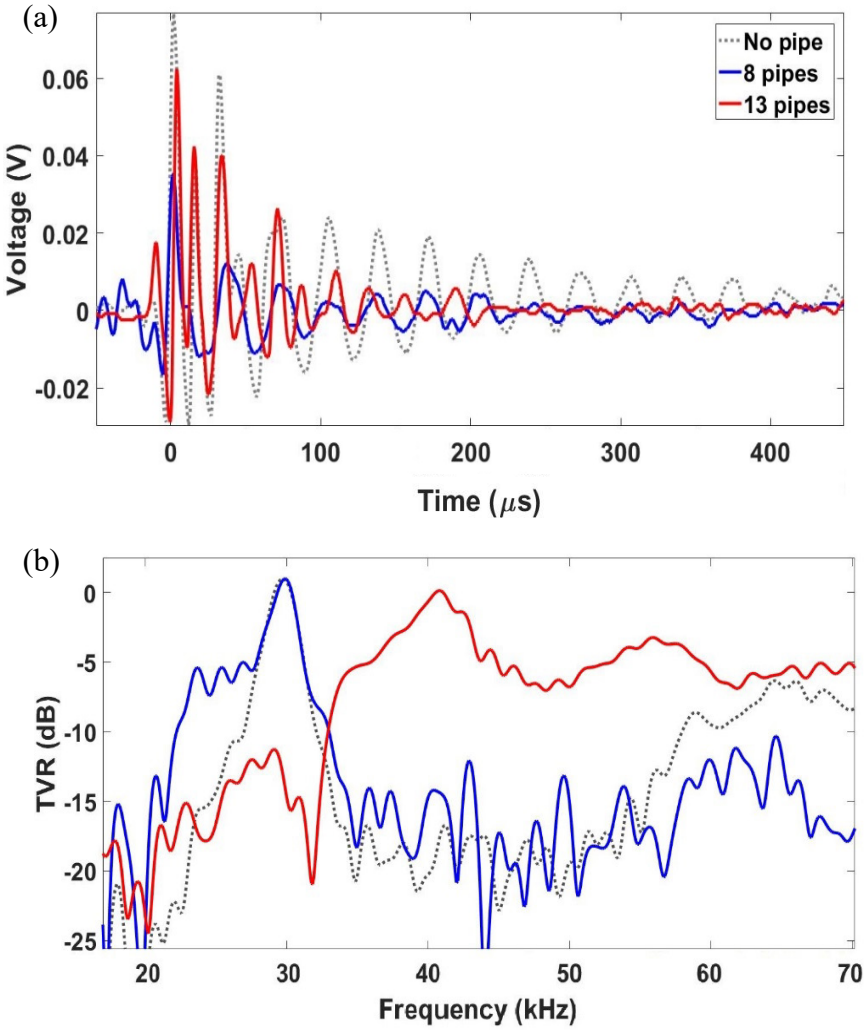

Figure 3.23. Transmitting voltage response (TVR) in (a) time domain (b) Frequency domain

In order to prove the repeatability of the "hedgehog" 13 pipes transducer another three samples were fabricated in order to re-measure their RVR (see Figure 17). The -6 dB bandwidth of those three devices are 52.9% (not a continuous bandwidth), 50.9% and 50.9% respectively which are very close to the first 13 pipes device in Table 3 (58.5%). Moreover, their frequency spectrums are also very similar (above 25kHz) except one of the

resonances was shifted at around 37 kHz. This was caused by the tolerance of fabrication when manually attaching the PVDF film with superglue.

Table 3.6 Experimental result of TVR and RVR.

Mode	Device	13 pipes	8 pipes	No pipe
TVR	-6 dB Bandwidth	55.7%	29.2%	12.3%
	Signal strength	0.091V	0.048V	0.106V
	Central frequency	47 kHz	27kHz	29kHz
	20% Peak-Peak Pulse length	8.8μs	20.1μs	20.5μs
RVR	-6 dB Bandwidth	58.5 %	26.0 %	9.7 %
	Signal strength	0.037 V	0.010V	0.015V
	Central frequency	41kHz	26kHz	30kHz
	20% Peak-Peak Pulse length	12.3μs	20.6μs	27μs

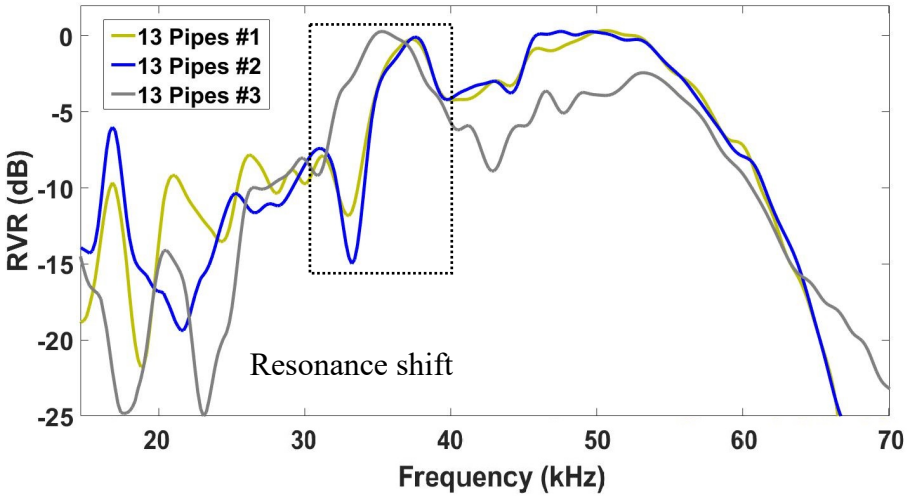

Figure 3.24. Repeatability experiment of three 13 pipes pipe organ transducers in RVR measurement

3.7. Simulation and Experiment Result Discussion

The pipe organ backplate is a resonator which is formed by a cavity with connecting of pipes of various length. Therefore, it includes many fundamental resonances and harmonics from those components. Section 3.1 and 3.1 evaluated those resonant frequencies from both mathematical and FEA model aspects to give the same conclusions. Section 3.1 investigated the resonance of the pipes and the cavity. The simulation results, shown in Figure 3.13, indicate that the resonant frequency of a pipe is mainly determined by its length, which can also be explained by equation (3.3). Furthermore, equation (3.4) indicates that the resonant frequency of the Helmholtz resonator depends on the area of the opening and the cavity volume. Therefore, samples III and IV have the same Helmholtz resonant frequency in Figure 3.13 boxes (a) and (c). Section 3.3.2 investigated the effect of the orientation of the pipes ("hedgehog" design). The pipes are designed to be orientated at different angles since previous 1D theoretical work concluded that the number of pipes should be as high as possible in order to have the widest bandwidth [5]. However, the number of pipes is limited by the resolution of the additive manufacturing technique in the lab. The "hedgehog" design provides a larger space to arrange the pipes because of the curved cavity surface. In other words, the "hedgehog" design increases the number of pipes with the same manufacturing resolution. Moreover, the "hedgehog" design provides additional benefits and Figure 3.15 and Figure 3.16 show that the "hedgehog" design has a larger Helmholtz resonance and more stable frequency response because the orientated pipes can focus ultrasound energy to the thin plate centre.

In the optimized designs, the resonant frequencies of the cavity, multiple pipes and the circular piezoelectric film were chosen to be close to each other in order to have a flat bandwidth response in both TVR and RVR. The results in Table 3.6 show that the bandwidth of the pipe organ devices is at least twice as wide as that of the no pipe device with comparable sensitivity. The “hedgehog” device has the largest bandwidth and shortest pulse length in both transmitting and receiving modes. However, the disadvantage is that the “hedgehog” device also requires a larger space to place the orientated pipes. The result from the 3D LDV (as shown in

Figure 3.20) indicates that the 1st flexure mode of those three transducers is around 29 kHz, which is very close to the theoretical value (30 kHz). The FEA simulation result has sharp gain peaks which caused the simulated bandwidth to be smaller than the experimental bandwidth. This is because the model did not include any electrical or mechanical damping and the sharp resonance peaks can help the designer locate individual resonance easily. However, the resonant frequencies from different components of the pipe organ backplate are a good match. The pipes’ fundamental and 2nd harmonic resonance varied from 20 to 25 kHz and 45 to 55 kHz respectively, and the Helmholtz resonance was located at 35kHz to fill the gap between the pipes’ resonance modes and increase the overall device sensitivity. This is why the 13 pipes pipe organ transducer can introduce a flat frequency response from 30 to 55 kHz in the experiment results. Although the vertical pipe design can have similar pipe lengths and cavity size, the “hedgehog” device can focus the ultrasound energy to the middle of the thin plate. Therefore, the “hedgehog” device has larger sensitivity improvement in the pipes’ resonant frequencies.

The repeatability experiment proved that the fabrication and the measurement stages are repeatable. All of the potential errors are from the tolerance of the fabrication.

3.8. Chapter Conclusions

The bandwidth of conventional PMUTs is too narrow to be used in wide-bandwidth applications [35]. This chapter presented a novel backplate design (resonator) to improve the bandwidth by selecting and enhancing the frequency range of interest. The frequency range can be carefully controlled through the specific parameters of the backplate. The principles were studied via mathematical equations and FEA models. The models indicated that the pipe organ backplate introduced Helmholtz resonances and multiple pipes' resonances to the circular thin plate's resonance to increase the device bandwidth without sensitivity loss. This also provided several conclusions to locate and quantify different types of resonances in the frequency domain. Two optimised designs were selected for the fabrication stage to compare against the custom-built standard device. An additive manufacturing technique for the pipe organ backplate is introduced. It is a faster prototyping method for fabricating piezoelectric diaphragm ultrasonic transducers. An improved resin formula was used to increase the manufacture resolution of the backplate. Finally, two experiments were designed to evaluate the response of two pipe organ transducers, and a standard transducer, in both TVR and RVR. The -6dB bandwidth of the "hedgehog" 13 pipes device was found to be up to 58.5% in RVR, which was 2.25 times larger than the vertical 8 pipe device, and 6 times larger than the custom-built standard device. In the TVR the -6dB bandwidth of the "hedgehog"13 pipe's device was up to 55.7%, which was 1.9 times larger than the 8 pipes device, and 4.6 times larger than the

customer-built standard device. The repeatability experiment shows that the fabrication and measurement progress are repeatable. The error originated from the manual fabrication process. With the ongoing development of additive manufacturing, some researchers [42] claim that they can use two-photon polymerization (TPP) for the fabrication of three-dimensional structures with a lateral resolution below 200 nm because it can indirectly create small structures in the UV curable resin which has been explained in chapter 2.2.3. However, it won't be able to fabricate a pipe organ transducer because draining the resin out of the small cavity and pipes will be a problem. Furthermore, it is possible to imagine that the fabrication could be achieved directly on a piezoelectric film in order to replace the gluing process used for this work's prototypes.

Chapter 4

Tailoring the "Pipe Organ" Inspired Ultrasonic Transducer Design to NDE Applications

4.1. Motivation

The preceding chapter presents a methodology for the design, simulation and prototyping of "pipe organ" inspired transducers. The $-6\,dB$ bandwidth of the "pipe organ" air-coupled transducer is 55.7% and 58.5% in transmitting and receiving modes, respectively, which is ~5 times wider than a custom-built standard device. Therefore, the broad bandwidth performance of the pipe organ design shows potential for improving imaging in medical or NDE applications. Limited by the manufacturing resolution available during this work, the central frequencies of the existing vertical and orientated pipes transducers are $27\,kHz$ and $\sim 50\,kHz$ [69] [7] respectively, which are much lower than the frequency range of most of NDE applications. Furthermore, the active area of the existed single element pipe organ transducer introduced in the preceding chapter is only $\sim 3\,mm^2$, that is too small for NDE applications. In addition, air-coupled ultrasound NDE requires a transducer with higher SNR to compensate for the energy losses. This is the motivation therefore to investigate a device with a larger active area and a higher

sensitivity. This chapter proposes two approaches, which are firstly a multiple element pipe organ with ~50 kHz central frequency, and secondly a single element pipe organ PMUT with ~500kHz central frequency, in order to tailor the pipe organ design to NDE applications and then use the commercial Finite Element (FE) software COMSOL MULTIPHYSICS to optimize the designs. Even though, the designs cannot be prototyped immediately, the optimized parameters can be used to inspire the next generation of pipe organ transducers. The required manufacturing resolution of the multiple element transducers is just lower than the best resolution CUE lab can achieve, this project can be finished after further optimizing the parameters of additive manufacturing. However, the required resolution of the 500 kHz PMUT is far smaller than that of the existing manufacturing technologies, this idea can be used to inspire the next generation of high frequency pipe organ transducer.

4.2. Multiple Elements "Pipe Organ" Ultrasonic Transducer with Wider Bandwidth and Higher Sensitivity

The concept of coupling multiple transducer elements has been well investigated in CMUTs [80] and PMUTs [19], where previous studies have proven enhancement of the sensitivity and/or bandwidth by summing up the energy from individual elements. This section will follow the same concept, simulating the transmitting and receiving performance of the pipe organ transducer with varied element numbers (from 1 to 16 elements) as shown in Figure 4.1 (a), and finally compare against the multiple elements conventional MUT (no pipe) design as shown in Figure 4.1 (b). The parameters of the

multiple-elements pipe organ transducer and the reference multiple-elements MUT (no pipe) design are given in Table 4.1.

Table 4.1. Parameters of the multiple-element (a) pipe organ transducer and (b) reference MUT (no pipe) design.

Device (μm)	**Multiple Element Pipe Organ Transducer**	**Multiple Element MUT (No Pipe) Design**
Depth of cavity h	450	450
Diameter of pipes d	400	400
Radius of thin plate R	1560	1560
Length of pipes L	3100, 2800, 2700, 2600, 2500	n/a
Membrane Thickness d_m	52	52
Membrane Material	PVDF	PVDF
Backplate Material	PEGDA	PEGDA
Element number	1, 2, 3, 4, 6, 9, 12, 16	1, 2, 3, 4, 6, 9, 12, 16

The model of the multiple element pipe organ transducer is modified by the four pipes transducer model which has been explained in Chapter 3. Similar to the previous model, this simulation model included the Shell Domain to simulate the mechanical vibration of the PVDF film, the Pressure Acoustic Domain to simulate the absolute pressure and coupling effect between the cavity and pipes, the Electrostatics Domain to simulate the charge migration inside the piezoelectric material, and finally a Multiphysics Model was applied to simulate the coupled boundaries between different physical domains. In order

to simplify the simulation and speed up the computation, this model also defined the backplate as a hard shell (Shell Domain). An air-sphere was defined to enclose the transducer to simulate its working environment. The boundary layer of the air-sphere was defined as a perfectly matching layer to make sure that sound waves can pass through the boundary without reflection. Viscous damping was added to the air-domains to make the model more realistic. Acoustic wave excitation (electric signals) were introduced to vibrate the thin film to simulate the receiving or transmitting modes of the transducer. In the TVR simulation, the measuring point is 2.5 mm which is further than the near field effect (~2 mm). Although both spacing of elements and element number may influence the performance of transducer, only the element number is considered in this model in this section. The selection of element spacing is based on the material property and manufacturing constraint. But this parameter also need to be optimized in the future.

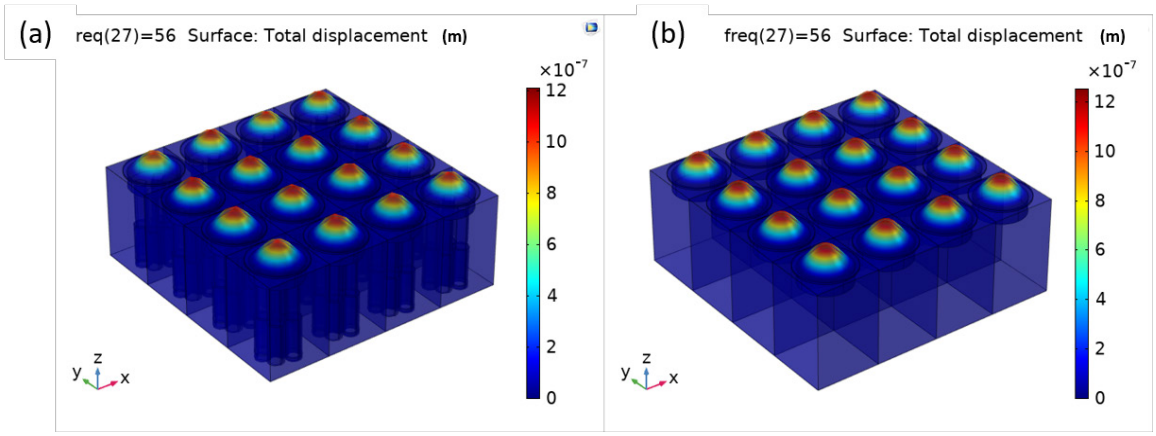

Figure 4.1 Multiple transducer elements in (a) pipe organ designs and (b) reference MUT (no pipe) design. Both figures are plotted at the resonant central frequency of transducer. The color bar shows the displacement in the transmitting mode.

Figure 4.2 and Figure 4.3 illustrate that the sensitivity can be improved in both of the transmitting and receiving modes when the element number is increased from 1 to 16. Figure 4.2 shows that adding the element number will not improve the bandwidth of the reference MUT design. The receiving response is different from the transmitting response at the resonant frequency in Figure 4.2 . The difference may be derived from the property of the piezoelectric thin film. However, further investigation is needed to confirm this assumption.

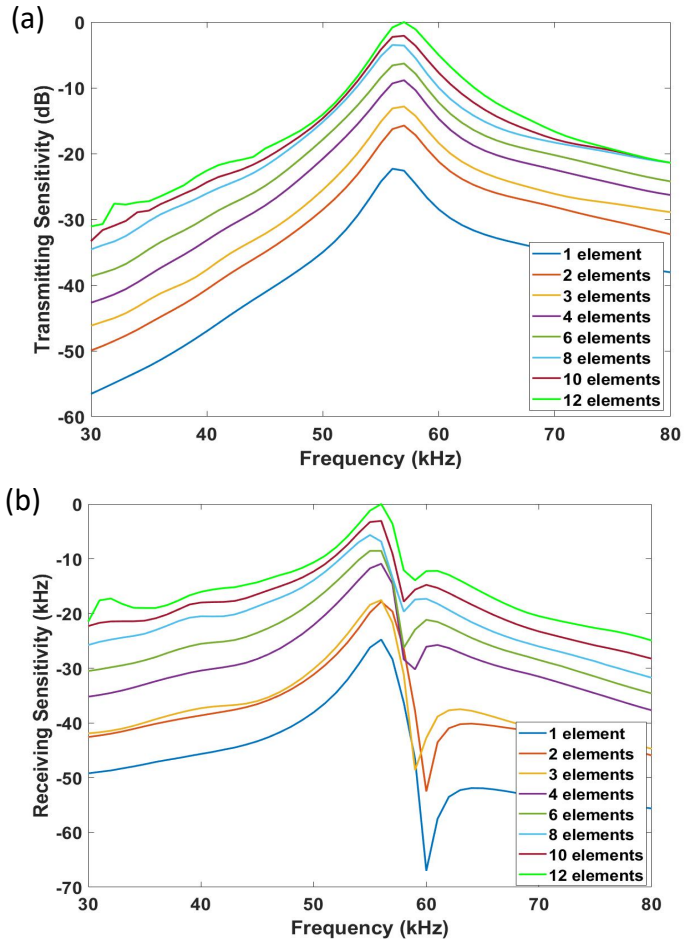

Figure 4.2. Normalized frequency response of (a) transmitting and (b) receiving when increasing the element number of reference MUT (no pipe) design

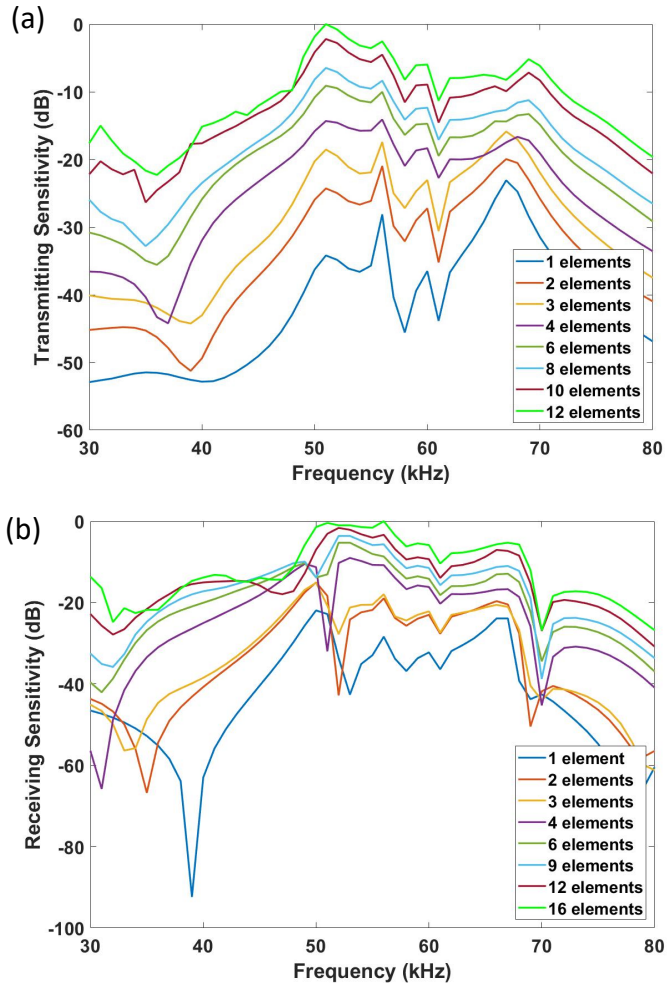

Figure 4.3. Normalized frequency response of (a) transmitting and (b) receiving when increasing the number of element of pipe organ transducer.

In contrast, the bandwidth of the pipe organ transducer as shown in Figure 4.3 is enhanced when the element number increases from 1 to 16. The central frequency of the multiple-element pipe organ transducer is designed to be $\sim 60\ kHz$ which can be used to conduct air-coupled low-frequency NDE [81]. In addition, the frequency response of the pipe organ transducers is much flatter than that of the reference MUT in both transmitting and receiving modes.

4.3. Single Elements "Pipe Organ" PMUT with ~500 kHz Operating Frequency

Even though, some air-coupled NDE applications use low frequency transducers ($\sim 50\ kHz$) to achieve deeper penetration [81], many NDE applications use air-coupled transducers with a frequency range around $\sim 500\ kHz$ [81].

This section aims to design a pipe organ transducer working at 480 kHz and then to optimize the design in a COMSOL model which is similar to the model in Chapter 3.3.2. The preceding chapter indicated that the orientated pipes could provide wider bandwidth and more considerable sensitivity, therefore the design of 500kHz pipe organ single element transducer is going to follow the orientated pipe structure as shown in Figure 4.4. The vital principle of a pipe organ transducer is designing the resonant frequencies of the cavity, multiple pipes and the circular thin film to be close, but not overlap with each other in order to have a flat frequency response (broad bandwidth). The mathematical equations of calculating the resonant frequencies of the cavity, pipes and the circular membrane have been given in (3.1), (3.2) and (3.3) respectively. The relationship between material properties, size of each part and their resonant frequencies is shown in Table 4.2, and it proves that the pipe organ transducer can operate in high frequency by miniaturizing all parts.

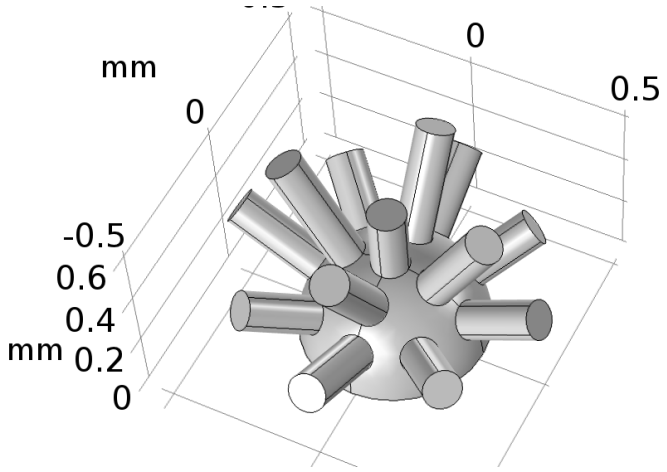

Figure 4.4. 3D CAD model of a 500kHz pipe organ inspired transducer.

The material of the thin film is chosen to be poly-silicon (Young's Modulus $E = 190$ [Pa], Density $\rho = 2320$ [kg/m^3] and Poisson Ratio $\mu = 0.22$) which is a relatively rigid material that widely used in conventional silicon based MUT or MEMS manufacturing. The thickness of the thin film is designed to be $10\ \mu m$. A thicker membrane can achieve a higher resonant frequency, however, it is much less sensitive. The material of the backplate should be rigid and thick enough to avoid the refraction of the sound wave. A $0.5\ \mu m$ double side coated piezoelectric AIN thin film is attached on the top of the silicon membrane. At the same time, the size of the pipes and the cavity are also reduced in order to enhance their resonant frequency. The dimension of the pipe organ PMUT is given in

Table 4.3. Figure 4.5 shows the simulated frequency response of the pipe organ PMUT and the reference PMUT (no pipe) in transmitting and receiving mode, and the central frequency of both transducers are around $480\ kHz$. In addition, there are several

resonance peaks distributed around the resonant frequency of the pipe organ PMUTs which increase the operating frequency range of the pipe organ transducer.

Table 4.2. Increase the resonant frequency of each component in the pipe organ transducers

Property / Resonance	Young's Modules (Rigidity) of Thin Film	Thin Film Thickness	Pipe Length	Cavity high	Diameter of cavity
Membrane	↑	↑	-	-	↓
Helmholtz	-	-	-	↓	↓
Pipes	-	-	↓	-	-

Table 4.3 Parameters of the single element (a) pipe organ PMUT and (b) the conventional reference PMUT

Device (μm)	**Single Pipe Organ PMUT**	**Single Conventional PMUT**
Depth of cavity h	270	270
Diameter of pipes d	60	60
Radius of thin plate R	540	540
Length of pipes L	250,250,260,270,280,290,300, 320,340,360,380,400,420	n/a
Passive Membrane	poly-silicon 10 μm	
Piezoelectric Layer	AIN 0.5 μm	
Backplate Material	poly-silicon	

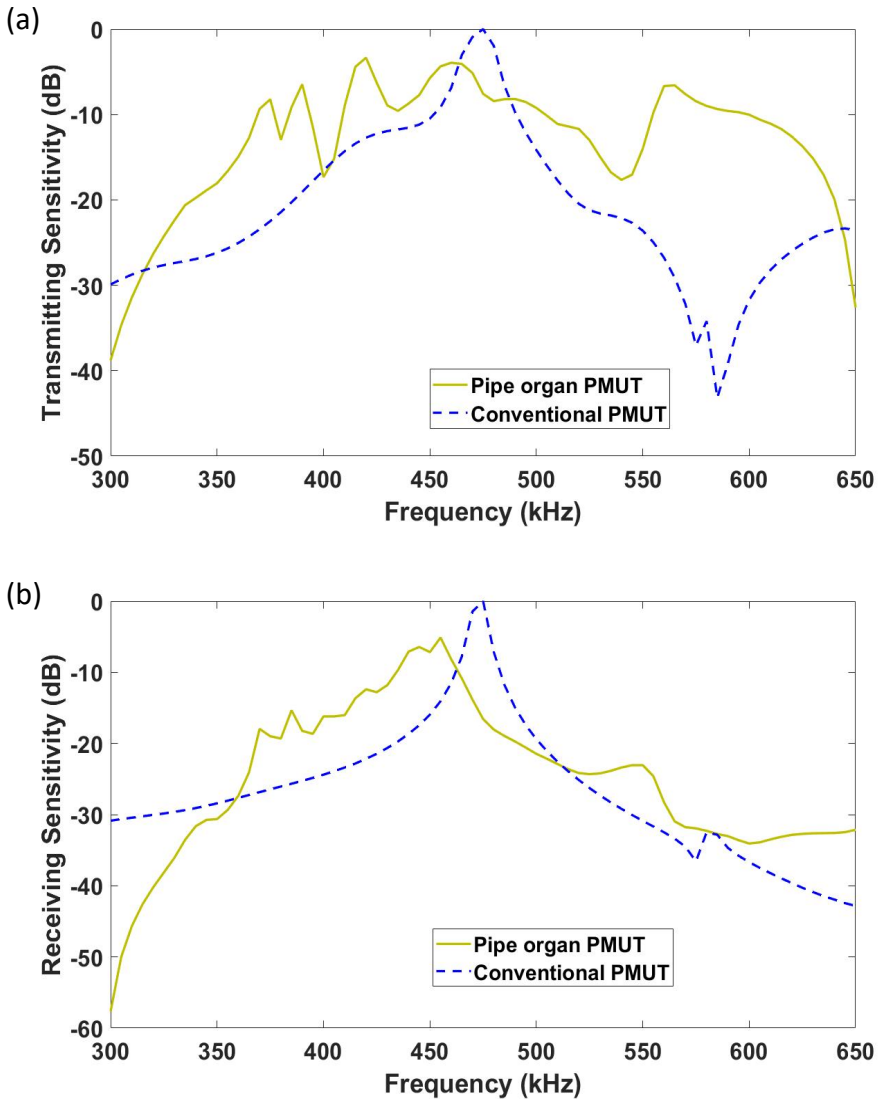

Figure 4.5. Normalized frequency response of the 480 kHz single element pipe organ transducer and conventional MUT in (a) transmitting and (b) receiving mode respectively.

4.4. Results

The pipe organ transducer introduced in the preceding chapter has a very promising performance in its bandwidth. However, it is clear that the prototypes are still far from practical applications in NDE because of the manufacturing limitation available during this work. With the development of the technology, the manufacturing resolution must be improved in the near future. This chapter can be regarded as a future work of Chapter 3. Two methods are proposed in this chapter in order to tailor the parameter of the pipe organ transducer to NDE application and then optimise them by using an FEA software COMSOL MULTIPHYSICS. As an initial stage study, the author found out some interesting phenomenon in the plot and then proposed several assumptions that need a more in-deep study to confirm it.

This FEA model only includes air damping (but not material damping) which makes the amplitude larger than realistic situation at the resonant frequency. This is the reason why all the results shown in this chapter are normalized to zero. However, this model can help the researchers to locate the resonant frequencies in the designing stage.

4.4.1. Multiple Elements Pipe Organ Transducers

Figure 4.2 and Figure 4.3 indicate that increasing the number of transducer elements can enhance the sensitivity in both transmitting and the receiving modes, and the central frequencies of the multiple element pipe organ transducer and reference MUT are ~55kHz. Moreover, Figure 4.3 shows that the bandwidths of the pipe organ transducers are enhanced by increasing the number of elements. In contrast, Figure 4.2 shows that the

bandwidth of the reference MUT doesn't change when the number of elements is increased. The prime reason is that the pipe organ backplate can be regarded as an artificial resonator to selectively amplify frequencies. The frequency responses of the resonators are coupled together when the element number increases [82]. The space of element havn't been investigated in this section because The material of the backplate is PEGDA, and the piezoelectric thin film is commercial PVDF, which are the same as for the pipe organ transducer introduced in chapter 3. The required fabricating resolution is just finer than the best resolution that could be achieved in this work. Therefore the prototyping and device characterization possibly can be done in the near future.

4.4.2. High-Frequency Pipe Organ PMUT

Figure 4.5 shows that the central frequency of both transducers is approximately 480 kHz which should be high enough for many air-coupled NDE applications. Similar to the low frequency single element pipe organ transducer shown in chapter 3, the high frequency single element pipe organ PMUT also shows the bandwidth improvement by comparing it against the reference PMUT. Due to the requirement of very high fabrication resolution, the high frequency pipe organ PMUT is difficult to be fabricated by using present additive manufacturing or silicon micromachining technologies. However, this FEA model can be used to inspire the next generation pipe organ PMUT by using advanced silicon or 2PP technique.

Chapter 5

Additive Manufacturing (AM) Capacitive Acoustic or Ultrasonic Transducers Using a Commercial Direct Light Processing (DLP) Printer

All of the results in this chapter were submitted to IEEE Sensor Journal (see Appendix 1: Additive Manufacturing (AM) Capacitive Acoustic Transducer Using a Commercial Direct Light Processing (DLP) Printer)

5.1. Introduction

Capacitive transducers for acoustic or ultrasonic measurement have been investigated for several decades. Currently, the performance of commercial capacitive transducers has reached a very high standard. However, most companies, for example, the well-known Danish company Brüel & Kjær (B&K), are still utilizing a traditional manufacturing technology and manually assembling these transducers from parts, resulting in low production volume and relatively higher cost [3]. Microelectromechanical systems (MEMS) is a more recent manufacturing technology that has commercially grown rapidly

during the last two decades and is used in a variety of applications, e.g. mobile devices and wearable devices. MEMS microphones can achieve reasonable sensitivity at low bias voltages due to their narrow air-gaps [4]. Many researchers have proposed several transducer or microphone designs with complex 3D structures in order to explore different ways to enhance their performance such as sensitivity [5] [6], bandwidth [7], [8] and directivity [9]. In recent years, there has also been increasing interest in using additive manufacturing (AM) technology (also known as 3D printing) in the fabrication of sensors or actuators owing to the possibility to create complex 3D geometries at micrometre-scale using highly flexible polymers. After integrating multiple nano-fillers with the passive base polymer, an AM nano-composite can exhibit different properties including conductivity [6] or piezoelectricity [7]–[9], which allow the transduction of mechanical energy into electrical form. There are many reports of actuators [10], [11] and sensors [8], [12]–[15], [67], [75] fabricated using AM processes. The 3D printed capacitive transducer was investigated in previous studies [18] that the diaphragm part was fabricated by using a 2D inkjet to print the conductive silver layer and then the diaphragm was manually attached on a 3D printed resonating cavity. The capacitive device can provide adequate sensitivity and predictable resonant frequency, however, the manual assembling process limits the resolution and operational frequency in the lower range.

This Chapter demonstrates a methodology for using a commercial digital light processing (DLP) printer to fabricate capacitive transducers which integrate a custom-made passive polymer with a custom-made conductive polymer. The transducer is small enough to be integrated with surface-mount electronics, and it is tested against a gold-standard

reference B&K microphone, showing comparable electro-acoustic sensitivity and following a predictable fabrication process. The novel transducer manufacturing technique has better repeatability because there is no manually assembling process. Nevertheless, the structure layout presented in this Chapter is a conventional capacitive transducer with a simple structure as shown in Figure 5.1. Additionally, this AM framework has the potential to benefit the fabrication of acoustic and ultrasonic diaphragm transducers with more complex geometries such as the ones used in biologically inspired transducer designs [8], [89], [91].

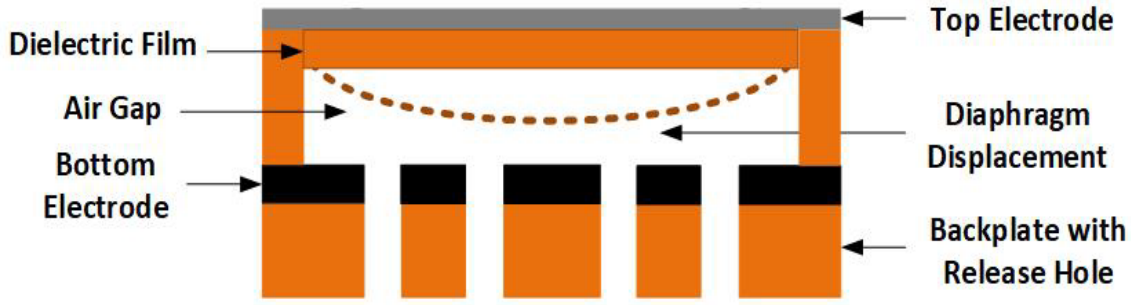

Figure 5.1. Simplified schematic of a conventional capacitive transducer.

5.2. Theoretical Background

5.2.1. Resin Optical Absorption

The absorption property of the material and the related light penetration can be explained by Beer's law as shown in (5.1) [71], where $I(z)$ is the intensity of the light in units of W/cm^{-2}, z is the depth of the penetration in the resin with $z \geq 0$ (as shown in Figure 5.3 (a)). Hua *et al.* [71] proposed a mathematical model assuming the light incident from a

source when the depth $z < 0$ is propagating along the $+z$ direction. I_0 is the initial light intensity on the boundary between the resin and tray (when $z = 0$). α is the absorbance of the resin with units of μm^{-1}.

$$I(z) = I_0 e^{-\alpha z} \tag{5.1}$$

The total dose of light $D(z,t)$ [71], in units of J/cm^{-2} can be expressed by (5.2), where the *t* is the exposure time.

$$D(z,t) = tI(z) = tI_0 e^{-\alpha z} \tag{5.2}$$

Current commercial stereolithography printers and their materials work better at millimetre scale ($> 1\, mm$) down towards sub-millimeter scale [92], and therefore are unlikely to meet the required resolution for the fabrication of micro-scale devices. Hua Gong *et.al* [71], [92] proposed an improved 3D printing resin formula by adding different absorbers (dyes) into the ultraviolet (UV) curable resin in order to increase absorbance (α) in equation *(5.1)* and (5.2). This improved formula increases the resolution to $\sim 100\ \mu m$ using a commercial DLP printer [71] and $\sim 20\ \mu m$ using a custom-built DLP-SLA printer [92]. The penetration depth and exposure time need to be adjusted by adding different amounts of absorbers. In this project, the absorber was SUDAN 1 and the optimized concentration was 0.5% by weight (wt. %).

5.2.2. Polymer/Multiwall Carbon Nanotubes (MWCNTs) Composite

Carbon nanotubes (CNTs) have emerged in recent years as one of the most promising nanofillers to enhance the mechanical properties (Young's modulus) [93], [94] and

conductivity of polymers [54], [95], [96]. CNTs are long cylinders of covalently bonded carbon atoms only a few nanometers in diameter, but lengths ca. tens of microns [54]. CNT/polymer composite based sensors have been studied for some time, but with limitations in terms of repeatability, sensitivity and stability [6]. However, those disadvantages could be improved through the use of AM technology. Researchers also indicate that beyond a certain weight fraction, which is known as the percolation threshold, of CNTs, there is a sharp rise in conductivity due to the formation of electrically conductive pathways inside the CNT/polymer composite [57]. The percolation threshold of multiwall (MW) CNTs was found to be hugely different when it is embedded in different polymer matrixes [57]. Polyethylene glycol diacrylate (PEGDA) is one of the conventional materials in stereolithography AM technology because of its UV curing properties. The conductivity of MWCNT/ PEGDA composite with the MWCNT concentration varied from 0.1% to 1.25% was previously studied [15], where it was concluded that there is a massive increase in the conductivity when the concentration increases from 0.1% to 0.5%, but this growth is dramatically slowed down when the concentration is greater than 0.5%. Also, several experimental trials indicate that the printability (resolution) becomes poorer when the CNT concentration is higher than 1.0% due to UV light scattering by the CNTs. Further, the composite layer must be at least $50\ \mu m$ thick to be conductive. Moreover, the composite resin becomes difficult to polymerize when the concentration is higher than 2%. Therefore, 0.5% (wt. %) is the optimized concentration [15] chosen for this study.

5.3. Material, Design and Fabrication

5.3.1. Material preparation

A stereolithography base resin usually includes at least two elements [71]: a monomer material and a photoinitiator. If some additional functionality (e.g. conductivity, flexibility, higher resolution, or piezoelectricity) is required, then nano-fillers can be added into the base resins. Two different functional stereolithography resins were synthesized in this project by using PEGDA (MW250), phenylbis (2,4,6-trimethylbenzoyl) phosphine oxide (Irgacure 819), SUDAN 1 (S1) and MWCNT (NC7000, average diameter 9.5 nm, average length 1.5 μm). PEGDA, Irgacure 819 and S1 were purchased from Sigma-Aldrich (St. Louis, MO) and the MWCNT was from Nanocyl (Sambreville, Belgium).

The first type of functional stereolithography resin used – the S1/PEGDA resin – was synthesized with PEGDA (98.5%, wt. %), Irgacure 819 (1%, wt. %), and S1 (0.5%, wt. %). The resin was then mixed in a Thinky ARE 250 planetary mixer (Intertronics) and sonicated for at least 30 minutes before use.

The second type of functional stereolithography resin – the MWCNT/PEGDA resin – was synthesized with PEGDA (98.5%, wt. %), Irgacure 819 (1%, wt. %) and MWCNT (0.5%, wt. %). The weighing and initial mixing process were carried out using vacuum glove bags in order to minimize any potential hazard from MWCNTs release. The mixture was then stirred for at least 24h with a magnetic stirrer before use.

5.3.2. Transducer Design

A conventional capacitive transducer consists of a dielectric thin film with one side metalized, a rigid conductive backplate and an air gap between the dielectric film and the bottom electrode (as shown in Figure 5.1). The resonant frequency of the capacitive transducer is mainly affected by the shape, thickness, size and the intrinsic stress of the thin film. Generally, the intrinsic stress is generated from the fabrication progress. When the transducer has an edge-clamped film with low intrinsic stress, the influence from the intrinsic stress is ignored, the resonant frequency of the thin circular plate (f_{tp}) can be estimated by the equations discussed in chapter sections 2.1.2. The squeeze film effect occurs when the air gap (depth of the cavity) is very narrow [72]. Squeeze film damping becomes more important than the drag force damping of air if the thickness of the gas gap is smaller than one-third of the thickness of the plate [72]. Even so, the air gap in a design should be thin enough to maximize sensitivity. Limited by the printing resolution of this project, the air gap of the transducer presented here is slightly thicker than the thin film. Therefore, the squeeze film effect is not significant in this transducer design. However, the design does include some releasing holes to minimize the squeeze film damping.

The computer designed 3D model was produced as shown in Figure 5.2 (a). The anchor and the backplate (orange parts) are made by a passive polymer which is synthesized with PEGDA and Sudan 1, the black layer between the air-gap and the backplate is the PEGDA/MWCNT composite polymer. The top silver round layer is an aluminate electrode. The transducer design used three diameters, chosen to be $1.8\ mm$, $2.1\ mm$ and $3.2\ mm$, in order to place the resonant frequencies at $19\ kHz$, $35\ kHz$ and $54\ kHz$

respectively. After testing the accuracy of fabrication, the height of the air gap was determined to be $\sim 120\ \mu m$ and the thickness of the dielectric film was $\sim 80\ \mu m$. The thickness of the top aluminum electrode was $0.11\ \mu m$ deposited using a thin film deposition system (E306, Edwards). The thickness of the bottom MWCNT electrode is $\sim 50\ \mu m$. Simulating the resonant frequency of the capacitive transducer requires knowledge of the mechanical properties of the S1/PEGDA composite. This depends on any variations in the exposure time and the concentration of the absorber during the AM. The estimated mechanical properties utilized in this work (Young's Modules $E = 1\ GPa$, Poisson Ratio $v = 0.32$ and Density $\rho = 1183\ kg/m^3$) are based on a previous study [15]. Figure 5.2 (b) shows the cross-sectional X-ray computerized tomography (CT) scan of the transducer. The aluminum electrode cannot be replaced by a 3D printed MWCNT/PEGDA layer since the limitations of the AM resolution and the conductivity in this study mean that such a layer would be too thick to vibrate with incident acoustic signal.

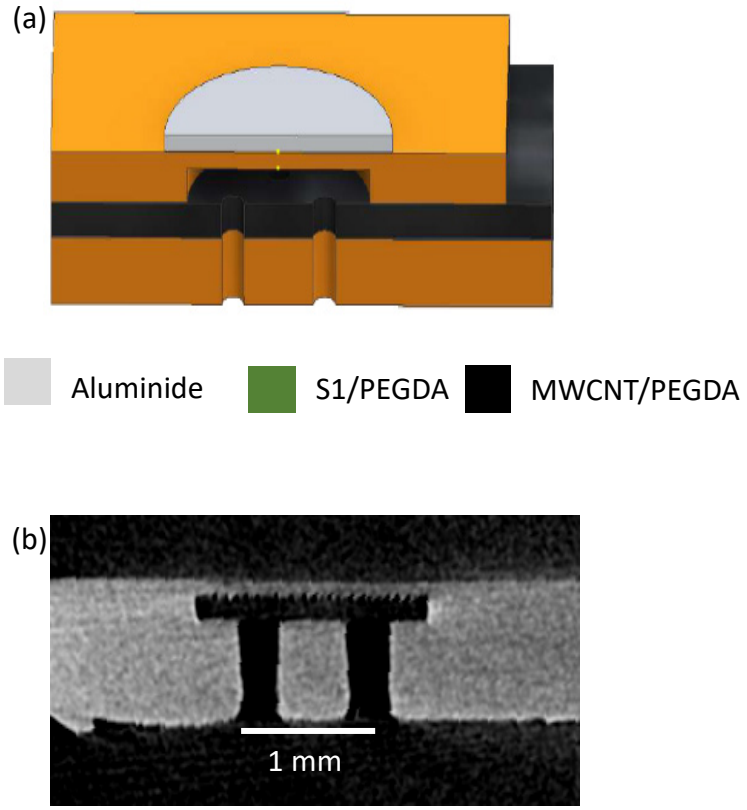

Figure 5.2. The cross-sectional view of an AM capacitive acoustic transducer: (a) 3D computer model and (b) X-ray CT scan. Fabrication

An ASIGA stereolithography printer (PICO 2 HD 27 μm) was utilized to fabricate the capacitive transducer. This printer has a 27 μm pixel size in the X-Y plane and 1 μm available resolution in the Z axis. The wavelength of the UV light source is 385 nm. A build layer of 10 μm and exposure time of 3.6 s allow an optimized resolution for the material formula introduced above. Figure 5.3 shows the workflow for the transducer's fabrication process.

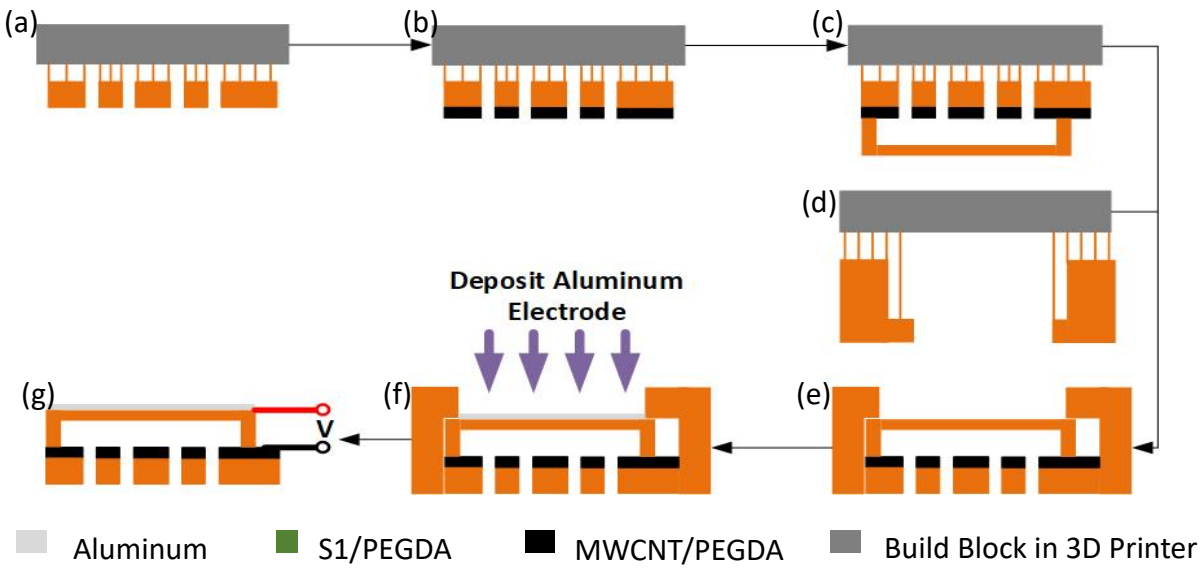

Figure 5.3. The fabrication flow for the capacitive transducer: (a) Print S1/PEGDA backplate with releasing holes. (b) Print MWCNT/PEGDA conductive layer with releasing holes as the bottom electrode. (c) Print S1/PEGDA air gap and dielectric thin film. (d) Print S1/PEGDA mask for top electrode coating. (e) Flip the transducer and mount the mask. (f) Deposit aluminium electrode on the top of the film as the top electrode. (g) Connect wires to the electrodes.

First of all, the S1/PEGDA backplate with support is printed on the building block. Then, any extra unpolymerized resin is cleaned away with Ethanol, and the system is manually swapped to a MWCNT/PEGDA resin tray to print the conductive bottom electrode layer. After that, the sample is cleaned again and the system is swapped to the S1/PEGDA build tray to print the air gap and dielectric thin film. The top electrode is finally deposited. A mask is printed after the transducer sample is removed from the build tray. The mask is mounted on the flipped transducer, and then the sample is placed into the thin film deposition system where the aluminum electrode is deposited on the top of the dielectric thin film. Finally, the mask is removed and wires connected to the device's top and bottom electrodes.

5.4. Results

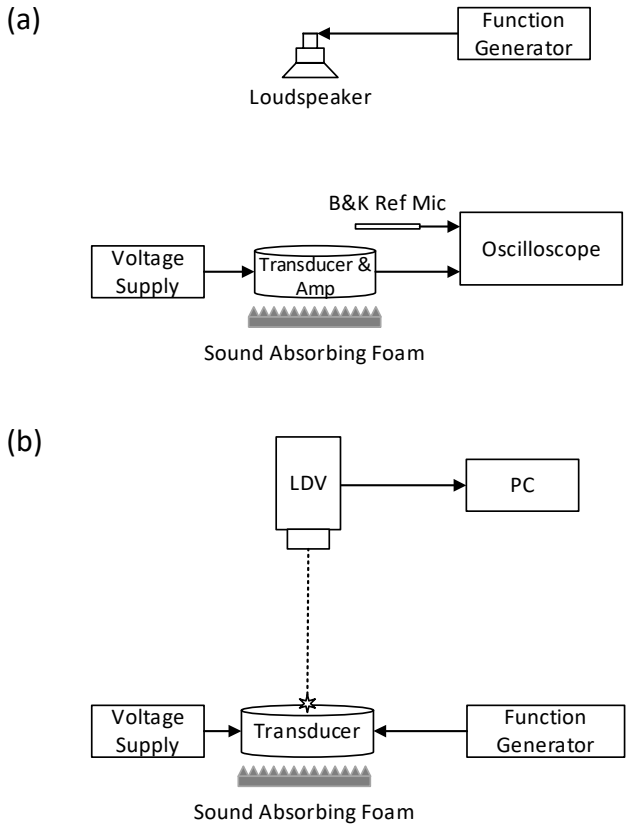

Figure 5.4. Simplified schematic of the experimental setup for the (a) sensing and (b) transmitting measurements.

Figure 5.4 (a) & (b) show the experimental setup for characterizing the transducer in sensing and transmitting modes, respectively. In Figure 5.4 (a), a function generator produced a 7 cycles tone-burst to drive a loudspeaker. The transducer was placed 20 cm away from the loudspeaker to avoid any near-field effects. A voltage supply provided different DC voltages from $0 - 150\ V$ to bias the transducer. The electrical output signal generated by the transducer was amplified by a custom-built electronic circuit (as shown in Figure 5.7) and finally acquired using an oscilloscope. A 1/8 inch reference microphone

(Brüel and Kjær, Type 4138) with an operational frequency range from 1 Hz to 110 kHz and a paired charge amplifier (Brüel and Kjær, type 2692) were used to measure the reference sound pressure around the transducer. The reference signal was then utilized to calibrate the sensitivity of our transducers. Sound absorbing foam was placed under the transducer and the B&K microphone to avoid acoustic reflections.

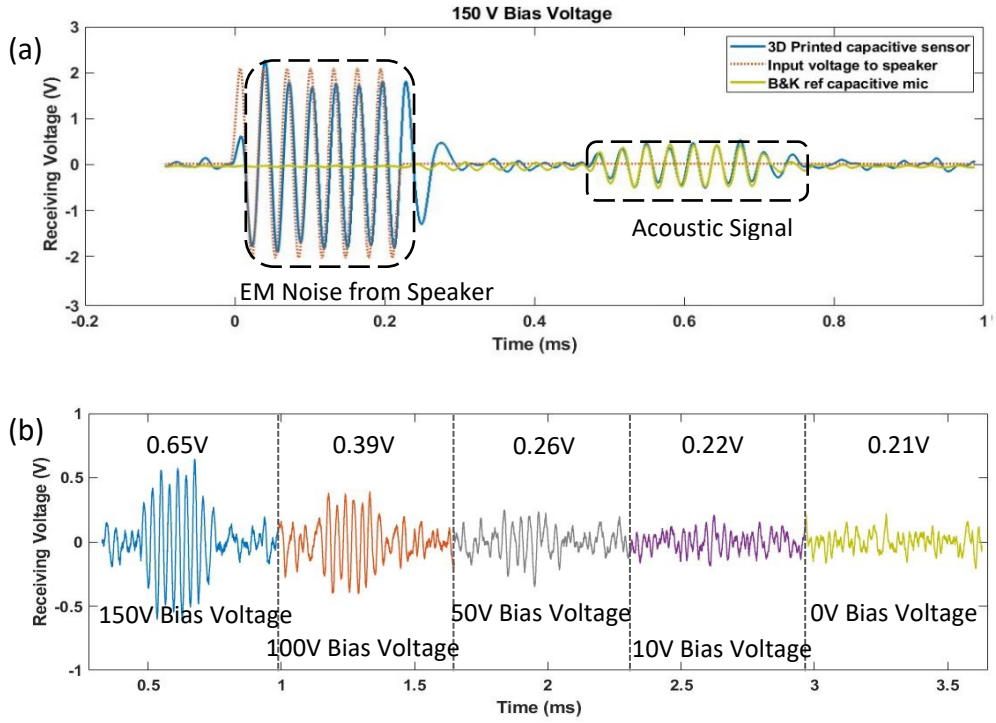

Figure 5.5. The electrical output time domain signal from the transducer (diameter=2.1mm) integrated with the amplification circuit when the loudspeaker played a 7 cycles tone-burst at 35 kHz*. (a) Shows the electrode magnetic and acoustic signal received by both of the 3D printed transducer and the B&K reference microphone under 150 V bias voltage. (b) Shows the maximum amplitude change of the acoustic signal when providing different bias voltages from 150-0 V.*

In Figure 5.4 (b), the function generator inputted a 10 V chirp signal to drive the transducer into vibration, which was detected by a 3D Laser Doppler Vibrometer (LDV:

MSA100-3D, Polytec, Inc., Waldbronn, Germany). A voltage supply was used to bias charge the capacitive transducer with varied DC voltage from $0 - 200\ V$.

Figure 5.5 gives the values of capacitance and receiving sensitivity with respect to different membrane diameters. The static capacitance of the transducer was measured using a 4194A Impedance/Gain-Phase Analyzer under a 150 V bias voltage. It was found that the capacitance of the transducer is proportional to its size. The receiving sensitivity (S) of the transducers was calculated by (5.3) with the unit mV/Pa where the Output (O) is the maximum amplitude of the amplified signal at the resonant frequency of the transducer, the Acoustic Pressure (AP) is the sound pressure level around the transducer measured by the reference B&K microphone and the Amplifier Gain (AG) is the gain of our custom-built amplifier across the interested frequency range.

$$S\ (mV/Pa) = \frac{O\ (mV)}{AP\ (Pa) \times AG} \tag{5.3}$$

The receiving sensitivity of the AM capacitive transducer can reach up to $0.4\ mV/Pa$ before amplification (as shown in Table 5.1).

Table 5.1. The receiving sensitivity and the static capacitance of the AM transducers with different film diameter measured with 150 V bias voltage at each resonant frequencies

Diameter	**$1.8\ mm$**	**$2.1\ mm$**	**$3.2\ mm$**
Frequency	54 kHz	35 kHz	19 kHz
Capacitance	$2.08\ pF$	$3.74\ pF$	$4.62\ pF$
Sensitivity	$0.009\ mV/Pa$	$0.013\ mV/Pa$	$0.4\ mV/Pa$

However, the receiving sensitivity rapidly decreases to 0.009 mV/Pa when the diameter of the transducers decreases. The reason for this is that the smaller active area results in lower sensing energy and smaller capacitance change [97]. Figure 5.5 (a) also shows that the sensitivity of the acoustic signal of the AM transducer operating at its resonant frequency can be compared to that of B&K microphone, nevertheless, this AM transducer set-up has less immunity to electromagnetic interference due to the absence of any shielding or proper packaging design. Similar to other capacitive transducers (as shown in Figure 5.5 (b)), this AM capacitive transducer requires a bias voltage to operate, and its sensitivity increases proportionally when providing higher bias voltages. The transmitting mode of the AM transducer was characterized by measuring the vibration of the thin film as shown in Figure 5.6 (b) as the transmitted sound field was too weak to be measured by the reference microphone. Figure 5.6 (a) shows the frequency response of the transducer with $2.1\ mm$ diameter. The output signal increases in amplitude when providing a larger bias voltage. Figure 5.6 (b) shows that the resonant frequency of the transducer with different diameters ($1.8\ mm$, $2.1\ mm$ and $3.2\ mm$) was characterized at $54\ kHz$, $35\ kHz$ and $19\ kHz$ respectively which were close to the the simulated resonant frequency curves. The simulation method assumes the intrinsic stress is low and the mechanical properties used in both methods are given in the transducer design section. Figure 5.7 (a) shows the AM transducer integrated with a custom-build amplifying circuit which was developed by Dr Jose Guerreiro at the Center for Ultrasonic Engineering, University of Strathclyde. The circuit board is $3\ cm \times 4\ cm$, and the silver part is the active area of the transducer. A hybrid JFET operational amplifier circuit was built in

order to amplify the signals captured by the 3D printed sensor, as illustrated in Figure 5.7 (b) [98]. This circuit was designed with a constant gain of 50dB between 1 - 100 kHz.

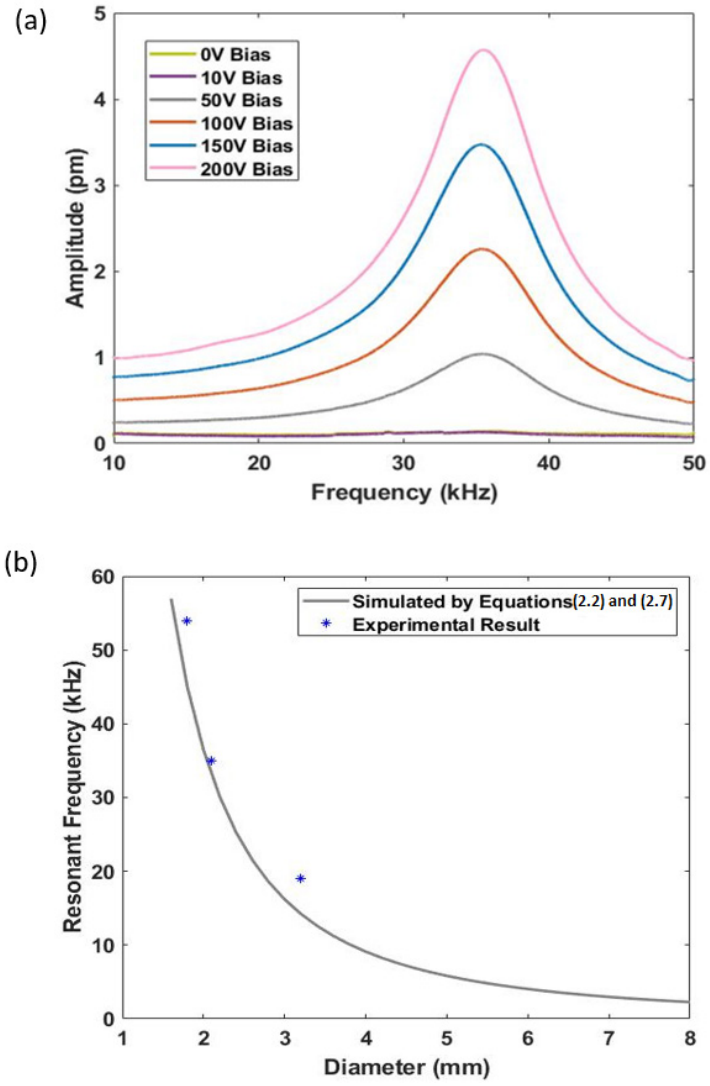

Figure 5.6. (a) The frequency response of the transducer (diameter=2.1 mm) was measured by LDV when the transducer was driven by 10 V chirp signal and different bias voltages. (b) The comparison between the simulated and experimental resonant frequency. The simulation assumes that the intrinsic stress is low.

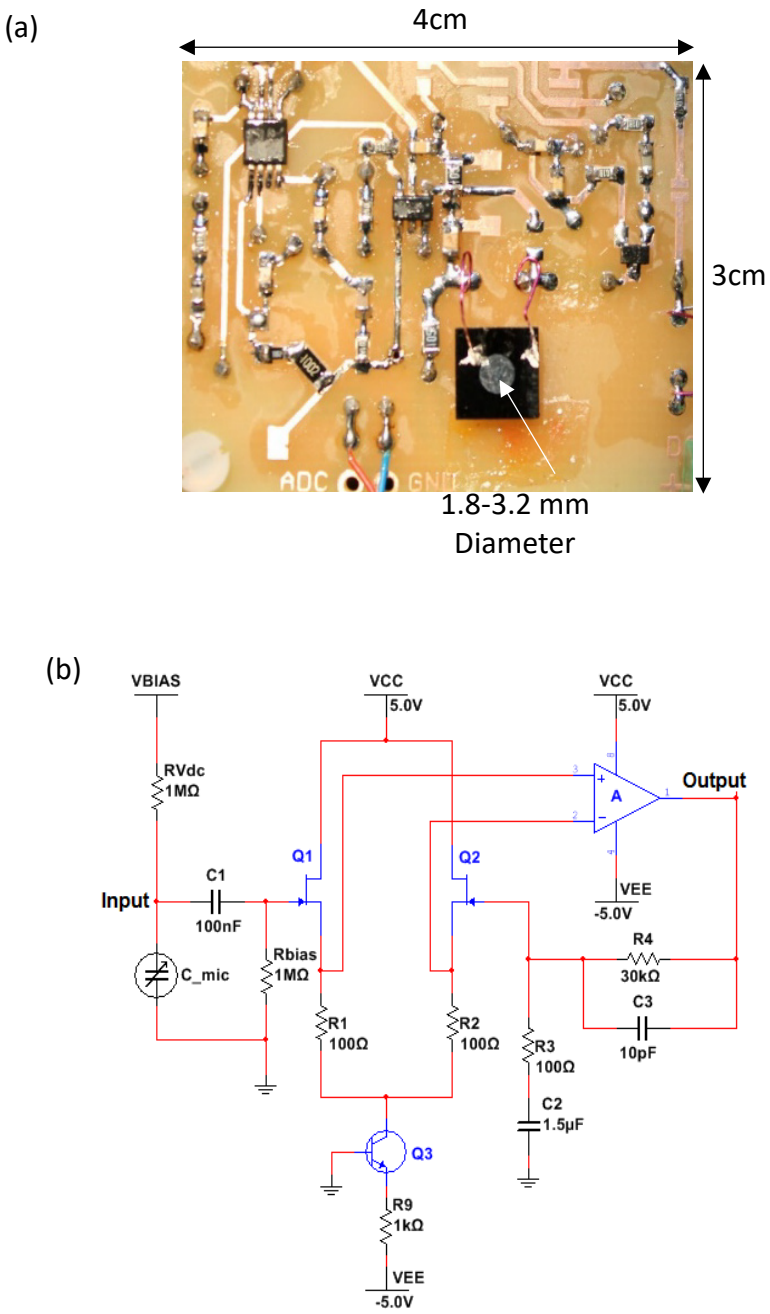

Figure 5.7. (a) Custom-built amplifying circuit integrated with the AM transducer. The size of the circuit board is $3\ cm \times 4\ cm$*, and the silver part with different diameters* $(1.8 - 3.2\ mm)$ *is the active area of the transducer. (b) Schematic of amplifying circuit. The custom-built amplifier provides a constant gain of approximately* $50\ dB$ *with operational bandwidth (*$-3\ dB$ *bandwidth) of* $1 - 100\ kHz$

5.5. Conclusion

This Chapter demonstrates the first submillimeter scale capacitive transducer fabricated with a commercial DLP 3D printer. Transducers with different size have been fabricated and integrated with appropriate electronics to characterize the overall performance. The characterization results indicate that the performance of the AM transducer in sensing mode can reach up to $0.4\ mV/Pa$ at its resonant frequency. In contrast, the receiving open circuit sensitivity of a circular-clamped MEMS microphone and the commercial B&K microphone (Type 4138) with similar size are reported to be $\sim 1\ mV/Pa$ at a bias voltage of $1\ V$ [86] and $1\ mV/Pa$ at a bias voltage of $200\ V$ [99], respectively. The collapse voltage of the conventional MEMS microphones is usually lower than $5\ V$ due to their narrow air gaps ($\sim 2\ \mu m$) [84]. The required bias voltage of the AM transducers is $150\ V$, which is much higher than the conventional MEMS microphone ($< 5\ V$) but lower than the B&K commercial microphone ($200\ V$). Different diameter transducers were fabricated and tested in this work. The resonant frequency of the transducers decreases from $52\ kHz$ to $19\ kHz$ and the received sensitivity increases from $0.009\ mV/P$a to $0.4\ mV/Pa$, respectively, when the diameter of the transducers increases from $1.8\ mm$ to $3.2\ mm$. The current AM transducers have better performance in sensing rather than transmitting due to their low transmitting sensitivity. Because of the limitations of the commercial AM printer used, the fabrication process still requires human interaction, for example, manually swapping the resin tray, post processing the AM samples and evaporation coating the top electrode. The AM fabricating process will not take longer than two hours and the speed of coating process depends on the technique. The yield rate

of the AM transducer is lower than 30% when the diameter is smaller than $1.8\ mm$. The AM transducers remained functional for a period of several months.

Due to the advantages of using the AM technology to create complex 3D geometries, there are possible applications for the AM transducers including integration with hearing prostheses, bio-inspired transducers with complex 3D structures, underwater sonar, and non-destructive testing (NDT). The maximum operating frequency achieved by these purpose-built AM transducers is limited by the printing resolution of the printer. However, recent developments in two-photon polymerization (TPP) can achieve a resolution below $200\ nm$ [42] which could provide for a reduction in the transducer size and thus lead to operation in higher frequency ranges. Nevertheless, the performance of the transducer might be further improved by decreasing the air gap, and also by increasing the conductivity of the MWCNT/PEGDA composite as a result of optimizing the formula and exposure time. Further to this, recent work has demonstrated AM fabrication with multiple materials automatically by using a custom-build 3D printer [100]. The fabrication process of AM capacitive transducers could therefore become far more automatic in the future.

Chapter 6

Characterization of Piezoelectric Nanocomposite Film for Stereolithographic Additive Manufacturing Applications

6.1. Introduction

Stereolithography (STL) resin is a type of liquid photopolymer that cures (polymerizes) under an ultraviolet (UV) light source. The existing single phase STL resins do not have piezoelectric property. A two-phase piezoelectric nanoparticle/polymer composite was developed in previous studies [15], [53] with Barium Titanate ($BaTiO_3$) nanopowder and a UV curable resin, PEGDA. However, the piezoelectric property of the two-phase nanocomposite was reported to be low ($1 - 4$ pC/N) [15], [53]. This is because there is a dielectric property mismatch between the insulating polymer and the piezoelectric powders [47], [49], [50] that decreases the polarization of the electric dipoles [47]. Several studies indicate that the piezoelectric properties of two-phase nanocomposite could be enhanced by adding another phase of material as an energy improver, e.g. adding multiwall carbon nanotubes (MWCNTs) [7], [47], [49]–[52] to match the dielectric property between the piezoelectric particles and the insulating base polymer.

The piezoelectric coefficient (d_{33}) of the material usually can be determined in two ways. One approach is the direct measurement of the piezoelectric effect by using a d_{33} meter. This machine applies a periodic force to the sample and then measures the resulting charges. The other approach is measuring the converse piezoelectric effect, which is measuring the strain generated by a known electric field. This method can be accomplished by measuring the thickness variation when applying a sine wave voltage. This measurement requires to use the equipment like Laser Doppler Vibrometer (LDV) or Atomic Force Microscopy (AFM) that have a resolution in picometer range in the vertical direction. The unit of d_{33} can be written as pm/V or pC/N that depends on which measuring technique is used. However, for the method using d_{33} meter, it is hard to produce a homogeneous uniaxial stress on the thin film without a bending effect, which generates additional charges through the transverse piezoelectric effect that affect the result [101]. Compared with the d_{33} meter, the LDV has ultra-high resolution in displacement, and so the piezoelectric coefficient of the ultra-thin films can be evaluated with good reliability.

The following chapter characterizes the piezoelectric effect (d_{33}) of the two-phase and three-phase nanocomposite films by varying the concentration of $BaTiO_3$, MWCNTs and the poling time by using the 3D LDV technique. And then optimizes the resin formula for applications with additive manufacturing (AM) ultrasonic transducers.

6.2. Methodology

6.2.1. Materials

Barium Titanate nanopowder ($BaTiO_3$, purity 99.5%) was purchased from US-NANO with a 500 nm average diameter.

Multi-Wall Carbon Nanotubes (MWCNTs, NC700) were purchased from Nanocyl (Sambreville, Belgium) with a 9.5 nm diameter and 1.5 mm length.

Polyethylene Glycol Diacrylate (PEGDA, MW 250) and the Irgacure 819 (I819) were purchased from Amiga Aldrich.

6.2.2. Preparation of Piezoelectric Nanocomposite Film

To make the different functional resins, materials were mixed together in various combinations. The base resin was synthesized with PEGDA (99%, wt. %) and I819 (1%, wt. %). This was then sonicated (Decon, Ultrasonics Ltd, England) for 15 mins until the I819 photoinitiator powder had been dissolved. To make the two-phase resin, a variety of weight fractions of $BaTiO_3$ (33-66%, wt. %) were added to the base mixture. To synthesize the three-phase resin, 0.01% to 0.07% (wt. %) of MWCNTs were added to the above two-phase resin. Both the two-phase and three-phase resins were sonicated for 30 minutes. The mixtures were then stirred (IKA RET Basic) for at least 24h with a magnetic stirrer before use. The weighing and initial mixing process were carried out using vacuum glove bags in order to minimize any potential hazard from MWCN T release. Materials

were weight by OHAUS Pioneer with an accuracy of 0.001g. To weigh 0.01% of CNTs, the quantity of three-phase nanocomposite must be more than 10g.

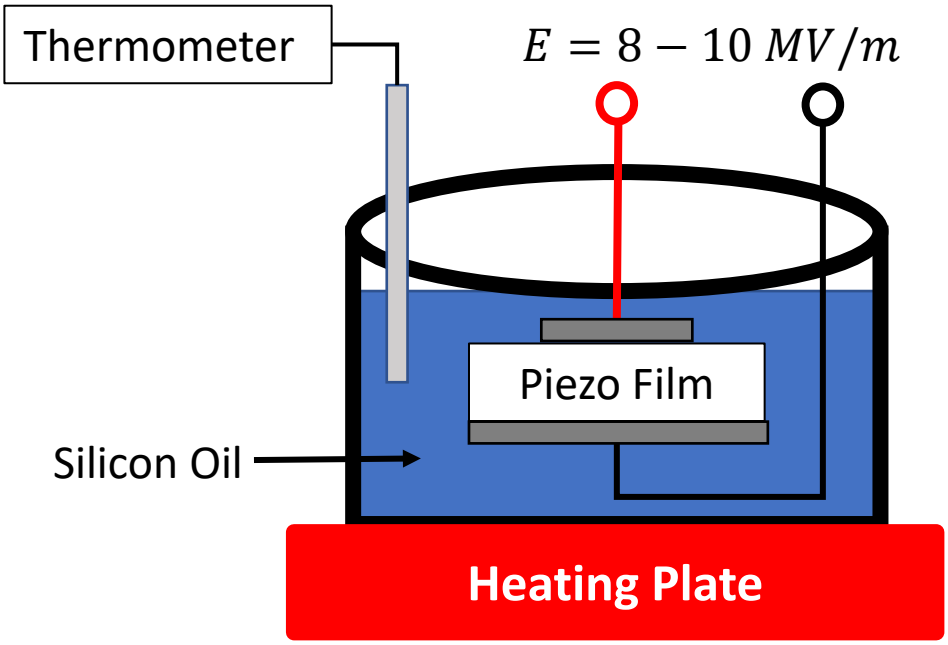

Figure 6.1. Direct poling of the composite sample in silicon oil tank heated to 100℃ *with an constant electric field.*

The film samples comprising the piezoelectric nanocomposite described above were polymerized by placing a droplet of resin between two glass slides with a spacer separation of 110 μm and then cured in a UV oven for 3 minutes. Circular electrodes with a diameter of 2 cm were painted on both sides of the sample using silver paint. The polling process is illustrated in Figure 6.1. The sample clamped by a metal stage was placed in a silicon oil tank heated to a constant temperature of 100 ℃ and a thermometer kept monitoring the temperature synchronously. An electric potential, which was just lower than the breakdown voltage of the sample (the sample cannot be poled if it is short-circuit), was applied across the terminals of the sample for a period $(1 - 12\ \text{hours})$. The applied

potential was reduced from 10 MV/m to 8 MV/m (values obtained from experiment) after embedding the CNTs, because adding MWCNT reduces the dielectric breakdown voltage.

6.2.3. Characterization of Piezoelectric Nanocomposite Film

The piezoelectric charge constant, d_{xy}, is the mechanical strain generated by a piezoelectric element per unit of electric energy applied, or conversely it is the electrical energy generated by the element per unit of mechanical stress applied. Both the LDV and d_{33} meter can be used to measure the d_{33} constant of piezoelectric material.

The characterization technology of using LDV to measure the d_{33} of the piezoelectric thin film can be illustrated in Figure 6.2. The sample was carefully glued on a glass slide and then clamped on a solid metal block to avoid any flexing vibration which could possibly affect the measured result [101], [102]. The voltage stimulus was generated by an internal function generating system of the LDV. The output data of the LDV was collected and analysed by the control PC and software.

In order to make sure the samples being well glued, it was first driven by a 10 V chirp signal over the frequency range from 1kHz to 20 kHz and the frequency response is shown in Figure 6.3 (a). The amplitude of the frequency response is almost flat from $4-20$ kHz when the film is well glued on the glass slide and no air bubble is trapped under the film because the thickness mode of a piezoelectric thin film should be higher than 10 MHz and there is no resonance between 4 and 20 kHz.. The low frequency noise in Figure 6.3 (a) was from the environment and equipment. Therefore, the measuring frequency

must be higher than 4 kHz to avoid the low frequency noise. A sinusoidal AC voltage of 10 V_{pp} and 5 kHz was then applied across both sides of the sample. As shown in Figure 6.3 (b), the maximum displacement of the piezoelectric thin film is ~170 pm. The d_{33} of this piezoelectric thin film can be calculated by equation (6.1), where w_{max} is the maximun displacement of the sample and V_{rms} is the effect voltage ($V_{rms}/\sqrt{2}$) of the input signal.

$$d_{33} = \frac{w_{max}}{V_{rms}} \tag{6.1}$$

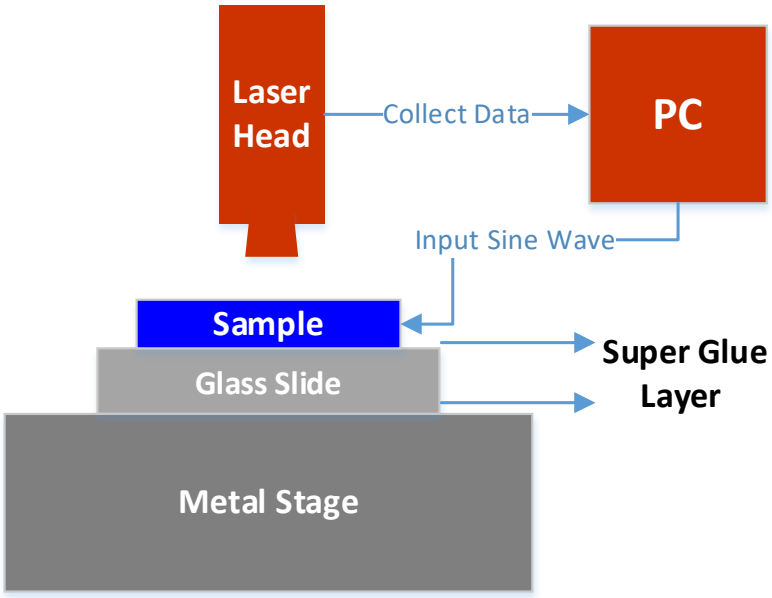

Figure 6.2. Characterize the piezoelectric thin film by using LDV.

When the sample was well glued, the displacement of the membrane should be similar to Figure 6.4. If the vibration in one area is different from that elsewhere (not vibrate in-plane), there must be air bubbles trapped under the thin film. Then the measured piezoelectric coefficient will be higher than the practical result.

(a)

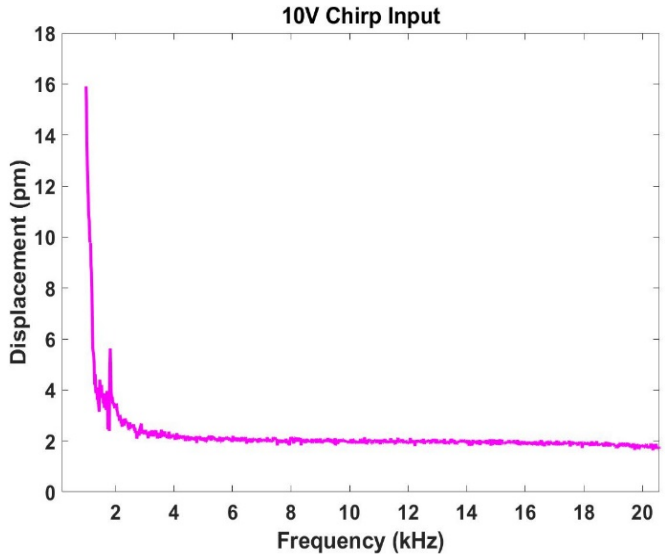

(b)

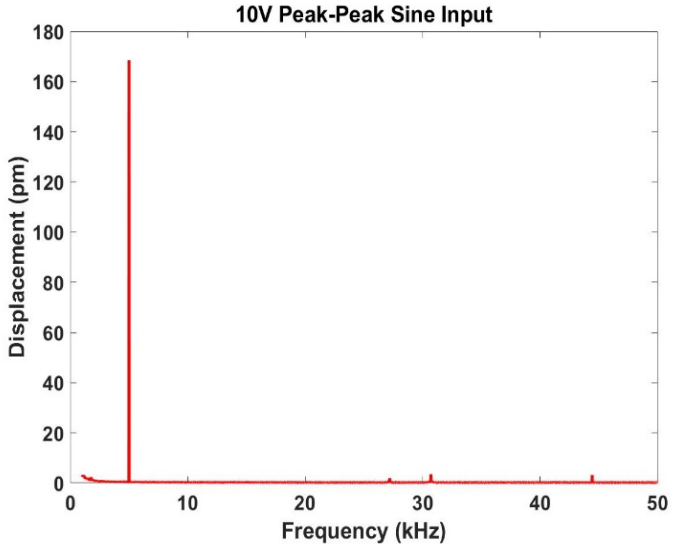

Figure 6.3. The frequency response of the piezoelectric thin film to (a) 10V chirp signal and (b) 10V peak-peak sine wave input signal. The frequency response in (a) must be flat from 4 to 20 kHz otherwise the measured displacement in (b) is not accurate.

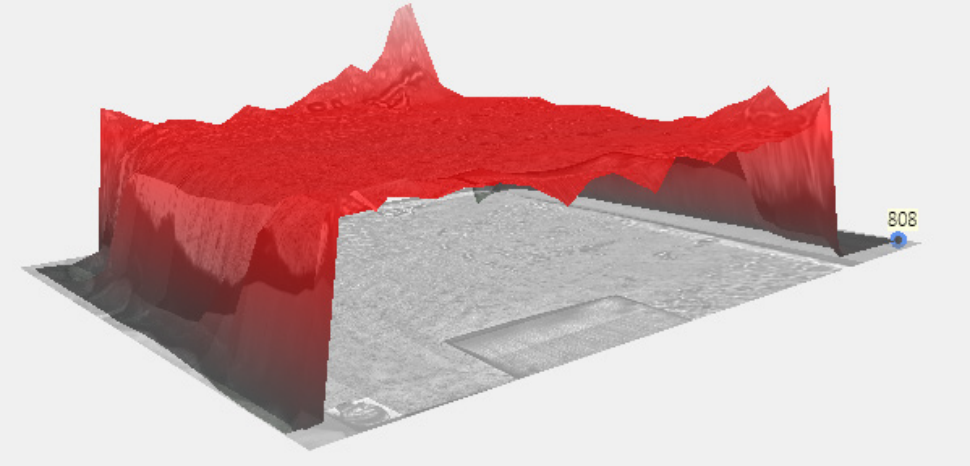

Figure 6.4. The measured displacement of piezoelectric thin film. The vibration should be in-plane if the piezoelectric thin film is well glued on the glass slide and metal block. Otherwise, the measured piezoelectric coefficient is not accurate.

d_{33} Meter

The d_{33} meter is a piece of equipment for directly measuring the piezoelectric constant of piezoelectric material like bulk ceramic and thick plate. The design and structure of the ZJ − 6B d_{33}/d_{31} meter is schematically shown in Figure 6.5. First of all, you turn the adjusting knob to drive the top probe up or down and then clamp the testing sample between the top and the bottom probes. The sample could not be pressed too tight or too loose. Secondly, the shaker generates a periodic $0.25\ N$ force with a frequency of 110 Hz. The sample will then generate an output electrical signal in response to the periodic force. The output signal is then amplified by the amplifying system. And finally, you record the value when the meter display is stable.

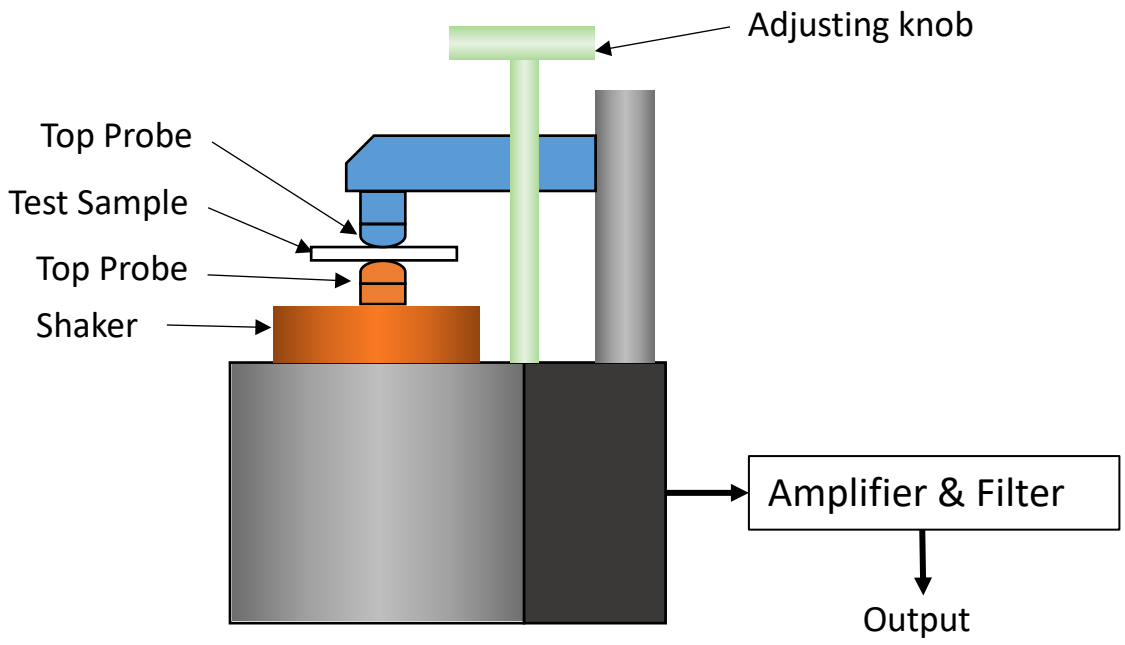

Figure 6.5. Schematic illustration of the ZJ − 6B d_{33}/d_{31} meter.

Calibration of the LDV method with d_{33} meter

For this chapter the LDV method was used to characterize the piezoelectric property of the sample because a previous study [101] indicated that the LDV method has better reliability in measuring ultra-thin piezoelectric film. Before using LDV technology, this method was firstly calibrated by a commercial quasi-static piezoelectric ZJ − 6B d_{33}/d_{31} meter (Institute of Acoustics Chinese Academy of Sciences) and a known PVDF film ($110\ \mu m$). The piezoelectric coefficient measured by the LDV method was 24.0 pm/V which was very close to the d_{33}/d_{31} meter result (22.5 pC/N) and the theoretical result (25 pC/N).

6.3. Results

Figure 6.6 indicates that the piezoelectric coefficient of the $BaTiO_3/PEDA$ nanocomposite increases when more $BaTiO_3$ is added into the resin. However, a previous study [15] shows that stereolithography manufacturing resolution in the X-Y axis are deleteriously affected by increasing the concentration of $BaTiO_3$, which is poorer than 1 mm when the weight fraction of $BaTiO_3$is higher than 50%. Therefore, the maximum possible d_{33} is restricted to about 2 pm/V when the concentration of $BaTiO_3$ is 50% (wt. %) poled for 2 hours. This is the reason why the maximum concentration of $BaTiO_3$ is fixed at 50% in the following experiments.

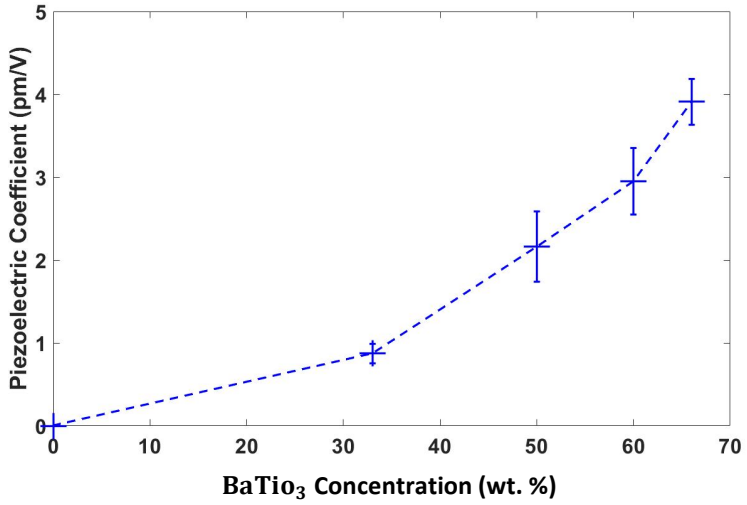

Figure 6.6. The d_{33} measurements of the two-phase $BaTio_3/PEGDA$ piezoelectric nanocomposite as the concentration of $BaTio_3$ is increased from 0% to 66% (wt. %). An electric potential of 10 MV/m was applied across the samples for two hours. The sample was placed in 100℃ silicon oil during the poling process. The error bars represents the standard deviation of the repeated measurement between three samples.

Figure 6.7 shows the d_{33} of the three-phase $BaTiO_3$/MWCNTs/PEDA nanocomposite. As the MWCNT concentration increases from 0 to 0.02%, the d_{33} slightly decreases from 2.2 pm/V to 1.7 pm/V. The value then remains constant when the fraction ratio of the MWCNT increases to 0.03%. When the concentration of MWCNTs reaches 0.05%, the number of d_{33} rises dramatically to 2.7 pm/V, which is also the maximum value in this plot. However, the d_{33} falls back to around 2.2 pm/V when the concentration of MWCNT increases to 0.07%. Several experimental trials indicate that the breakdown voltage of the sample becomes very low when the MWCNT concentration is higher than 0.07%. In addition, adding MWCNT will further reduce the X-Y resolution.

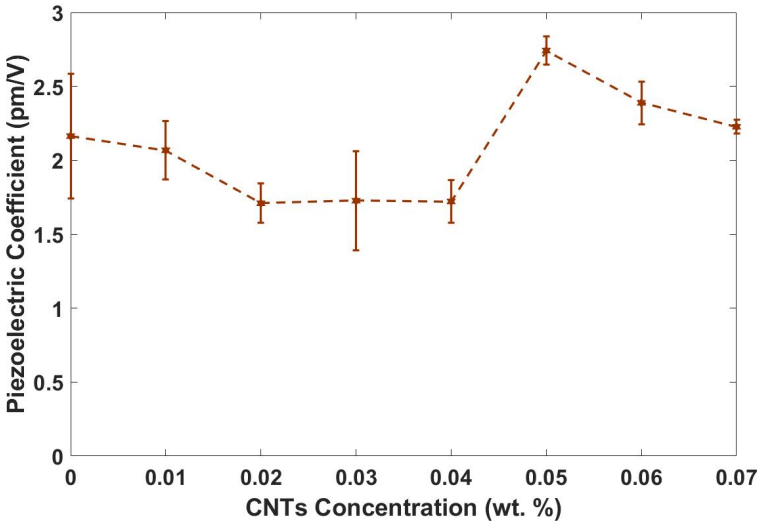

Figure 6.7. The d_{33} measurements of the three phase $BaTio_3/MWCNT/PEGDA$ piezoelectric nanocomposite as the concentration of $MWCNTs$ is increased from 0% to 0.07% (wt. %). The concentration of $BaTio_3$ was fixed at 50%. With increasing the concentration of MWCNT, the poling electric potential was decreased from 10 MV/m to 8 MV/m in order to avoid dielectric breakdown. The samples were placed in 100℃ silicon oil for 2 hours during the poling process. The error bars represents the standard deviation of the repeated measurement between three samples.

The piezoelectric coefficient as a function of poling time is studied as shown in Figure 6.8, where the blue line represents the optimized three-phase nanocomposite (50% $BaTiO_3$, 0.05% MWCNT and 49.95% PEDA), and the red line represents the reference two-phase nanocomposite (50% $BaTiO_3$ and 50% PEDA). Figure 6.8 indicates that there is a roughly proportionally increment of the d_{33} value of the nanocomposite as a function of poling time. The d_{33} of the three-phase nanocomposite increases faster than that of the two-phase nanocomposite. However, the d_{33} of the two-phase nanocomposite is slightly higher than that of the three-phase nanocomposite when the samples are poled longer than three hours. After poling for 12 hours, the d_{33} of both nanocomposites are very close.

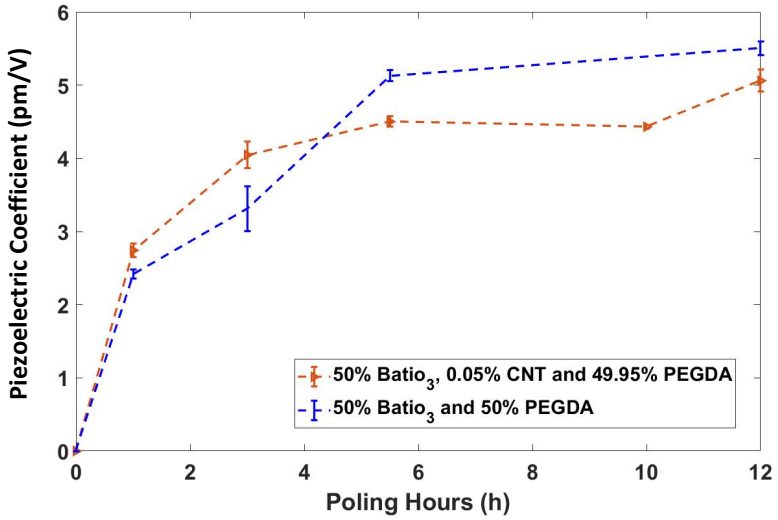

Figure 6.8. The d_{33} measurements of the two phases and three-phase piezoelectric nanocomposite as the poling time increased from 0 to 12 hours. The poling electric potentials applied on the two-phase and three-phase nanocomposites are 10 MV/m and 8 MV/m, respectively. The samples were placed in 100℃ silicon oil during the poling process. The error bars represent the standard deviation of the repeated measurement between three samples.

6.4. Conclusions and Future Work

This chapter characterizes the piezoelectric coefficient of the piezoelectric nanocomposites in order to optimize the formula to SLA AM application. Two-phase ($BaTiO_3/PEDA$) and three-phase ($BaTiO_3/MWCNT/PEDA$) nanocomposite thin films have been fabricated. The nanocomposites show an enhancement in the piezoelectric strain coefficient with increasing in the weight fraction of $BaTiO_3$ and the poling time. The high concentration of $BaTiO_3$ is desirable. However, it makes the printing resolution become poorer than $1\ mm$ when the concentration of the $BaTiO_3$ is higher than 50%. The measured piezoelectric coefficient of the two-phase nanocomposites in the range of $5-6\ pm/V$ is lower than most of the conventional piezoelectric materials, e.g. PVDF ($25\ pC/N$) and PZT ($\sim 350\ pC/N$). Several studies [7], [47], [49]–[52] reported that adding MWCNT to the polymer matrix could significantly (~6 times) [7] enhance the d_{33} of the two-phase nanocomposite. However, this reported promising result could not be repeated in these experiments. The following researchers do not need to repeat the experiments which have been done in this Chapter. Some possible reasons were concluded in order to inspired future experiments:

- The polling time is not long enough. The samples were not fully polled.
- The nanopowder ($BaTiO_3$ and MWCNT) are not well dispersed.
- The concentration of MWCNT is too low. Using corona polling can avoid the dielectric breakdown. Covering the sample with a thin layer of insulating polymer can also prevent shorting [7].

Due to the requirement of more piezoelectric materials for transducer application, future work might involve using piezoelectric nanopowders with smaller particle size [7], higher piezoelectric coefficient, e.g. PZT [48] and PMNT [67], using another energy improver like TMSPM [53]. Sintering the nanocomposite is another option, but this causes polymer shrinkage and material's mechanical properties (e.g. Young's modulus) changed [67].

Chapter 7

Conclusion and Future Work

7.1. Conclusion

7.1.1. General Overview

This thesis describes the development of AM air-coupled ultrasonic transducers through proposing pipe organ inspired designs to improve operational bandwidth, using AM technology to fabricate acoustic capacitive transducers, and developing piezoelectric materials for the AM piezoelectric transduces application.

High resolution is one of the essential requirements in ultrasonic technologies. A broad bandwidth ultrasonic transducer can achieve this requirement because its pulse length in the time domain is short. Previous studies indicated that the bandwidth of conventional PMUTs are narrow [16], [18], [22] thus making them unsuitable for wide bandwidth applications [19], [35]. The pipe organ inspired designs introduce multiple lengths of pipes into the conventional cavity backplate which results in multiple resonances within a single element transducer. Hence, the operational bandwidth of the pipe organ transducer can be enhanced if the pipes are appropriately configured. Although the characterization results indicate that the operational bandwidth of the pipe organ transducers is ~5 times broader than the custom-built conventional diaphragm transducers, the central operating frequency of the pipe organ transducers (~50 kHz) is too low for most NDE applications

In order to increase the central frequency of the transducer, the air cavity and the diameter of the pipes should be as small as possible. However, a 0.424 mm diameter pipe is the smallest diameter that can be fabricated with the current AM technology in CUE lab. Moreover, the active area of the single element pipe organ transducer also needs to be increased in order to achieve better SNR in air-coupled NDE inspection. Two designs were proposed in Chapter 4 in order to tailor the pipe organ design to more NDE applications. The multiple element pipe organ transducer design aims to further enhance the overall sensitivity and the bandwidth of the pipe organ transducer by integrating multiple elements together. The multiple element pipe organ transducer proposed in this thesis is still a single transducer because the diaphragms vibrate in phase. It is possible to create a pipe organ phased array by firing individual pipe organ elements with a time delay. However, this thesis does not demonstrate that functionality. A single element high-frequency PMUT design was proposed to prove that the central frequency of the pipe organ transducer can reach ~500 kHz after reducing the size of the backplate. The FEA simulated results for both designs seem to be promising, where the sensitivity of the multiple element pipe organ transducer has a 40 dB improvement after increasing the element number from 1 to 16, and the high-frequency pipe organ transducer can reach 480 kHz with ~50% bandwidth. However, considering the time and cost, it was not possible to pursue these during the PhD. The optimized parameters can still be used to inspire the next generation pipe organ transducers for NDE applications.

Chapter 5 demonstrates a novel methodology for using a DLP 3D printer to fabricate acoustic capacitive transducers which integrates a custom-made passive polymer with a

custom-made conductive polymer. These AM transducers are small enough to be integrated with surface-mount electronics. The transducers are tested against a gold-standard reference B&K microphone, showing a comparable electro-acoustic sensitivity with a predictable fabrication process. A set of capacitive acoustic transducers was fabricated and tested using different diaphragm diameters from $1.8 - 2.2\,mm$, for comparison, with central operating frequency between $19 - 54\,kHz$, respectively. Additionally, this AM framework has potential to the applications of integrating with hearing prostheses, bio-inspired ultrasonic transducer with a complex 3D geometries, underwater sonar and NDE.

Stereolithography (STL) resin is a type of liquid photopolymer that cures (polymerizes) under an ultraviolet (UV) light source. The known single-phase STL resins do not have a piezoelectric property. A two-phase piezoelectric nanoparticle/polymer composite was studied in the literature [15], [53] using Barium Titanate nanopowder as a filler in a UV curable resin, PEGDA. Chapter 6 optimized the formula and then characterized the piezoelectric nanocomposite in order to improve the performance of the additive manufactured piezoelectric thin film. After characterization, the d_{33} of the two-phase nanocomposites were found to be up to $6\,pm/V$ which is much lower than most of conventional piezoelectric materials. Previous studies [7], [47], [49]–[52] reported that the adding MWCNT into the two-phase matrix could significantly (~6 times) enhance the d_{33} of the two-phase nanocomposite However, this promising result could not be repeated during this PhD research.

7.1.2. Main Findings of this Thesis

From the model analysis and the experimental characterization of the pipe organ designs, the following conclusions have been made for the development of the air-coupled pipe organ transducers, multiple elements pipe organ transducers and the high-frequency single element pipe organ transducers, respectively.

- The pipe organ backplate is an artificial resonator which is formed by a cavity (Helmholtz resonator) with connecting of pipes of various length. Therefore, it includes many fundamental resonances and harmonics from those components.
- The bandwidth of the pipe organ transducer increased as the number of pipes increased.
- The overall gain of the pipe organ transducer is larger than the conventional transducer in receiving mode because the Helmholtz resonance can improve the overall sensitivity.
- The orientated pipes ("hedgehog") design has larger sensitivity improvement in the pipes resonant frequencies because the orientated pipes can focus the ultrasonic energy to the middle of the thin diaphragm.
- The -6dB bandwidth of the "pipe organ" air-coupled transducer is 55.7% and 58.5% in transmitting and receiving modes, respectively, which is ~5 times wider than a custom-built standard device.
- The central frequency of the pipe organ transducer prototype is up to 50 kHz which is limited by the manufacturing constraints in the CUE lab.

- According to the FEA simulated results and the theory of pipe organ backplate, the resonant frequency of the pipe organ inspired design can reach 480 kHz which should be high enough for many air-coupled NDE applications. Similar to the low-frequency pipe organ transducers, the high-frequency pipe organ design has much broader bandwidth than the conventional design. However, the required manufacturing constraint is finer than that the CUE lab can provide.
- According to the FEA simulated results for the multiple element pipe organ design, the bandwidth and the overall gain of the pipe organ transducer are enhanced by increasing the number of element.

Chapter 5 introduced the design, fabrication and the characterization process of the AM ultrasonic capacitive transducers. Several conclusions were made below:

- Different diameters of transducers were fabricated and tested during this study. The resonant frequency of the transducers decreases from 52 kHz to 19 kHz and the received sensitivity increases from 0.009 mV/Pa to 0.4 mV/Pa, respectively, when the diameter of the transducers increases from 1.8 mm to 3.2 mm.
- The performance of the AM transducer in sensing mode can reach up to 0.4 mV/Pa at its resonant frequency. In contrast, the receiving open circuit sensitivity of a circular-clamped MEMS microphone and the commercial B&K microphone (Type 4138) with similar size are reported to be ~ 1 mV/Pa.
- Comparing with the B&K reference microphone, the AM transducers set-up has less immunity to electromagnetic interference due to lack of any shielding and packaging design.

- The required bias voltage of the AM transducers is 150 V because of the larger air-gaps, which is much higher than the conventional MEMS microphone (<5 V) but lower than the B&K commercial microphone (200 V).
- The current AM transducers have better performance in sensing rather than transmitting due to their low transmitting sensitivity.
- Because of the limitations of the commercial AM printer used, the fabrication process still requires human interaction, for example, manually swapping the resin tray, post-processing the AM samples and evaporation coating the top electrode.

Different ratios of two-phase ($BaTiO_3$/PEDA) and three-phase ($BaTiO_3$/MWCNT/ PEDA) nanocomposite thin films have been fabricated and then tested. From the characterization of the multiple-phase piezoelectric materials, as shown in Chapter 6, the following conclusions have been made.

- The nanocomposites show an enhancement in the piezoelectric strain coefficient with an increase in the weight fraction of $BaTiO_3$ and the poling time.
- The piezoelectric coefficient of both the two and three phase nanocomposite increased from 2.5 to 5.5 pm/V when the polling time increases from 1 to 6 hours, but this growth is dramatically slowed down when the poling time is greater than 6 hours.
- Measured piezoelectric coefficient of the two and three phase nanocomposites in the range of $5-6$ pm/V is lower than most of the conventional piezoelectric materials, e.g. PVDF (25 pC/N) and PZT (~350 pC/N).

- There is no significant improvement after embedding the MWCNTs to the two-phase nanocomposite as an energy improver.

7.2. Future Work

Overall, the future work can be divided into the short term and the long term. The short term work is based on the existing technology and equipment, while the long term work could be done after further improving the performance of the equipment and the 3D printable materials.

In the short term, efforts should be focused on three areas. First of all, the simulation results in Chapter 4 indicate that the sensitivity and the bandwidth of the pipe organ transducer could be enhanced by coupling multiple pipe organ elements together. The required manufacturing resolution, which is just above the best resolution in CUE lab, can be achieved by further optimizing the formula of the resin and the exposure time. Secondly, fabricating a pipe-organ inspired AM capacitive transducer by integrating the pipe organ backplate and the AM capacitive transducer technologies could be listed as a short term work because the existing theory and fabrication technology can support this research. Finally, more studies should be performed to improve the piezoelectric property (d_{33}) of the piezoelectric nanocomposite by using piezoelectric nanopowder with smaller particle size [103], higher piezoelectric coefficient, e.g. PZT [48] and PMNT [67] and using another energy improver like TMSPM [53].

In the long term, effort should be concentrated on improving the resolution and automation of AM technology. Recent developments in two-photon polymerization (TPP) can achieve

a resolution below $200\ nm$ [42] which could provide for a reduction in the transducer size and thus lead to operation in higher frequency ranges of the transducers as explaining in Chapter 4. However, the 2PP is much slower than the SLA technology and it is difficult to drain the resin from the small cavity and pipes. Nevertheless, the AM capacitive transducer can also achieve better performance (higher sensitivity and lower bias voltage) by decreasing the air gap and increasing the conductivity of the 3D printed material. Further to this, recent work has demonstrated AM fabrication with multiple materials automatically by using a custom-built 3D printer [100]. The fabrication process of AM acoustic transducers could, therefore, become far more automatic in the future. In addition, after enhancing the piezoelectric property of the nanocomposite, it is possible to replace the commercial PVDF thin film and directly print the piezoelectric thin film on the pipe organ backplate.

After completing this future work, the transducer could then be used to conduct practical NDE. The size of the single element pipe organ transducer will be around $1\ mm \times 1\ mm\ \times 0.5\ mm$. It is possible to integrate over 1000 elements in a single transducer (30 mm) to superimpose their sensitivity and/or bandwidth. The pipe organ PMUT can also be integrated with a robot arm to conduct rapid scanning due to its small size, dry coupling, and no bias voltage required. The central frequency of the single element transducer can reach $\sim 480\ kHz$ with a bandwidth of ~50%. This transducer is suggested to be used in the low-frequency air-coupled NDT applications like foam and other very highly attenuative materials in the aerospace and infrastructure industries which have proved to be hard to be penetrated with high-frequency ultrasound [81].

References

[1] W. Hillger, R. Oster, J. Schuller, R. Stößel, and S. Lang, “Automated Air-Coupled Ultrasonic Technique for the Inspection of the EC145 Tail Boom,” in *Automated Air-Coupled Ultrasonic Technique for the Inspection of the EC145 Tail Boom*, 2012, pp. 1–7.

[2] R. A. Mattar and R. Kalai, “Development of a Wall-Sticking Drone for Non-Destructive Ultrasonic and Corrosion Testing,” *Drones*, vol. 2, no. 8, pp. 1–11, 2018.

[3] H. Fang, Z. Qiu, R. L. O’Leary, A. Gachagan, and A. J. Mulholland, “Improving the operational bandwidth of a 1-3 piezoelectric composite transducer using Sierpinski Gasket fractal geometry,” in *IEEE International Ultrasonics Symposium, IUS*, 2016, vol. 2016-Novem, pp. 8–11.

[4] P. C. Eccardt and K. Niederer, “Micromachined ultrasound transducers with improved coupling factors from a CMOS compatible process,” *Ultrasonics*, vol. 38, no. 1, pp. 774–780, 2000.

[5] A. J. Walker and A. J. Mulholland, “A pipe organ-inspired ultrasonic transducer,” *IMA J. Appl. Math. (Institute Math. Its Appl.*, vol. 82, no. 6, pp. 1135–1150, 2017.

[6] M. O. F. Emon and J. W. Choi, “Flexible piezoresistive sensors embedded in 3D printed tires,” *Sensors (Switzerland)*, vol. 17, no. 3, p. 656, 2017.

[7] K. Kim, W. Zhu, X. Qu, C. Aaronson, and W. R. Mccall, “3D Optical Printing of

Piezoelectric Materials," *ACS Nano*, vol. 8, no. 10, pp. 9799–9806, 2014.

[8] R. Domingo-Roca, J. C. Jackson, and J. F. C. Windmill, "Bioinspired 3D-printed piezoelectric device for acoustic frequency separation," *Sensors Actuators A Phys.*, vol. 271, pp. 1–8, 2018.

[9] J. H. Jung, M. Lee, J. Il Hong, Y. Ding, C. Y. Chen, L. J. Chou, and Z. L. Wang, "Lead-free NaNbO 3 nanowires for a high output piezoelectric nanogenerator," *ACS Nano*, vol. 5, no. 12, pp. 10041–10046, 2011.

[10] A. Zolfagharian, A. Z. Kouzani, S. Y. Khoo, A. A. A. Moghadam, I. Gibson, and A. Kaynak, "Evolution of 3D printed soft actuators," *Sensors Actuators, A Phys.*, vol. 250, pp. 258–272, 2016.

[11] A. Miriyev, K. Stack, and H. Lipson, "Soft material for soft actuators," *Nat. Commun.*, vol. 8, no. 1, p. 596, 2017.

[12] C. Liu, N. Huang, F. Xu, J. Tong, Z. Chen, X. Gui, Y. Fu, and C. Lao, "3D Printing Technologies for Flexible Tactile Sensors toward Wearable Electronics and Electronic Skin," *Polymers (Basel).*, vol. 10, no. 6, pp. 1–31, 2018.

[13] M. S. Mannoor, Z. Jiang, T. James, Y. L. Kong, K. A. Malatesta, W. O. Soboyejo, N. Verma, D. H. Gracias, and M. C. Mcalpine, "3D Printed Bionic Ears," *NANO Lett*, no. 13, pp. 2634–2639, 2013.

[14] R. Haque, E. Ogam, P. Benaben, and X. Boddaert, "Inkjet-Printed Membrane for a Capacitive Acoustic Sensor: Development and Characterization Using Laser Vibrometer," *Sensors*, vol. 17, no. 5, p. 1056, 2017.

[15] B. Tiller, A. Reid, B. Zhu, J. Guerreiro, R. Domingo-Roca, J. Curt Jackson, and J. F. C. Windmill, "Piezoelectric microphone via a digital light processing 3D printing process," *Mater. Des.*, vol. 165, pp. 1–27, 2019.

[16] A. Guedes, S. Shelton, R. Przybyla, I. Izyumin, B. Boser, and D. A. Horsley, "Aluminum nitride pMUT based on a flexurally-suspended membrane," in *2011 16th International Solid-State Sensors, Actuators and Microsystems Conference, TRANSDUCERS'11*, 2011, pp. 2062–2065.

[17] S. Akhbari, F. Sammoura, C. Yang, A. Heidari, D. Horsley, and L. Lin, "Self-curved diaphragms by stress engineering for highly responsive pMUT," in *Proceedings of the IEEE International Conference on Micro Electro Mechanical Systems (MEMS)*, 2015, pp. 837–840.

[18] Y. Qiu, J. V. Gigliotti, M. Wallace, F. Griggio, C. E. M. Demore, S. Cochran, and S. Trolier-McKinstry, "Piezoelectric micromachined ultrasound transducer (PMUT) arrays for integrated sensing, actuation and imaging," *Sensors (Basel).*, vol. 15, no. 4, pp. 8020–8041, 2015.

[19] T. Wang, T. Kobayashi, and C. Lee, "Micromachined piezoelectric ultrasonic transducer with ultra-wide frequency bandwidth," *Appl. Phys. Lett.*, vol. 106, no. 1, pp. 6–11, 2015.

[20] F. Griggio, C. E. M. Demore, H. Kim, J. Gigliotti, Y. Qiu, T. N. Jackson, K. Choi, R. L. Tutwiler, S. Cochran, and S. Trolier-Mckinstry, "Micromachined diaphragm transducers for miniaturised ultrasound arrays," in *IEEE International Ultrasonics*

Symposium, IUS, 2012, pp. 1–4.

[21] F. Akasheh, T. Myers, J. D. Fraser, S. Bose, and A. Bandyopadhyay, "Development of piezoelectric micromachined ultrasonic transducers," *Sensors Actuators, A Phys.*, vol. 111, no. 2–3, pp. 275–287, 2004.

[22] D. E. Dausch, J. B. Castellucci, D. R. Chou, and O. T. Von Ramm, "Theory and operation of 2-D array piezoelectric micromachined ultrasound transducers," *IEEE Trans. Ultrason. Ferroelectr. Freq. Control*, vol. 55, no. 11, pp. 2484–2492, 2008.

[23] I. O. Wygant and M. Kupnik, "Analytically Calculating Membrane Displacement and the Equivalent Circuit Model of a Circular," in *2008 IEEE Ultrasonics Symposium*, 2008, pp. 2111–2114.

[24] L. E. Kinsler, A. R. Frey, A. B. Coppens, and J. V Sanders, *Fundamentals of acoustics*. 1999.

[25] N. Fantuzzi, F. Tornabene, and E. Viola, "Generalized differential quadrature finite element method for vibration analysis of arbitrarily shaped membranes," *Int. J. Mech. Sci.*, vol. 79, pp. 216–251, 2014.

[26] Polytec GmbH, "Laser Doppler vibrometry," *Polytec*, 2019. [Online]. Available: https://www.polytec.com/int/vibrometry/technology/.

[27] R. H. Silverman, E. Vinarsky, S. M. Woods, F. L. Lizzi, and D. J. Coleman, "The effect of transducer bandwidth on ultrasonic image characteristics," *Retina*, vol. 15, no. 1, pp. 37–42, 1995.

[28] R. Banks, R. L. O'Leary, and G. Hayward, "Enhancing the bandwidth of piezoelectric composite transducers for air-coupled non-destructive evaluation," *Ultrasonics*, vol. 75, pp. 132–144, 2017.

[29] S. N. Ramadas, R. L. O'Leary, A. Gachagan, G. Hayward, and R. Banks, "A wideband annular piezoelectric composite transducer configuration with a graded active layer profile," in *Proceedings - IEEE Ultrasonics Symposium*, 2009.

[30] H. Fang, S. Member, Z. Qiu, A. J. Mulholland, R. L. O. Leary, and A. Gachagan, "Broadband 1-3 Piezoelectric Composite Transducer Design using Sierpinski Gasket Fractal Geometry," *IEEE Trans. Ultrason. Ferroelectr. Freq. Control*, vol. 65, no. 12, pp. 2429–2439, 2018.

[31] C. M. Wong, Y. Chen, H. Luo, J. Dai, K. H. Lam, and H. L. wa Chan, "Development of a 20-MHz wide-bandwidth PMN-PT single crystal phased-array ultrasound transducer," *Ultrasonics*, vol. 73, pp. 181–186, 2017.

[32] K. Yamada, D. Yamazaki, and K. Nakamura, "A Functionally Graded Piezoelectric Material Created by an Internal Temperature Gradient," *Jpn. J. Appl. Phys.*, vol. 40, pp. 49–52, 2001.

[33] G. Harvey, A. Gachagan, J. W. MacKersie, T. McCunnie, and R. Banks, "Flexible Ultrasonic Transducers Incorporating Piezoelectric Fibres," *IEEE Trans. Ultrason. Ferroelectr. Freq. Control*, vol. 52, no. 9, pp. 1999–2009, 2009.

[34] B. Bayram, O. Oralkan, a S. Ergun, E. Haeggström, G. G. Yaralioglu, and B. T. Khuri-Yakub, "Capacitive micromachined ultrasonic transducer design for high

power transmission.," *IEEE Trans. Ultrason. Ferroelectr. Freq. Control*, vol. 52, no. 2, pp. 326–339, 2005.

[35] P. Muralt, N. Ledermann, J. Paborowski, A. Barzegar, S. Gentil, B. Belgacem, S. Petitgrand, A. Bosseboeuf, and N. Setter, "Piezoelectric micromachined ultrasonic transducers based on PZT thin films," *IEEE Trans. Ultrason. Ferroelectr. Freq. Control*, vol. 52, no. 12, pp. 2276–2288, 2005.

[36] T. Wang, R. Sawada, and C. Lee, "A piezoelectric micromachined ultrasonic transducer using piston-like membrane motion," *IEEE Electron Device Lett.*, vol. 36, no. 9, pp. 957–959, 2015.

[37] R. Komaragiri, "Investigation on better Sensitive Silicon based MEMS Pressure Sensor for High Pressure Measurement," *Int. J. Comput. Appl.*, vol. 72, no. 8, pp. 40–47, 2013.

[38] A. Hajati, D. Latev, D. Gardner, A. Hajati, D. Imai, M. Torrey, and M. Schoeppler, "Three-dimensional micro electromechanical system piezoelectric ultrasound transducer," *Appl. Phys. Lett.*, vol. 101, no. 253101, pp. 1–5, 2012.

[39] F. Marga, K. Jakab, C. Khatiwala, B. Shepherd, S. Dorfman, B. Hubbard, S. Colbert, and F. Gabor, "Toward engineering functional organ modules by additive manufacturing," *Biofabrication*, vol. 4, no. 2, pp. 1–12, 2012.

[40] ISO/TC 261 Additive manufacturing, "Additive Manufacturing-General Principle-Overview of Process Categories and Feedstock," *International Organization for Standardization (ISO)*. .

[41] M. Bernhard, “Additive manufacturing technologies: Rapid prototyping to direct digital manufacturing,” *Assem. Autom.*, vol. 32, no. 2, 2012.

[42] J. Serbin, A. Egbert, A. Ostendorf, and B. N. Chichkov, “Femtosecond laser-induced two-photon polymerization of inorganic – organic hybrid materials for applications in photonics,” vol. 28, no. 5, pp. 301–303, 2003.

[43] D. W. Rosen, “Stereolithography and Rapid Prototyping,” in *BioNanoFluidic MEMS*, P. J. Hesketh, Ed. Boston, MA: Springer US, 2008, pp. 175–196.

[44] C. E. Hoyle and J. F. Kinstle, “Radiation curing of polymeric materials,” in *Radiation Curing of Polymeric Materials/Volume 417 of ACS Symposium Series, Eds. Charles E Hoyle and James F Kinstle. Washington DC: American Chemical Society, c1990.*, 1990, vol. 417.

[45] J. Stampfl, S. Baudis, C. Heller, R. Liska, A. Neumeister, R. Kling, A. Ostendorf, and M. Spitzbart, “Photopolymers with tunable mechanical properties processed by laser-based high-resolution stereolithography,” *J. Micromechanics Microengineering*, vol. 18, no. 12, 2008.

[46] P. Dineva, D. Gross, R. Müller, and T. Rangelov, *Dynamic Fracture of Piezoelectric Materials*, vol. 212. 2014.

[47] SANKHA BANERJEE, “An experimental investigation of lead zirconate titanate-epoxy-multi-walled carbon nanotube bulk and flexible thick film composites,” 2014.

[48] V. Pascariu, L. Padurariu, O. Avadanei, and L. Mitoseriu, “Dielectric properties of

PZT-epoxy composite thick films," *J. Alloys Compd.*, vol. 574, pp. 591–599, 2013.

[49] K. Park, C. K. Jeong, J. Ryu, G. Hwang, and K. J. Lee, "Flexible and Large-Area Nanocomposite Generators Based on Lead Zirconate Titanate Particles and Carbon Nanotubes," *Adv. Energy Mater.*, vol. 3, no. 12, pp. 1539–1544, 2013.

[50] H. Kim, F. Torres, M. Islam, and Md, "Increased piezoelectric response in functional nanocomposites through multiwall carbon nanotube interface and fused-deposition modeling three-dimensional printing," *MRS Commun.*, vol. 7, no. 4, pp. 960–966, 2017.

[51] H. Ning, N. Hu, T. Kamata, J. Qiu, X. Han, L. Zhou, and C. Christiana, "Improved piezoelectric properties of poly (vinylidene fluoride) nanocomposites containing multi-walled carbon nanotubes," *Smart Mater. Struct.*, vol. 22, no. 6, pp. 1–9, 2013.

[52] C. Baur, J. R. Dimaio, E. Mcallister, R. Hossini, E. Wagener, J. Ballato, S. Priya, A. Ballato, and D. W. Smith, "Enhanced piezoelectric performance from carbon fluoropolymer nanocomposites Enhanced piezoelectric performance from carbon fluoropolymer nanocomposites," vol. 124104, no. 2012, 2017.

[53] K. Kim, J. L. Middlebrook, J. E. Chen, W. Zhu, S. Chen, and D. J. Sirbuly, "Tunable Surface and Matrix Chemistries in Optically Printed (0 − 3) Piezoelectric Nanocomposites," *ACS Appl. Mater. Interfaces*, no. 8, pp. 8–12, 2016.

[54] V. Choudhary and A. Gupta, "Polymer/Carbon Nanotube Nanocomposites," in *Carbon Nanotubes - Polymer Nanocomposites*, 2011, pp. 66–90.

[55] X. Wang, Q. Li, J. Xie, Z. Jin, J. Wang, Y. Li, K. Jiang, and S. Fan, "Fabrication

of Ultralong and Electrically Uniform Single-Walled Carbon Nanotubes on Clean Substrates 2009," *NANO Lett.*, vol. 9, no. 9, pp. 1–5, 2009.

[56] M. Siegrist, "Human and Ecological Risk Assessment Predicting the Future : Review of Public Perception Studies of Nanotechnology Predicting the Future : Review of Public Perception Studies of Nanotechnology," vol. 7039, 2010.

[57] W. Bauhofer, J. Z. Kovacs, T. Swan, T. Swan, and T. Swan, "A review and analysis of electrical percolation in carbon nanotube polymer composites," *Compos. Sci. Technol.*, vol. 69, no. 10, pp. 1486–1498, 2009.

[58] V. Skakalova, U. Dettlaff-Weglikowska, and S. Roth., "Electrical and mechanical properties of nanocomposites of single wall carbon nanotubes with PMMA," *ELSEVIER*, vol. 152, pp. 349–352, 2005.

[59] Y. Xu, X. Wu, X. Guo, B. Kong, M. Zhang, and X. Qian, "The Boom in 3D-Printed Sensor Technology," *Sensors*, vol. 17, no. 5, pp. 1–37, 2017.

[60] F. Garnier, R. Hajlaoui, A. Yassar, and P. Srivastava, "All-polymer field-effect transistor realized by printing techniques," *Science (80-.).*, vol. 265, no. 5179, pp. 1684–1686, 1994.

[61] Z. Bao, Y. Feng, A. Dodabalapur, V. R. Raju, and A. J. Lovinger, "High-Performance Plastic Transistors Fabricated by Printing Techniques," *Chem. Mater.*, vol. 9, no. 6, pp. 1299–1301, 1997.

[62] B. A. Ridley, B. Nivi, and J. M. Jacobson, "All-inorganic field effect transistors fabricated by printing," *Science (80-.).*, vol. 286, no. 5440, pp. 746–749, 1999.

[63] Y. Ni, R. Ji, K. Long, T. Bu, K. Chen, and S. Zhuang, "A review of 3D-printed sensors," *Appl. Spectrosc. Rev. ISSN*, vol. 52, no. 7, pp. 623–652, 2017.

[64] H. Chabok, Y. Chen, and K. Shung, "Ultrasound Transducer Array Fabrication Based on Additive Manufacturing of Piezocomposite," in *Proceedings of the ASME/ISCIE 2012 International Symposium on Flexible Automation*, 2018, no. ISFA2012-7119, pp. 1–12.

[65] Z. Chen, X. Song, L. Lei, X. Chen, C. Fei, C. T. Chiu, X. Qian, T. Ma, Y. Yang, K. Shung, Y. Chen, and Q. Zhou, "3D printing of piezoelectric element for energy focusing and ultrasonic sensing," *Nano Energy*, vol. 27, pp. 78–86, 2016.

[66] M. Cheverton, P. Singh, L. S. Smith, K. P. Chan, J. A. Brewer, and V. Venkataramani, "Ceramic-Polymer Additive Manufacturing System for Ultrasound Transducers," in *Proceedings of solid freeform fabrication symposium*, 2012, pp. 863–875.

[67] D. I. Woodward, C. P. Purssell, D. R. Billson, D. A. Hutchins, and S. J. Leigh, "Additively-manufactured piezoelectric devices," *Appl. Mater. Sci.*, vol. 212, no. 10, pp. 2107–2113, 2015.

[68] O. Access, M. Schult, E. Buckow, and H. Seitz, "Experimental studies on 3D printing of barium titanate ceramics for medical applications," *Curr. Dir. Biomed. Eng.*, vol. 2, no. 1, pp. 95–99, 2016.

[69] E. Campbell, W. Galbraith, and G. Hayward, "A new electrostatic transducer incorporating fluidic amplification," in *Proceedings - IEEE Ultrasonics*

Symposium, 2006, no. 1, pp. 1445–1448.

[70] B. Zhu, B. Tiller, J. F. C. Windmill, A. J. Mulholland, and A. . Walker, "' Pipe Organ ' Air-coupled Broad Bandwidth Transducer," in *EEE Int. Ultrason. Symp. IUS*, 2017, pp. 1–4.

[71] H. Gong, M. Beauchamp, S. Perry, T. Woolley, and G. P. Nordin, "Optical approach to resin formulation for 3D printed microfluidic," *RSC Adv.*, vol. 11, no. 5, pp. 106621–106632, 2015.

[72] M. Bao and H. Yang, "Squeeze film air damping in MEMS," *Sensors Actuators, A Phys.*, vol. 136, no. 1, pp. 3–27, 2007.

[73] J. E. Mclennan and J. Close, "A0 and A1 Studies on the Violin Using CO 2 , He , and Air / Helium Mixtures," *Acta Acust.*, vol. 89, no. April 2002, pp. 176–180, 2003.

[74] S. B. Horowitz, M. Sheplak, L. N. Cattafesta, and T. Nishida, "A MEMS acoustic energy harvester," *J. Micromechanics Microengineering*, vol. 16, no. 9, 2006.

[75] M. Jabrullah and R. A. Rahim, "Design And Simulation of MEMS Helmholtz Resonator for Acoustic Energy Harvester," pp. 505–510, 2016.

[76] H. Takahashi, A. Suzuki, E. Iwase, K. Matsumoto, and I. Shimoyama, "MEMS microphone with a micro Helmholtz resonator," *J. Micromechanics Microengineering*, vol. 22, no. 8, 2012.

[77] A. J. Walker and A. J. Mulholland, "A theoretical model of an electrostatic

ultrasonic transducer incorporating resonating conduits," *IMA J. Appl. Math. (Institute Math. Its Appl.*, vol. 75, no. 5, pp. 796–810, 2010.

[78] A. J. Walker, A. J. Mulholland, E. Campbell, and G. Hayward, "A theoretical model of a new electrostatic transducer incorporating fluidic amplification," in *Proceedings - IEEE Ultrasonics Symposium*, 2008, pp. 1409–1412.

[79] H. Gong, M. Beauchamp, S. Perry, A. T. Woolley, and G. P. Nordin, "Optical approach to resin formulation for 3D printed microfluidics," *RSC Adv.*, vol. 5, no. 129, pp. 106621–106632, 2015.

[80] C. Bayram, S. Olcum, M. N. Senlik, and A. Atalar, "Bandwidth improvement in a cMUT array with mixed sized elements," *Proc. - IEEE Ultrason. Symp.*, vol. 4, pp. 1956–1959, 2005.

[81] J. O. Strycek, H. Loertscher, and C. Mesa, "Ultrasonic Air-Coupled Inspection of Advanced Material," *QMI Inc.*, 1999. .

[82] C. Casarini, B. Tiller, C. Mineo, C. N. MacLeod, J. F. C. Windmill, and J. C. Jackson, "Enhancing the Sound Absorption of Small-Scale 3-D Printed Acoustic Metamaterials Based on Helmholtz Resonators," *IEEE Sens. J.*, vol. 18, no. 19, pp. 7949–7955, 2018.

[83] P. R. Scheeper, B. Nordstrand, J. O. Gulløv, B. Liu, T. Clausen, L. Midjord, and T. Storgaard-larsen, "A New Measurement Microphone Based on MEMS Technology," vol. 12, no. 6, pp. 880–891, 2003.

[84] P. R. Scheepera, A. G. . Van der Donk, W. Olthuis, and P. Bergveld, "A review of

silicon microphones," *Sensors Actuators A*, vol. 44, pp. 1–11, 1994.

[85] J. Liu, D. T. Martin, T. Nishida, L. N. Cattafesta, M. Sheplak, and B. P. Mann, "Harmonic balance nonlinear identification of a capacitive dual-backplate MEMS microphone," *J. Microelectromechanical Syst.*, vol. 17, no. 3, pp. 698–708, 2008.

[86] M. Füldner, A. Dehé, and R. Lerch, "Analytical analysis and finite element simulation of advanced membranes for silicon microphones," *IEEE Sens. J.*, vol. 5, no. 5, pp. 857–862, 2005.

[87] P. Mattila, F. Tsuzuki, and V. Heli, "Electroacoustic Model for Electrostatic Ultrasonic Transducers with V-Grooved Backplates," vol. 42, no. 1, pp. 1–7, 1995.

[88] B. Zhu, B. Tiller, A. J. Walker, A. J. Mulholland, and J. F. C. Windmill, "'Pipe Organ' Inspired Air-coupled Ultrasonic Transducers with Broader Bandwidth," *IEEE Trans. Ultrason. Ferroelectr. Freq. Control*, pp. 1–10, 2018.

[89] R. N. Miles and R. R. Hoy, "The development of a biologically-inspired directional microphone for hearing aids," *Audiol. Neurotol.*, vol. 11, no. 2, pp. 86–94, 2005.

[90] S. J. Leigh, R. J. Bradley, C. P. Purssell, D. R. Billson, and D. A. Hutchins, "A Simple, Low-Cost Conductive Composite Material for 3D Printing of Electronic Sensors," *PLoS One*, vol. 7, no. 11, pp. 1–6, 2012.

[91] Y. Zhang, J. F. C. Windmill, and D. Uttamchandani, "Biomimetic MEMS directional microphone structures for multi-band operation," *IEEE SENSORS 2014 Proc.*, pp. 440–443, 2014.

[92] H. Gong, B. P. Bickham, A. T. Woolley, and G. P. Nordin, “Custom 3D printer and resin for 18 μm × 20 μm microfluidic flow channels,” vol. 17, no. 17, 2017.

[93] D. Qian, E. C. Dickey, R. Andrews, and T. Rantell, “Load transfer and deformation mechanisms in carbon nanotube-polystyrene composites,” *Appl. Phys. Lett.*, vol. 76, no. 20, pp. 2868–2870, 2000.

[94] M. J. Biercuk, M. C. Llaguno, M. Radosavljevic, J. K. Hyun, A. T. Johnson, and J. E. Fischer, “Carbon nanotube composites for thermal management,” *Appl. Phys. Lett.*, vol. 80, no. 15, pp. 2767–2769, 2002.

[95] H. Ishikawa, S. Fudetani, and M. Hirohashi, “Mechanical properties of thin films measured by nanoindenters,” *Appl. Surf. Sci.*, vol. 178, pp. 56–62, 2001.

[96] B. Kracke and B. Damaschke, “Measurement of nanohardness and nanoelasticity of thin gold films with scanning force microscope,” *Appl. Phys. Lett.*, vol. 77, no. 3, pp. 361–363, 2000.

[97] A. Dehé, M. Wurzer, M. Füldner, U. Krumbein, and I. T. Ag, “The Infineon Silicon MEMS Microphone,” *IEEE Sens. J.*, vol. 15, no. 3, pp. 95–99, 2013.

[98] Alexandrov G and C. N., *Some Tips on Making a FETching Discrete Amplifier*. Analog Dialogue, 2013.

[99] Brüel & Kjær, “Product Data: 1/8″ Pressure - field Microphone Type 4138,” *Datasheet*. .

[100] M. Vaezi, S. Chianrabutra, B. Mellor, and S. Yang, “Multiple material additive

manufacturing – Part 1: a review," *Virtual Phys. Prototyp.*, vol. 8, no. 1, pp. 19–50, 2013.

[101] J. M. Liu, B. Pan, H. L. W. Chan, S. N. Zhu, Y. Y. Zhu, and Z. G. Liu, "Piezoelectric coefficient measurement of piezoelectric thin films: An overview," *Mater. Chem. Phys.*, vol. 75, no. 1–3, pp. 12–18, 2002.

[102] K. Yao and F. E. H. Tay, "Measurement of longitudinal piezoelectric coefficient of thin films by a laser-scanning vibrometer," *IEEE Trans. Ultrason. Ferroelectr. Freq. Control*, vol. 50, no. 2, pp. 113–116, 2003.

[103] K. Kim, W. Zhu, X. Qu, C. Aaronson, W. R. Mccall, S. Chen, and D. J. Sirbuly, "3D Optical Printing of Piezoelectric Nanoparticle-Polymer Composite Materials," pp. 1–7.

Appendix 1 - Published Work

Conference paper

Part of the work in Chapter 3 of this thesis has been presented at the conference:

- B. Zhu, B. Tiller, A. J. Walker, A. J. Mulholland, J. F. C. Windmill, ""Pipe Organ" Air-Coupled Broad Bandwidth Transducer," IEEE International Ultrasonics Symposium (IUS), pp. 1–4, 2017.

Journal Paper

The work in Chapter 3 of this thesis has been published in the following journal:

- B. Zhu, B. Tiller, A. J. Walker, A. J. Mulholland, J. F. C. Windmill, ""Pipe Organ" Inspired Air-Coupled Ultrasonic Transducers With Broader Bandwidth" IEEE Trans. Ultrason. Ferroelectr. Freq. Control, 65 (10), pp. 1873-1881, 2018.

The work in Chapter 5 of this thesis is under the second review of the following journal:

- B. Zhu, J. Guerreiro, Y. Zhang, B. Tiller, J. F.C. Windmill, "Additive Manufacturing (AM) Capacitive Acoustic Transducer Using a Commercial Direct Light Processing (DLP) Printer" IEEE Sens J, under review

Part of the work in Chapter 6 of this thesis has been published in the following journal:

- B. Tiller, A. Reid, B. Zhu et al., “Piezoelectric microphone via a digital light processing 3D printing process” Material & Design, 165, pp. 1-27, 2019.

"Pipe Organ" Air-coupled Broad Bandwidth Transducer

B. Zhu, B. Tiller and J.F.C. Windmill
Centre for Ultrasonic Engineering
University of Strathclyde
Glasgow, UK G1 1XW
Email: botong.zhu@strath.ac.uk

A.J. Mulholland
Department of Mathematics and Statistics
University of Strathclyde
Glasgow, UK G1 1XH

A.J. Walker
School of Science and Sport
University of the West of Scotland
Paisley, UK PA1 2BE

***Abstract*—Air-coupled transducers are used to conduct fast non-contact inspections in NDT. Normally, the bandwidth of a conventional transducer can be enhanced, but with a cost to its sensitivity. However, low sensitivity is very disadvantageous in air-coupled devices. This paper presents a methodology for improving the bandwidth of an air-coupled micro-machined ultrasonic transducer (MUT) without sensitivity loss by connecting a number of resonating pipes of various length to a cavity in the backplate. The design is inspired by the pipe organ musical instrument, where the resonant frequency (pitch) of each pipe is mainly determined by its length.**

Keywords—Air-Coupled; Broad Bandwidth; 3D Print; NDT/E; Ultrasonic Transducer; MUT

I. Introduction

Air-coupled transducers are widely used to conduct fast non-contact inspections for many materials including wood, electronic packages, aero-space carbon fiber, honeycomb structures, sandwich laminates and so on [1]. This technology can also improve the ease and the speed of non-destructive testing (NDT) [2]. The most common air-coupled transducers are piezoelectric bulk and micro-machined transducers (MUT). Many research studies [1,2,3] indicate that compared with piezoelectric devices, MUTs have a greater bandwidth and are better coupled to air, but have a lower sensitivity. Moreover, the bandwidth of a conventional piezoelectric bulk transducer can also be further enhanced by a backing layer, but with a cost to its sensitivity [1,2]. The aim is therefore to design high sensitivity devices for air-coupled NDT. This paper presents a methodology for improving the bandwidth of air-coupled MUT transducers without sensitivity loss by using a novel design of backplate.

A pipe organ produces sound by driving pressurized air into each individual pipe via the keyboard and pump system. The shape of individual pipes affects the sound produced. However, the resonant frequencies of pipes are mainly determined by the length of the pipes and the velocity of sound. The resonant frequency can be calculated by the theory of pipes [4] which states that the fundamental resonant frequency of an open pipe (both ends open) occurs when the length of pipe is equal to $\lambda/2$ and the fundamental resonant frequency of a closed pipe (one end is closed and the other end is open) occurs when the length of pipe is equal to $\lambda/4$, where λ is the wavelength of sound. The resonant frequency of open cylindrical pipes is given by equation (1), where n is a positive integer which represents the resonance node, v is the speed of sound in air, L is the length of pipe and r is radius of the pipe.

$$f_o = \frac{nv}{2(L + 1.6r)} \quad (1)$$

Figure 1(a) is a standard MUT design. Basically, this device consists of a thin diaphragm over a rigid backplate where the resonance of the membrane depends on the size of cavity and the membranes' material [3]. The new pipe organ transducer is based on this conventional design, but connects many acoustic amplifying pipes with different lengths to the backplate (as in Figure 1(b)). The design stage involves optimising each pipe's length so their resonant frequencies are very close but not equal to the membrane's resonant frequency and in so doing the overall bandwidth is increased. The pipe organ backplate can be thought of as a "musical instrument" which can play different frequencies (pitches) at the same time.

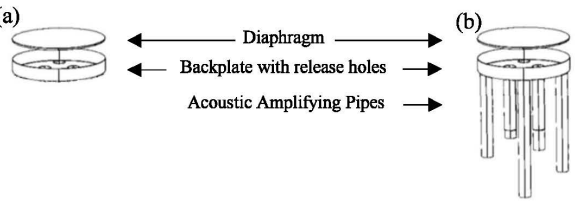

Figure 1. (a) Conventional micro-machined transducer, (b) Pipe organ transducer.

The next section describes the design and manufacture of the pipe organ transducer, including the 1D mathematical simulation, 3D finite element (FE) simulation and 3D printing of the pipe organ backplate. Section 3 describes and analyses the experimental results in order to demonstrate that the pipe organ backplate can improve the bandwidth of the MUT without sensitivity loss. Section 4 then gives conclusions for the work.

II. Methodology

A. 1D Mathematical model

The mathematical model used in this paper is a transmission line model introduced by Walker and Mulholland [5,6]. This 1D

The work was supported by the Engineering and Physical Sciences Research Council (EPSRC) under grant EP/L022125/1, and by the European Research Council under the European Union's Seventh Framework Programme (FP/2007-2013) / ERC Grant Agreement n. [615030].

model can simulate the transmission voltage response (TVR) and reception force response (RFR) of both a conventional transducer and the pipe organ transducer. The bandwidth and sensitivity of both transducers can then be calculated and compared. Generally speaking, the 1D mathematical model can be divided into 3 parts. First of all, the acoustic impedance of one amplifying pipe is computed. Secondly, a lumped impedance profile of the entire backplate is calculated, which includes many amplifying pipes with different lengths and an air-filled cavity. Finally, the membrane's displacement model is inserted into the backplate's model to compute the bandwidth and sensitivity of the TVR and RFR. This model runs extremely quickly and takes less than 1 second for each design.

Table 1. Initial parameters of backplate design.

Design Parameters	**μm**
Height of cavity (h)	35
Diameter of pipes (d)	52
Radius of cavity/membrane (R)	300

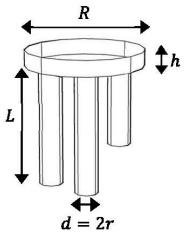

Figure 2. Parameters of the pipe organ backplate.

In order to set up the simulation, the material and the size of each component on the transducer must be considered. The initial parameters of the backplate design are given in Table 1 & Figure 2 and five thousand different designs are simulated and compared. Each design is given a random number of pipes from 10 to 100. Each pipe has the same radius but the length was randomly chosen from a linear distribution between 0.4mm and 1.4mm. The bandwidth of the TVR and RFR are generated and plotted against the number of pipes as shown in Figure 3.

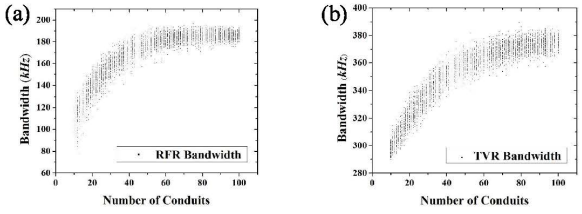

Figure 3. The bandwidth of (a) RVR and (b) TVR measured from 5000 sample devices. Plots are generated from the 1D mathematical model [5,6,8].

The 1D mathematical model indicates that the more amplifying pipes present in the device, the larger the bandwidth improvement. And if the pipe number is more than 90, the bandwidth will no longer be significantly improved.

B. 3D FEA model

Even though the 1D mathematical result suggests around 90 pipes for the backplate, in this work there are manufacturing constraints and so a study of 8 pipes emerging from the back cavity is presented. Figure 4(a) is a schematic of the pipe organ transducer which is simulated by using a commercial FE software COMSOL Multiphysics (Comsol AB, Stockholm, Sweden) to further optimize the design parameters. The transducer is located in the middle of the spherical computational region and surrounded by an air sphere. This model can calculate the resonant frequencies of the circular membrane, pipes and cavity accurately and can simulate the coupling effect between them. After considering the limitations of manufacturing and optimizing the coupling of pipes and the circular membrane, the practical parameters of the backplate are given in Table 2. Figure 4(a) indicates that the resonance frequency of the membrane is 34 kHz. Figure 4(c) (d) and (e) are the pressures inside the pipes and the cavity. When the frequency of the incident sound is 27 kHz, the shortest pipe starts to resonate. When the frequency is 36 kHz, the longest pipe reaches its resonance. When the frequency is 11 kHz, all the pipes are coupled together with the cavity and start to resonate. The pipe organ backplate has introduced the different pipes' resonances between 27 kHz and 36 kHz in order to improve the bandwidth of the membrane, and a Helmholtz resonance located at 11 kHz that will improve the overall sensitivity. Compared with the 1D mathematical model, the 3D FE model took ~2 hours for each design, but is much more realistic.

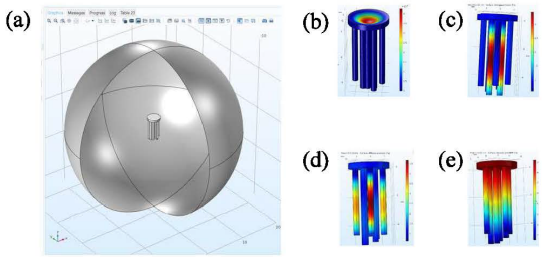

Figure 4. (a) Schematic of the COMSOL Model. (b) The circular membrane resonates at 34kHz. The pressure (resonance) in the pipes and cavity when frequency is (c) 36kHz (d) 27kHz (e) 11kHz.

Table 2. Practical parameters of the backplate design.

Device (mm)	**8 pipes**	**4 pipes**	**0 pipes**
Height of cavity (h)	0.4	0.4	0.4
Diameter of pipes (d)	0.48	0.6	n/a
Radius of cavity/membrane (R)	1.5	1.5	1.5
Length of pipes (L)	5.4 5.4 5.2 5.0 4.8 4.6 4.4 4.4	5.0 4.8 4.8 4.5	n/a

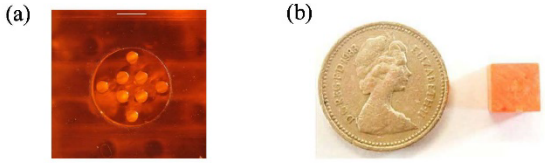

Figure 5. (a) Plan view of the 3D printed pipe organ backplate, (b) £1 coin and 3D printed pipe organ backplate for scale.

C. 3D Printing

After building a CAD model, an Asiga Pico Plus 27 3D printer was utilized to fabricate the pipe organ backplate (see figure 5). This is a commercial stereolithography 3D printer with 27 µm resolution in the X-Y plane and 1 μm resolution in Z plane. Instead of using commercial resins directly, the improved resins [7] we used in this project are prepared by mixing Polyethylene (glycol) Diacrylate (PEGDA) along with (2, 4, 6-trimethylbenzoyl) phenylphosphane oxide (Irgacure 819) (1% by weight) and Sudan I (0.1% by weight) vigorously in a spinner. Hua Gong et al [7] proposed that the resins formed by this improved formula will present long-term stability in water and higher printing resolution. The exposure time is set to be 2 seconds with a 10 μm build layer.

During manufacture, the actual printed size was found to always be smaller than the target size. So a correction factor was required to compensate for this. The calculation steps for the correction factor are illustrated in Figure 6. First of all, calibration pipes were printed with different lengths and diameters. Secondly, a high-resolution micrometer was used to measure the radii. The mean value between five measurements was then calculated. Finally, the correction factor was calculated from equation (2) and the data plotted in Figure 7, with an error bar to show that when the diameter is less than 0.5mm, the correction factor dramatically decreases. In other words, ~0.5mm diameter is the smallest diameter that can be fabricated with this technology. In order to connect more pipes to the cavity, the diameter of the pipes should be as small as possible. This is the reason why d= 0.48mm is chosen for this work.

$$\text{Correction factor} = \frac{Actual\ Diameters}{Target\ Diameters} \qquad (2)$$

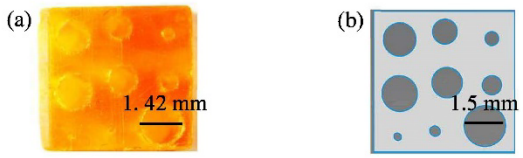

Figure 7. (a) 3D printed calibration pipes, (b) CAD modelling calibration pipes.

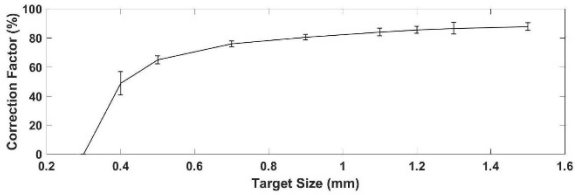

Figure 8. Correction factor against target diameter. The error bar was from five measurements.

III. Experiment and Result

A. Experimental Set-up

Before adding an electrical circuit to the transducer, the average displacement of the membrane was measured using a laser vibrometer to estimate the bandwidth and sensitivity. The performance of the pipe organ design and the conventional cavity-only design were then compared. The membrane was a passive Kapton diaphragm of thickness $d_m = 125\mu m$ which was attached to the top of the 3D printed backplate with general purpose superglue. The experimental setup is illustrated in Figure 8. Initially, wideband periodic chirps covering frequencies from 5 kHz to 50 kHz were generated by a signal generator, and passed through a voltage amplifier, to a broadband ultrasound transmitter (Ultra Sound Advice Loudspeaker). The transmitter was enough far away from the sample to ensure that there were no near field effects. A 1/8 inch reference microphone (Brüel and Kjær, Type 4138) was used to measure the reference sound pressure around the sample. An amplitude correction algorithm was utilized to compensate for the transmitter's output variance. The front face displacement of the sample was obtained by using a Polytec PSV-300 scanning laser vibrometer (LDV) (Polytec, Inc., Waldbronn,Germany).

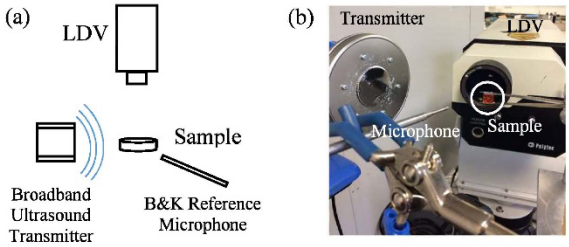

Figure 6. (a) Simplified schematic of the experimental setup (b) Photo of experimental setup.

B. Experiment and Simulation Result

In this section, the frequency response of a device with no pipes (customer built standard device), is compared with a 4 pipes device and an 8 pipes device in terms of bandwidth, central frequency and sensitivity. The design parameters are those given in Table 2, and the simulation and experimental results

are shown in Figure 9(a) and (b) respectively. The Comsol model does not include any loss factors, and the fluctuations in the simulation result arise from the resonances of different pipes or the cavity. In the simulation result, the Helmholtz resonance is located at 11 kHz and this enhances the overall sensitivity of the transducer. The multiple pipes' resonances vary from 30 kHz to 37 kHz, which are close to the membrane's resonance frequency. Compared with the 4 pipes device, there are more fluctuations in the 8 pipes device at ~31 kHz. So the bandwidth of the 8 pipes device should be larger than the 4 pipes device. Figure 9 (b) is the average displacement of the three devices, a noise floor is defined as 6dB below peak gain of each individual device to calculate the bandwidth of displacement. The central frequency and sensitivity are also evaluated and shown in Table 3.

Table 3. Bandwidth, central frequency and sensitivity comparison with respect to no pipe, 4 pipes and 8 pipes device.

	Bandwidth	Central Frequency	Sensitivity
No pipe device	3.8%	33.5 kHz	-103dB
4 pipes device	7.2%	34.2 kHz	-97.9dB
8 pipes device	9.6%	36.2 kHz	-102.8dB

The results in Table 3 and Figure 9 indicate that the respective bandwidths of the pipe organ devices are much larger than the device with no pipes. The central frequency shift is due to manufacturing tolerance. When attaching the Kapton membrane with super glue, some of the super glue may enter the cavity which makes the cavity smaller (or larger) than the designed size. However, the frequency shift is less than 8%. There is no sensitivity loss because the pipe organ backplate improves the bandwidth by amplifying the frequencies instead of damping the resonance. Both the device with no pipes and the 8 pipes device have the same gain. The sensitivity of the 4 pipes device is slightly larger than the other two devices because the resonant frequency of the circular membrane overlaps with one of the pipes' resonances.

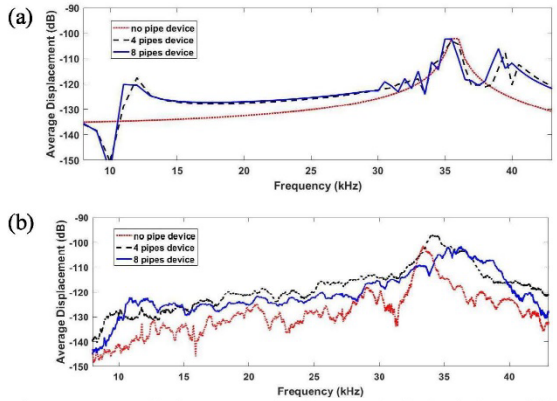

Figure 9. Average displacement against frequency in (a) simulation and (b) experiment.

IV. Conclusion

This paper presents a pipe organ inspired backplate which can replace the conventional backplate to increase the bandwidth of an air-coupled micro-machined transducer without sensitivity loss. The 1D mathematical model proves that more resonant pipes leads to larger bandwidth improvement. The FEA (Comsol Multiphysics) simulation was used to locate the membrane's and pipes' resonant frequencies more accurately and also simulated the coupling effects between the membrane, pipes and cavity. An 8 pipe backplate was built with an improved resin formula and a commercial stereolithography 3D printer. In the experiment, the -6dB bandwidth of average displacement improvement was found to be up to 9.6% (2.5 times larger than the customer-build conventional device).

The future work on this project includes changing the passive Kapton membrane to an active piezoelectric PVDF membrane, optimizing the lengths of the pipes to further increase the bandwidth, increasing the number of pipes by improving the materials and/or developing a smart backplate design to fit more pipes, and increasing the central frequency to over 60 kHz for use with air-coupled ultrasound NDT applications.

References

[1] T. H. Gan, D. A. Hutchins, D. R. Billson, and D. W. Schindel, "The use of broadband acoustic transducers and pulse-compression techniques for air-coupled ultrasonic imaging," Ultrasonics, vol. 39, no. 3, pp. 181–194, 2001.

[2] D. W. Schindel, D. A. Hutchins, and W. A. Grandia, "Capacitive and piezoelectric air-coupled transducers for resonant ultrasonic inspection," Ultrasonics, vol. 34, no. 6, pp. 621–627, 1996.

[3] Y. Qiu, J. V Gigliotti, M. Wallace, F. Griggio, C. E. M. Demore, S. Cochran, and S. Trolier-mckinstry, "Piezoelectric Micromachined Ultrasound Transducer (PMUT) Arrays for Integrated Sensing, Actuation and Imaging," vol. 15, no. April, pp. 8020–8041, 2015.

[4] E. Campbell, W. Galbraith, and G. Hayward, "A new electrostatic transducer incorporating fluidic amplification," Proc. - IEEE Ultrason. Symp., vol. 1, no. 1, pp. 1445–1448, 2006.

[5] A. J. Walker and A. J. Mulholland, "A theoretical model of an electrostatic ultrasonic transducer incorporating resonating conduits," IMA J. Appl. Math., vol. 75, no. 5, pp. 796–810, 2010.

[6] A. J. Walker, A. J. Mulholland, E. Campbell, and G. Hayward, "A theoretical model of a new electrostatic transducer incorporating fluidic amplification," 2008 IEEE Int. Ultrason. Symp. Proc., vol. 1, no. 1, pp. 1409–1412, 2008.

[7] H. Gong, M. Beauchamp, S. Perry, T. Woolley, and G. P. Nordin, "Optical approach to resin formulation for 3D printed microfluidic," RSC Adv., vol. 11, no. 5, pp. 106621–106632, 2015.

[8] A. J. Walker and A. J. Mulholland, "A Pipe Organ-Inspired Ultrasonic Transducer," IMA J. Appl. Math., to appear.

"Pipe Organ" Inspired Air-Coupled Ultrasonic Transducers With Broader Bandwidth

Botong Zhu, *Student Member, IEEE*, Benjamin P. Tiller, Alan J. Walker, A. J. Mulholland, and James F. C. Windmill, *Senior Member, IEEE*

***Abstract*— Piezoelectric micromachined ultrasonic transducers (PMUTs) are used to receive and transmit ultrasonic signals in industrial and biomedical applications. This type of transducer can be miniaturized and integrated with electronic systems since each element is small and the power requirements are low. The bandwidth of the PMUT may be narrow in some conventional designs; however, it is possible to apply modified structures to enhance this. This paper presents a methodology for improving the bandwidth of air-coupled PMUTs without sensitivity loss by connecting a number of resonating pipes of various lengths to a cavity. A prototype piezoelectric diaphragm ultrasonic transducer is presented to prove the theory. This novel device was fabricated by additive manufacturing (3-D printing), and consists of a polyvinylidene fluoride thin film over a stereolithography designed backplate. The backplate design is inspired by a pipe organ musical instrument, where the resonant frequency (pitch) of each pipe is mainly determined by its length. The −6-dB bandwidth of the "pipe organ" air-coupled transducer is 55.7% and 58.5% in transmitting and receiving modes, respectively, which is ∼5 times wider than a custom-built standard device.**

***Index Terms*— 3-D print, additive manufacture, air-coupled ultrasound, broad bandwidth, piezoelectric diaphragm ultrasonic transducer, polyvinylidene fluoride (PVDF).**

I. Introduction

HIGHER resolution is the one of the most important requirements in nondestructive evaluation (NDE), biomedical imaging, and underwater sonar [1]. A broad bandwidth ultrasonic probe can achieve this requirement because the pulsewidth in the time domain is shorter when the bandwidth is wider. Piezoelectric composite transducers can have wide bandwidths by optimizing their electrical and mechanical properties [1], [2]. However, the composite transducer has much better performance in water compared to air because the acoustic impedance of the composite piezoelectric material is closer to that of water. A solution to this is to add matching layers or damping materials to broaden the frequency response around resonances [2]. However, this will also decrease the device's sensitivity. Whereas the piezoelectric transducers use thickness mode resonances, the micromachined ultrasonic transducers (MUTs) have a thin flexible film to transmit and receive ultrasound. MUTs have better performance in air because the flexible film is easier to couple with the media, with a more closely matched mechanical impedance. Further, as the film stores much less kinetic energy than bulk piezoceramic, the MUTs have larger bandwidths when in resonance [2]. The MUTs' family includes piezoelectric MUTs (PMUTs) and capacitive MUTs (CMUTs). Both of these device designs have the same flexure thin film and rigid backplate structure as shown in Fig. 1(a). The flexure vibrations of CMUTs are caused by an electrostatic force generated from an electric field between the conducting backplate and metalized film. The deflection of the PMUTs' membrane is caused by lateral strain generated from the piezoelectric effect of its piezoelectric layer [3]. Different vibration mechanism provides PMUTs with a larger transmission sensitivity, and furthermore no bias voltage is required [3], [4]. However, the bandwidths of conventional PMUTs are narrow [3]–[5], thus making them unsuitable for wide bandwidth applications [6], [7]. A PMUT's bandwidth can be broadened by applying some modified structures [3], [8], such as overlapping and arranging the frequency spectrum of membranes of different sizes and shapes [9], or using rectangular membranes [6].

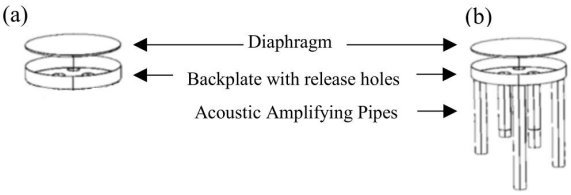

Fig. 1. (a) Conventional MUT. (b) Pipe organ piezoelectric diaphragm ultrasonic transducer.

The pipe organ backplate proposed in this paper is a novel design that can improve the bandwidth of air-coupled PMUTs without sensitivity loss or increase of active area. The concept and the mathematical model was proposed by Walker and Mulholland [10], [12] and Walker *et al.* [11] and the principle was validated via prototyping [13], [14].

Section II describes the theoretical background of the pipe organ backplate. Section III uses an FEA model to simulate the device and explain the resonant frequencies created from the

Manuscript received May 9, 2018; accepted July 17, 2018. Date of publication July 31, 2018; date of current version October 3, 2018. This work was supported in part by the Engineering and Physical Sciences Research Council under Grant EP/L022125/1 and in part by the European Research Council through the European Union's Seventh Framework Program under Grant P/2007-2013 and ERC Grant 615030. *(Corresponding author: Botong Zhu.)*

B. Zhu, B. P. Tiller, and J. F. C. Windmill are with the Centre for Ultrasonic Engineering, Electronic and Electrical Engineering Department, University of Strathclyde, Glasgow G1 1XW, U.K. (e-mail: botong.zhu@strath.ac.uk; benjamin.tiller@strath.ac.uk; james.windmill@strath.ac.uk).

A. J. Walker is with the School of Science and Sport, University of the West of Scotland, Paisley PA1 2BE, U.K. (e-mail: Alan.Walker@uws.ac.uk).

A. J. Mulholland is with the Department of Mathematics and statistics, University of Strathclyde, Glasgow G1 1XH, U.K. (e-mail: anthony.mulholland@strath.ac.uk).

Digital Object Identifier 10.1109/TUFFC.2018.2861575

backplate. Section IV introduces the manufacturing technique for the stereolithography pipe organ backplate, an improved resin formula, and the rest of the fabrication steps of the prototypes using the stereolithography backplate and commercial polyvinylidene fluoride (PVDF) thin film. Section V shows the experiment results of the prototypes, and Section VI discusses and concludes this paper.

II. Theoretical Background

A PMUT utilizes a piezoelectric layer on the top of a silicon membrane and operates in a flexural mode. After applying an electrical field to the thin plate, the lateral strain in its thickness direction makes the structure bend [15]. The vibrating membrane compresses the air and produces ultrasound. In contrast, the received ultrasound wave vibrates the film which causes charge migration between the two electrodes on the piezoelectric layer, which then can be detected by a receiving circuit [15]. The intrinsic stress of the thin plate is the factor that can dominate the resonant frequency of transducer. When the transducer has an edge-clamped film with low intrinsic stress, the resonant frequency of the circular thin plate (f_{tp}) can be estimated in (1) and (2) [3], where n is the number of the resonance mode, R is the radius of the thin plate, D_E is the flexural rigidity of the circular thin plate, h is the height of the cavity, ρ is the density of the thin plate, E is the Young's modulus, and μ is the Poisson ratio. The squeeze film effect occurs when the air gap (depth of cavity) is very narrow [16]. Squeeze film damping becomes more important than the drag force damping of air if the thickness of the gas film is smaller than one-third of the width of the plate [16]. However, this effect can be ignored in the pipe organ design presented here because the air gap is four times higher than the thickness of the thin plate. Moreover, the change of the gap depth introduced by the vibration of the thin plate is always less than 1% of the depth of the gap

$$f_{\text{tp}} = \frac{n}{2\pi R^2}\sqrt{\frac{D_E}{\rho h}} \tag{1}$$

$$D_E = \frac{Eh^3}{12(1-\mu^2)}. \tag{2}$$

A pipe organ produces sound by driving pressurized air into each individual pipe via the keyboard and pump system. The shape of individual pipes affects the sound produced; however, the resonant frequencies of the pipes are mainly determined by the length of the pipes and the velocity of sound [12]. The resonant frequency can be calculated by the theory of pipes [13] which states that the fundamental resonant frequency of an open pipe (both ends open) occurs when the length of pipe is equal to $\lambda/2$, where λ is the wavelength of sound, and the fundamental resonant frequency of a closed pipe (one end is closed and the other end is open) occurs when the length of pipe is equal to $\lambda/4$. The resonant frequency of open cylindrical pipes is given in (3), where v is the speed of sound in air, L is the length of pipe, and r is the radius of the pipe

$$f_p = \frac{nv}{2(L+1.6r)}. \tag{3}$$

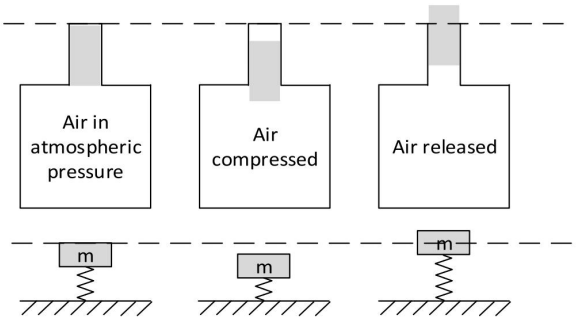

Fig. 2. Schematic of a Helmholtz Resonator.

The pipes connecting the cavity to the atmosphere enable air to flow in and out which can further reduce the effect of squeeze film damping and squeeze film resistance.

A Helmholtz resonator is an air-filled cavity with one open end. When a sound wave gives an initial force to a portion of air (depicted as the gray part in Fig. 2), the air will vibrate since the air inside the cavity acts as a spring. Therefore, the Helmholtz resonator can be regarded as a very classic spring-mass system that can support harmonic motion. In the pipe organ backplate, the pipes and cavity are formed into a Helmholtz resonator [17]. Similar to the organ pipes with different lengths and resonant frequencies, this resonator also has a resonant frequency (f_h) that can improve the sensitivity in a specific frequency range. The central frequency can be calculated in (4), where S is the total cross-sectional area of the pipe and V is the volume of the cavity

$$f_h = \frac{v}{2\pi}\sqrt{\frac{S}{VL}}. \tag{4}$$

Helmholtz resonators are well documented in many acoustic applications including acoustic energy harvesters [18], [19] and microelectromechanical system microphones [20], where they are used to enhance the sensitivity when receiving sound. The pipe organ diaphragm ultrasonic transducer proposed in this paper is based on the conventional MUT's design [as in Fig. 1(a)], but connects many acoustic amplifying pipes with different lengths to the backplate [as in Fig. 1(b)] to enhance the bandwidth in both transmitting and receiving modes. The design stage involves optimizing each pipe's length, and the cavity's size, so their resonant frequencies are close but not equal to the thin plate's resonant frequency and in so doing the overall bandwidth is increased. Moreover, the pipe-organ inspired resonator can amplify selected frequencies in receiving and transmitting ultrasound. As shown in Fig. 3, the metalized PVDF layer is clamped on the top of the backplate as an active part to produce (or receive) ultrasound and the pipe organ backplate can be thought of as a "musical instrument" which can amplify different selected frequencies (pitches) at the same time.

III. Finite-Element Modeling

Walker and Mulholland [10], [12] and Walker *et al.* [11] investigated the relationship between the number of pipes and

TABLE I

SIX DESIGNS TO ILLUSTRATE THE COUPLING EFFECT BETWEEN THE CAVITY, THE MULTIPLE PIPES, AND THE CIRCULAR MEMBRANE

Device	No pipe (I)	4 pipes (II)	4 pipes (III)	8 pipes (IV)	8 pipes (V)	13 pipes (VI)
Orientation pipe	n/a	No	No	No	Yes	Yes
Volume of cavity V (mm^3)	6.38	6.38	6.38	6.38	6.38	6.38
Depth of cavity h (mm)	0.97	0.97	0.97	0.97	1.45	1.45
Diameter of pipes d (mm)	n/a	0.424	0.6	0.424	0.424	0.424
Radius of cavity R (mm)	1.45	1.45	1.45	1.45	1.45	1.45
Length of pipes L (mm)	n/a	7.1, 6.8, 6.6, 6.4	7.1, 6.8, 6.6, 6.4	7.1, 7.0, 6.9, 6.8, 6.7, 6.6, 6.5, 6.4	7.1, 7.0, 6.9, 6.8, 6.7, 6.6, 6.5, 6.4	7.3, 7.2, 7.1, 7.0, 6.9, 6.8, 6.7, 6.6, 6.5, 6.4, 6.3, 6.2
Total area of the pipe S (mm^2)	n/a	0.56	1.13	1.13	1.13	1.68

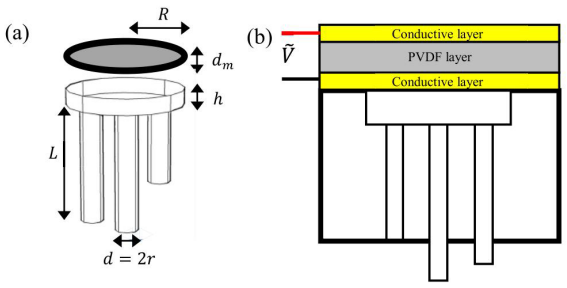

Fig. 3. (a) Parameters of the pipe organ transducer. (b) Sectional-cut plot of the backplate and the piezoelectric membrane.

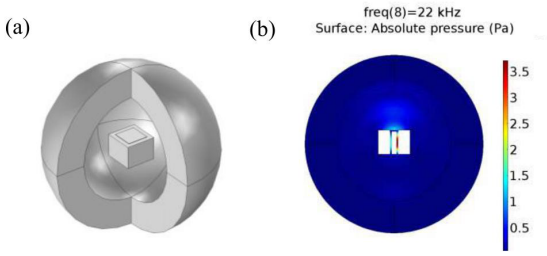

Fig. 4. (a) Schematic of the COMSOL model. (b) The x-z cut plane of a pressure plot in the cavity, pipes, and the surrounding air sphere.

the bandwidth improvement of the pipe organ transducers through 1-D mathematical models. They concluded that the bandwidth increased as the number of pipes increased, up to a perceived limit when over 80 pipes were used. In this present work, there were manufacturing constraints and so the study investigated devices with no pipes, four pipes, eight pipes, and 13 pipes emerging from the back cavity. The effect of the orientation of pipes on the performance of the transducers was also investigated.

Fig. 4(a) shows a schematic of the pipe organ transducer which was simulated by using a commercial FE software COMSOL Multiphysics (Comsol AB, Stockholm, Sweden) to optimize the design parameters. This model can calculate the resonant frequencies of the circular thin plate, pipes, and cavity accurately and also simulate the transducer in transmitting and receiving modes. The simulation model included the solid mechanics domain to simulate the mechanical vibration of both the pipe organ backplate and the PVDF film, the pressure acoustic domain to simulate the absolute pressure and coupling effect between the cavity and pipes, the electrostatics domain to simulate the charge migration inside the piezoelectric material, and finally, a multiphysics model was applied to simulate the coupled boundaries between different physical domains. An air sphere was defined to enclose the transducer to simulate its working environment. The boundary layer of the air sphere was defined as a perfectly matching layer to make sure that sound waves can pass through the boundary without reflection, as shown in Fig. 4(b). Viscous damping was added to the air domains to make the model more realistic. Acoustic wave excitation (electric signals) was introduced to vibrate the thin film to simulate the receiving or transmitting modes of the transducer. Finally, a frequency domain simulation evaluated the system from 15 to 70 kHz with a 0.5-kHz sampling rate.

Sections III-A and III-B investigate the resonant frequency and amplitude of the circular membrane, cavity, and pipes when changing the pipe's number and orientation. Section III-C (Table II) provides the parameters of three optimized samples which can be used in practical manufacturing.

A. Investigating the Resonance of the Cavity and Pipes

The relationship between the parameters of the pipes and the absolute pressure level inside the cavity of the transducer was investigated with the COMSOL model described above. The absolute pressure level inside the cavity directly correlates with the vibration and the electric potential of the piezoelectric thin plate [19]. There are four designs (as shown in Table I) which have different sizes or numbers of pipes for comparison: no-pipe device (I), four-pipe devices with different pipe diameters (II) and (III), and eight-pipe device (IV). The simulated frequency spectrum is given in Fig. 6, and the related pressure and displacements plot are given in Fig. 5. The dashed boxes in Fig. 6 from left to right represent: (a) the fundamental mode of the Helmholtz resonator, (b) the fundamental mode of the pipes, (c) the second harmonic mode of the Helmholtz resonator, (d) the fundamental mode of the circular thin plate, (e) the second harmonic mode of pipes, and (f) the third harmonic mode

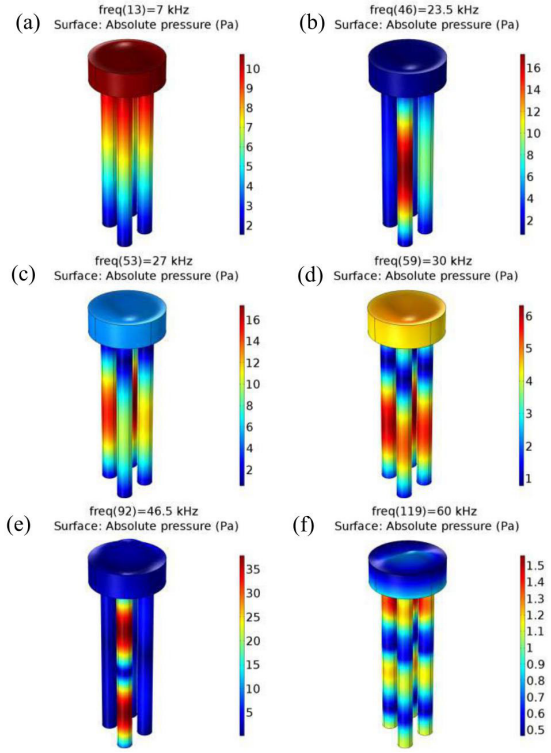

Fig. 5. The pressure (different resonances) in the pipes and cavity and the vibration of the thin plate when frequency is (a) 7kHz, (b) 23.5 kHz, (c) 27 kHz, (d) 30 kHz, (e) 46.5 kHz, and (f) 60 kHz for the 4 pipes device (III), with (a)–(f) corresponding to the frequency in Fig. 6.

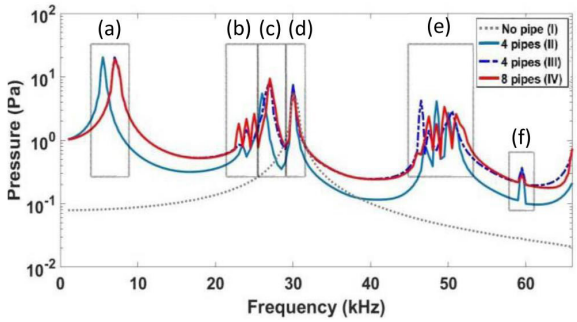

Fig. 6. Absolute pressure in the cavity against frequency to investigate the number and length of pipes. (a) Fundamental mode of the Helmholtz resonator. (b) Fundamental mode of the pipes. (c) Second harmonic mode of the Helmholtz resonator. (d) Fundamental mode of the circular thin plate. (e) Second harmonic mode of pipes. (f) Third harmonic mode of the Helmholtz resonance.

of the Helmholtz resonance, respectively. Three conclusions can be obtained from Fig. 6:

1) Designs III and IV have the same first (a) and second (c) Helmholtz resonance because their cross-sectional area, volume of cavity, and the average pipe length are equal [as shown in (4)].
2) Design IV has more frequency spectrum fluctuations in area (b) than designs II and III because it has more pipes.
3) All of the pipe organ designs (II, III, IV) have larger gain than the reference no-pipe device (I) because the Helmholtz resonance can improve the overall sensitivity.

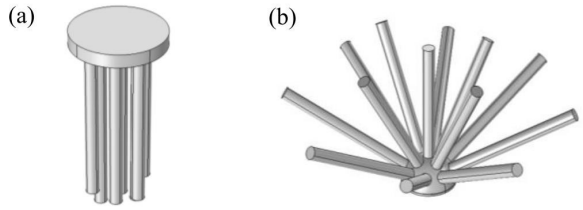

Fig. 7. Air domain of the pipe organ backplate (a) without and (b) with pipe orientation.

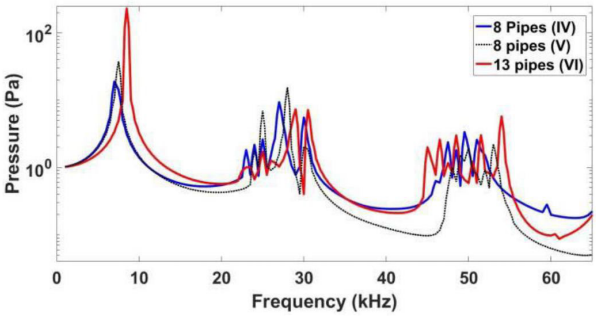

Fig. 8. Absolute pressure in the cavity against frequency to investigate the orientation of pipes.

B. Investigating the Orientation of the Pipes

A further improved pipe organ backplate design was proposed in order to increase the number of pipes [as in Fig. 7(b)] with the same fabrication resolution, which was called the "hedgehog" design. The half-sphere cavity gives a larger surface area to accommodate more pipes and also helps the ultrasonic energy focus to the center of the thin plate. In this section, there are three designs (as shown in Table I) for comparison: eight pipes without orientation (IV), eight pipes with orientation (V), and 13 pipes with orientation (VI). Two conclusions can be obtained from Fig. 8.

1) The "hedgehog" 13-pipes device (VI) provides the greatest Helmholtz resonance pressure, which is around 7 kHz, and the "hedgehog" eight-pipes device (V) has larger resonance pressure than the vertical eight-pipes device (IV).
2) The 13-pipes "hedgehog" device (VI) gives more frequency spectra fluctuations in the pipes' second harmonics than the other two devices around 50 kHz.

C. Optimized Samples

The parameters given in Table I were only used to study and quantify the resonant frequencies of the pipe organ backplate. The resonances are far away from each other in order to locate individual ones clearly. In a practical design, the resonances should be much closer to each other in order to provide more stable gain in a specific frequency range. This section provides two optimized pipe organ (vertical and hedgehog pipes) designs to compare against the standard device (as in Table II).

TABLE II
THREE OPTIMIZED SAMPLES IN PRACTICAL MANUFACTURING

Device	13 pipes	8 pipes	No pipe
Orientation pipe	Yes	No	n/a
Depth of cavity h (mm)	1.45 (half-sphere)	0.4	0.4
Diameter of pipes d (mm)	0.424	0.424	n/a
Radius of thin plate R (mm)	1.45	1.45	1.45
Length of pipes L (mm)	5.1, 5.1, 5.2, 5.3, 5.4, 5.5, 6.2, 5.5, 6.0, 6.6, 6.7, 6.9, 7.0	7.9, 7.9, 7.8, 7.7, 7.6, 7.4, 7.2, 7.2	n/a
Overall Size (mm^2)	126.7	50.2	2.46

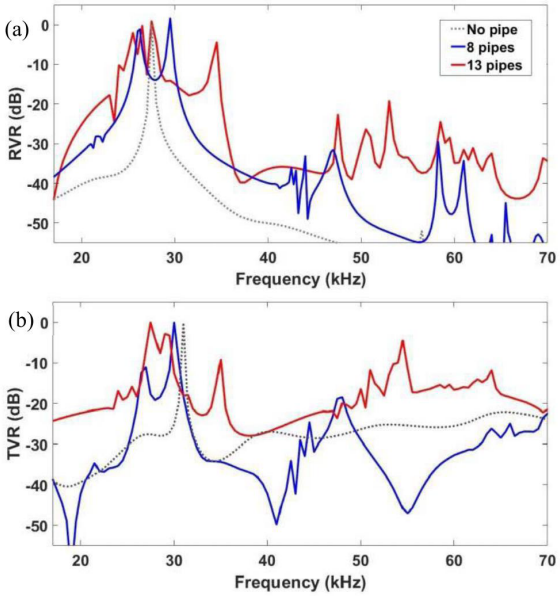

Fig. 9. Simulated normalized (a) receiving voltage response (RVR) and (b) transmitting voltage response (TVR).

The extra overall size of this pipe organ transducers arise from the length of the pipes. The active areas (piezoelectric thin plate) are the same. With ongoing developments in manufacturing resolution, it is possible to miniaturize the whole device to increase the central frequency. The normalized transmitting voltage response (TVR) and receiving voltage response (RVR) are shown in Fig. 9. The no-pipe device has a very narrow bandwidth at 29 kHz, whereas the pipe organ devices have many small peaks at around 30 kHz and 55 kHz. In other words, the pipe organ transducers should have larger operating frequency ranges (wider bandwidth), which matches the 1-D theoretical conclusions made by Walker and Mulholland [12]. This model only includes the air damping (but not the material damping) which makes the amplitude infinitely large at resonant frequency. Manually adding a material damping does improve the simulation result, but it will take away the possibility of easily locating different resonant frequencies in the design stage. Therefore, the bandwidth of the transducers is not compared in the simulation section of this paper, but will be in the experimental section.

Fig. 10. £1 coin and stereolithography pipe organ backplates for scale.

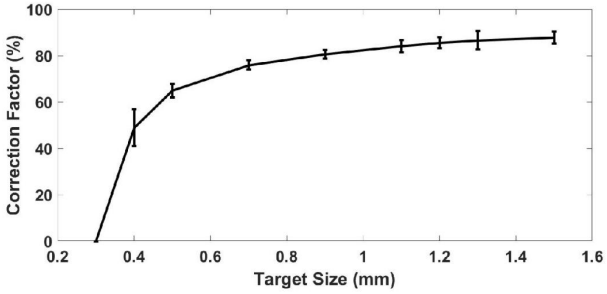

Fig. 11. Correction factor against target diameter. The error bar was from five measurements.

IV. FABRICATION

A. Stereolithography Backplates

After building a CAD model, an Asiga Pico Plus 27 additive manufacturing machine was utilized to fabricate the pipe organ backplate (see Fig. 10). This is a commercial stereolithography 3-D printer with 27-μm pixel resolution in the xy plane and $\sim 1\mu m$ in z-resolution. However, the actual print resolution is worse than this as it also depends on many other factors such as the constituents of the printer resin and the exposure time for each layer, among other things. Instead of using commercial resins directly, the improved resins [21] used in this project are prepared by mixing polyethylene (glycol) diacrylate with molecular weight of 250 along with (2-, 4-, 6-trimethylbenzoyl) phenylphosphane oxide (Irgacure 819) (1% by weight) and Sudan I (0.2% by weight) vigorously in a spinner. Gong *et al.* [21] proposed that the resins formed by this improved formula will present long-term stability in water and higher printing resolution. The exposure time is set to be 2 s with a 10-μm build layer.

During manufacture, the actual printed size was found to always be smaller than the target size because of polymer shrinkage [22]. So a correction factor was required to compensate for this. First of all, calibration pipes were printed with different lengths and diameters. Second, a high-resolution optical microscope system was used to measure the radii. The mean value between five measurements was then calculated. Finally, the correction factor was calculated from (5) and the data plotted in Fig. 11, with an error bar to show that when the diameter is less than 0.5 mm, the correction factor dramatically decreases. In other words, a ~0.5-mm diameter pipe is the smallest diameter that can be fabricated with this technology.

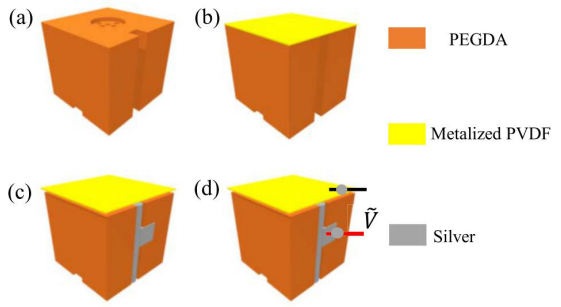

Fig. 12. Four steps fabricate the pipe organ transducer. (a) Stereolithography pipe organ backplate. (b) Gluing metalized PVDF thin film. (c) Silver paint the gap. (d) Connect copper wire to the electrode.

In order to connect more pipes to the cavity, the diameter of the pipes should be as small as possible. This is the reason why $d = 0.48$ mm is chosen for this work

$$\text{Correction factor} = \frac{\text{Actual Diameters}}{\text{Target Diameters}}. \tag{5}$$

B. PVDF Thin Film and Circuit

Fig. 12 shows a schematic illustrating the further four steps of the fabrication. The manufacture starts with (a) the additive manufactured pipe organ backplate with a gap on the side; (b) two-side-metalized PVDF film (Precision Acoustics Ltd, Dorset, U.K.) is attached on the top backplate with superglue; (c) the gap is filled with silver paint to connect the bottom surface of PVDF thin film. Finally, (d) a copper wire is connected to the silver gap and another one to the top surface of the film. When attaching the PVDF film with superglue, some of the superglue may enter the cavity which makes the diameter smaller (or larger) than the designed size, and thus changes the resonance of the thin plate's flexure mode.

V. Experimental Setup and Results

The evaluation of the pipe organ ultrasonic transducer includes measuring the vibration of the active film and the electrical signal in both time and frequency domains.

A. 3-D Laser Doppler Vibrometer

Initially, 10-V wideband periodic chirps with equal energy across frequencies from 15 to 70 kHz were generated by a signal generator to drive the active film into vibration. Second, the front face average displacement was obtained by a 3-D LDV (MSA100-3D, Polytec, Inc., Waldbronn, Germany). Finally, the frequency spectrum and the vibration modes of the resonant frequencies were shown (see Fig. 13). From this test, the fundamental and second harmonic flexure modes of the circular PVDF film between the three devices (as in Table II) were 29 ± 3 and 58 ± 6 kHz, respectively (which are the same as the theoretical prediction).

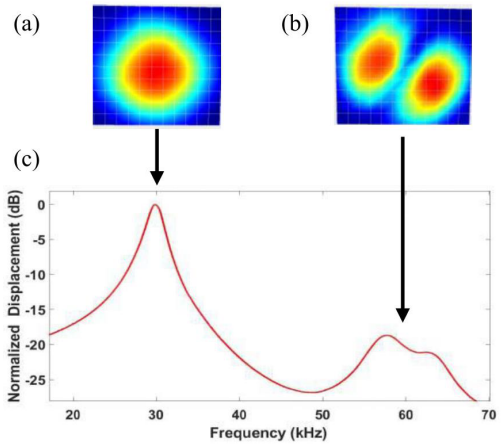

Fig. 13. (a) Fundamental, (b) 2nd harmonic flexure mode of the circular PVDF film and the colors represent the displacement in the out of plane direction and (c) average displacement spectrum of the active area measured by 3-D LDV.

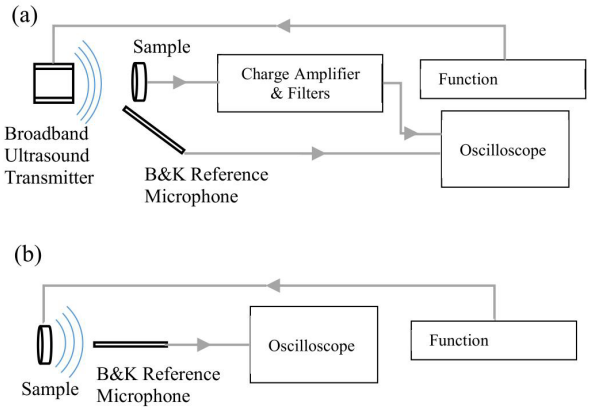

Fig. 14. Simplified schematic of the experimental setup of the receiving and transmitting modes.

B. Electrical Signal Measurement

The experimental setup for measuring the receiving and transmitting bandwidth is shown in Fig. 14(a) and (b), respectively. In Fig. 14(a), the function generator produced a 70-kHz pulse which has equal energy up to ~70 kHz to drive a broadband ultrasonic transmitter (Ultra Sound Advice Loudspeaker). The sample was far enough away from the transmitter to avoid near-field effects. The electrical signal generated from the sample was amplified by a commercial charge amplifier (Brüel and Kjær type 2692) with a custom-built filter (bandwidth 10–100 kHz) system, and finally acquired on an oscilloscope. A 1/8 in reference microphone (Brüel and Kjær, Type 4138) was used to measure the reference sound pressure around the sample. The frequency response of this microphone is calibrated to be flat up to 110 kHz. An amplitude correction algorithm was utilized to compensate for the transmitter's output variance. In Fig. 14(b), the function generator produced a 10-V pulse to drive the film into vibration and the ultrasound

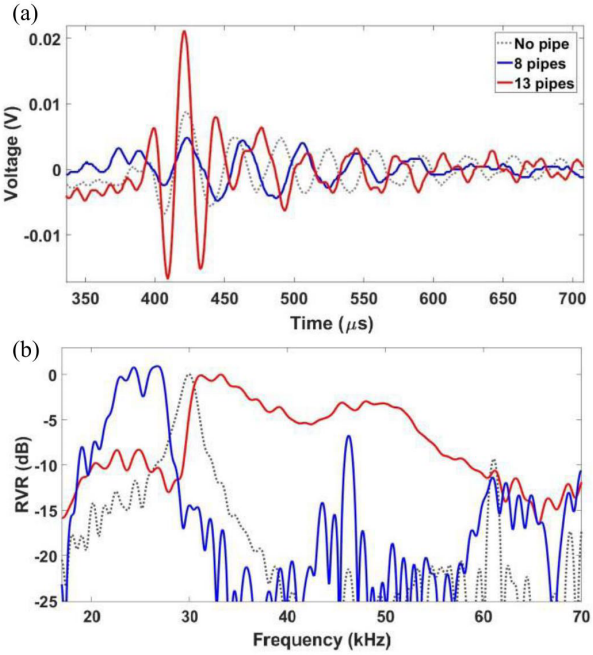

Fig. 15. Receiving voltage response (RVR) in (a) time domain and (b) frequency domain.

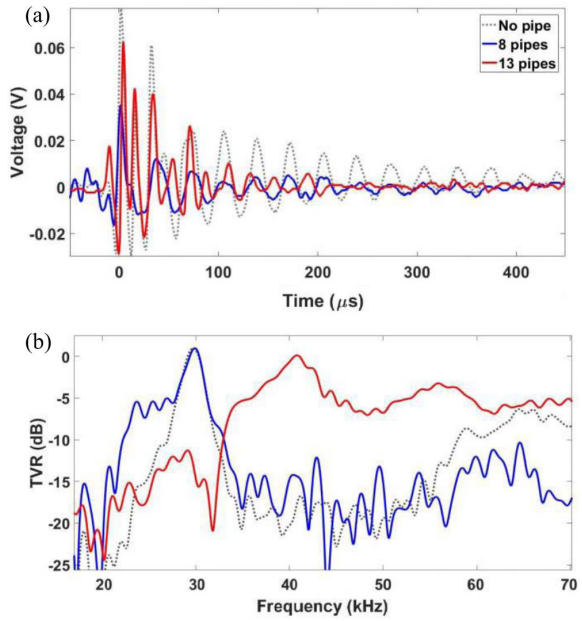

Fig. 16. Transmitting voltage response (TVR) in (a) time domain and (b) frequency domain.

field generated by the sample was measured by the reference microphone directly. Since the frequency range of our device is narrower than 110 kHz, no amplitude compensation is required. Figs. 15 and 16 show the electrical signal response in TVR and RVR between the standard no-pipe, eight-pipe, and "hedgehog" 13-pipe devices.

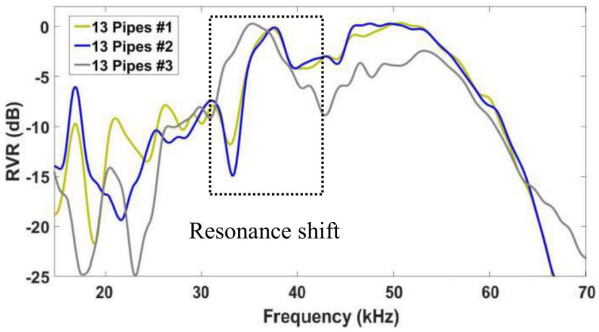

Fig. 17. Repeatability experiment of three 13-pipes pipe organ transducers in RVR measurement.

TABLE III
EXPERIMENTAL RESULT OF TVR AND RVR

Mode	Device	13 pipes	8 pipes	No pipe
TVR	-6 dB Bandwidth	55.7%	29.2%	12.3%
	Signal strength	0.091V	0.048V	0.106V
	Central frequency	47 kHz	27kHz	29kHz
	20% Peak-Peak Pulse length	8.8μs	20.1μs	20.5μs
RVR	-6 dB Bandwidth	58.5 %	26.0 %	9.7 %
	Signal strength	0.037 V	0.010V	0.015V
	Central frequency	41kHz	26kHz	30kHz
	20% Peak-Peak Pulse length	12.3μs	20.6μs	27μs

C. Repeatability Experiment

In order to prove the repeatability of the "hedgehog" 13-pipe transducer, another three samples were fabricated in order to remeasure their RVR (see Fig. 17). The −6-dB bandwidth of those three devices are 52.9% (not a continuous bandwidth), 50.9%, and 50.9%, respectively, which are very close to the first 13-pipes device in Table III (58.5%). Moreover, their frequency spectrums are also very similar (above 25 kHz) except one of the resonances was shifted at around 37 kHz. This was caused by the tolerance of fabrication when manually attaching the PVDF film with superglue.

VI. DISCUSSION AND CONCLUSION

A. Simulation and Experimental Result Discussion

The pipe organ backplate is a resonator which is formed by a cavity with connecting of pipes of various lengths. Therefore, it includes many fundamental resonances and harmonics from those components. Sections II and III evaluated those resonant frequencies from both mathematical and FEA model aspects to give the same conclusions. Section III-A investigated the resonance of the pipes and the cavity. The simulation results, shown in Fig. 6, indicate that the resonant frequency of a pipe is mainly determined by its length, which can also be explained by (3). Furthermore, (4) indicates that the resonant frequency of the Helmholtz resonator depends on the area of the opening and the cavity volume. Therefore, samples III and IV have the same Helmholtz resonant frequency in Fig. 6 boxes

(a) and (c). Section III-B investigated the effect of the orientation of the pipes ("hedgehog" design). The pipes are designed to be orientated at different angles since previous 1-D theoretical work concluded that the number of pipes should be as high as possible in order to have the widest bandwidth [12]. However, the number of pipes is limited by the resolution of the additive manufacturing technique in the laboratory. The "hedgehog" design provides a larger space to arrange the pipes because of the curved cavity surface. In other words, the "hedgehog" design increases the number of pipes with the same manufacturing resolution. Moreover, the "hedgehog" design provides additional benefits and Figs. 8 and 9 show that the "hedgehog" design has a larger Helmholtz resonance and more stable gain, because the orientated pipes can focus ultrasound energy to the thin plate center.

In the optimized designs, the resonant frequencies of the cavity, multiple pipes, and the circular piezoelectric film were chosen to be close to each other in order to have a flat bandwidth response in both TVR and RVR. The results in Table III show that the bandwidth of the pipe organ devices is at least twice as wide as that of the no-pipe device with comparable sensitivity. The "hedgehog" device has the largest bandwidth and shortest pulselength in both transmitting and receiving modes. However, the disadvantage is that the "hedgehog" device also requires larger space to place the orientated pipes. The result from the 3-D LDV (as shown in Fig. 13) indicates that the first flexure mode of those three transducers is around 29 kHz, which is the same as the FEA result and the value calculated from (1) and (2). The FEA simulation result has sharp gain peaks which caused the simulated bandwidth to be smaller than the experimental bandwidth. This is because the model did not include any electrical or mechanical damping. However, the resonant frequencies from different components of the pipe organ backplate are a good match. The pipes' fundamental and second harmonic resonance varied from 20 to 25 kHz and 45 to 55 kHz, respectively, and the Helmholtz resonance was located at 35 kHz to fill the gap between the pipes' resonance modes and increase the overall device sensitivity. This is why the 13-pipes pipe organ transducer can introduce a stable gain from 30 to 55 kHz in the experiment results. Although the vertical pipe design can have similar pipe lengths and cavity size, the "hedgehog" device can focus the ultrasound energy to the middle of the thin plate. Therefore, the "hedgehog" device has larger sensitivity improvement in the pipes' resonant frequencies. The repeatability experiment proved that the fabrication and the measurement stages are repeatable. All of the potential errors are from the tolerance of the fabrication.

B. Conclusion

The bandwidth of conventional PMUTs is too narrow to be used in wide-bandwidth applications [7]. This paper presented a novel backplate design (resonator) to improve the bandwidth by selecting and enhancing the frequency range of interest. The frequency range can be carefully controlled through the specific parameters of the backplate. The principles were studied via mathematical equations and FEA models. The models indicated that the pipe organ backplate introduced Helmholtz resonances and multiple pipes' resonances to the circular thin plate's resonance to increase the device bandwidth without sensitivity loss. This also provided several conclusions to locate and quantify different types of resonances in the frequency domain. Two optimized designs were selected for the fabrication stage to compare against the custom-built standard device. An additive manufacturing technique for the pipe organ backplate is introduced. It is a faster prototyping method for fabricating piezoelectric diaphragm ultrasonic transducers. An improved resin formula was used to increase the manufacture resolution of the backplate. Finally, two experiments were designed to evaluate the response of two pipe organ transducers, and a standard transducer, in both TVR and RVR. The -6-dB bandwidth of the "hedgehog" 13-pipes device was found to be up to 58.5% in RVR, which was 2.25 times larger than the vertical eight-pipe device, and 6 times larger than the custom-built standard device. In the TVR, the -6-dB bandwidth of the "hedgehog" 13-pipes device was up to 55.7%, which was 1.9 times larger than the eight-pipes device, and 4.6 times larger than the customer-built standard device. The repeatability experiment shows that the fabrication and measurement progress are repeatable. The error originated from the manual fabrication process. With the ongoing development of additive manufacturing, some researchers [23] claim that they can use TPP for fabrication of 3-D structures with a lateral resolution below 200 nm. The authors latest simulation results suggest that the overall size of the pipe organ air-coupled transducer can be miniaturized to be ~ 500 μm, which will result in an operating frequency of 480 kHz, which is more applicable to applications such as NDE. Furthermore, it is possible to imagine that the fabrication could be achieved directly on a piezoelectric film to order to replace the gluing process used for this paper's prototypes.

ACKNOWLEDGMENT

The authors would like to thank Y. Zhang for designing and fabricating the custom-built filters for measuring the electrical signal. They would also like to thank other staff and researchers at the Centre for Ultrasonic Engineering, University of Strathclyde, Glasgow, U.K., for their support throughout this research work. Data set available: http://dx.doi.org/10.15129/fa341875-f1b1-4bfd-b052-41b965de95c4

REFERENCES

[1] H. Fang, Z. Qiu, R. L. O'Leary, A. Gachagan, and A. J. Mulholland, "Improving the operational bandwidth of a 1–3 piezoelectric composite transducer using Sierpinski Gasket fractal geometry," in *Proc. IEEE Int. Ultrason. Symp. (IUS)*, Nov. 2016, pp. 8–11.

[2] P. C. Eccardt and K. Niederer, "Micromachined ultrasound transducers with improved coupling factors from a CMOS compatible process," *Ultrasonics*, vol. 38, nos. 1–8, pp. 774–780, 2000.

[3] Y. Qiu *et al.*, "Piezoelectric micromachined ultrasound transducer (PMUT) arrays for integrated sensing, actuation and imaging," *Sensors*, vol. 15, no. 4, pp. 8020–8041, 2015.

[4] D. E. Dausch, J. B. Castellucci, D. R. Chou, and O. T. von Ramm, "Theory and operation of 2-D array piezoelectric micromachined ultrasound transducers," *IEEE Trans. Ultrason., Ferroelectr., Freq. Control*, vol. 55, no. 11, pp. 2484–2492, Nov. 2008.

[5] A. Guedes, S. Shelton, R. Przybyla, I. Izyumin, B. Boser, and D. A. Horsley, "Aluminum nitride pMUT based on a flexurally-suspended membrane," in *Proc. 16th Int. Solid-State Sens., Actuators Microsyst. Conf. TRANSDUCERS*, Jun. 2011, pp. 2062–2065.
[6] T. Wang, T. Kobayashi, and C. Lee, "Micromachined piezoelectric ultrasonic transducer with ultra-wide frequency bandwidth," *Appl. Phys. Lett.*, vol. 106, no. 1, p. 013501, 2015.
[7] P. Muralt *et al.*, "Piezoelectric micromachined ultrasonic transducers based on PZT thin films," *IEEE Trans. Ultrason., Ferroelectr, Freq. Control*, vol. 52, no. 12, pp. 2276–2288, Dec. 2005.
[8] T. Wang, R. Sawada, and C. Lee, "A piezoelectric micromachined ultrasonic transducer using piston-like membrane motion," *IEEE Electron Device Lett.*, vol. 36, no. 9, pp. 957–959, Sep. 2015.
[9] A. Hajati *et al.*, "Monolithic ultrasonic integrated circuits based on micromachined semi-ellipsoidal piezoelectric domes," *Appl. Phys. Lett.*, vol. 103, no. 20, p. 202906, 2013.
[10] A. J. Walker and A. J. Mulholland, "A theoretical model of an electrostatic ultrasonic transducer incorporating resonating conduits," *IMA J. Appl. Math.*, vol. 75, no. 5, pp. 796–810, 2010.
[11] A. J. Walker, A. J. Mulholland, E. Campbell, and G. Hayward, "A theoretical model of a new electrostatic transducer incorporating fluidic amplification," in *Proc. IEEE Ultrason. Symp.*, Nov. 2008, pp. 1409–1412.
[12] A. J. Walker and A. J. Mulholland, "A pipe organ-inspired ultrasonic transducer," *IMA J. Appl. Math.*, vol. 82, no. 6, pp. 1135–1150, 2017.
[13] E. Campbell, W. Galbraith, and G. Hayward, "A new electrostatic transducer incorporating fluidic amplification," in *Proc. IEEE Ultrason. Symp.*, Oct. 2006, pp. 1445–1448.
[14] B. Zhu, B. Tiller, A. Walker, A. Mulholland, and J. Windmill, "'Pipe organ' air-coupled broad bandwidth transducer," in *Proc. IEEE Int. Ultrason. Symp. (IUS)*, Sep. 2017, pp. 6–9.
[15] F. Akasheh, T. Myers, J. D. Fraser, S. Bose, and A. Bandyopadhyay, "Development of piezoelectric micromachined ultrasonic transducers," *Sens. Actuators A, Phys.*, vol. 111, nos. 2–3, pp. 275–287, 2004.
[16] M. Bao and H. Yang, "Squeeze film air damping in MEMS," *Sens. Actuators A, Phys.*, vol. 136, no. 1, pp. 3–27, 2007.
[17] J. E. Mclennan and J. Close, "A0 and A1 studies on the violin using CO_2, he, and air/helium mixtures," *Acta Acust.*, vol. 89, no. 1, pp. 176–180, Apr. 2002.
[18] S. B. Horowitz, M. Sheplak, L. N. Cattafesta, III, and T. Nishida, "A MEMS acoustic energy harvester," *J. Micromech. Microeng.*, vol. 16, no. 9, p. S174, 2006.
[19] R. A. Rahim and M. J. B. Johari, "Design and simulation of MEMS helmholtz resonator for acoustic energy harvester," in *Proc. Int. Conf. Comput. Commun. Eng. (ICCCE)*, Jul. 2016, pp. 505–510.
[20] H. Takahashi, A. Suzuki, E. Iwase, K. Matsumoto, and I. Shimoyama, "MEMS microphone with a micro Helmholtz resonator," *J. Micromech. Microeng.*, vol. 22, no. 8, p. 085019, 2012.
[21] H. Gong, M. Beauchamp, S. Perry, A. T. Woolley, and G. P. Nordin, "Optical approach to resin formulation for 3D printed microfluidics," *RSC Adv.*, vol. 5, no. 129, pp. 106621–106632, 2015.
[22] J. Stampfl *et al.*, "Photopolymers with tunable mechanical properties processed by laser-based high-resolution stereolithography," *J. Micromech. Microeng.*, vol. 18, no. 12, p. 125014, 2008.
[23] J. Serbin *et al.*, "Femtosecond laser-induced two-photon polymerization of inorganic–organic hybrid materials for applications in photonics," *Opt. Lett.*, vol. 28, no. 5, pp. 301–303, 2003.

Botong Zhu (S'17) received the bachelor's degree from the University of Strathclyde, Glasgow, U.K., in 2015, where he is currently pursuing the Ph.D. degree with the Department of Electronic and Electrical Engineering. He is also a Ph.D. student with the EPSRC Centre for Doctoral Training of Quantitative NDE, U.K.

His current research interests include air-coupled transducer development.

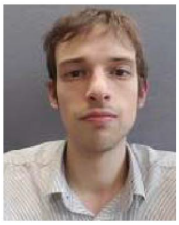

Benjamin P. Tiller received the M.Sc. degree in physics with theoretical physics from the University of Nottingham, Nottingham, U.K., and the Ph.D. degree from the University of Glasgow, Glasgow, U.K., with a focus on the frequency scaling relationship of acoustic streaming in microfluidic environments.

He is currently a Research Associate with the Department of Electronics and Electrical Engineering, University of Strathclyde, Glasgow. His current research interests include development of novel 3-D printed techniques that enable new sensing technologies.

Alan J. Walker received the B.Sc. (Hons.) and Ph.D. degrees in mathematics from the University of Strathclyde, Glasgow, U.K., in 2003 and 2008, respectively.

He is a Member of the Institute of Mathematics and its Applications, and a Chartered Mathematician. He joined the University of the West of Scotland, Hamilton, U.K., as a Lecturer in mathematics, in 2015. He has over 10 years of research experience in the area of ultrasonics. His current research interests include mathematical modeling of physical and biological systems.

A. J. Mulholland was born in Glasgow, U.K., in 1966. He received the B.Sc. degree (Hons.) in mathematics from the University of Glasgow, Glasgow, in 1987, the M.Sc. degree in industrial mathematics from the University of Strathclyde, Glasgow, in 1991, and the Ph.D. degree in mathematical biology from Glasgow Caledonian University, Glasgow, in 1994.

Since 1999, he has been an Academic Member of Staff with the Department of Mathematics and Statistics, University of Strathclyde, Glasgow, where he is currently a Professor and the Head of the Department. He has been with the Centre for Ultrasonic Engineering, University of Strathclyde, since 1996, and he leads the analytical modeling activities of the center. He has authored over 100 papers in applied mathematics, particularly in the modeling of ultrasonic devices and systems.

Dr. Mulholland is a fellow of the Institute of Mathematics and its Applications.

James F. C. Windmill (M'99–SM'17) received the B.Eng. degree in electronic engineering and the Ph.D. degree in magnetic microscopy from the University of Plymouth, Plymouth, U.K., in 1998 and 2002, respectively.

He joined the Centre for Ultrasonic Engineering, University of Strathclyde, Glasgow, U.K., as a Lecturer in 2008. He is currently a Professor with the Department of Electronic and Electrical Engineering, University of Strathclyde. He has over 18 years of research and development experience in the areas of sensors and hearing systems. His current research interests include biologically inspired acoustic systems, from the fundamental biology to various engineering application topics.

Materials and Design 165 (2019) 107593

Contents lists available at ScienceDirect

Materials and Design

journal homepage: www.elsevier.com/locate/matdes

Piezoelectric microphone via a digital light processing 3D printing process

Benjamin Tiller, Andrew Reid*, Botong Zhu, José Guerreiro, Roger Domingo-Roca, Joseph Curt Jackson, J.F.C. Windmill

University of Strathclyde, Centre for Ultrasonic Engineering, Glasgow G1 1RD, UK

HIGHLIGHTS

- Demonstration of fully 3D printed working piezoelectric microphone.
- Characterization of resin properties and print results for Barium Ti- tanate nanoparticles and Multi-Walled Car- bon Nanotube in a polymer matrix.
- Adaptation of commercial digital light processing 3D printer to multi- material integrated build.

GRAPHICAL ABSTRACT

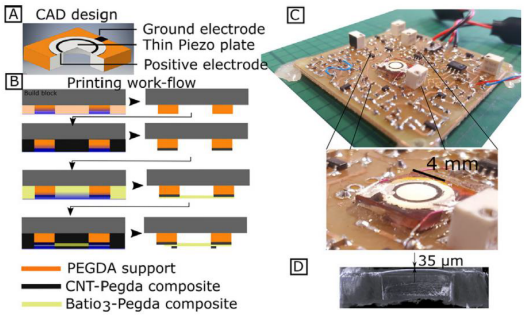

ARTICLE INFO

Article history:
Received 9 November 2018
Received in revised form 4 January 2019
Accepted 5 January 2019
Available online 11 January 2019

Keywords:
Digital light processing
Bio-inspired hearing
Nanocomposites

ABSTRACT

In nature sensors possess complex interlocking 3D structures and extremely localized material properties that allow processing of incredibly complex information in a small space. Acoustic sensor design is limited by fabrication processes, often MEMS based, where there is limited scope for fully 3D creations due to planer fabrication methods. Here we investigate the application of 3D printing via digital light processing (DLP) to integrate piezoelectric, conductive and structural polymer layers to create a complete electro-mechanical device. We demonstrate a working piezoelectric acoustic sensor, capable of sending electric signals that can be picked up by pre-amp circuitry fabricated using a commercially available 3D printer. We show that the 3D printing of mechanically sensitive membranes with thicknesses down to 35 µm and tunable resonant frequencies is possible and further show it is possible to create a fully working electro-acoustic device by embedding 3D printed piezoelectric and conductive parts. Realizing this design opens up the possibility of generating truly 3D structured functional prints that may be used in bio-inspired design.

1. Introduction

Additive manufacturing technologies are known to offer benefits in terms of the speed, cost and versatility of the platform for small scale production and rapid prototyping, but beyond this the use of additive manufacturing to create materials with complex, locally tuned physical properties or complex micro-structures not accessible to conventional production techniques is only beginning to be explored [1,2]. Biological sensors represent a paradigm shift in design approach since the sensors are rarely passive recorders of information, but complex micro-controllers in their own right performing much of the task of signal processing and filtering before export to the nervous system. In acoustic communication such signal processing often relies on mechanical coupling between strongly anisotropic diaphragms which is difficult to reproduce using traditional micro-machining techniques. Examples such as the helical

* Corresponding author.
E-mail address: andrew.reid@strath.ac.uk (A. Reid).

https://doi.org/10.1016/j.matdes.2019.107593

shaped cochlear and associated Basilar membrane in mammalian hearing, capable of highly tonotopic mechanical frequency filtering [3] or the highly structured acoustic trachea in crickets and grasshoppers [4] have been studied due to their remarkable physical features. These examples are all highly complex 3D structures on a micro/millimeter length scale and pose a challenge to researchers in how to reproduce the essential physical mechanisms that these systems exploit, and yet be possible to fabricate with currently available technology [5,6].

A prime example is the coupled tympanic membranes of *Ormia ochracea*, which have extremely accurate directional sensing capabilities given the small size and spacing of the ears [7]. In *O. ochracea* the tympana are coupled via a raised bridge attached at the centre of each tympanum, where the mechanical properties of the coupling bridge must be closely tailored to the resonant frequencies and damping conditions of the system [8]. Many *Ormia* inspired directional microphones have been developed, with most seeking to flatten the natural 3D structure in a centrally supported see-saw like structure [9,10]. While this fits the requirements of MEMS fabrication very well, since it is often difficult and expensive to fabricate designs requiring much variation in the Z-plane, it introduces compromises such as requiring an air gap around the periphery of the diaphragms making the devices susceptible to problems of sensitivity and sound path difference around the device. Other examples of biological acoustic sensors such as the tonotopic localization of the Basilar membrane rely on considerably graded thickness variation in which would be extremely difficult to reproduce with MEMS fabrication techniques.

Additive manufacturing holds some promise as a method for creating true 3D biologically inspired sensors. Using fused deposition modelling techniques researchers have printed an acoustically sensitive membrane mimicking the geometric shape of a human tympanic membrane [11], and thickness varying membranes for sound absorption [12]. 2D ink-jet and 3D poly-jet printing have been used to build a complete capacitive microphone by printing conductive material onto a thin Mylar film which was then clamped to a 3D printed body [13]. Of particular interest are digital light processing (DLP) based stereo-lithographic printing techniques due to the high achievable print resolutions, 25–50 μm in commercially available systems, with custom-built printers reported that lower this still further to 10 μm [14], speed of fabrication [15] and compatibility with multi-material printing techniques [16].

Multi-material printing requires the printable resin to be switched during the build, and has been shown for different coloured resins using a top-down stereo-lithographic process with a solvent cleaning step between each material swap [17] and for hydrogels using digital light processing with an air drying stage between each material swap [18]. Base polymer resins for 3D printing may be enhanced or given entirely new properties via the addition of nanofillers to the resin, for example by adding barium titanate ($BaTiO_3$) nanopowder into a 3D-printable fluid piezoelectric parts may be created [19-22, or the dielectric properties of the resin may be enhanced [23-25]. Incorporating carbon nanotubes, silvers salts or silica nanoparticles may produce conductive parts [26-29]. Combining such functionally enhanced resins with recent DLP based multi-material printing techniques has allowed fully 3D printed micro-electromechanical devices such as capacitive microphones designed using multi-walled carbon nanotube-polymer composites as conductive layers [30].

In this work we demonstrate a piezoelectric microphone, comprising conductive, piezoelectric and inert polymer based parts, in a single integrated build. Functional 3D-printable composite resins are created by mixing barium titanate nanopowder and multi-walled carbon nanotubes into a PEGDA base monomer resin to make the piezoelectric and conductive parts. The 3D-printed microphone is integrated into a custom build pre-amplifier printed circuit board and the response characterized.

2. Materials and methods

All devices and test samples were created using a commercially available 3D printer (Asiga Pico plus 27), with slicing of CAD models performed by the manufacturer's software (Asiga Composer). The resolution is advertised as 27 μm in the X-Y plane with a minimum build layer thickness of 1 μm.

Resins for DLP 3D printing must comprise a base monomer material together with a photoinitiator. An absorber can be included to control the penetration depth of the light in the material. The monomer used here was poly(ethylene glycol) diacrylate (PEGDA, MW 250), with phenylbis(2,4,6-trimethylbenzoyl) phosphine oxide (Irgacure 819) as the photoinitiator. Sudan 1 (S1) was used as an absorber in concentrations of 0.1%, 0.2%, 0.4% and 0.8% by weight/weight, together with 1% (w/w) Irgacure 819. Preparations are sonicated for 30 min before use and stored in foiled wrapped containers to protect the resins from light.

For the piezoelectric parts barium titanate nanopowder ($BaTiO_3$) with an average particle diameter of 500 nm in concentrations ranging from 33% to 66% (w/w) was added to the base resin. The barium titanate resin composite was then mixed in a Thinky ARE 250 planetary mixer (INTERTRONICS) before the sonication step. For the conductive parts multi-walled carbon nanotubes (MWCNT) with an average diameter of 9.5 nm and length 1.5 mm were added in concentrations from 0.1% to 1.25% (w/w). The conductive composite was mixed for 24 h in a magnetic stirrer before use.

PEGDA, Irgacure 819 and Sudan 1 were purchased from Sigma Aldrich. Barium titanate nanoparticles were purchased from US-NANO. Multi-walled carbon nanotubes were purchased from Nanocyl. All materials were used as received.

Successful DLP manufacture requires that the exposure time for each layer be tailored to the material's absorption and intensity of the light source [31]. If we consider the photopolymerizable resin with a surface at $z = 0$ and an optical irradiance at the surface of the material of I_0 in W/cm^2 then the irradiance at depth z is given by Beer's law.

$$I(z) = I_0 e^{-\alpha z} \tag{1}$$

The parameter α is the absorption coefficient of the material in m^{-1}. The corresponding dose at that depth is then $D(z,t) = tI(z)$, where t is the time in seconds. At some critical dose the polymerization of the resin will have progressed sufficiently for the material to be considered solid. Fig. 1 illustrates how the absorption properties of the fluid and the exposure time influence the total UV dose at increasing depth. The minimum dose required to cure the fluid at depth z is shown as a horizontal grey line, with the resulting print thickness (D_t) being the point at which the dose energy drops below this critical dose. The depth of cured material can then be expressed in terms of the dose energy.

$$D_t = \frac{1}{\alpha}(lnD_0 - lnD_c) \tag{2}$$

By measuring the cured height (z_p) of a 3D printed membrane (or other structure printed onto free space) at a range of exposure times values for the critical dose (D_c) and absorption coefficient (α) can be estimated by fitting the results to Eq. (2). Fig. 2 gives measured membrane thicknesses for PEGDA with Sudan 1 concentrations of 0.2%, 0.4% and 0.8% (w/w) and for PEGDA with added barium titanate nanoparticles and with multi-walled carbon nanotubes in concentrations of 33%, 66% and 1% (w/w) respectively. Sudan 1 concentrations for all composites of barium titanate/PEGDA and MWCNT/PEDGA are held at 0.1% (w/w). Estimated absorption coefficients and critical doses for the materials are given in Table 1.

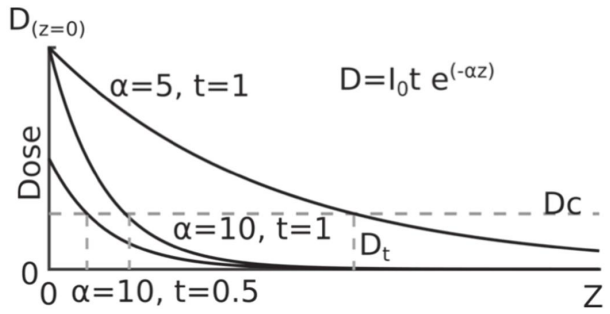

Fig. 1. Illustration of variation in dose energy with depth (z) for absorption coefficients of $\alpha = 10\mu m^{-1}$, $t = 0.5$ s, $\alpha = 10\mu m^{-1}$, $t = 1$ s and $\alpha = 5\mu m^{-1}$, $t = 1$ s.

In addition to the depth calibration tests of the X-Y resolution of the printer were made using square arrays of blocks with dimensions ranging from 200 µm to 1000 µm. This additional test was deemed necessary as the diameter of the barium titanate nanoparticles was expected to significantly scatter the 3D printers 412 nm UV LED light source. The results of the print resolution tests may be found in Fig. 3.

Material changes during the print process were performed by manually pausing the Asiga pico plus at the correct layer height. Sliced CAD files were generated with gaps one or two build layers thick to facilitate this process. The parts were then cleaned in isopropyl alcohol for 30 s and immediately dried while the printable resin was changed and the printer restarted.

Acouso-mechanical behaviour of 3D printed diaphragms was measured with a scanning laser Doppler vibrometer (Polytec PSV MSA-100-3D). The acoustic source was an ESS Heil Air-Motion Transformer placed 50 cm from the device under test, with signals generated by an Agilent 3325A. A Bruel and Kjaer 4138 1/8 inch microphone was placed within 1 cm of the diaphragm to provide the reference signal. Electrical signals were recorded with the 3D printed diaphragm glued to a PCB circuit board with a custom built pre-amplifier circuit. Signals from the circuit were recorded with a Tektronix DPO 2014 oscilloscope with a sampling frequency of 31.25 MHz and averaged ($N = 16$).

Thickness and morphology measurements were taken with a digital micrometer and confirmed via X-Ray Computer Tomography

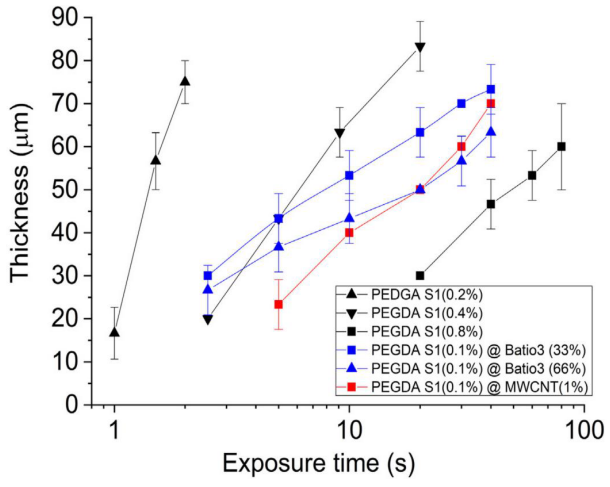

Fig. 2. Measured membrane thickness for resin and resin composites with increasing exposure time.

Table 1
Estimated attenuation coefficients and critical dose from cured height values in Fig. 2.

Resin	Attenuation (μm^{-1})	Critical dose (mJ/cm^2)
0.2% Sudan 1	0.00839	18.80
0.4% Sudan 1	0.0247	39.70
0.8% Sudan 1	0.0462	156.40
33% $BaTiO_3$	0.0863	2.92
66% $BaTiO_3$	0.136	1.13
1% CNT	0.0530	32.40

using the Bruker Skyscan 1172 with SHT 11 Megapixel camera and Hamamatsu 80 kV (100 µA) source.

Testing of d_{33} of the barium titanate/PEGDA composite were made by laser Doppler vibrometer measurements of the thickness mode resonant frequency [32, 33]. Test samples were polymerized between two glass slides with a spacer separation of 150 µm and cured in a UV oven for 10 min. Samples were poled for 2 h in silicone oil at 100° at 10 MV/m before removal and cleaning. The resistivity measurements of PEGDA-MWCNT composites were taken with an ohmmeter on similarly prepared samples with silver paint to reduce the contact resistance between the ohmmeter and the sample.

Models of the 3D-printed diaphragm were created using COMSOL Multiphysics 5.3a. Simulations primarily used the solid-acoustic interaction interface, where the diaphragms and 3D-printed block were simulated from CAD designs. Resonance frequencies and damping were simulated using the thermo-viscous acoustics physics and eigenfrequency analysis in two phases: the first using a plain PEGDA model where the mechanical properties of the material are estimated as a density of 1183 kg/m^3, Young's modulus of 52.9 MPa and Poisson's ratio of 0.32. These models could be compared to impedance analogy and 3D-printed PEGDA only diaphragms and informed the generation of complete electro-mechanical models. The model was reduced to a 1/12 slice of the diaphragm relying on its axial symmetry to reduce computation time.

Simulating the electro-mechanical behaviour of the diaphragm requires knowledge of the mechanical properties of the piezoelectric nanocomposite, which was taken as having a Young's modulus of approximately 1 GPa from nano-indentation tests and a density of 1832 kg/m^3. The mechanical properties of the conductive layers were not simulated, but simply treated as boundary terminals. Estimates of the piezoelectric behaviour of the barium titanate composite were made using the strain-charge form with a symmetrical compliance matrix based on the Young's modulus of 1 GPa above, and a coupling matrix, d, shown as follows:

$$d = \begin{bmatrix} 0 & 0 & 1\times10^{-12} \\ 0 & 0 & 1\times10^{-12} \\ 0 & 0 & 3\times10^{-12} \\ 0 & 1\times10^{-12} & 0 \\ 1\times10^{-12} & 0 & 0 \\ 0 & 0 & 0 \end{bmatrix} \text{C/m} \quad (3)$$

Estimates of the stress on the membrane was made from impedance analogy, representing the compliances of the diaphragm and cavity as capacitances, damping as resistances and the mass of the diaphragm as an inductance [34]. The lumped diaphragm compliance (C_d) is evaluated with reference to the deflection (w) and potential energy of the system (E_p).

$$C_d = \frac{w^2}{2E_p} = \frac{9r^2(1-\mu^2)}{16\pi E t^3} \quad (4)$$

Here r is the diaphragm radius, μ is the Poisson's ratio, E is the Young's modulus of the diaphragm material and t is the diaphragm thickness. The lumped back cavity compliance can be given as [35]

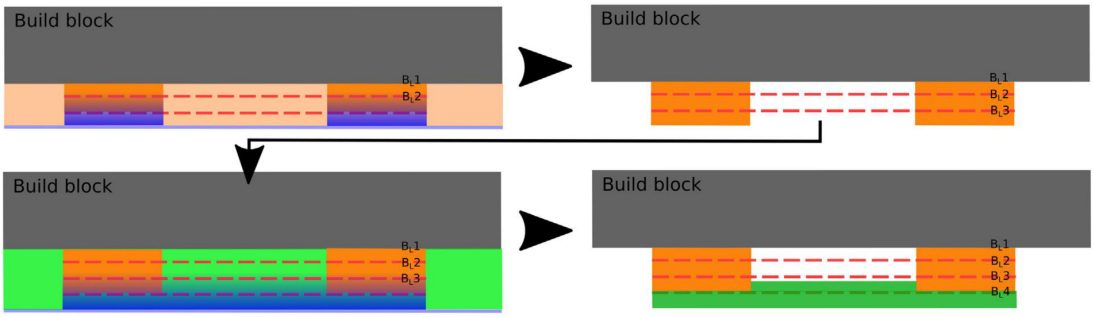

Fig. 3. The process steps for changing materials mid-print. By pausing the print just before the diaphragm layer is printed the printer ink can be exchanged.

$$C_{bc} = \frac{V_{bc}}{\rho_0 c_0^2 A_v^2} \tag{5}$$

where V_{bc} is the volume of the back cavity, ρ_0 is the density of air, c_0 is the velocity of sound in air and A_v is the effective area of the diaphragm (here taken from an effective diameter of 2/3 the measured diaphragm diameter). The resonance frequencies of the mechanical system can then be calculated as a simple resonance equation with M as the mass of the diaphragm.

$$f_0 = \frac{1}{2\pi(C_d||C_{bc})M} \tag{6}$$

3. Results and discussion

The process used to make the 3D printed microphones is illustrated in Fig. 3. As the diaphragm is not being printed directly onto a previously printed layer, diaphragm thickness must necessarily be greater than 1 build layer thickness since the minimum dose energy for the membrane layer must be sufficient to bond the membrane layer to the previous layer. All results shown here are for a diaphragm thickness of 35 µm (Fig. 4) which was found to be a repeatable and reliable construction when printing with the barium titanate composite.

The effect of barium titanate and MWCNT nanofillers on the print accuracy are shown in Fig. 5 for the base PEGDA resin, barium titanate-PEGDA composite and MWCNT-PEGDA composite. The barium titanate-PEGDA composite's minimum resolution was 0.35 mm in the X-Y plane, compared to 0.2 mm for the PEGDA resin. Higher concentrations of barium titanate (50% and 66% w/w) were unable to resolve a square array of 1 mm edge/1 mm separation, the largest array tested.

Results for measurements of the d_{33} of the barium titanate PEGDA composite and for the resistivity of the MWCNT-PEDGA composite are given in Fig. 6. While higher concentrations of barium titanate nanoparticles are clearly desirable the results of the print resolutions tests in Fig. 3 indicate that for feature sizes at the millimeter scale prints are limited to composites with less than 50% barium titanate by weight. For the piezoelectric diaphragm printed here the X-Y resolution was not important and so the higher concentration of 66% by weight was used, resulting in a predicted d_{33} of 3–4 pC/N.

Conductivity tests with the MWCNT-PEGDA composite indicated little benefit from increasing concentration beyond 0.5% by weight. Samples printed on the Asiga pico plus 27 and samples created by polymerizing between two glass sides showed no noticeable differences in resistivity. Resistivity was also found to be invariant with the geometry of the 3D printed part.

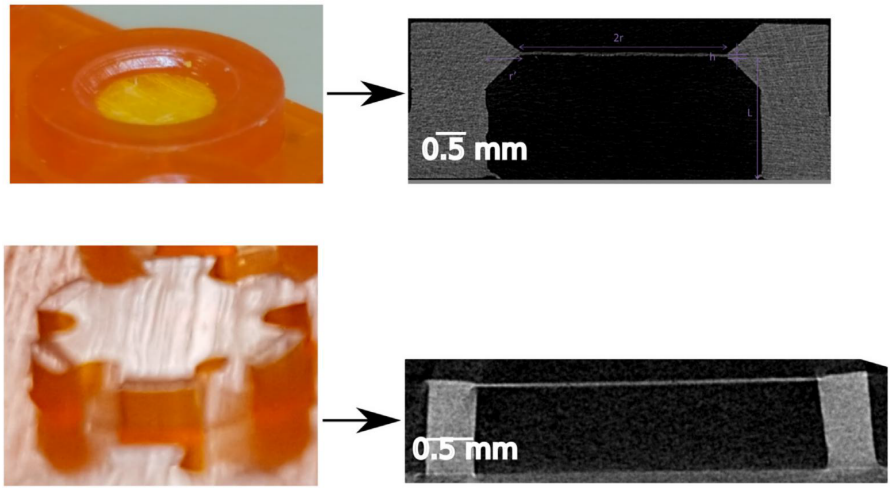

Fig. 4. Photos of two different diaphragm designs (with and without holes) printed as base PEGDA (0.1% S1). CT scans of the prints are also shown, which were used to confirm printed dimensions and evaluate any curvature of the diaphragm resulting from residual stress.

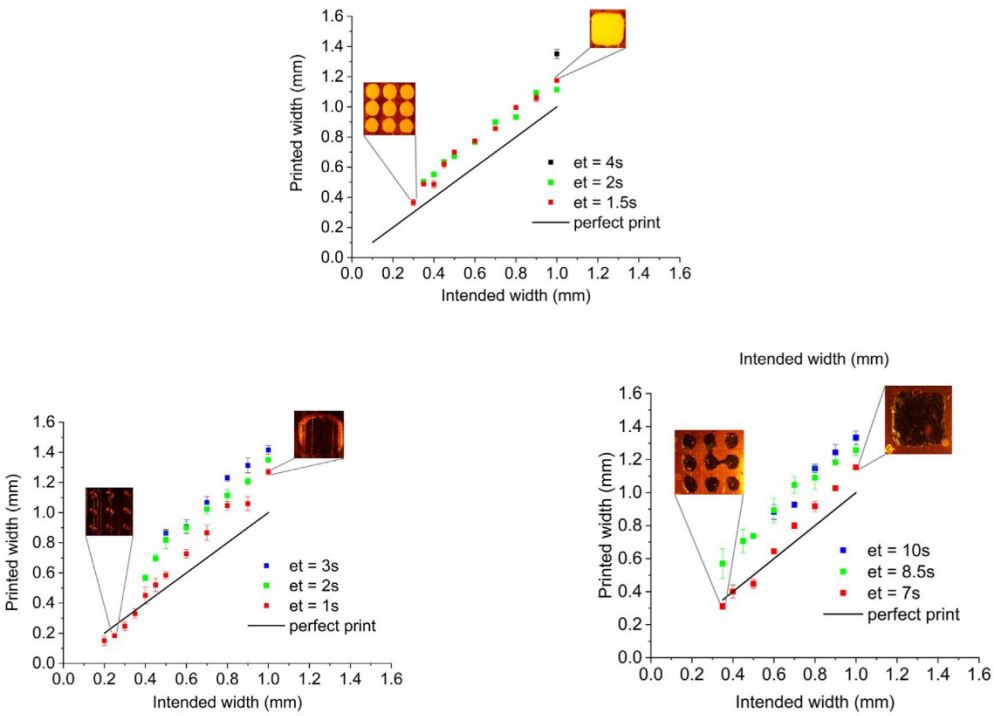

Fig. 5. X-Y print resolution for a square array of blocks with side lengths and separation of 0.2–1 mm. Results show printed width and intended width for a resin comprised of (top) 0.1% Sudan 1, 1% Irgacure 819 and PEGDA monomer for exposure times (et) of 1, 2 and 3 s (left) of 33% barium titanate, 0.1% Sudan 1, 1% Irgacure 819 and PEGDA monomer for exposure times (et) of 1.5, 2 and 4 s and (right) 1% multi-walled carbon nanotubes, 0.1% Sudan 1, 1% Irgacure 819 and PEGDA monomer for exposure times of 7, 8.5 and 10 s.

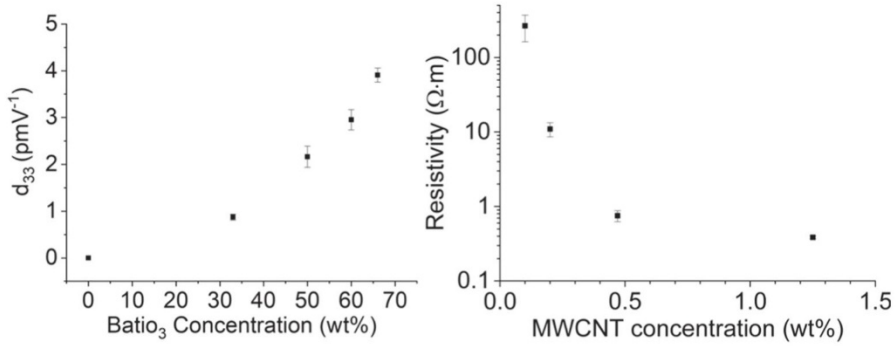

Fig. 6. Graphs of d_{33} (left) and resistivity (right) with increasing weight of barium titanate nanofillers and MWCNTs respectively.

Table 2
Calculated resonance frequencies for lumped parameter model compared with experimental results. Models used are for diaphragm compliance only, diaphragm compliance in parallel with adiabatic compliance of cavity and both diaphragm and adiabatic compliance with an additional radial stress of 1.6 MPa.

Model	Diaphragm diameter (mm)				
	1	1.5	2	3	3.5
Experiment	20.43 kHz	12.36 kHz	8.06 kHz	5.73 kHz	3.20 kHz
Diaphragm	15.48 kHz	6.88 kHz	3.87 kHz	1.72 kHz	1.26 kHz
+Back cavity	15.61 kHz	7.32 kHz	4.81 kHz	3.75 kHz	3.77 kHz
+Initial stress	19.55 kHz	11.05 kHz	7.87 kHz	5.67 kHz	4.42 kHz

The vibration behaviour of 3D printed membranes was modelled in COMSOL Multiphysics. Materials properties of the base PEGDA resin and PEGDA composites would be expected to vary significantly with the conditions during polymerization and display some anisotropy, which here have been reduced to a single bulk property via impedance analogy. Given the relatively high compliance of the diaphragms the acoustic compliance of the back cavity and the residual stress in the diaphragms would be expected to play a significant role. Results of calculations of resonance frequency from the diaphragm compliance only, diaphragm compliance with acoustic compliance of the cavity and diaphragm and acoustic compliance

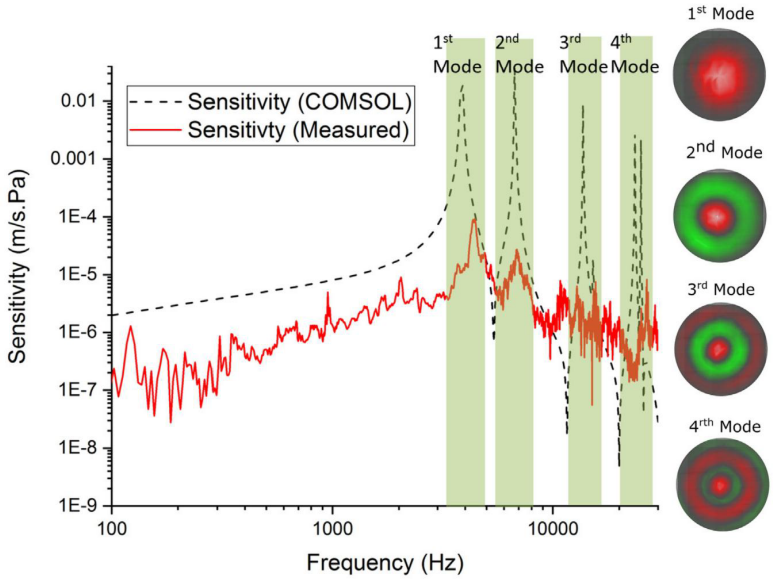

Fig. 7. Frequency response function for 3.5 mm PEGDA-barium titanate composite diaphragm and comparison with COMSOL simulation. The first 4 axisymmetric resonance modes are highlighted in green with a good fit found between simulation and measurement.

with an additional radial stress of 1.6 MPa are given in Table 2. All material property estimates are treated here as bulk properties and are obtained by curve-fitting calculated and simulated models to experimental results. For PEGDA-barium titanate composites the diaphragm compliance was much lower and calculations based purely on this gave a reasonable agreement with experimental results (Fig. 7).

The final integration of these components into a single build comprised the PEGDA resin base support structure and two conductive layers on either side of a PEGDA-barium titanate composite diaphragm. A 4 mm diaphragm was chosen as having suitable resonance characteristics for an acoustic microphone while maximizing the mechanical sensitivity of the device. Electrode placement for the conductive layers was restricted to the outer 200 μm of the diaphragm, where the expected strain would be concentrated. The full design and 3D printing work flow are shown in Fig. 3. The (0,0) mode resonance for this diaphragm was recorded at 22 kHz, with a maximum electrical output in response to a stimulating sound field of 80 dB SPL (ref 20 μPa) at 1 kHz of −87 dB (V/Pa) with a signal to noise ratio, before averaging, of less than 0 dB. A trace of the microphone and pre-amplifier output is given in Fig. 8, showing the electrical output of the device first in response to the electromagnetic bang of the speakers followed by the true signal after an acoustic delay.

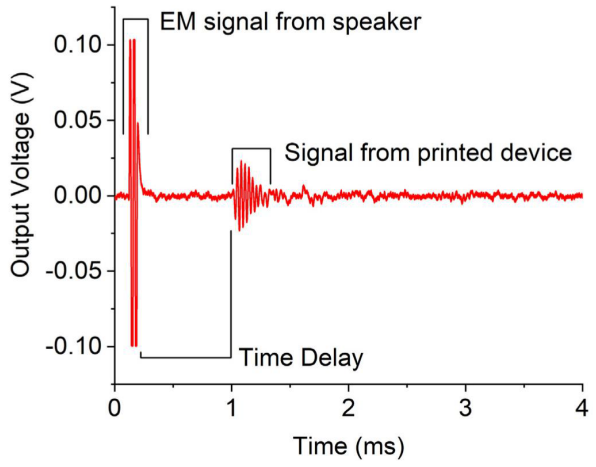

Fig. 8. Electrical output of the complete device and pre-amplifier to a tone-burst signal at 30 kHz (80 dB SPL, ref 20 μPa), with the electro-magnetic interference from the speaker coincident with the tone-burst signal and the measured electrical response being seen after a propagation delay of 0.78 ms.

4. Conclusions

This work demonstrates the creation via a digital light processing method of additive manufacturing of a complete, working piezoelectric microphone using a commercially available 3D printer. The process adopted here works within the limitations of a commercially available printer, necessitating manual changeovers of the printing vats in order to integrate multiple materials into a single build. A great scope for improving the manufacturing ease and timescales of the process exists if a more bespoke system is adopted, as demonstrated by Kowsari et al. [16]. for example, making material changes within a single layer practical however a far more fundamental limitation on the system has been the properties of the piezo-composite material. Measured values of d_{33} in the range of 2–3 pC/N place the composite's piezoelectric response in a similar range to that of sputtered aluminium nitride layers, and considerably poorer than that of PVDF at 20–30 pC/N, with a resulting poor signal to noise ratio. Higher piezoelectric coupling factors have been shown using smaller, or higher aspect ratio barium titanate nanoparticles [36,19] or the addition of surfactants or MWCNTs to the polymer matrix [37].

One of the more interesting, and complex, issues which has not been investigated here is the relationship between the polymerization process and post-curing and the anisotropy of material properties and stresses. For PEGDA resins the issues of polymer shrinkage are well known [10] and sometimes exploited to provide folding

structures [38], however printing a single layer membrane brings a unique set of modelling challenges. As the membrane's thickness is determined by the threshold of dose energy in the polymer, material at the base of the layer must necessarily be at the onset of solidification. The cross-link density in this region is therefore significantly changed from that of the bulk material, which for thin layers can have a noticeable impact on the stiffness and stress of the membrane. Both the issues of stress and enhancement of the piezo-composite are worthy of further work, with predictive models of polymerization threshold and light intensity such as those described by Gong et al. [14] having potential to be adapted for estimating tension in the diaphragm and improved patterning of piezoelectric composites to create a predictive model for fully integrated 3D printed functional and passive layers.

Data availability

The raw data required to reproduce these findings are available to download from doi.org/10.15129/f7d88ee2-14a9-42be-b3a8-54e7086f6e5e. The processed data required to reproduce these findings are available to download from doi.org/10.15129/f7d88ee2-14a9-42be-b3a8-54e7086f6e5e.

CRediT authorship contribution statement

Benjamin Tiller: Methodology, Investigation, Writing - original draft. **Andrew Reid:** Formal analysis, Investigation, Conceptualization, Writing - original draft, Writing - review & editing. **Botong Zhu:** Investigation, Methodology. **José Guerreiro:** Investigation, Methodology. **Roger Domingo-Roca:** Investigation, Resources. **Joseph Curt Jackson:** Supervision, Writing - review & editing. **J.F.C. Windmill:** Supervision, Funding acquisition, Conceptualization, Writing - review & editing.

Acknowledgments

This research was funded by the European Research Council under the European Union's Seventh Framework Programme (FP/2007–2013)/ERC Grant Agreement no. 615030, and received funding from the European Research Council under the European Union's Horizon 2020 research and innovation programme (grant agreement no. 812938), and the Engineering and Physical Sciences Research Council (EPSRC) under grant EP/L022125/1.

References

[1] A.R. Studart, Additive manufacturing of biologically-inspired materials, Chem. Soc. Rev. 45 (2016) 359–376.
[2] J. Gardan, Additive manufacturing technologies: state of the art and trends, Int. J. Prod. Res. 54 (2016) 3118–3132.
[3] H. Reimann, Signal processing in the cochlea: the structure equations, J. Math. Neurosci. (2011).
[4] A. Michelsen, A.V. Popov, B. Lewis, Physics of directional hearing in the cricket *Gryllus bimaculatus*, J. Comp. Physiol. A. (1994).
[5] J. Hyun, J.H. Kwak, D. Juhyung, S. Kwang, H. Seung, J. Hwan, S. Hur, K. Jae, Basilar membrane-inspired self-powered acoustic sensor enabled by highly sensitive multi tunable frequency band, Nano Energy 53 (2018) 198–205.
[6] R. Domingo-Roca, J.C. Jackson, J.F. Windmill, Bioinspired 3D-printed piezoelectric device for acoustic frequency separation, Proceedings of IEEE Sensors 2017-Decem, 2017, pp. 1–3.
[7] A.C. Mason, M.L. Oshinsky, R.R. Hoy, Hyperacute directional hearing in a microscale auditory system, Nature (2001).
[8] H. Liu, L. Currano, D. Gee, T. Helms, M. Yu, Understanding and mimicking the dual optimality of the fly ear, Sci. Rep. 3 (2013) 2489.
[9] R. Miles, Comparisons of the performance of commercially-available hearing aid microphones to that of the Binghamton Ormia-inspired gradient microphone, J. Acoust. Soc. Am. (2017).
[10] J. Zhang, P. Xiao, 3D printing of photopolymers, Polym. Chem. 9 (2018) 1530–1540.
[11] J.-y. Yoon, G.-w. Kim, Harnessing the bilinear nonlinearity of a 3D printed biomimetic diaphragm for acoustic sensor applications, Mech. Syst. Signal Process. 116 (2019) 710–724.
[12] A. Leblanc, A. Lavie, Three-dimensional-printed membrane-type acoustic metamaterial for low frequency sound attenuation, J. Acoust. Soc. Am. 141 (2017) EL538–EL542.
[13] R.I. Haque, E. Ogam, C. Loussert, P. Benaben, X. Boddaert, Fabrication of capacitive acoustic resonators combining 3D printing and 2D inkjet printing techniques, Sensors (Switzerland) 15 (2015) 26018–26038.
[14] H. Gong, B.P. Bickham, A.T. Woolley, G.P. Nordin, Custom 3D printer and resin for 18 μm × 20 μm microfluidic flow channels, Lab Chip 17 (2017) 2899–2909.
[15] J.R. Tumbleston, D. Shirvanyants, N. Ermoshkin, R. Janusziewicz, A.R. Johnson, D. Kelly, K. Chen, R. Pinschmidt, J.P. Rolland, A. Ermoshkin, E.T. Samulski, J.M. Desimone, Continuous liquid interface of 3D objects, Science 347 (2015) 1349–1352.
[16] K. Kowsari, S. Akbari, D. Wang, N.X. Fang, Q. Ge, High-efficiency high-resolution multimaterial fabrication for digital light processing-based three-dimensional printing, 3D Printing and Additive Manufacturing, 5, 2018, pp. 185–193.
[17] R.B. Wicker, E.W. MacDonald, Multi-material, multi-technology stereolithography, Virtual Phys. Prototyp. 7 (2012) 181–194.
[18] A.K. Miri, D. Nieto, L. Iglesias, H. Goodarzi Hosseinabadi, S. Maharjan, G.U. Ruiz-Esparza, P. Khoshakhlagh, A. Manbachi, M.R. Dokmeci, S. Chen, S.R. Shin, Y.S. Zhang, A. Khademhosseini, Microfluidics-enabled multimaterial maskless stereolithographic bioprinting, Adv. Mater. 30 (2018) 1–9.
[19] K. Kim, W. Zhu, X. Qu, C. Aaronson, W.R. McCall, S. Chen, D.J. Sirbuly, 3D optical printing of piezoelectric nanoparticle-polymer composite materials, ACS Nano 8 (2014) 9799–9806.
[20] Z. Chen, X. Song, L. Lei, X. Chen, C. Fei, C.T. Chiu, X. Qian, T. Ma, Y. Yang, K. Shung, Y. Chen, Q. Zhou, 3D printing of piezoelectric element for energy focusing and ultrasonic sensing, Nano Energy 27 (2016) 78–86.
[21] D.I. Woodward, C.P. Purssell, D.R. Billson, D.A. Hutchins, S.J. Leigh, Additively-manufactured piezoelectric devices, Phys. Status Solidi A 212 (2015) 2107–2113.
[22] X. Song, Z. Chen, L. Lei, K. Shung, Q. Zhou, Y. Chen, Piezoelectric component fabrication using projection-based stereolithography of barium titanate ceramic suspensions, Rapid Prototyp. J. 23 (2017) 44–53.
[23] H. Kim, J. Johnson, L.A. Chavez, C.A.G. Rosales, T.-L.B. Tseng, Y. Lin, Enhanced dielectric properties of three phase dielectric MWCNTs/BaTiO3/PVDF nanocomposites for energy storage using fused deposition modeling 3D printing, Ceram. Int. 44 (2018) 9037–9044.
[24] S. Guan, H. Li, S. Zhao, L. Guo, Novel three-component nanocomposites with high dielectric permittivity and low dielectric loss co-filled by carboxyl–functionalized multi-walled nanotube and BaTiO3, Compos. Sci. Technol. 158 (2018) 79–85.
[25] J.Y. Park, Y.Y. Kang, H.W. Yoon, N.K. Park, Y. Jo, S. Jeong, J.C. Won, Y.H. Kim, Viscoelastic properties of a 3D-printable high-dielectric paste with surface–modified $BaTiO_3$, Compos. Sci. Technol. 159 (2018) 225–231.
[26] S.J. Lee, W. Zhu, M. Nowicki, G. Lee, D.N. Heo, J. Kim, Y.Y. Zuo, L.G. Zhang, 3D printing nano conductive multi-walled carbon nanotube scaffolds for nerve regeneration, J. Neural Eng. 15 (2018).
[27] G. Gonzalez, A. Chiappone, I. Roppolo, E. Fantino, V. Bertana, F. Perrucci, L. Scaltrito, F. Pirri, M. Sangermano, Development of 3D printable formulations containing CNT with enhanced electrical properties, Polymer (United Kingdom) 109 (2017) 246–253.
[28] G. Taormina, C. Sciancalpore, M. Messori, F. Bondioli, Advanced resins for stereolithography: in situ generation of silver nanoparticles, AIP Conf. Proc. 1981 (2018).
[29] J. Odent, T.J. Wallin, W. Pan, K. Kruemplestaedter, R.F. Shepherd, E.P. Giannelis, Highly elastic, transparent, and conductive 3D-printed ionic composite hydrogels, Adv. Funct. Mater. 27 (2017) 1–10.
[30] Q. Mu, L. Wang, C.K. Dunn, X. Kuang, F. Duan, Z. Zhang, H.J. Qi, T. Wang, Digital light processing 3D printing of conductive complex structures, Addit. Manuf. 18 (2017) 74–83.
[31] H. Gong, M. Beauchamp, S. Perry, A.T. Woolley, G.P. Nordin, Optical approach to resin formulation for 3D printed microfluidics, RSC Adv. 5 (2015) 106621–106632.
[32] K. Yao, F.E.H. Tay, Measurement of longitudinal piezoelectric coefficient of thin films by a laser-scanning vibrometer, IEEE Trans. Ultrason. Ferroelectr. Freq. Control 50 (2003) 113–116.
[33] J. Hernando, J.L. Sánchez-Rojas, S. González-Castilla, E. Iborra, A. Ababneh, U. Schmid, Simulation and laser vibrometry characterization of piezoelectric AlN thin films, J. Appl. Phys. 104 (2008).
[34] M. Kleiner, Electroacoustics, CRC Press. 2013.
[35] J.Y. Chen, Y.C. Hsu, T. Mukherjee, G.K. Fedder, Modeling and simulation of a condenser microphone, TRANSDUCERS and EUROSENSORS '07 - 4th International Conference on Solid-State Sensors, Actuators and Microsystems, 146, 2007, pp. 1299–1302.
[36] W. Choi, K. Choi, G. Yang, J.C. Kim, C. Yu, Improving piezoelectric performance of lead-free polymer composites with high aspect ratio $BaTiO_3$ nanowires, Polym. Test. 53 (2016) 143–148.
[37] J. Yan, Y.G. Jeong, Roles of carbon nanotube and $BaTiO_3$ nanofiber in the electrical, dielectric and piezoelectric properties of flexible nanocomposite generators, Compos. Sci. Technol. 144 (2017) 1–10.
[38] Z. Zhao, J. Wu, X. Mu, H. Chen, H.J. Qi, D. Fang, Origami by frontal photopolymerization, Sci. Adv. 3 (2017) e1602326.

Additive Manufacturing (AM) Capacitive Acoustic and Ultrasonic Transducers Using a Commercial Direct Light Processing (DLP) Printer

B. Zhu, J. Guerreiro, *Member, IEEE*, Y. Zhang, B. Tiller and J. F. C. Windmill, *Senior Member, IEEE*

Abstract— **In recent years, there has been increasing interest in using additive manufacturing (3D printing) technology to fabricate sensors and actuators due to rapid prototyping, low-cost manufacturing processes, customized features and the ability to create complex geometries at micrometre scale. State of the art additive manufactured acoustic and ultrasonic transducers show limitations in miniaturization, repeatability (defects) and sensitivity. This new work encompasses the development of a capacitive acoustic and ultrasonic transducer, including its fabrication process using a commercial digital light processing printer and output signal characterization with a custom-made amplification circuit. A set of capacitive acoustic and ultrasonic transducers was fabricated and tested using different diaphragm diameters from $1.8-2.2\ mm$, for comparison, with central operating frequency between $19-54\ kHz$, respectively. This capacitive transducer design has a receiving sensitivity of up to $0.4\ mV/Pa$ at its resonant frequency, and a comparison with a commercial reference microphone is provided.**

Index Terms — **Additive Manufacture, AM, 3D printing, Transducer, Sensor, Direct Light Processing, DLP**

I. Introduction

Capacitive transducers for acoustic or ultrasonic measurement have been investigated for several decades. Currently, the performance of commercial capacitive transducers has reached a very high standard. However, most companies, for example, the well-known Danish company Brüel & Kjær (B&K), are still utilizing a traditional manufacturing technology and manually assembling these transducers from parts, resulting in low production volume and relatively higher cost [1]. Microelectromechanical systems (MEMS) is a more recent manufacturing technology that has commercially grown rapidly during the last two decades and is used in a variety of applications, e.g. mobile devices and wearable devices. MEMS microphones can achieve reasonable sensitivity at low bias voltages due to their narrow air-gaps [2]. Many researchers have proposed several transducer or microphone designs with complex 3D structures in order to explore different ways to enhance their performance such as sensitivity [3] [4], bandwidth [5], [6] and directivity [7]. In recent years, there has also been increasing interest in using additive manufacturing (AM) technology (also known as 3D printing) in the fabrication of sensors or actuators owing to the possibility to create complex 3D geometries at micrometre-scale using highly flexible polymers. After integrating multiple nano-fillers with the passive base polymer, an AM nano-composite can exhibit different properties including conductivity [8] or piezoelectricity [9]–[11], which allow the transduction of mechanical energy into electrical form. There are many reports of actuators [12], [13] and sensors [10], [14]–[17] fabricated using AM processes, however, various limitations in miniaturization [16], repeatability (defects) [16] and low sensitivity [10], [17] are also reported.

This paper demonstrates a methodology for using a commercial digital light processing (DLP) printer to fabricate capacitive transducers which integrate a custom-made passive polymer with a custom-made conductive polymer. The transducer is small enough to be integrated with surface-mount electronics, and it is tested against a gold-standard reference B&K microphone, showing comparable electro-acoustic sensitivity and following a predictable fabrication process. Nevertheless, the structure layout presented in this paper is a conventional capacitive transducer with a simple structure as shown in Figure 1. Additionally, this AM framework has the potential to benefit the fabrication of acoustic and ultrasonic diaphragm transducers with more complex geometries such as the ones used in biologically inspired transducer designs [7], [10], [18].

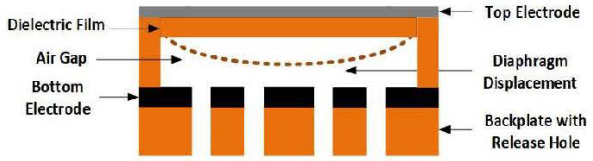

Figure 1. Simplified schematic of a conventional capacitive transducer.

This paragraph of the first footnote will contain the date on which you submitted your paper for review. It will also contain support information, including sponsor and financial support acknowledgment. For example, "This work was supported in part by the U.S. Department of Commerce under Grant BS123456."

B. Zhu, J.Guerreiro, Y Zhang, B. Tiller and J.F.C. Windmill are members of the Centre for Ultrasonic Engineering, Electronic and Electrical Engineering Department, University of Strathclyde, Glasgow, Scotland, UK, G1 1XW (e-mail: {botong.zhu, jose guerreiro, yansheng.zhang.101, benjamin.tiller, james.windmill} @strath.ac.uk).

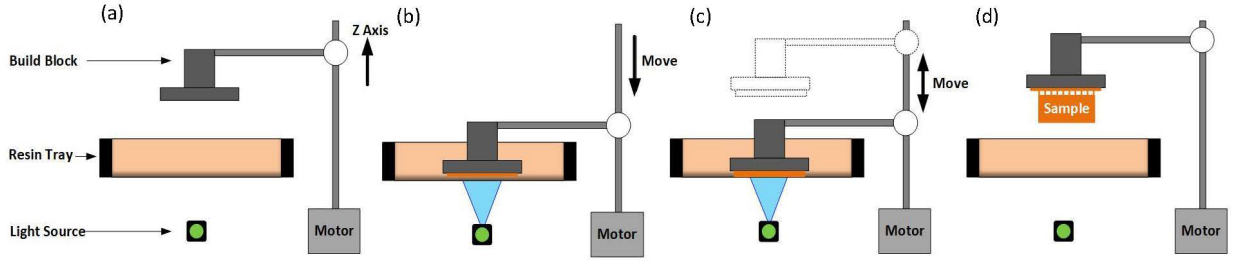

Figure 2. The workflow of the DLP printer: (a) Starting point of the 3D printing progress and main components inside the DLP printer. (b) The building block moves down and submerges into the resin tray to print the first layer. (c) The build block moves up and down to create the object layer by layer. (d) Finish printing.

II. Theoretical Background

A. Direct Light Processing (DLP) Printer

DLP is a type of stereolithography AM technology using a liquid photopolymer resin that cures (polymerizes) under an ultraviolet light source. Figure 2 shows a schematic of the DLP 3D printing process. Once the 3D printing design slices are uploaded to the printer, the light source (DLP projector) projects the first slice image to a vat of liquid resin. Figure 2 (a) shows the starting point of the 3D printing process. The build block moves down and submerges into the resin tray as shown in Figure 2 (b). The exposed resin hardens on the surface of the build block to create the first layer. The block then moves up and down to print the rest of the structure layer by layer as shown in Figure 2 (c). The process is repeated until the 3D structure is completed as shown in Figure 2 (d). Then the sample is moved up from the build tray, cleaned of any extra resin, support structures are removed, and the final finished structure is ready for characterisation.

B. Resin Optical Absorption

The absorption property of the material and the related light penetration can be explained by Beer's law as shown in (1) [19], where $I(z)$ is the intensity of the light in units of W/cm^{-2}, z is the depth of the penetration in the resin with $z \geq 0$ (as shown in Figure 2 (a)). Hua *et al.* [19] proposed a mathematical model assuming the light incident from a source when the depth $z < 0$ is propagating along the $+z$ direction. I_0 is the initial light intensity on the boundary between the resin and tray (when $z = 0$). α is the absorbance of the resin with units of μm^{-1}.

$$I(z) = I_0 e^{-\alpha z} \tag{1}$$

The total dose of light $D(z,t)$ [19], in units of J/cm^{-2} can be expressed by (2), where the t is the exposure time.

$$D(z,t) = tI(z) = tI_0 e^{-\alpha z} \tag{2}$$

Current commercial stereolithography printers and their materials work better at millimetre scale ($> 1\,mm$) down towards sub-millimeter scale [20], and therefore are unlikely to meet the required resolution for the fabrication of micro-scale devices. Hua Gong *et.al* [19], [20] proposed an improved 3D printing resin formula by adding different absorbers (dyes) into the ultraviolet (UV) curable resin in order to increase absorbance (α) in equation (1) and (2). This improved formula increases the resolution to $\sim 100\ \mu m$ using a commercial DLP printer [19] and $\sim 20\ \mu m$ using a custom-built DLP-SLA printer [20]. The penetration depth and exposure time need to be adjusted by adding different amounts of absorbers. In this project, the absorber was SUDAN 1 and the optimized concentration was 0.5% by weight (wt. %).

C. Polymer/Multiwall Carbon Nanotubes (MWCNTs) Composite

Carbon nanotubes (CNTs) have emerged in recent years as one of the most promising nanofillers to enhance the mechanical properties (Young's modulus) [21], [22] and conductivity of polymers [23]–[25]. CNTs are long cylinders of covalently bonded carbon atoms only a few nanometers in diameter, but with lengths ca. tens of microns [24]. CNT/polymer composite based sensors have been studied for some time, but with limitations in terms of repeatability, sensitivity and stability [8]. However, those disadvantages could be improved through the use of AM technology. Researchers also indicate that beyond a certain weight fraction, which is known as the percolation threshold, of CNTs, there is a sharp rise in conductivity due to the formation of electrically conductive pathways inside the CNT/polymer composite [26]. The percolation threshold of multiwall (MW) CNTs was found to be hugely different when it is embedded in different polymer matrixes [26]. Polyethylene glycol diacrylate (PEGDA) is one of the conventional materials in stereolithography AM technology because of its UV curing properties. The conductivity of MWCNT/ PEGDA composite with the MWCNT concentration varied from 0.1% to 1.25% was previously studied [17], where it was concluded that there is a massive increase in the conductivity when the concentration increases from 0.1% to 0.5%, but this growth is dramatically slowed down when the concentration is greater than 0.5%. Also, several experimental trials indicate that the printability (resolution) becomes poorer when the CNT concentration is higher than 1.0% due to UV light scattering by the CNTs. Further, the composite layer must be at least $50\ \mu m$ thick to be conductive. Moreover, the composite resin becomes difficult to polymerize when the concentration is higher than 2%. Therefore, 0.5% (wt. %) is the optimized concentration chosen for this study.

III. Material, Design and Fabrication

A. Material preparation

A stereolithography base resin usually includes at least two elements [19]: a monomer material and a photoinitiator. If some additional functionality (e.g. conductivity, flexibility, higher resolution, or piezoelectricity) is required, then nano-fillers can be added into the base resins. Two different functional stereolithography resins were synthesized in this project by using PEGDA (MW250), phenylbis (2,4,6-trimethylbenzoyl) phosphine oxide (Irgacure 819), SUDAN 1 (S1) and MWCNT (NC7000, average diameter 9.5 nm, average length 1.5 μm). PEGDA, Irgacure 819 and S1 were purchased from Sigma-Aldrich (St. Louis, MO) and the MWCNT was from Nanocyl (Sambreville, Belgium).

The first type of functional stereolithography resin used – the S1/PEGDA resin – was synthesized with PEGDA (98.5%, wt. %), Irgacure 819 (1%, wt. %), and S1 (0.5%, wt. %). The resin was then mixed in a Thinky ARE 250 planetary mixer (Intertronics) and sonicated for at least 30 minutes before use.

The second type of functional stereolithography resin – the MWCNT/PEGDA resin – was synthesized with PEGDA (98.5%, wt. %), Irgacure 819 (1%, wt. %) and MWCNT (0.5%, wt. %). The weighing and initial mixing process were carried out using vacuum glove bags in order to minimize any potential hazard from MWCNTs release. The mixture was then stirred for at least 24h with a magnetic stirrer before use.

B. Transducer Design

A conventional capacitive transducer consists of a dielectric thin film with one side metalized, a rigid conductive backplate and an air gap between the dielectric film and the bottom electrode (as shown in Figure 1). The resonant frequency of the capacitive transducer is mainly affected by the shape, thickness, size and the intrinsic stress of the thin film. Generally, the intrinsic stress is generated from the fabrication progress. When the transducer has an edge-clamped film with low intrinsic stress the influence from the intrinsic stress is ignored, and the resonant frequency of the thin circular plate (f_{tp}) can be expressed by (3) & (4) [27], where K_n is a constant that takes the value 10.22 for a clamped circular thin film in the fundamental resonance mode, R is the radius of the thin plate, D_E is the flexural rigidity of the circular thin plate, h is the thickness of the thin film, ρ is the density of the thin plate, E is the Young's modulus and μ is the Poisson ratio. When the intrinsic stress is large enough, the resonant frequency of the thin plate (f_{tp}) is dominated by the intrinsic stress (T) rather than by the flexural rigidity (as shown in (5)). The squeeze film effect occurs when the air gap (depth of cavity) is very narrow [28]. Squeeze film damping becomes more important than the drag force damping of air if the thickness of the gas gap is smaller than one-third of the thickness of the plate [28]. Even so, the air gap in a design should be thin enough to maximize sensitivity. Limited by the printing resolution of this project, the air gap of the transducer presented here is slightly thicker than the thin film. Therefore, the squeeze film effect is not significant in this transducer design. However, the design does include some releasing holes to minimize squeeze film damping.

$$f_{tp} = \frac{K_n}{2\pi R^2}\sqrt{\frac{D_E}{\rho h}} \tag{3}$$

$$D_E = \frac{Eh^3}{12(1-\mu^2)} \tag{4}$$

$$f_{tp} = \frac{K_n}{2\pi R^2}\sqrt{\frac{T}{\rho h}} \tag{5}$$

The computer designed 3D model was produced as shown in Figure 3(a). The anchor and the backplate (orange parts) are made by a passive polymer which is synthesized with PEGDA and Sudan 1, the black layer between air-gap and the backplate is the PEGDA/MWCNT composite polymer. The top silver round layer is an aluminate electrode. The transducer design used three diameters, chosen to be 1.8 mm, 2.1 mm and 3.2 mm, in order to place resonant frequencies at 19 kHz, 35 kHz and 54 kHz respectively. After testing the accuracy of fabrication, the height of the air gap was determined to be ~120 μm and the thickness of the dielectric film was ~80 μm. The thickness of the top aluminum electrode was 0.11 μm deposited by using a thin film deposition system (E306, Edwards). The thickness of the bottom MWCNT electrode is ~50 μm. Simulating the resonant frequency of the capacitive transducer requires knowledge of the mechanical properties of the S1/PEGDA composite. This depends on any variations in the exposure time and the concentration of the absorber during the AM. The estimated mechanical properties utilized in this work (Young's Modules $E = 1\ GPa$, Poisson Ratio $v = 0.32$ and Density $\rho = 1183\ kg/m^3$) are based on a previous study [17]. Figure 3 (b) shows the cross-sectional X-ray computerized tomography (CT) scan of the transducer. The aluminum electrode cannot be replaced by a 3D printed MWCNT/PEGDA layer since the limitations of the AM resolution and the conductivity in this study mean that such a layer would be too thick to vibrate with incident acoustic energy.

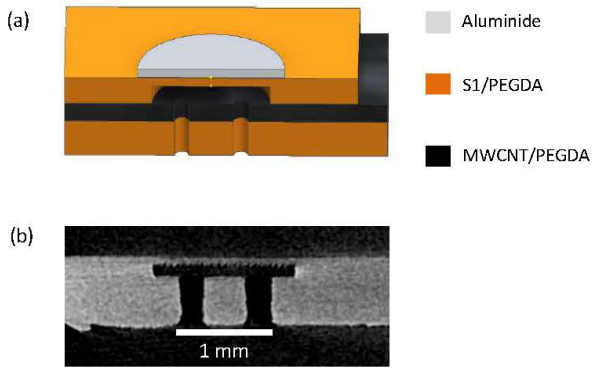

Figure 3. The cross-sectional view of an AM capacitive acoustic transducer: (a) 3D computer model and (b) X-ray CT scan.

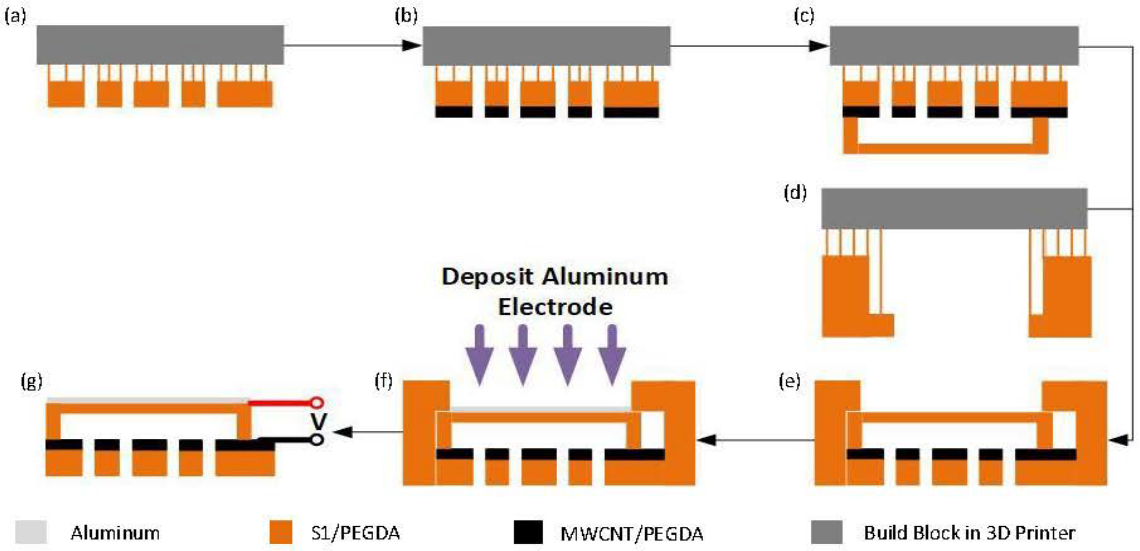

Figure 4. The fabrication flow for the capacitive transducer: (a) Print S1/PEGDA backplate with releasing holes. (b) Print MWCNT/PEGDA conductive layer with releasing holes as the bottom electrode. (c) Print S1/PEGDA air gap and dielectric thin film. (d) Print S1/PEGDA mask for top electrode coating. (e) Flip the transducer and mount the mask. (f) Deposit aluminium electrode on the top of the film as the top electrode. (g) Connect wires to the electrodes.

C. *Fabrication*

An ASIGA stereolithography printer (PICO 2 HD 27 μm) was utilized to fabricate the capacitive transducer. This printer has a 27 μm pixel size in the X-Y plane and 1 μm available resolution in the Z axis. The wavelength of the UV light source is 385 nm. A build layer of 10 μm and exposure time of 3.6 s allow an optimized resolution for the material formula introduced above. Figure 4 shows the workflow for the transducer's fabrication process. First of all, the S1/PEGDA backplate with support is printed on the building block. Then, any extra unpolymerized resin is cleaned away with Ethanol, and the system is manually swapped to a MWCNT/PEGDA resin tray to print the conductive bottom electrode layer. After that, the sample is cleaned again and the system is swapped to the S1/PEGDA build tray to print the air gap and dielectric thin film. The top electrode is final deposited. A mask is printed after the transducer sample is removed from the build tray. The mask is mounted on the flipped transducer, and then the sample is placed into the thin film deposition system where the aluminum electrode is deposited on the top of the dielectric thin film. Finally, the mask is removed and wires connected to the device's top and bottom electrodes.

IV. Results

Figure 5(a) & (b) show the experimental setup for characterizing the transducer in sensing and transmitting modes, respectively. In Figure 5 (a), a function generator produced a 7 cycles tone-burst to drive a loudspeaker. The transducer was placed 20 cm away from the loudspeaker to avoid any near-field effects. A voltage supply provided different DC voltages from $0-150\ V$ to bias the transducer. The electrical output signal generated by the transducer was

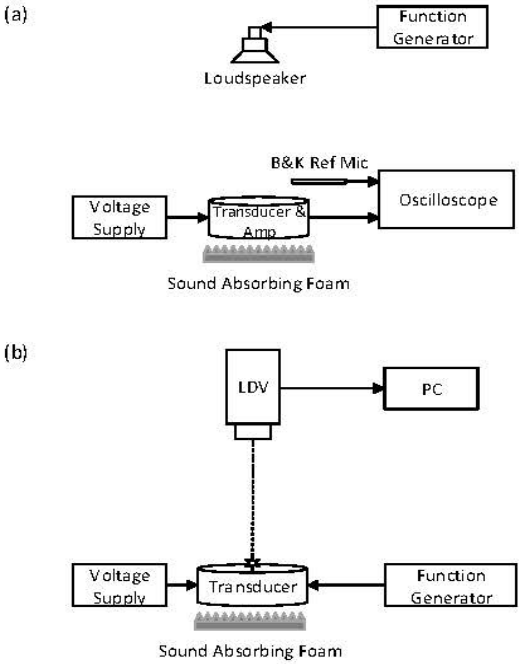

Figure 5. Simplified schematic of the experimental setup for the (a) sensing and (b) transmitting measurements.

amplified by a custom-built electronic circuit and finally acquired using an oscilloscope. A 1/8 inch reference microphone (Brüel and Kjær, Type 4138) with an operational frequency range from 1 Hz to 110 kHz and a paired charge

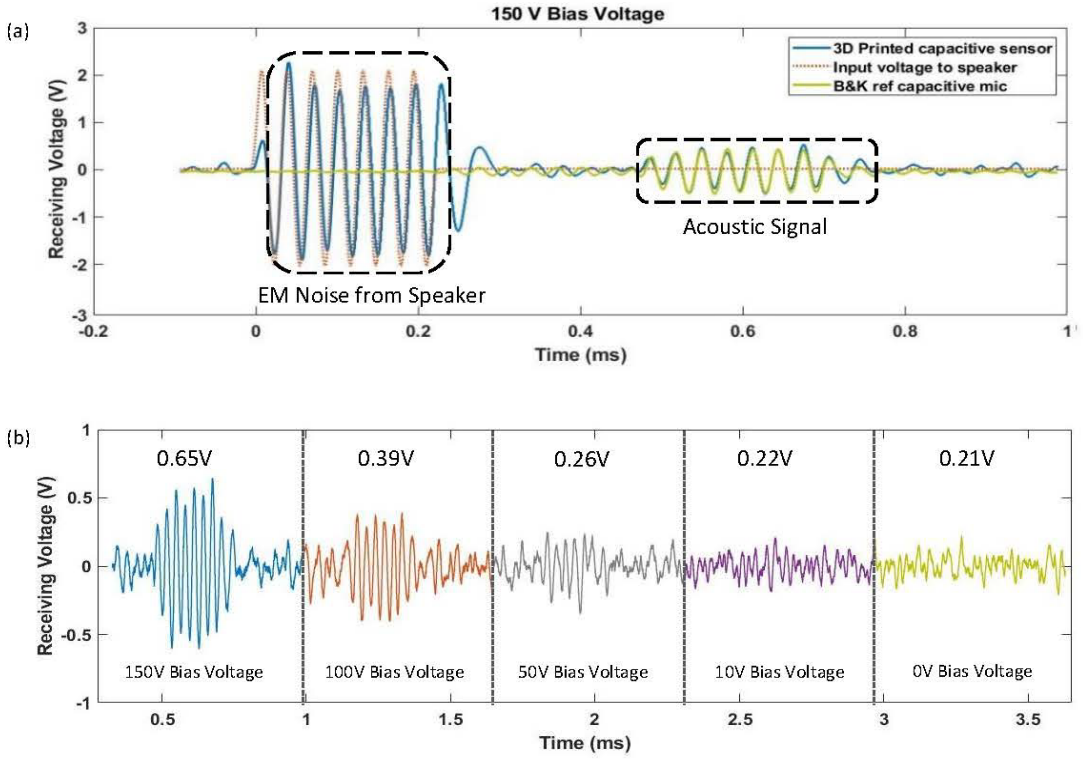

Figure 6. The electrical output time domain signal from the transducer (diameter=2.1mm) integrated with the amplification circuit when the loudspeaker played a 7 cycles tone-burst at 35 kHz. (a) Shows the electrode magnetic and acoustic signal received by both of the 3D printed transducer and the B&K reference microphone under 150 V bias voltage. (b) Shows the maximum amplitude change of the acoustic signal when providing different bias voltages from 150-0 V.

amplifier (Brüel and Kjær, type 2692) were used to measure the reference sound pressure around the transducer. The reference signal was then utilized to calibrate the sensitivity of our transducers. Sound absorbing foam was placed under the transducer and the B&K microphone to avoid acoustic reflections. In Figure 5 (b), the function generator inputted a 10 V chirp signal to drive the transducer into vibration which was detected by a 3D Laser Doppler Vibrometer (LDV: MSA100-3D, Polytec, Inc., Waldbronn, Germany). A voltage supply was used to charge the capacitive transducer with varied DC voltage from $0-150\ V$.

Table 1. The receiving sensitivity and the static capacitance of the AM transducers with different film diameter measured with 150 V bias voltage at each resonant frequencies

Diameter	**1.8 mm**	**2.1 mm**	**3.2 mm**
Frequency	54 kHz	35 kHz	19 kHz
Capacitance	2.08 pF	3.74 pF	4.62 pF
Sensitivity	0.009 mV/Pa	0.013 mV/Pa	0.4 mV/Pa

Table 1 gives the value of capacitance and receiving sensitivity with respect to different membrane diameters. The static capacitance of the transducer was measured by using a 4194A Impedance/Gain-Phase Analyzer under a 150 V bias voltage. It is found that the capacitance of the transducer is proportional to its size. The receiving sensitivity (S) of the transducers was calculated by (6) with the unit mV/Pa where the Output (O) is the maximum amplitude of the amplified signal at the resonant frequency of the transducer, the Acoustic Pressure (AP) is the sound pressure level around the transducer measured by the reference B&K microphone and the Amplifier Gain (AG) is the gain of our custom-built amplifier.

$$S\ (mV/Pa) = \frac{O\ (mV)}{AP\ (Pa) \times AG} \tag{6}$$

The receiving sensitivity of the AM capacitive transducer can reach up to 0.4 mV/Pa before amplification (as shown in Figure 6), however, the receiving sensitivity rapidly decreases to 0.009 mV/Pa when the diameter of the transducers decreases. The reason for this is that the smaller active area results in lower sensing energy and smaller capacitance change [29]. Figure 6 (a) also shows that the sensitivity of the acoustic signal of the AM transducer operating at its resonant frequency can be compared to that of B&K microphone, nevertheless, this AM transducer set-up has less immunity to electromagnetic interference due to the absence of any shielding or proper packaging design. Similar to other capacitive transducers (as shown in Figure 6 (b)), this AM capacitive transducer requires a bias voltage to operate, and its sensitivity increases proportionally when providing higher bias voltages. The transmitting mode of the AM transducer was characterized by measuring the vibration of the thin film as shown in Figure 5 (b) as the transmitted sound field was too weak to be measured by the reference microphone. Figure 7(a) shows the frequency

response of the transducer with $2.1\ mm$ diameter. The output signal increases in amplitude when providing a larger bias voltage. Figure 7 (b) shows that the resonant frequency of the transducer with different diameters ($1.8\ mm$, $2.1\ mm$ and $3.2\ mm$) was characterized at $54\ kHz$, $35\ kHz$ and $19\ kHz$ respectively which can be matched with the simulated resonant frequency curve. The simulation method assumes the intrinsic stress is low and the mechanical properties used in both methods are given in the transducer design section. Figure 8(a) shows the AM transducer integrated with a custom-built amplifying circuit. The circuit board is $3\ cm \times 4\ cm$, and the silver part is the active area of the transducer. A hybrid JFET operational amplifier circuit was built in order to amplify the signals captured by the 3D printed sensor, as illustrated in Figure 8 (b) [30]. This circuit was designed with a constant gain of 50 dB between 1 - 100 kHz.

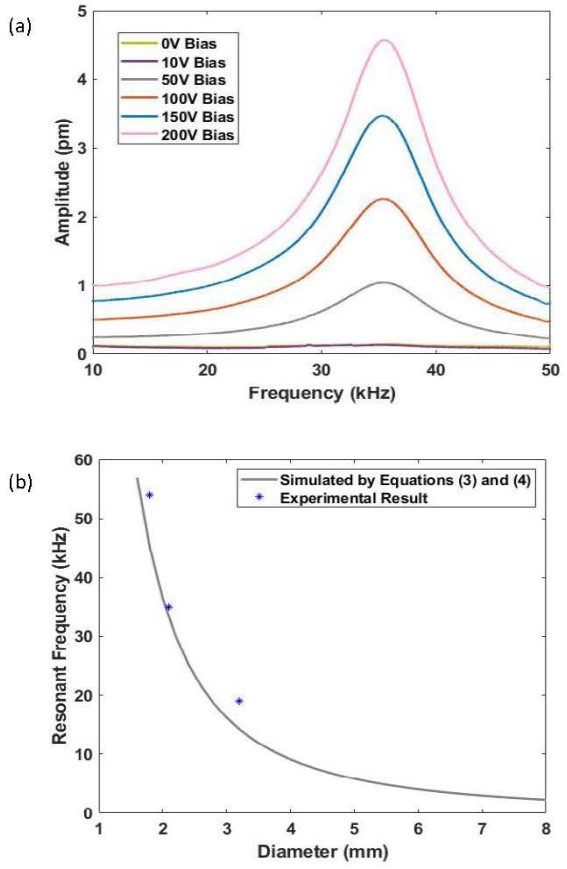

Figure 7. (a) The frequency response of the transducer (diameter=2.1 mm) was measured by LDV when the transducer was driven by 10 V chirp signal and different bias voltages. (b) The comparison between the simulated and experimental resonant frequency. The simulation assumes that the intrinsic stress is low.

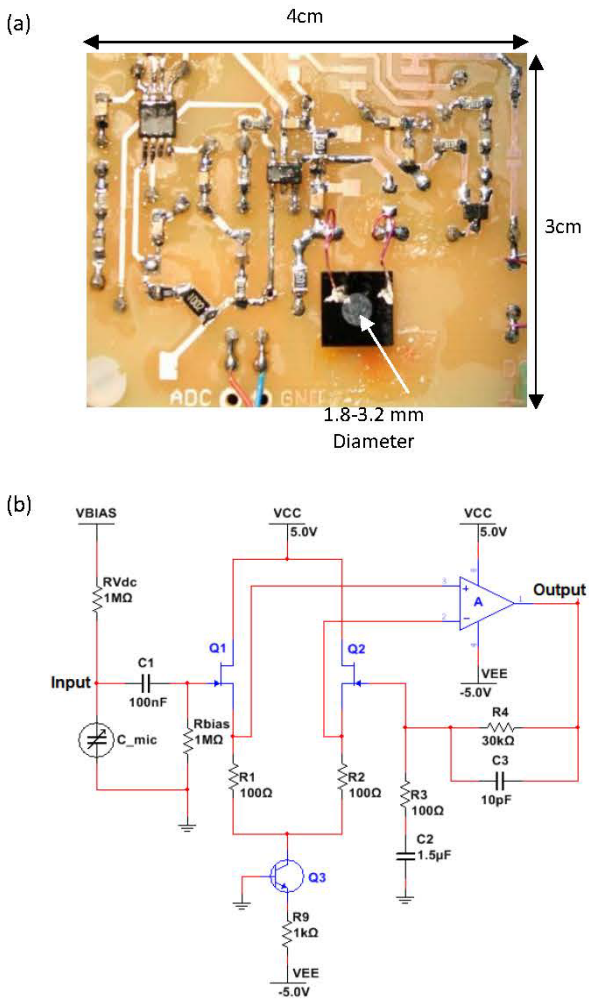

Figure 8. (a) Custom-built amplifying circuit integrated with the AM transducer. The size of the circuit board is $3\ cm \times 4\ cm$, and the silver part with different diameters ($1.8 - 3.2\ mm$) is the active area of the transducer. (b) Schematic of amplifying circuit. The custom-built amplifier provides a constant gain of approximately $50\ dB$ with operational bandwidth ($-3\ dB$ bandwidth) of $1 - 100\ kHz$

V. Conclusion

This paper demonstrates the first micron-scale capacitive transducer fabricated with a commercial DLP 3D printer. Transducers with different size have been fabricated and integrated with electronics to characterize the overall performance. The characterization results indicate that the performance of the AM transducer in sensing mode can reach up to $0.4\ mV/Pa$ at its resonant frequency. In contrast, the receiving open circuit sensitivity of a circular-clamped MEMS microphone and the commercial B&K microphone (Type 4138) with similar size are reported to be $\sim 1\ mV/Pa$ at a bias voltage of $1\ V$ [4] and $1\ mV/Pa$ at a bias voltage of $200\ V$ [31], respectively. The collapse voltage of conventional MEMS microphones is usually lower than $5\ V$ due to their narrow air gaps ($\sim 2\ \mu m$) [2]. The required bias voltage of the AM transducers is $150\ V$, which is much higher than the

conventional MEMS microphone ($< 5\,V$) but lower than the B&K commercial microphone ($200\,V$). Different diameters of transducer were fabricated and tested in this research study. The resonant frequency of the transducers decreases from $52\,kHz$ to $19\,kHz$ and the received sensitivity increases from $0.009\,mV/Pa$ to $0.4\,mV/Pa$, respectively, when the diameter of the transducers increases from $1.8\,mm$ to $3.2\,mm$. The current AM transducers have better performance in sensing rather than transmitting due to their low transmitting sensitivity. Because of the limitations of the commercial AM printer used, the fabrication process still requires human interaction, for example, manually swapping the resin tray, post processing the AM samples and evaporation coating the top electrode. The AM fabricating process will not take longer than two hours and the speed of coating process depends on the technique. The yield rate of the AM transducer is lower than 30% when the diameter is smaller than $1.8\,mm$. The AM transducers remained functional for several months before the manuscript was submitted.

Due to the advantages of using the AM technology to create complex 3D geometry, there are possible applications for the AM transducers including integration with hearing prostheses, bio-inspired transducers with complex 3D structures, underwater sonar, and non-destructive testing (NDT). The maximum operating frequency achieved by these purpose-built AM transducers is limited by the printing resolution of the printer. However, recent developments in two-photon polymerization (TPP) can achieve a resolution below $200\,nm$ [32] which could provide for a reduction in the transducer size and thus lead to operation in higher frequency ranges. Nevertheless, the performance of the transducer might be further improved by decreasing the air gap, and also by increasing the conductivity of the MWCNT/PEGDA composite as a result of optimizing the formula and exposure time. Further to this, recent work has demonstrated AM fabrication with multiple materials automatically by using a custom-build 3D printer [33]. The fabrication process of AM capacitive transducers could therefore become far more automatic in the future.

ACKNOWLEDGMENT

This work was supported by the EPSRC under grants EP/L022125/1 and EP/M026701/1, and by the European Research Council under the European Union's Seventh Framework Programme (FP/2007-2013)/ERC Grant Agreement n. [615030].

REFERENCES

[1] P. R. Scheeper *et al.*, "A New Measurement Microphone Based on MEMS Technology," vol. 12, no. 6, pp. 880–891, 2003.

[2] P. R. Scheepera, A. G. . Van der Donk, W. Olthuis, and P. Bergveld, "A review of silicon microphones," *Sensors Actuators A*, vol. 44, pp. 1–11, 1994.

[3] J. Liu, D. T. Martin, T. Nishida, L. N. Cattafesta, M. Sheplak, and B. P. Mann, "Harmonic balance nonlinear identification of a capacitive dual-backplate MEMS microphone," *J. Microelectromechanical Syst.*, vol. 17, no. 3, pp. 698–708, 2008.

[4] M. Füldner, A. Dehé, and R. Lerch, "Analytical analysis and finite element simulation of advanced membranes for silicon microphones," *IEEE Sens. J.*, vol. 5, no. 5, pp. 857–862, 2005.

[5] P. Mattila, F. Tsuzuki, and V. Heli, "Electroacoustic Model for Electrostatic Ultrasonic Transducers with V-Grooved Backplates," vol. 42, no. 1, pp. 1–7, 1995.

[6] B. Zhu, B. Tiller, A. J. Walker, A. J. Mulholland, and J. F. C. Windmill, "'Pipe Organ' Inspired Air-coupled Ultrasonic Transducers with Broader Bandwidth," *IEEE Trans. Ultrason. Ferroelectr. Freq. Control*, pp. 1–10, 2018.

[7] R. N. Miles and R. R. Hoy, "The development of a biologically-inspired directional microphone for hearing aids," *Audiol. Neurotol.*, vol. 11, no. 2, pp. 86–94, 2005.

[8] M. O. F. Emon and J. W. Choi, "Flexible piezoresistive sensors embedded in 3D printed tires," *Sensors (Switzerland)*, vol. 17, no. 3, p. 656, 2017.

[9] K. Kim, W. Zhu, X. Qu, C. Aaronson, and W. R. Mccall, "3D Optical Printing of Piezoelectric Materials," no. 10, pp. 9799–9806, 2014.

[10] R. Domingo-Roca, J. C. Jackson, and J. F. C. Windmill, "Bioinspired 3D-printed piezoelectric device for acoustic frequency separation," *Sensors Actuators A Phys.*, vol. 271, pp. 1–8, 2018.

[11] J. H. Jung *et al.*, "Lead-Free NaNbO3 Nanowires for a High Output Piezoelectric," *ACS Nano*, vol. 5, no. 12, pp. 10041–10046, 2011.

[12] A. Zolfagharian, A. Z. Kouzani, S. Y. Khoo, A. A. A. Moghadam, I. Gibson, and A. Kaynak, "Evolution of 3D printed soft actuators," *Sensors Actuators, A Phys.*, vol. 250, pp. 258–272, 2016.

[13] A. Miriyev, K. Stack, and H. Lipson, "Soft material for soft actuators," *Nat. Commun.*, pp. 1–8.

[14] C. Liu *et al.*, "3D Printing Technologies for Flexible Tactile Sensors toward Wearable Electronics and Electronic Skin," pp. 1–31, 2018.

[15] M. S. Mannoor *et al.*, "3D Printed Bionic Ears," *NANO Lett*, no. 13, pp. 2634–2639, 2013.

[16] R. Haque, E. Ogam, P. Benaben, and X. Boddaert, "Inkjet-Printed Membrane for a Capacitive Acoustic Sensor: Development and Characterization Using Laser Vibrometer," *Sensors*, vol. 17, no. 5, p. 1056, 2017.

[17] B. Tiller *et al.*, "Piezoelectric microphone via a digital light processing 3D printing process," *Mater. Des.*, vol. 165, pp. 1–27, 2019.

[18] Y. Zhang, J. F. C. Windmill, and D. Uttamchandani, "Biomimetic MEMS directional microphone structures for multi-band operation," *IEEE SENSORS 2014 Proc.*, pp. 440–443, 2014.

[19] H. Gong, M. Beauchamp, S. Perry, T. Woolley, and G. P. Nordin, "Optical approach to resin formulation for 3D printed microfluidic," *RSC Adv.*, vol. 11, no. 5, pp. 106621–106632, 2015.

[20] H. Gong, B. P. Bickham, A. T. Woolley, and G. P. Nordin, "Custom 3D printer and resin for 18 μm × 20 μm microfluidic flow channels," vol. 17, no. 17, 2017.

[21] D. Qian, E. C. Dickey, R. Andrews, and T. Rantell,

"Load transfer and deformation mechanisms in carbon nanotube-polystyrene composites," *Appl. Phys. Lett.*, vol. 76, no. 20, pp. 2868–2870, 2000.
[22] M. J. Biercuk, M. C. Llaguno, M. Radosavljevic, J. K. Hyun, A. T. Johnson, and J. E. Fischer, "Carbon nanotube composites for thermal management," *Appl. Phys. Lett.*, vol. 80, no. 15, pp. 2767–2769, 2002.
[23] H. Ishikawa, S. Fudetani, and M. Hirohashi, "Mechanical properties of thin films measured by nanoindenters," *Appl. Surf. Sci.*, vol. 178, pp. 56–62, 2001.
[24] V. Choudhary and A. Gupta, "Polymer/Carbon Nanotube Nanocomposites," in *Carbon Nanotubes - Polymer Nanocomposites*, 2011, pp. 66–90.
[25] B. Kracke and B. Damaschke, "Measurement of nanohardness and nanoelasticity of thin gold films with scanning force microscope," *Appl. Phys. Lett.*, vol. 77, no. 3, pp. 361–363, 2000.
[26] W. Bauhofer, J. Z. Kovacs, T. Swan, T. Swan, and T. Swan, "A review and analysis of electrical percolation in carbon nanotube polymer composites," *Compos. Sci. Technol.*, vol. 69, no. 10, pp. 1486–1498, 2009.
[27] W. C. Young and R. G. Budynas, *Roark's Formulas for Stress and Strain*. 2017.
[28] M. Bao and H. Yang, "Squeeze film air damping in MEMS," *Sensors Actuators, A Phys.*, vol. 136, no. 1, pp. 3–27, 2007.
[29] A. Dehé, M. Wurzer, M. Füldner, U. Krumbein, and I. T. Ag, "The Infineon Silicon MEMS Microphone," *IEEE Sens. J.*, vol. 15, no. 3, pp. 95–99, 2013.
[30] Alexandrov G and C. N., *Some Tips on Making a FETching Discrete Amplifier*. Analog Dialogue, 2013.
[31] Brüel & Kjær, "Product Data: 1/8" Pressure - field Microphone Type 4138," *Datasheet.* .
[32] J. Serbin, A. Egbert, A. Ostendorf, and B. N. Chichkov, "Femtosecond laser-induced two-photon polymerization of inorganic – organic hybrid materials for applications in photonics," vol. 28, no. 5, pp. 301–303, 2003.
[33] M. Vaezi, S. Chianrabutra, B. Mellor, and S. Yang, "Multiple material additive manufacturing – Part 1: a review," *Virtual Phys. Prototyp.*, vol. 8, no. 1, pp. 19–50, 2013.

Botong Zhu received the bachelor's degree from the University of Strathclyde in 2015, where he is currently pursuing the Ph.D. degree with the Department of Electronic and Electrical Engineering. He is also a PhD student in EPSRC Centre for Doctoral Training in Quantitative NDE. His research interests are in the field of air-coupled transducer development and novel additive manufacturing technologies.

José Guerreiro (S'15-M'18) was born in Lisbon, Portugal, in 1988. He received the B.S. and M.S. degrees in electronic and telecommunications engineering from the High Institute of Engineering of Lisbon, Lisbon, Portugal, in 2013, and he is currently working toward the Ph.D. degree in electronic and electrical engineering at the University of Strathclyde, Glasgow, U.K.

Yansheng Zhang received the bachelor's degree from the University of Strathclyde in 2012, where she is currently pursuing the Ph.D. degree with the Department of Electronic and Electrical Engineering. She is currently a Research Assistant with the Department of Electronic and Electrical Engineering, University of Strathclyde. Her research interests are in the field of biologically-inspired MEMS microphone development.

Benjamin P Tiller is a Research Associate at the University of Strathclyde, in the Department of Electronics and Electrical Engineering, Glasgow, United Kingdom. He did his PhD at University of Glasgow focusing on the frequency scaling relationship of acoustic streaming in microfluidic environments. Before that he completed an MSc in Physics with Theoretical Physics at University of Nottingham. His current research interests involve developing novel 3D printed techniques that enable new sensing technologies.

James F. C. Windmill (M'99-SM'18) is a Professor in the Department of Electronic and Electrical Engineering at the University of Strathclyde, Glasgow, United Kingdom. He received a B.Eng. degree in electronic engineering from the University of Plymouth, UK, in 1998 and a Ph.D. degree in magnetic microscopy from University of Plymouth, UK, in 2002. He joined the Centre for Ultrasonic Engineering (CUE) at the University of Strathclyde as a lecturer in 2008. He has over 18 years of research and development experience in the areas of sensors and hearing systems. His research interests are in the field of biologically-inspired acoustic systems, from the fundamental biology to various engineering application topics.